



**HAL**  
open science

# Numerical modeling and analysis of heat and mass transfers in an adsorption heat storage tank : Influences of material properties, operating conditions and system design on storage performances

Damien Gondre

## ► To cite this version:

Damien Gondre. Numerical modeling and analysis of heat and mass transfers in an adsorption heat storage tank : Influences of material properties, operating conditions and system design on storage performances. Thermics [physics.class-ph]. Université de Lyon, 2016. English. NNT : 2016LYSEI022 . tel-01497406

**HAL Id: tel-01497406**

**<https://theses.hal.science/tel-01497406>**

Submitted on 28 Mar 2017

**HAL** is a multi-disciplinary open access archive for the deposit and dissemination of scientific research documents, whether they are published or not. The documents may come from teaching and research institutions in France or abroad, or from public or private research centers.

L'archive ouverte pluridisciplinaire **HAL**, est destinée au dépôt et à la diffusion de documents scientifiques de niveau recherche, publiés ou non, émanant des établissements d'enseignement et de recherche français ou étrangers, des laboratoires publics ou privés.

N° d'ordre NNT : 2016LYSEI022

**THESE de DOCTORAT DE L'UNIVERSITE DE LYON**  
préparée au sein de  
**I'INSA LYON**

**Ecole Doctorale N° 162**  
**Mécanique, Énergétique, Génie Civil, Acoustique**

**Spécialité de doctorat : Énergétique**

Soutenue publiquement le 21/03/2016, par  
**Damien Gondre**

---

**Numerical modeling and analysis  
of heat and mass transfers  
in an adsorption heat storage tank**  
**Influences of material properties, operating conditions  
and system design on storage performances**

---

Devant le jury composé de :

FAVERGEON Loïc	Maître de Conférences HDR, ENSM de Saint-Etienne	Examineur
JOHANNES Kévin	Maître de Conférences, Université Lyon I	Co-directeur de thèse
KERSKES Henner	Dr-Eng., Stuttgart University	Examineur
KUZNIK Frédéric	Professeur des Universités, INSA de Lyon	Directeur de thèse
LUO Lingai	Directrice de Recherche, LTN - CNRS - Université de Nantes	Examinatrice
PONS Michel	Directeur de Recherche, LIMSI - CNRS - Université de Paris-Saclay	Rapporteur
ROUX Jean-Jacques	Professeur des Universités, INSA de Lyon	Examineur
TOUTAIN Jean	Maître de Conférences HDR, ENSCBP – Bordeaux INP	Rapporteur



## INSA Direction de la Recherche - Liste des Écoles Doctorales

SIGLE	ÉCOLE DOCTORALE	NOM ET COORDONNÉES DU RESPONSABLE
CHIMIE EDA 206	<b>CHIMIE DE LYON</b> <a href="http://www.edchimie-lyon.fr">http://www.edchimie-lyon.fr</a> Sec. : Renée EL MELHEM Bât. Blaise Pascal 3ème étage Tél. : 04 72 43 80 46 Insa : R. GOURDON <a href="mailto:secretariat@edchimie-lyon.fr">secretariat@edchimie-lyon.fr</a>	<b>M. Jean-Marc LANCELIN</b> Université de Lyon - Collège Doctoral Bât. ESCPE 43 bd du 11 novembre 1918 69622 VILLEURBANNE Cedex Tél. : 04 72 43 13 95 <a href="mailto:directeur@edchimie-lyon.fr">directeur@edchimie-lyon.fr</a>
E.E.A. EDA 160	<b>ÉLECTRONIQUE, ÉLECTROTECHNIQUE, AUTOMATIQUE</b> <a href="http://edeea.ec-lyon.fr">http://edeea.ec-lyon.fr</a> Sec. : M. C. HAVGOUDOUKIAN <a href="mailto:ecole-doctorale.eea@ec-lyon.fr">ecole-doctorale.eea@ec-lyon.fr</a>	<b>M. Gérard SCORLETTI</b> École Centrale de Lyon 36, avenue Guy de Collongue 69134 ECULLY Tél. : 04 72 18 60 97 / Fax. : 04 78 43 37 17 <a href="mailto:gerard.scorletti@ec-lyon.fr">gerard.scorletti@ec-lyon.fr</a>
E2M2 EDA 341	<b>ÉVOLUTION, ÉCOSYSTEME, MICROBIOLOGIE, MODÉLISATION</b> <a href="http://e2m2.universite-lyon.fr">http://e2m2.universite-lyon.fr</a> Sec. : Bât. Atrium - UCB Lyon I Tél. : 04 72 44 83 62 Insa : S. REVERCHON <a href="mailto:secretariat.e2m2@univ-lyon1.fr">secretariat.e2m2@univ-lyon1.fr</a>	<b>M. Fabrice CORDEY</b> Laboratoire de Géologie de Lyon Université Claude Bernard Lyon I Bât. Géode - Bureau 225 43, bvd du 11 novembre 1918 69622 VILLEURBANNE Cedex Tél. : 04 72 44 83 74 <a href="mailto:fabrice.cordey@univ-lyon1.fr">fabrice.cordey@univ-lyon1.fr</a>
EDISS EDA 205	<b>INTERDISCIPLINAIRE SCIENCES-SANTÉ</b> <a href="http://ediss-lyon.fr">http://ediss-lyon.fr</a> Bât. Atrium - UCB Lyon I Tél. : 04 72 44 83 62 <a href="mailto:infomaths@univ-lyon1.fr">infomaths@univ-lyon1.fr</a>	<b>Mme Emmanuelle CANET-SOULAS</b> INSERM U1060, CarMeN lab, Univ. Lyon I Bâtiment IMBL 11, avenue Jean Capelle 69621 VILLEURBANNE Cedex Tél. : 04 72 11 90 13 <a href="mailto:emmanuelle.canet@univ-lyon1.fr">emmanuelle.canet@univ-lyon1.fr</a>
INFOMATHS EDA 512	<b>INFORMATIQUE ET MATHÉMATIQUES</b> <a href="http://infomaths.univ-lyon1.fr">http://infomaths.univ-lyon1.fr</a> Sec. : Renée EL MELHEM Bât. Blaise Pascal - 3ème étage <a href="mailto:infomaths@univ-lyon1.fr">infomaths@univ-lyon1.fr</a>	<b>Mme Sylvie CALABRETTO</b> LIRIS - INSA de Lyon - Bât. Blaise Pascal 7, avenue Jean Capelle 69622 VILLEURBANNE Cedex Tél. : 04 72 43 80 46 / Fax. : 04 72 43 16 87 <a href="mailto:sylvie.calabretto@insa-lyon.fr">sylvie.calabretto@insa-lyon.fr</a>
Matériaux EDA 034	<b>MATÉRIAUX DE LYON</b> <a href="http://ed34.universite-lyon.fr">http://ed34.universite-lyon.fr</a> Sec. : M. LABOUNE-DAHMANI Bât. Direction - 1er étage Tél. : 04 72 43 71 70 <a href="mailto:ed.materiaux@insa-lyon.fr">ed.materiaux@insa-lyon.fr</a>	<b>M. Jean-Yves BUFFIERE</b> MATEIS - INSA de Lyon - Bât. Saint Exupéry 7, avenue Jean Capelle 69621 VILLEURBANNE Cedex Tél. : 04 72 43 71 70 / Fax. : 04 72 43 85 28 <a href="mailto:ed.materiaux@insa-lyon.fr">ed.materiaux@insa-lyon.fr</a>
MEGA EDA 162	<b>MÉCANIQUE, ÉNERGÉTIQUE, GÉNIE CIVIL, ACOUSTIQUE</b> <a href="http://mega.universite-lyon.fr">http://mega.universite-lyon.fr</a> Sec. : M. LABOUNE-DAHMANI Bât. Direction - 1er étage Tél. : 04 72 43 71 70 <a href="mailto:mega@insa-lyon.fr">mega@insa-lyon.fr</a>	<b>M. Philippe BOISSE</b> LAMCOS - INSA de Lyon Bât. Jacquard 25 bis, avenue Jean Capelle 69621 VILLEURBANNE Cedex Tél. : 04 72 43 71 70 / Fax. : 04 72 43 72 37 <a href="mailto:philippe.boisse@insa-lyon.fr">philippe.boisse@insa-lyon.fr</a>
ScSo EDA 483	<b>AMÉNAGEMENT, URBANISME, ARCHÉOLOGIE, SCIENCES POLITIQUES, SOCIOLOGIE, ANTHROPOLOGIE</b> <a href="http://recherche.univ-lyon2.fr/scso/">http://recherche.univ-lyon2.fr/scso/</a> Sec. : Viviane POLSINELLI Brigitte DUBOIS Insa : Jean-Yves TOUSSAINT <a href="mailto:viviane.polsinelli@univ-lyon2.fr">viviane.polsinelli@univ-lyon2.fr</a>	<b>Mme Isabelle VON BUELTZINGLOEWEN</b> Université Lyon II 86, rue Pasteur 69365 LYON Cedex 07 Tél. : 04 78 77 23 86 / Fax. : 04 37 28 04 48 <a href="mailto:isavonb@dbmail.com">isavonb@dbmail.com</a>



« Pour arriver au but, il faut être têtus »  
*Ferdinand Cheval*



# Remerciements

Je tiens tout d'abord remercier mes directeurs de thèse, Frédéric Kuznik et Kéryn Johannes, qui ont accepté de me faire confiance pour mener à bien ce projet. Je souhaite souligner la grande liberté qu'ils m'ont laissée dans l'organisation de mon travail et dans le développement de mon projet de recherche. Cela m'a amené à développer mes capacités à travailler en autonomie et à persévérer devant les obstacles les plus grands.

Je tiens à remercier Jean Toutain et Michel Pons d'avoir accepté de rapporter cette thèse en y apportant des commentaires constructifs et encourageants. Je remercie également Lingai Luo, Loïc Favergeon, Henner Kerskes et Jean-Jacques Roux qui se sont déplacés, parfois de loin, pour compléter la composition de mon jury et examiner mes travaux avec un regard neuf et complémentaire.

Je souhaite également remercier toutes les personnes qui m'ont conseillé ou apporté un soutien scientifique ou technique. Je pense notamment à Shihe (pour les méthodes numériques), à Étienne (pour les maths), à Christian (pour Beamer) et à Lucie (pour  $\LaTeX$ ).

La vie au laboratoire ne serait bien entendu pas la même sans la bonne ambiance entre collègues. Je remercie donc Sylvain, Wei, Damien et Luyi, mes co-bureaux successifs, de m'avoir supporté (dans les deux sens du terme) pendant quelques mois voire quelques années. Une petite pensée également pour la team VTT, qui m'a offert quelques moments d'évasion. Pour Kévin et Rémi, mes partenaires de natation. Pour Rodolphe, qui a su prendre le temps de m'écouter et de me remotiver par moment. Pour tous les collègues doctorants, de la génération précédente et actuelle (bon courage pour la fin de vos thèses !), pour les bons moments passés autour de la machine à café et autour de parties de coinche. Une pensée un peu plus particulière pour Aurélia, Olivier et Rémi, qui ont vraiment été présents pour moi quand j'en avais le plus besoin et sans qui il aurait sûrement été plus difficile d'avoir envie de me lever chaque matin pour aller au labo.

Etre soutenu scientifiquement, techniquement et humainement au laboratoire est important, mais serait vain sans tout le soutien que j'ai reçu en dehors. De la part des copains pour commencer. Alex, Blandine, Charlotte, Marie, Mathilde, Solène, Alex, Bastien, Damien, Gaël, JD, Jérémie, John, Marc, Max, Mehdi, Olivier, Rémi, Timo. Ca m'a fait chaud au coeur de vous voir aussi nombreux à ma soutenance, à prendre une demi-journée avant (pour les optimistes) et/ou après (pour les pragmatiques).

Je remercie également ma famille, à commencer par mes parents, qui m'ont toujours fait confiance et m'ont toujours soutenu quelles que soient mes décisions, qui se sont fait du souci pour moi, mais qui ont su rester toujours positifs malgré leurs doutes. Une pensée émue pour

mes deux frères, leurs compagnes, et pour Zélie et Émile. Un grand merci à Noëlle et Juan, mes beau-parents, d'avoir pris régulièrement des nouvelles de ma thèse et surtout d'être venu assister à la soutenance, et d'avoir participé à l'organisation du pot. Merci également à Papalu, mon grand-père, d'avoir fait le trajet depuis Paris pour assister à la soutenance, un peu longue et en anglais. Merci aussi à François, d'avoir fait un passage par Lyon pour l'occasion.

J'ai gardé le meilleur pour la fin, puisqu'il me reste à remercier Jeanne. Tu m'as tellement soutenu, écouté, suppléé, remotivé, chouchouté que cette thèse est aussi un accomplissement pour toi. J'aurai du mal à te rendre ce que tu m'as donné pendant ces 3 ans et demi, et plus particulièrement pendant la dernière année, mais j'ai toute la vie pour refaire petit à petit mon retard, alors je ne perds pas espoir d'y arriver un jour.





# Abstract

The development of energy storage solutions is a key challenge to enable the energy transition from fossil resources to renewable energies. The need to store energy actually comes from a dissociation between energy sources and energy demand. Storing energy meets two principal expectations: have energy available *where* and *when* it is required. Low temperature heat, for dwellings and offices heating, represents a high share of overall energy consumption (i.e. about 35 %). The development of heat storage solutions is then of great importance for energy management, especially in the context of the growing part of renewable energies.

The storage system volume is among the most important limitation for feasibility and user acceptance. Several heat storage technologies are worth considering, among which adsorption technologies are promising in terms of heat storage density and performances over several cycles. This PhD thesis thus focuses on adsorption heat storage and addresses the enhancement of storage performances and system integration. The approach developed to address these issues is numerical. Then, a model of an adsorption heat storage tank is developed, and validated using experimental data.

Currently, the outlet power is the limiting factor in the development of effective storage solutions. The influence of material thermophysical properties on output power but also on storage density and system autonomy is thus investigated. This analysis enables a selection of particularly influencing material properties and a better understanding of heat and mass transfers. The influence of operating conditions is also underlined. It shows the importance of inlet humidity on both storage capacity and outlet power and the great influence of discharge flowrate on outlet power. Finally, it is shown that heat storage capacity depends on the storage tank volume, while outlet power depends on cross section area and system autonomy on bed length.

Besides, an analysis of energy conversion shows that the conversion efficiency from absorbed energy (charge) to released energy (discharge) is 70 %. But during the charging process, about 60 % of incoming heat is not absorbed by the material and directly released. The overall conversion efficiency from energy provided to energy released is as low as 25 %. This demonstrates that an adsorption heat storage system cannot be thought of as a self-standing component but must be integrated into the building systems and control strategy. A clever use of heat losses for heating applications (in winter) or inlet fluid preheating (in summer) enhances global performances.

Heating needs covered by the storage system can be increased (or the volume decreased at constant coverage) by an optimization of the use of available solar resource, especially in winter. Contrary to received wisdom, a direct use of solar energy for heating purposes is not necessarily

the best option. When solar energy is not powerful enough to provide heat at a sufficiently high temperature to start a charging phase, low temperature solar heat can be used for storage tank preheating (with an internal heat exchanger). It enables a more qualitative use of high temperature heat. Indeed, if the material is already warm, high temperature steam shows a higher desorption efficiency since less energy is wasted in sensible heat. Moreover, available solar heat used for system preheating is not wasted. A part is instantly retrieved at the outlet of the storage tank and can be used for direct heating. Another part is stored as sensible heat and can be retrieved a few hours later. At least, it has the advantage of turning the adsorption storage tank into a combined sensible-adsorption storage tank that offers short-term and long-term storage solutions. It may then differ avoidable discharges of the sorption potential and increase the overall autonomy (or coverage fraction), in addition to optimizing chances of partial system recharge.

# Résumé

Le développement de solutions de stockage de l'énergie est un défi majeur pour permettre la transition énergétique d'un mix énergétique fortement carboné vers une part plus importante des énergies renouvelables. La nécessité de stocker de l'énergie vient de la dissociation, spatiale et temporelle, entre la source et la demande d'énergie. Stocker de l'énergie répond à deux besoins principaux : disposer d'énergie à l'endroit et au moment où on en a besoin. La consommation de chaleur à basse température (pour le chauffage des logements et des bureaux) représente une part importante de la consommation totale d'énergie (environ 35 % en France en 2010). Le développement de solutions de stockage de chaleur est donc d'une grande importance, d'autant plus avec la montée en puissance des énergies renouvelables.

Le volume d'un système est un critère important pour la viabilité d'une technologie de stockage et pour son acceptation par ses utilisateurs. Plusieurs technologies de stockage sont envisageables, parmi lesquelles le stockage par adsorption est le plus prometteur en termes de densité de stockage et de maintien des performances sur plusieurs cycles de charge-décharge. Cette thèse se focalise donc sur le stockage de chaleur par adsorption, et traite de l'amélioration des performances du stockage ainsi que de l'amélioration de l'intégration du système au bâtiment. L'approche développée pour répondre à ces questions est numérique. Un modèle de réacteur de stockage de chaleur par adsorption est donc développé et validé par des données expérimentales.

A l'heure actuelle, la puissance récupérable en sortie de réacteur est le facteur limitant le développement de solutions viables technologiquement et économiquement. L'influence des propriétés thermophysiques de l'adsorbant et du fluide sur la densité de puissance d'une part, mais aussi sur la densité de stockage et l'autonomie du système, est étudiée. L'analyse des résultats permet de sélectionner les propriétés des matériaux les plus influentes et de mieux comprendre les transferts de chaleur et de masse au sein du réacteur. L'influence des conditions opératoires est aussi mise en avant. Cela montre l'importance de l'humidité relative à la fois sur la capacité de stockage et sur la puissance récupérable et la très grande influence du débit de décharge sur la puissance. Enfin, il est montré que la capacité de stockage est linéairement dépendante du volume de matériau, tandis que la puissance dépend de la surface de section et que l'autonomie dépend de la longueur du lit d'adsorbant.

Par ailleurs, une analyse de la chaîne énergétique montre que le rapport entre l'énergie absorbée (charge) et relâchée (décharge) est d'environ 70%. Mais pendant la phase de charge, environ 60% de la chaleur entrant dans le réacteur n'est pas absorbée et est directement relâchée à la sortie. La conversion globale entre l'énergie récupérable et l'énergie fournie n'est donc que de 25%.

Cela montre qu'un système de stockage de chaleur par adsorption ne peut pas être pensé comme un système autonome mais doit être intégré aux autres systèmes de chauffage du bâtiment et aux lois de commande qui les régissent. Une réutilisation intelligente des pertes de chaleur pour le chauffage direct du bâtiment (en hiver) ou pour le préchauffage du fluide chaud (en été) améliore les performances énergétiques globales du bâtiment.

La couverture des besoins par le système de stockage peut être améliorée (ou le volume du stockage diminué, à couverture équivalente) par une optimisation de l'utilisation de la ressource solaire disponible, particulièrement en hiver. Contrairement aux idées reçues, l'utilisation de la ressource solaire pour chauffer directement le bâtiment n'est pas forcément la meilleure façon d'optimiser la part solaire dans le mix énergétique. Quand l'énergie solaire n'est pas suffisante pour atteindre des températures raisonnablement hautes pour envisager une phase de stockage, le flux à basse température peut être utilisé pour préchauffer le réacteur. En effet, si le matériau de stockage est déjà chaud, le flux à haute température sera plus rapidement utilisé pour désorber de l'eau puisque moins d'énergie sera utilisée pour chauffer le matériau. La ressource solaire utilisée pour le préchauffage n'est pour autant pas perdue. La part récupérée en sortie peut être réutilisée pour le chauffage direct du bâtiment. La part stockée sous forme sensible peut être récupérée plusieurs heures plus tard. Cela confère, a minima, l'avantage de transformer le système de stockage de chaleur par adsorption en un système de stockage combiné sensible/adsorption, avec une solution pour du stockage à long terme et pour du stockage à court terme. L'utilisation du stockage sensible permet en outre d'éviter des décharges sur le potentiel d'adsorption et ainsi d'augmenter l'autonomie globale du système de stockage, tout en optimisant les chances de recharges partielles en hiver.

# Nomenclature

## Symbols

$b$	Shape coefficient of adsorption isotherm at low pressures	(—)	$A$	Void fraction in the adsorbent bed	(—)
$c$	Heat capacity	(J kg <sup>-1</sup> K <sup>-1</sup> )	$B_a$	Weighting factor for adsorption phenomenon	(—)
$d_p$	Beads diameter	(m)	$B_s$	Weighting factor for thermophysical properties	(—)
$dx$	Mesh spacing in $\vec{e}_x$ direction	(m)	$C_p$	Heat capacity	(J kg <sup>-1</sup> K <sup>-1</sup> )
$dy$	Mesh spacing in $\vec{e}_y$ direction	(m)	$D_b$	Bed diameter	(m)
$dz$	Mesh spacing in $\vec{e}_z$ direction	(m)	$E$	Energy	(J)
$h$	Convection heat transfer coefficient	(W m <sup>-2</sup> K <sup>-1</sup> )	$K$	Bed permeability	(m <sup>-2</sup> )
$k_m$	Global mass transfer coefficient	(s <sup>-1</sup> )	$L$	Bed length	(m)
$m$	Mass	(kg)	$M$	Molar mass	(kg mol <sup>-1</sup> )
$p$	Pressure	(Pa)	$Nu$	Nusselt number	(—)
$q$	Adsorbed layer density	(kg <sub>w</sub> m <sup>-3</sup> )	$P_d$	Outlet heat power density	(W m <sup>-3</sup> )
$q_n$	Adsorption capacity of the first layer	(kg <sub>w</sub> m <sup>-3</sup> )	$Pr$	Prandtl number	(—)
$q_{cap}$	Adsorption capacity of capillary condensation	(kg <sub>w</sub> m <sup>-3</sup> )	$Q$	Heat load	(J)
$t$	Time	(s)	$\dot{Q}_v$	Airflow rate	(m <sup>3</sup> h <sup>-1</sup> )
$t_{step}$	Duration of high temperature stage on discharge	(s)	$R$	Ideal gas constant	(JK <sup>-1</sup> mol <sup>-1</sup> )
$\vec{u}$	Local velocity	(m s <sup>-1</sup> )	$S$	Surface	(m <sup>2</sup> )
$v$	Mean velocity	(m s <sup>-1</sup> )	$S_{exch}$	Exchange surface of adsorbent material	(m <sup>2</sup> )
			$Re$	Reynolds number	(—)
			$T$	Temperature	(K)

$U_b$	Global heat transfer coefficient ( $\text{W m}^{-2} \text{K}^{-1}$ )	$V$	Volume ( $\text{m}^3$ )
		$V_{LJ}$	Lennard-Jones potential (eV)

### Greek letters

$\alpha$	Coefficients of the statistical model	$\mu$	dynamic viscosity ( $\text{Pa s}^{-1}$ )
$\beta$	$T_{film} = \beta T_s + (1 - \beta) T_f$ (—)	$\rho$	Density ( $\text{kg m}^{-3}$ )
$\gamma$	Weighting factor (—)	$\sigma$	Equilibrium distance (m)
$\epsilon$	Error between statistical and numerical model (chapter 3)	$\vec{\varphi}$	Conduction heat flux density ( $\text{W m}^{-2}$ )
$\epsilon_b$	Porosity between beads interstices (—)	$\varphi$	Relative humidity (—)
$\epsilon_p$	Beads internal porosity (—)	$\Delta p$	Pressure drop (Pa)
$\lambda$	Thermal conductivity ( $\text{W m}^{-1} \text{K}^{-1}$ )	$\Delta H$	Differential heat of sorption ( $\text{J kg}^{-1}$ )

### Subscripts notations

0	Initial	$f$	Fluid
$a$	Adsorbed water	$film$	Film (interface between solid and gas phase)
$b$	Bed	$i$	Initial
$cond$	Conductive	$in$	Inlet property
$conv$	Convective	$num$	Numerical result
$c$	Charge	$s$	Solid
$d$	Discharge (or default)	$sf$	Solid-fluid interaction
$da$	Dry air	$v$	Water vapor
$eq$	Equivalent property		
$exp$	Experimental result		

# Contents

Abstract	xv
Nomenclature	xvii
Contents	xvii
List of figures	xix
List of tables	xxiii
Introduction	1
<b>I Adsorption heat storage: a state of the art</b>	<b>7</b>
I.1 Adsorption heat storage interest . . . . .	8
I.1.1 Heat storage technologies overview . . . . .	8
I.1.2 Storage technologies comparison . . . . .	14
I.1.3 Why is this thesis focusing on adsorption heat storage? . . . . .	16
I.2 Adsorption heat storage systems: a state of the art . . . . .	18
I.2.1 Adsorption principle . . . . .	18
I.2.2 Adsorption Materials . . . . .	18
I.2.3 Reactors types . . . . .	20
I.2.4 Existing prototypes: performance evolution and enhancement . . . . .	22
I.3 Heat storage system description . . . . .	27
I.3.1 Systems typology . . . . .	27
I.3.2 Adsorber geometry . . . . .	28
I.3.3 Case study definition . . . . .	28
<b>II Numerical model development of an adsorption heat storage system</b>	<b>31</b>
II.1 Equations formulation . . . . .	32
II.1.1 Definitions . . . . .	32

II.1.2	Numerical modeling of an heterogeneous medium . . . . .	32
II.1.3	Asumptions . . . . .	34
II.1.4	Energy conservation . . . . .	35
II.1.5	Mass conservation . . . . .	37
II.2	Heat and mass transfers in porous media . . . . .	39
II.2.1	A multi-scale approach . . . . .	39
II.2.2	Advection in porous media . . . . .	40
II.2.3	Diffusion in porous media . . . . .	41
II.2.4	Selected approach on kinetic modeling . . . . .	44
II.2.5	Numerical modeling of adsorption equilibrium . . . . .	45
II.2.6	Differential heat of adsorption $\Delta H$ . . . . .	52
II.3	Numerical developments . . . . .	53
II.3.1	Possible numerical methods for spatial discretization . . . . .	54
II.3.2	Model dimension and coordinate system . . . . .	55
II.3.3	Discretization operators . . . . .	57
II.3.4	Model implementation . . . . .	60
II.3.5	Coupled equations . . . . .	61
<b>III</b>	<b>Numerical model validation and reactor first analysis</b>	<b>63</b>
III.1	Mesh dependency . . . . .	63
III.2	Model validation . . . . .	66
III.2.1	Validation of the convection-diffusion model . . . . .	66
III.2.2	Validation of the complete model . . . . .	67
III.3	Dimensionless analysis . . . . .	81
III.3.1	Dimensionless variables . . . . .	81
III.3.2	Nondimensionalization of conservation equations . . . . .	82
III.4	Analysis of energy conversion efficiency . . . . .	87
<b>IV</b>	<b>Detailed analysis of the system: towards material selection and system optimization</b>	<b>95</b>
IV.1	Definition of quantities of interest . . . . .	96
IV.2	Study of thermophysical properties influence . . . . .	96
IV.2.1	Selection of factors, levels and variation ranges . . . . .	97
IV.2.2	Optimization of model parameters . . . . .	97
IV.2.3	Conclusion on the influence and optimization of material properties . . . . .	105
IV.3	Optimization of operating conditions and system geometry . . . . .	106
IV.3.1	Influence of inlet relative humidity $\varphi_{in}$ (on both charge and discharge) . . . . .	107

---

IV.3.2	Influence of inlet fluid velocity $v_{in}$ (on both charge and discharge) . . . . .	108
IV.3.3	Influence of charging inlet temperature $T_{in,charge}$ . . . . .	110
IV.3.4	Influence of bed length $L_z$ and cross section area $S$ . . . . .	112
IV.3.5	Conclusion on the influence and optimization of operating conditions . . . . .	115
IV.4	Development of a metamodel . . . . .	116
<b>V</b>	<b>Integration of the storage system in its building environment and sizing methodology</b>	<b>123</b>
V.1	Sizing methodology . . . . .	124
V.1.1	Thermal energy needs and maximal power estimations using heating degree-hours . . . . .	124
V.1.2	Detailed design information for a long-term energy storage system . . . . .	129
V.1.3	Conclusion on the sizing methodology . . . . .	136
V.2	Storage system integration in a building context . . . . .	137
V.2.1	Possible system operation strategies . . . . .	137
V.2.2	Integrated system design . . . . .	139
V.2.3	Command laws . . . . .	141
V.3	Operating strategies for partial charges optimization . . . . .	143
V.3.1	Influence of initial temperature on system charge . . . . .	143
V.3.2	Enhancement of the full system: utility of an internal heat exchanger . . . . .	145
V.3.3	Cascaded use of heat for system performances increase . . . . .	146
V.3.4	Charging strategy for parallel reactors . . . . .	147
	<b>Conclusions and perspectives</b>	<b>151</b>
	<b>Bibliography</b>	<b>154</b>
	<b>Appendices</b>	<b>162</b>
A	Appendix 1: Detailed coefficients of statistical models . . . . .	165
A.1	Statistical model of outlet power value . . . . .	165
A.2	Statistical model of storage density . . . . .	167
A.3	Statistical model of system autonomy . . . . .	169
B	Appendix 2: Detailed results from energy analysis . . . . .	172
C	Appendix 3: Possible system configurations . . . . .	173



# List of Figures

1	Sankey diagram (NegaWatt Institute) . . . . .	2
2	Comparison between worldwide energy resources and consumption . . . . .	4
I.1	Working principles of absorption and adsorption chillers . . . . .	11
I.2	Classification of heat storage technologies and performances of some storage materials . . . . .	14
I.3	Sorption materials classification . . . . .	16
I.4	Energy storage density against charging temperature for different sorption materials	17
I.5	Lennard Jones potential . . . . .	18
I.6	Schematic representation of different zeolites framework structures . . . . .	20
I.7	Two examples of fixed bed reactors . . . . .	21
I.8	Effect of fins on temperature profile in the adsorbent bed of a closed system . . . . .	22
I.9	Illustration of a fluidized bed and of an external reactor . . . . .	23
I.10	Performances achieved by prototypes or full-scale experiments of different adsorption heat storage projects . . . . .	24
I.11	Illustration of the shape of two existing prototypes . . . . .	25
I.12	Scheme of a rotating prototype . . . . .	25
I.13	Picture of the STAID project prototype . . . . .	26
I.14	Schematic representation of an open adsorption heat storage tank . . . . .	28
I.15	Schematic representation of the adsorber of a closed adsorption heat pump . . . . .	28
II.1	Illustration of equivalent thermal conductivity calculation with <i>COMSOL Multiphysics</i> <sup>®</sup> . . . . .	33
II.2	Energy balance on an elementary volume $dV = dx dy dz$ . . . . .	35
II.3	Mass balance on an elementary volume $dV = dx dy dz$ . . . . .	37
II.4	Adsorption kinetic mechanisms with a double porosity bead . . . . .	39
II.5	Comparison between dynamic responses from diffusion model (Fick) and LDF model	44
II.6	Brunauer classification of equilibrium isotherms . . . . .	46
II.7	Derivation of models for water adsorption on carbons . . . . .	47

II.8	Schematic representation of types I and II isotherms . . . . .	51
II.9	Experimental data and numerical model of water uptake as a function relative humidity and partial pressure . . . . .	52
II.10	Differential heat of adsorption at 40°C . . . . .	53
II.11	Example of the influence of mesh number on calculation time . . . . .	55
II.12	Radial velocity distribution along the bed . . . . .	56
II.13	Subscripts notation for spatial discretization of the adsorbent bed . . . . .	58
III.1	Influence of radial mesh number $nx$ on outlet power and energy storage densities .	64
III.2	Influence of axial mesh number $nz$ on outlet power and energy storage densities . .	65
III.3	Simulation time against mesh number . . . . .	66
III.4	Model validation with glass beads (no adsorption) . . . . .	67
III.5	Experimental setup used for convection-diffusion validation . . . . .	68
III.6	Experimental setup used in STAID project . . . . .	68
III.7	Influence of model coefficients $b$ and $q_{cap}$ on isotherm shape . . . . .	69
III.8	Influence of $b$ and $q_{cap}$ on the shape of temperature profile on charge and discharge	70
III.9	Influence of $q_n$ on the shape of temperature profile on charge and discharge . . . . .	71
III.10	Comparison between charge and discharge values of $k_m$ , $U_b$ , $b$ , $q_n$ and $q_{cap}$ . . . . .	73
III.11	Adsorption isotherm at three different temperature (60°C, 120°C, 180°C) . . . . .	74
III.12	Validation of test case 2 . . . . .	75
III.13	Validation of test case 4 . . . . .	76
III.14	Validation of test case 1 . . . . .	77
III.15	Validation of test case 8 . . . . .	77
III.16	Validation of test case 5 . . . . .	78
III.17	Validation of test case 7 . . . . .	79
III.18	Validation of test case 6 . . . . .	79
III.19	Validation of test case 3 . . . . .	80
III.20	Illustration of absorbed, wasted and released sensible heat on a full charge-discharge cycle (Sankey diagram) . . . . .	90
III.21	Heat conversion ratio against energy released for some of most influencing parameters . . . . .	91
III.22	Temperature profiles on charge for three different values of $L_z$ and $\dot{Q}_{in,charge}$ . . . . .	92
IV.1	Influence of differential heat of adsorption $ \Delta H $ . . . . .	101
IV.2	Influence of vapor molar mass $M_v$ . . . . .	101
IV.3	Influence of adsorption equilibrium value $q_e$ . . . . .	102
IV.4	Influence of adsorbed layer heat capacity $c_a$ . . . . .	103

IV.5	Influence of water vapor heat capacity $C_{p_v}$ . . . . .	104
IV.6	Influence of fluid thermal conductivity $\lambda_f$ . . . . .	104
IV.7	Influence of solid density $\rho_s$ . . . . .	105
IV.8	Influence of bed porosity $\epsilon_b$ . . . . .	106
IV.9	Influence inlet relative humidity . . . . .	109
IV.10	Influence of inlet fluid velocity $v_{in}$ . . . . .	111
IV.11	Influence of inlet fluid temperature $T_{in,charge}$ . . . . .	112
IV.12	Influence of bed length $L_z$ and cross section area $S$ . . . . .	114
IV.13	Linear distributions of outlet power against cross section area, heat storage capacity against storage tank volume, and charging time and autonomy against bed length . . . . .	115
IV.14	Error distribution in the metamodel . . . . .	119
V.1	Storage volume of a TES system as a function of storage density and HDH . . . . .	125
V.2	Occupancy schedules, internal gains and setpoint temperatures for weekdays and weekends as a function of time . . . . .	127
V.3	Annual energy needs and maximal power as a function of HDH . . . . .	129
V.4	Heat coverage fraction calculation as a function of system autonomy . . . . .	130
V.5	Energy to be stored as a function of HDH and system autonomy . . . . .	131
V.6	Decay coefficient . . . . .	132
V.7	Power sizing chart . . . . .	133
V.8	Trend of storage fraction and power fraction as a function of sizing parameters . . . . .	134
V.9	Relationship between normalized storage capacity and normalized design power . . . . .	136
V.10	Average relationship between normalized storage capacity and normalized design power for different system autonomies . . . . .	136
V.11	Four different possible control strategies . . . . .	139
V.12	Sketch of the storage system integration to its building environment . . . . .	140
V.13	Influence of initial temperature on heat storage potential for different partial charging times . . . . .	145
V.14	Internal heat exchanger and associated connections required to enable storage tank preheat, sensible storage and cascaded direct heating of the building . . . . .	146
V.15	Fraction of water weight desorbed as a function of charging time, for three different charging strategies . . . . .	148
V.1	Sankey diagram . . . . .	151
V.2	Full integrated system with internal heat exchanger . . . . .	152
1	System variants . . . . .	174
2	System variants . . . . .	175
3	Enhanced system variants . . . . .	176



# List of Tables

1	Thermal energy mix of residential sector . . . . .	3
I.1	Specificities of different heat storage technologies applied to long term heat storage - quantitative approach . . . . .	15
I.2	Examples of solid adsorption heat storage prototypes performances . . . . .	23
I.3	Closed and open systems features . . . . .	27
II.2	Some correlations for equivalent thermal conductivity calculation . . . . .	33
III.1	Mesh number and distribution used for the study of mesh number influence . . . . .	64
III.2	Deviation observed from asymptotic value on outlet power and energy storage density results for different axial mesh numbers . . . . .	65
III.3	Configurations of STAID project experiments . . . . .	69
III.4	Coefficients used in the equilibrium adsorption model . . . . .	72
III.5	Mean error on charge and discharge for each validation indicator . . . . .	74
III.6	Lower and upper limits used for equations nondimensionalization . . . . .	82
III.7	Summary of dimensionless numbers formulation, default value and physical meaning	88
III.8	Nomenclature for energy conversion analysis . . . . .	89
III.9	Equation formulation for the study of energy conversion within the whole heat storage process . . . . .	94
IV.1	List of thermophysical properties ranked by importance . . . . .	98
IV.2	Analysis of variance on outlet power density and heat storage density, for selected thermophysical properties . . . . .	99
IV.3	Mean difference on outlet power density, heat storage density, charging time and system autonomy between sets of maximum and sets of minimum physical parameters value . . . . .	100
IV.4	Analysis of variance on outlet power density and heat storage density, for different operating conditions . . . . .	108

IV.5	Mean difference on outlet power density, heat storage density, charging time and system autonomy between sets of maximum and sets of minimum operating conditions parameter value . . . . .	109
IV.6	Metamodel variables . . . . .	120
V.1	Wall layout and material properties . . . . .	126
V.2	Wall surfaces and glazing ratios . . . . .	126
V.3	List of cities included in the study . . . . .	127
V.4	Possible configurations . . . . .	140
V.5	Control values of each valve and airflow rates in each branch of the system . . . . .	141
V.6	Nomenclature for command laws . . . . .	142
V.7	Command laws . . . . .	143
1	Correspondence between coded variables $x_i$ and physical variables and minimum/-maximum values used for nondimensionalization . . . . .	165
2	sorted coefficients labels and values and error characteristics of a statistical model for the prediction of outlet power density . . . . .	165
4	sorted coefficients labels and values and error characteristics of a statistical model for the prediction of storage density . . . . .	167
6	sorted coefficients labels and values and error characteristics of a statistical model for the prediction of system autonomy . . . . .	169
8	Influence of thermophysical properties on heat conversion and heat losses. Heat variations are expressed in $kWh.m^{-3}$ . . . . .	172
9	Influence of operating conditions and reactor shape on heat conversion and heat losses. Heat variations are expressed in $kWh.m^{-3}$ . . . . .	173

# Introduction

The development of energy storage solutions is a key challenge to enable the energy transition from fossil resources to renewable energies. The need to store energy actually comes from a **dissociation** between **energy sources** and **energy demand**. Energy supply and demand are both characterized by their geographic location, instant power and flexibility, that might be different. The most primary form of energy is, by definition, something we find in our environment and that we cannot produce but only take advantage of (when available). **Primary energy** are generally classified into fuel resources (oilfield, coal mine, uranium deposit, wood, etc.), and flux energies (wind, solar radiation, hydropower, etc.). Energy plants transform primary energy into useful transportable energy. If supply and demand are geographically distant, an **energy carrier** will be required to transfer energy from the production site to the consumption site. Energy carriers don't produce any energy but only contain and transport it. Electricity, petroleum, gas, coal or firewood are some examples of energy carriers.

Figure 1 displays the share of each primary source in energy production in France. It also shows how primary production is carried, transformed and consumed. This Sankey diagram outlines three principal energy usages: heat (49.1% of overall energy consumption), mobility (32.8%) and electrical devices (15.0%). Primary energy is provided at 88.1% from non-renewable fossil resources<sup>1</sup> and at 11.9% from renewable energies<sup>2</sup> but solar thermal energy only represents 0.03% of total energy production. It is worth noting that as these numbers date from 2010, the share of renewable energies has probably sensibly increased since then.

In a world without storage solutions, energy production should always exactly compensate energy consumption and distribution losses.

$$\underbrace{\text{production}}_{\text{primary energy}} = \underbrace{\text{consumption}}_{\text{final energy}} + \text{distribution losses}$$

Fortunately, it is not mandatory to cut a tree before starting a fire but simply necessary to retrieve a log from the wood store. The wood store can be considered as a storage system. The fuel tank of a car is also an energy storage system, so as the battery of a cellphone. These simple examples show we already use energy storage systems in everyday life. Storing energy actually

---

<sup>1</sup>fossil resources consumption in France in 2010 (share of overall energy consumption): coal (5.3%), oil (39.7%), fossil gas (22.8%), uranium (20.3%) ([Salomon et al., 2012](#))

<sup>2</sup>Solid biomass (6.5%), hydropower (3.1%), liquid biomass (1.2%), wind energy (0.5%) and wastes (0.3%) have the highest shares of renewable energies ([Salomon et al., 2012](#)).



---

Energy source	Final consumption	Share
Fossil gas	188.1 TWh	39.0%
Electricity	104.0 TWh	21.5%
Liquid fuel	81.0 TWh	16.8%
Solid biomass	75.6 TWh	15.7%
Liquid petroleum gas	18.3 TWh	3.8%
District heating	12.2 TWh	2.5%
Coal	2.7 TWh	0.6%
Solar thermal energy	0.7 TWh	0.1%

Table 1 – Thermal energy mix of residential sector in France in 2010 (data from [Salomon et al. \(2012\)](#))

meets two principal expectations: **have energy available *where and when it is required***. This underlines a possible dissociation in space and/or in time of energy supply and demand. An energy storage system solves the problem by satisfying constraints on both supply and demand sides.

This statement is true for a lot of production/usage pairs. Among other energy-consuming sectors such as transports or industry, the **building sector** represents about one third of the total energy consumption of the UE-27 ([IEA, 2009](#); [Eurostat, 2010](#)), and heat production for housing (heating and domestic hot water (DHW)) represents from 19 % ([IEA, 2009](#)) to 24 % of the overall energy consumption of UE-27 ([Eurostat, 2010](#)). The outline of this work focuses, at most, on this share of total energy consumption. Thermal energy accounts for about 80 % of building energy consumption<sup>3</sup> ([Belz et al., 2015](#)). The final application of our concern then involves **thermal energy**, which is one particular form of energy (among others like electrical, mechanical or chemical energies).

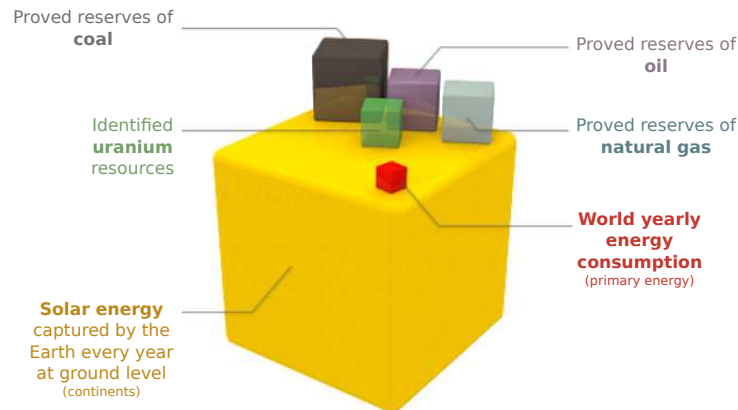
Thermal energy can be generated from a primary source (such as fossil resources or solar energy) or from a secondary source (such as electricity). A careful analysis of figure 1 provides detailed information on the thermal energy mix of residential sector, displayed in table 1. It shows fossil gas (39.0 %), electricity (21.5 %), liquid fuel (16.8 %) and solid biomass (15.7 %) account for 93 % of heat production in residential buildings. The high share of electricity in heat production mix leads to an electricity peak demand around 7 PM in winter<sup>4</sup>, due to a high heat demand in residential buildings. And still it is during peak demand that electricity production is the most expensive and the most pollutant (since thermal power plants run intensively). The use of a storage system in electrically heated dwellings could shift heat demand and thereby reduce electricity peak consumption. Adjustment of the load is known as **demand side management** (DSM) or load management. DSM would be of interest for both energy suppliers, who seek more flexibility in supply balance, and for final consumers, who seek lower energy bills. Load

---

<sup>3</sup>68 % for space heating and 12 % for DHW

<sup>4</sup>Electricity production charts are available online on the website of RTE (Réseau de Transport d'Électricité - *Electricity Transmission Network*). url: [http://clients.rte-france.com/lang/fr/visiteurs/vie/vie\\_reconst\\_flux\\_C10.jsp](http://clients.rte-france.com/lang/fr/visiteurs/vie/vie_reconst_flux_C10.jsp)

Figure 2 – Comparison between solar yearly resource, total worldwide energy consumption, and proven reserves of fossils energies (Ramos, 2013)



management would also reduce harmful emission since peaking plants are often less efficient or dirtier than base load power plants.

Heat can be stored in numerous ways (sensible, latent, thermochemical) that are all relevant for different applications. It is then important to clearly **define the specifications** prior to choose a **technical solution**. A storage system is characterized by several indicators such as energy density, specific power, autonomy, conversion efficiency and cost. Volume and cost of heat storage systems are among the most important issues for **user acceptance**. Sizing a building heat storage system provides information on energy and power requirements based on the knowledge of building envelope, climate, heat store usage and desired system autonomy. A sizing methodology is developed in chapter 5.

Once the interest of energy storage systems is settled, one can think of the best way to make good use of it. As stated earlier, a heat storage system helps meeting supply and demand requirements by allowing load management. It may also open up new perspectives of heat generation that were not likely possible without the use of a storage solution. This is particularly true for **renewable energies** such as solar potential. About 21 % of building sector heat share is produced from renewable energy sources like wood<sup>5</sup>, waste<sup>6</sup> or hydropower<sup>7</sup>. It means that about 79 % of heat generated in residential buildings comes from fossil resources. And still the total amount of solar energy received yearly on earth is more than 1000 times greater than the world yearly energy consumption (Ramos, 2013). A part of this incoming flux is naturally converted into renewable energies<sup>8</sup>. But direct use of solar thermal energy is not widely developed (0.1 %). And still it is the most direct way to produce heat locally (Ampatzi et al., 2013), as opposed to wind power or hydropower that would call for electricity as an energy carrier. Figure 2 graphically compares known reserves of fossil resources to the solar energy potential and to the world energy consump-

<sup>5</sup>15.7 % for solid biomass

<sup>6</sup>2.5 % for district heating

<sup>7</sup>12.0 % of electricity production, meaning about 2.6 % of heat production through electricity

<sup>8</sup>Photosynthesis converts solar energy into biomass. Water evaporation converts solar energy into potential energy used in hydroelectric power plants. And ground surface heating generates pressure differences and thermal updraught that maintains movements of air masses exploited by wind turbines.

---

tion. A comparison with data from table 1 clearly shows a lack of consistency between available resources and primary resources actually used. Increasing the share of renewable energies in building heating would make sense both economically and environmentally since fossil energies are bound to cost more and more with rarefaction (and increasing extraction complexity), while renewable energies are freely available in our direct environment.

But as solar potential (high in summer and low in winter) and heat demand (high in winter and low in summer) are shifted, an increase of the share of solar thermal energy necessarily requires heat storage solutions that are technically, economically and environmentally effective. Such systems should be able to store energy during a long time (several weeks or months) (Hadorn, 2005). The main issue is to propose a high storage density in order to minimize the storage system volume, while allowing a good discharge power. Many research projects in recent years have focused on inter seasonal heat storage (Pinel et al., 2011; Hongois et al., 2011; Bauer et al., 2010; Michel et al., 2012; Metchueng Kamdem et al., 2012; Duquesne et al., 2014; Tatsidjodoung, 2014; Fopah Lele et al., 2015) but few have addressed the problem with a view to the system performances in realistic conditions (chapter 5).

Several storage techniques are well suited for long-term energy storage such as geothermal, absorption, physical adsorption or chemical heat storage. As explained in the first chapter, this thesis focuses on adsorption heat storage. A numerical model of an open adsorption heat storage system is developed (chapter 2) and validated with experimental data (chapter 3). This model is then used in order to assess the influence of material properties, system geometry and operating conditions on the results (chapter 4). The objective is to provide some specification requirements for material development and storage tank design. Finally, the integration of the storage system in its building's environment is discussed (chapter 5). A fully integrated system design is evoked, with a reflection on control strategy that would enable partial charges and discharges in winter season.



# Chapter I

## Adsorption heat storage: a state of the art

### Contents

---

I.1	Adsorption heat storage interest . . . . .	8
I.1.1	Heat storage technologies overview . . . . .	8
I.1.2	Storage technologies comparison . . . . .	14
I.1.3	Why is this thesis focusing on adsorption heat storage? . . . . .	16
I.2	Adsorption heat storage systems: a state of the art . . . . .	18
I.2.1	Adsorption principle . . . . .	18
I.2.2	Adsorption Materials . . . . .	18
I.2.3	Reactors types . . . . .	20
I.2.4	Existing prototypes: performance evolution and enhancement . . . . .	22
I.3	Heat storage system description . . . . .	27
I.3.1	Systems typology . . . . .	27
I.3.2	Adsorber geometry . . . . .	28
I.3.3	Case study definition . . . . .	28

---

Introduction part has shown the growing interest in heat storage. Development of heat storage technologies is not only interesting as a **scientific challenge** or a potentially profitable activity, this is interesting as a **key technology** in the development of more balanced energy distribution networks. This is particularly true with the increase of renewable energies in the energy mix. The need for heat storage solutions comes with **specification requirements**. The objective is to develop, as far as possible, a system that is capable of **storing heat on the long run** (several months), with a **high energy storage density** in order to reduce volume. Reaching **high outlet power** is also of great interest for building heating applications (or even domestic hot water). Several others criteria such as system cost, security and low environmental impacts are of great importance to ensure a good user acceptance but this will not be addressed in this thesis. Adsorption heat storage seems to be a promising technology that could meet all these criteria within a few years after some ongoing research developments.

This first chapter is not intended to include all bibliographical researches conducted in the framework of this thesis. Technical points are addressed gradually, when needed. The present chapter gives an overview of available technologies that enable long-term heat storage. Benefits, drawbacks and applications of each technology is discussed prior to a comparison that justify a focus on adsorption systems. A state of the art of adsorption heat storage systems is then developed. It describes physical principles, available materials and existing prototypes. The goal of this section is to select a case study. This case study will then be used in the remainder of the thesis to conduct a research work on the influence of material properties, system geometry and operating conditions on system performances.

## I.1 Adsorption heat storage interest

### I.1.1 Heat storage technologies overview

Storing heat is fairly different than storing others forms of energy (electricity or mechanical energy for instance). It calls on different techniques depending on the purpose and on the time span of the storage. There are mainly three different heat storage categories: sensible, latent and thermochemical heat storage (including absorption, physical adsorption and chemical adsorption).

#### I.1.1.1 Sensible heat storage

Sensible heat storage takes advantage of a change in the temperature of a material. Sensible heat storage capacity is expressed in equation I.1 through first law of thermodynamics.

$$Q_{sensible} = \rho V C_p (T_f - T_i) \quad (I.1)$$

$Q_{sensible}$  [J] heat is stored in a volume  $V$  [m<sup>3</sup>] of material with a density  $\rho$  [kg m<sup>-3</sup>], a specific heat capacity  $C_p$  [J kg<sup>-1</sup> K<sup>-1</sup>] and a temperature elevation  $\Delta T$  [K] from initial temperature  $T_i$  to final storage temperature  $T_f$ .

**Storage media** Sensible heat storage materials are mainly divided into two categories: liquid storage media like water, salty water or oil, and solid storage media like rocks, building fabric materials or metals (Hasnain, 1998). Tatsidjodoung et al. (2013) provides a list of potential solid and liquid materials for sensible heat storage.

**Benefits** Sensible heat storage systems are well-known and produced at low cost. It can store energy as soon as the hot source temperature is higher than the tank temperature.

**Drawbacks** Temperature difference is a driving force for heat transfers. A greater temperature difference will lead to a greater rate of heat losses. A good thermal insulation is then required. Besides, the temperature difference of liquids storage media can be limited by the phase change temperature. Dilation effects may also be hard to handle on solids storage media.

**Applications** Most applications are intended to store heat for daily (or weekly) spans. Domestic hot water storage is probably the most widespread application. Thermal mass of buildings materials can cleverly be used to upgrade thermal comfort and shift solar gains from daytime to night time (Braun, 2003). Some projects plan on storing heat for longer periods, in the ground or in wide semi-buried insulated storage tanks (Bauer et al., 2010; Pinel et al., 2011; Schneider, 2013). Several wide scale experiments have been developed on the framework of *Solarthermie 2000* project (Belz et al., 2015).

Xu et al. (2013, table 2) dress a list of 38 achieved sensible seasonal heat storage projects detailing - if available - location, heated living area, district heat demand, solar collector area, storage volume and solar fraction. A 45% solar fraction is obtained on average. The solar collector area represents 18 % of the heated area (but wide disparities are observed among results). An average calculation over all projects with available data (7/38) shows that sensible storage average volume is  $0.32 \text{ m}^3 \text{ m}^{-2}$ . In others words, a sensible storage system requires an average volume equivalent to the whole heated surface area on a 32 cm height.

### I.1.1.2 Latent heat storage

Heat is stored using heat of transformation absorbed or released by a material that goes from one physical state to another (solid, liquid or gas). For example, in a solid/liquid transformation, latent heat storage capacity is expressed in the following equation I.2.

$$Q_{latent} = \rho V (C_{p_s} (T_m - T_i) + \Delta H_{fus} + C_{p_l} (T_f - T_m)) \quad (\text{I.2})$$

$Q_{latent}$  [J] heat is stored in a volume  $V$  [ $\text{m}^3$ ] of material with a density  $\rho$  [ $\text{kg m}^{-3}$ ], specific heat capacity  $C_{p_s}$  and  $C_{p_l}$  [ $\text{J kg}^{-1} \text{K}^{-1}$ ] (for solid and liquid states), enthalpy of fusion  $\Delta H_{fus}$  [ $\text{J kg}^{-1}$ ], melting temperature  $T_m$  [K] and a temperature elevation  $\Delta T$  [K] from initial temperature  $T_i$  to final storage temperature  $T_f > T_m$  (Sharma et al., 2009).

**Storage media** Solid-solid transformations are interesting because of a negligible volume change but their heats of transformation are too small. Most promising materials are organic solid solution of pentaerythritol and pentaglycerine (Sharma et al., 2009). Solid-gas and liquid-gas transformations imply large volume change which is difficult to handle. Most researches on phase change materials (PCM) then focused on solid-liquid transformations. PCMs can be sorted in organic, inorganic and eutectic (alloys) materials. Zalba et al. (2003) and Tatsidjoudoung et al. (2013) both provide a classification scheme and a list of PCMs properties with melting temperature and heat of fusion. Most values of latent heat of fusion lie in the range from 150 to  $250 \text{ kJ kg}^{-1}$ .

**Benefits** Latent heat storage allows a higher heat storage density than sensible heat storage with a lower temperature difference. Literature is sufficiently complete to provide materials for a wide range of melting points and therefore a wide range of applications. It is noteworthy used for short term heat storage when embedded in walls (Kuznik et al., 2011) or in a PCM to air heat exchanger (Arzamendia Lopez et al., 2013; Labat et al., 2014).

**Drawbacks** Like sensible heat storage, latent heat storage is subject to heat losses which implies a time constraint in the use of heat stored. Furthermore, use of PCM may require economical and environmental considerations. Work achieved at HEIG-VD in the framework of IEA task 32 has shown that the use of PCM can account for 30 % of non-recurring engineering (NRE) and 20 % of global warming potential (GWP) in a heat storage system. This report also underlines that PCM materials cost from 1 to 4€ kg<sup>-1</sup> and does not lead to significant energy retrofit compared to long-term sensible heat storage (Streicher et al., 2007).

**Applications** Sharma et al. (2009) and (Zalba et al., 2003, table 10) list several applications for PCMs materials. PCMs can be included in water heating systems, air heating systems or directly in building materials. Main objectives are to reduce systems volume, increase systems autonomy or maximize the use of solar resource and lower auxiliary energy needs. PCMs materials are often used in a passive way. Such systems are not completely controllable and have low solar fractions. It is then intended to store energy for periods ranging from one hour to a few days. Among active PCMs systems, a few projects reached high solar fractions (Xu et al., 2013). Subcooling PCMs for long term heat storage was investigated through simulations at the Department of Civil Engineering of Technical University of Denmark. It enabled to reach a 100 % solar fraction with a 10m<sup>3</sup> storage tank supplying a 135 m<sup>2</sup> floor area passive house with 15 kWh m<sup>-2</sup> y<sup>-1</sup> heating needs (Streicher et al., 2008). Even if this volume is still very large to consider wide scale commercial applications, it is a good attempt with a specific volume of 0.07 m<sup>3</sup> m<sup>-2</sup>.

### I.1.1.3 Absorption heat storage

*Absorption heat storage systems* consist in associating a gaseous working fluid called *sorbate* and a liquid sorption solution referred to as the *sorbent*. Sorbent releases sorbate vapor when heated and releases heat when retaining sorbate molecules (Bales et al., 2005b). Sorption heat storage potential is expressed with the following equation I.3.

$$Q_{sorption} = -V |\Delta H| \Delta q \quad (I.3)$$

A  $Q_{sorption}$  heat potential is stored in a volume  $V$  [m<sup>3</sup>] of absorption solution characterized by a specific heat of sorption  $|\Delta H|$  [J kg<sup>-1</sup>] and a sorbate uptake capacity  $\Delta q$  [kg m<sup>-3</sup>] during unload phase (with  $\Delta q = q_{load} - q_{unload}$ ).

**Storage media** Absorption materials are liquid solutions (salt-hydrates) with a high affinity for water.

**Benefits** Sorption storage solutions are less dependent on heat losses than sensible or PCM heat storage. It makes absorption heat storage suitable for long-term energy storage. It also has good abilities to maintain performances over several cycles. Xu et al. (2013, table 8) sum up data on absorption material properties. It shows that energy storage density of absorption solutions varies from 193 kJ kg<sup>-1</sup> (glycerin/H<sub>2</sub>O) to 4387 kJ kg<sup>-1</sup> (LiCl/H<sub>2</sub>O), which is very interesting. Besides, absorption technologies can run continuously as opposed to adsorption systems that are alternating. This is a good point for solar cooling applications, since the solar resource and

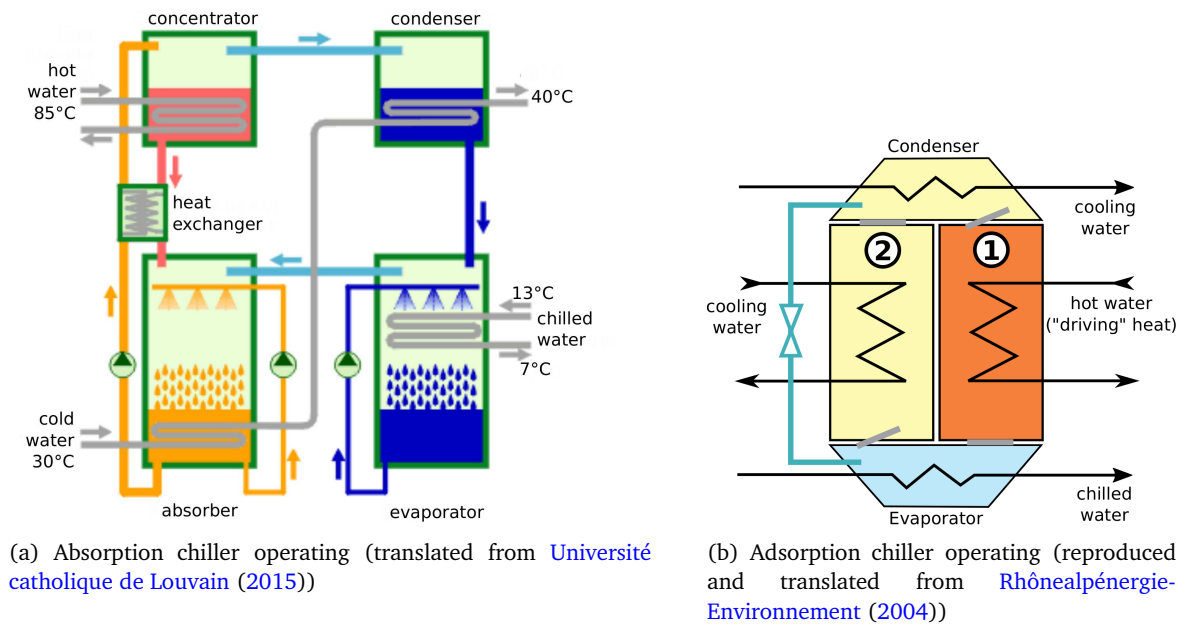


Figure I.1 – Working principles of absorption and adsorption chillers

the cold needs generally occur simultaneously. Nevertheless, this is pointless for heat storage applications since solar resource is used for system charge and will thereby never be used at the same time than discharge process. In this case, it would be of greater interest to directly use the solar resource, or to recover heat at the outlet of the reactor while charging.

**Drawbacks** The use of absorption systems in heat storage provides good energy densities but poor outlet temperature which are limiting heating applications ([Zondag et al., 2013](#)). [N'Tsoukpoe et al. \(2012\)](#) get outlet temperature of about 30°C which is barely acceptable for low temperature floor heating systems. Nonetheless, other researches have proven a good capacity to produce heat at acceptable temperatures, to the cost of a lower energy storage density ([Zhang et al., 2014](#)). Besides, absorption systems run at low pressure with working pairs that are potentially harmful for the environment. It then requires to prevent the system from any leakage. [N'Tsoukpoe et al. \(2012\)](#) also underline that cost of absorption pairs is an important issue for system viability.

**Applications** As stated earlier, absorption systems are widely spread for cooling applications. It enables the use of low temperature sources ( $\approx 70 - 100^\circ\text{C}$ ) that can come from wasted heat or from solar heat. Figure I.1a illustrates the operating of adsorption chillers, that act like a heat pump.

An absorption chiller (figure I.1a) is made of four principal components: an absorber, an evaporator, a concentrator and a condenser. The **absorber** contains the sorbent solution (LiBr, LiCl, CaCl<sub>2</sub> or KOH for instance). The **evaporator** contains pure water that is sprayed on a water loop. A low pressure is maintained in the evaporator and fosters water evaporation, that retrieve heat from the water loop (cold production). Water vapor thus generated is transferred to the absorber through a vapor line. Vapor is absorbed by the solution which maintains a **low pressure** in the absorber and in the evaporator. Absorption generates heat and tends to warm the absorber.

A temperate water loop maintains the solution to an acceptable temperature. The sorbent solution is continuously regenerated in the **concentrator** where hot water is used to separate water vapor from the solution. Water vapor is condensed in a **condenser** and flows back in the evaporator.

Researches are also conducted on the use of absorption systems for heat storage applications. [Fumey et al. \(2014\)](#) propose a prototype of 43 m<sup>3</sup> on 19 m<sup>2</sup> to fulfill whole energy requirements for a single family house. It is a first step towards more compactedness. [Hui et al. \(2011\)](#) evaluate the performances of seven absorption couples and show crystallization of the sorbent solution improves thermal performances. [Zhang et al. \(2014\)](#) developed a prototype of an absorption hybrid system using LiBr – H<sub>2</sub>O. This prototype is capable of producing 42 kWh m<sup>-3</sup> of cold at 7 °C, 88 kWh m<sup>-3</sup> of domestic hot water at 65 °C, and 110 kWh m<sup>-3</sup> of heat at 43 °C.

#### I.1.1.4 Adsorption heat storage

*Physical adsorption heat storage systems* use a very similar physical process than absorption. The main difference remains in the association of a gaseous working fluid (sorbate) (mostly water) with a *solid* sorption material (sorbent).

**Storage media** Adsorption materials are porous solids (like zeolites, activated carbon, silica gel, etc.) that offer a large exchange surface. The greater the surface is, the more adsorption sites are available to the sorbate.

**Benefits** Sorption heat storage potential can be retained as long as needed while the storage tank remains sealed. Furthermore, a good cyclability of the adsorption process is observed and may even improve storage performances ([Neuhaus, 2013](#)). With theoretical energy storage densities from 250 to 750 kJ kg<sup>-1</sup> ([Yu et al., 2013](#)), storage densities for adsorption technologies are higher than for latent storage which results in lower storage volumes.

**Drawbacks** Heat is generated deeply inside the sorption material and must be retrieved from the reactor. But heat and mass transfers are slowed down by the material porosity. It results in poor heating powers. Moreover, sorption materials may be quite expensive resulting in high cost of storage systems.

**Applications** A review of adsorption and absorption heat pumps systems and applications is provided by [Wongsuwan et al. \(2001\)](#). In sorption storage systems, heat may be stored for long periods since heat losses (from sensible storage part) are not dominant compared to the overall heat potential stored (as a sorption potential). Furthermore, charging temperatures vary from 100 to 180 °C which makes it suitable for solar heat storage applications. Adsorption heat storage systems are then intended to store heat from a week to several months.

Cold production is also possible with adsorption chillers ([Pons and Grenier, 1986](#)). Figure I.1b displays the working principle of an adsorption chiller. As the sorbent material is solid, it stays in its vessel. Two adsorbent beds are then used in alternation as an adsorber (marked 2 on figure I.1b) or as a desorber (marked 1 on figure I.1b). Once the adsorber is saturated, roles are interchanged with a system of valves.

### I.1.1.5 Chemical heat storage

In chemical adsorption heat storage systems, thermal energy is used - when available - to drive a reversible and endothermic<sup>1</sup> reaction. It generally involves one reactant (AB) and gives two products (A and B). The inverse reaction is triggered whenever it is relevant to retrieve heat. Both products of the first reaction (A and B) are then put in touch and merge to one molecule (AB) (Kuznik et al., 2011). This reaction is exothermic due to energy released with bond making (Van Berkel, 2005). This process is expressed in the following relation.



with  $\Delta H_r$  [J m<sup>-3</sup>] the heat of reaction,  $M_{AB}$  [kg mol<sup>-1</sup>] the molar mass of molecule AB and  $\rho_{AB}$  [kg m<sup>-3</sup>] its density. The potential chemical energy  $Q_{chemical}$  [J] is stored in a volume  $V$  [m<sup>3</sup>] of reactants.

$$Q_{chemical} = V \Delta H_r \quad (\text{I.5})$$

**Storage media** Van Berkel (2005) and Pardo et al. (2014) list main reactant families (metallic hydrides, carbonate, hydroxydes, redox, ammonia and organic systems) and give a list of potential reactions with associated heats of reaction. Trausel et al. (2014) also give a list of potential salt hydrates suitable for chemical heat storage with heats of reaction and cost estimation.

**Benefits** Potential storage heat density is by far the highest among investigated storage technologies since heats of reaction are very high. It ranges from 330 kJ kg<sup>-1</sup> (PbCO<sub>3</sub>, charged at 450 °C) to 2850 kJ kg<sup>-1</sup> (MgH<sub>2</sub>, charged at 380 °C) and 2919 kJ kg<sup>-1</sup> (NH<sub>4</sub>HSO<sub>4</sub>, charged at 927 °C) (Pardo et al., 2014). Reaction kinetics are also promising for maximizing heat transfer rate during unloading phases.

**Drawbacks** Reaction temperatures are high (150 - 1000 °C) and only those lower than 250 °C could be considered for solar heat storage applications with domestic collectors. Moreover, **cyclability problems** have been reported in practice due to the formation of a crust and a swelling of the grains (Hongois et al., 2011; Kuznik et al., 2015b).

**Applications** Dehydration of salt hydrates and other chemical materials generally requires higher regeneration temperatures than sorption materials (from 180 to 1000 °C). Chemical storage systems also provide higher heats of reactions and discharging temperatures. It then must be associated with a high temperature energy source. Fujimoto et al. (2002) propose for example a chemical heat pump system that uses CaO/Ca(OH)<sub>2</sub> as a reactant. Charging process is achieved at 673 K (400 °C) which is unreasonable for solar applications. Azpiazu et al. (2003) use a furnace to dehydrate the same reaction pair at 550 °C.

---

<sup>1</sup>The reaction is endothermic because of the energy required for bond breaking

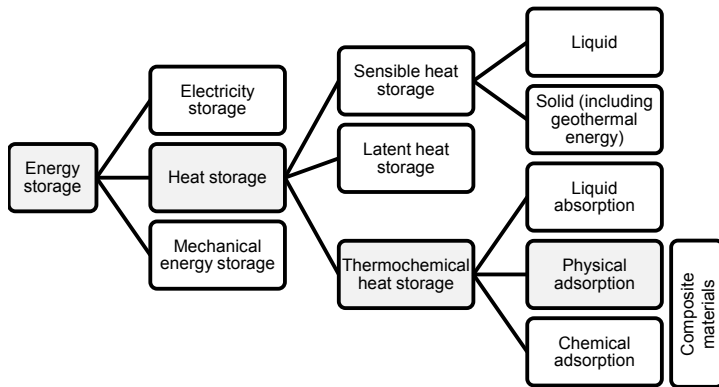
**I.1.1.6 Composite materials**

Composite materials aim at combining the main advantage of chemical materials (high heat of reaction) without their main drawback (lack of reaction reversibility due to reactant agglomeration). It uses a porous (adsorption) material impregnated with a chemical material.

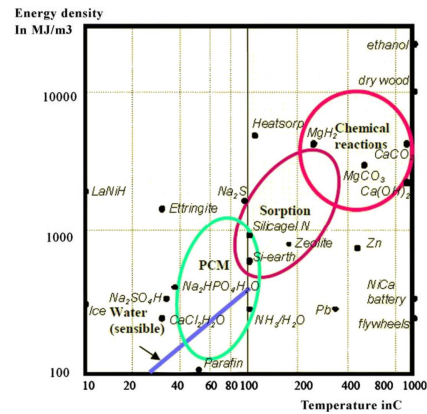
Results from [Hongois et al. \(2011\)](#) have shown that energy density is not much higher for Zeolite 13X impregnated with 5% to 15% of  $MgSO_4$  than for pure Zeolite 13X. But researches are still in progress in this field.

**I.1.2 Storage technologies comparison**

A brief overview of available heat storage technologies has been given in the previous section (I.1.1). It is graphically displayed in figure I.2a. This enables to keep in mind that adsorption heat storage is only one possible technology, among many others. It is also worth mentioning heat storage is one field in energy storage technologies. A lot of researches are conducted on improvement of electricity storage solutions. It is especially intended to develop mobile applications autonomy (electronic devices or electric cars for instance), independent local networks, and to balance more easily electricity production and demand.



(a) The place of adsorption technologies among others heat storage technologies



(b) Energy storage density against operating temperature for different heat storage materials ([N'Tsoukpoie et al., 2009](#))

Figure I.2 – Classification of heat storage technologies and performances of some storage materials

Figure I.2b displays energy density against operating temperature of several storage materials. It clearly shows a trend between storage technologies. Table I.1 provides some additional information on investment cost and on more qualitative points such as system lifetime, suitability for long-term storage, or environmental impact.

Figure I.2b shows sensible storage has the lowest energy density potential, but also operates at low temperatures. Phase change materials reach higher storage densities in the same range of temperature. It is then more promising than sensible storage in terms of system compactedness. Sorption materials offer higher storage densities to the cost of higher charging temperatures. It nonetheless remains in an acceptable range for solar applications. Finally, chemical reactions

Table I.1 – Specificities of different heat storage technologies applied to long term heat storage - quantitative approach

decision points			heat storage technology				
			Geothermal	Latent	Absorption	Adsorption	Chemical
Energy density ( $\text{kWh m}_{\text{mat}}^{-3}$ )	min		15 <sup>a</sup>	50 <sup>a</sup>	50 <sup>a</sup>	60 <sup>a</sup>	400 <sup>b</sup>
	max		40 <sup>a</sup>	130 <sup>a</sup>	475 <sup>a</sup>	180 <sup>a</sup>	1000 <sup>b</sup>
			★☆☆☆☆	★★★★☆	★★★★☆	★★★★☆	★★★★★
High heat power			★★☆☆☆	★★★★☆	★★★★☆	★★★★☆	★★★★★
Low charging temperature (°C)	min		25	40 <sup>b</sup>	50 <sup>d</sup>	120 <sup>b</sup>	180 <sup>b</sup>
	max		-	100 <sup>b</sup>	160 <sup>d</sup>	200 <sup>b</sup>	1000 <sup>b</sup>
			★★★★★	★★★★☆	★★★★★	★★★★☆	☆☆☆☆☆
Investment cost ( $\text{€ m}_{\text{water equivalent}}^{-3}$ )	min		50 <sup>a</sup>		35 <sup>a</sup> ◇	800 <sup>c</sup> ◇	
	max		450 <sup>a</sup>		825 <sup>c</sup> ◇	5000 <sup>c</sup> ◇	
			★★★★☆		★★★★☆	☆☆☆☆☆	
System lifetime (number of cycles)			★★★★★	★★★★★	★★★★★	★★★★★	★★★★☆
Suitable for long-term storage			★★★★☆	★★★★☆	★★★★★	★★★★★	★★★★★
Low environmental impact			★★☆☆☆	☆☆☆☆☆	☆☆☆☆☆	★★★★☆	★★★★☆

◇. Calculated value a. Xu et al. (2013) b. N<sup>o</sup>Tsoukpoé et al. (2009) c. Bales et al. (2008) d. Yu et al. (2013)

Each decision point is evaluated and marked with up to five black stars ★ (low *guaranteed* level) and/or gray stars ☆ (high *hypothetical* level). Grades are attributed arbitrarily and are intended to compare one solution to another.

reach highest storage densities. But two severe limitations are noticed. A too high temperature range rules out these materials for solar applications (from 200 °C to 1000 °C). Moreover, researchers are currently facing loss of performances as the number of charge-decharge cycles increases. This is due to irreversibilities in some reactions that lead to an agglomeration of reactive particles. A classical workaround consists in using a support material as a matrix that is impregnated with the reactant material (Azpiazu et al., 2003; Hongois, 2011; Kim et al., 2013; Mastronardo et al., 2016). Some researches are nonetheless claiming good reversibility for up to 20 cycles (Molenda et al., 2013).

Figure I.2b globally demonstrates sorption materials are good candidates to maximize energy storage density while remaining in acceptable temperature ranges (100 °C - 180 °C) for solar applications. But sorption is a term that refers to different families. It refers to **liquid absorption** or **solid adsorption**. And to some extent, it can also refer to **composite materials** that combines adsorption effect on a matrix impregnated with a reactant that participates in chemical reactions. Finally, **chemisorption** can also be included in sorption systems since it also calls for a reaction between a solid surface and a bulk phase. The main difference between *physisorption* and *chemisorption* lies in interaction forces that are weak Van der Waals forces and electrostatic interactions for what physisorption is concerned (Sun and Meunier, 2003), and strong interactions created by chemical bonds ( $> 40 \text{ kJ mol}^{-1}$ ) for what chemisorption is concerned (Duval, 2012). Figure I.3 presents different examples of materials and species for each of these four classes of sorbents.

Now that the meaning of *sorption* term is clarified, questions are raised about specific performances of sorption materials. Figure I.4 displays energy storage density against charging temper-

ature for different sorption materials. Materials are grouped together under five families. Among chemical reactions, composite materials and liquid absorption, solid adsorption is split into zeolites and silica gels. **Silica gels** presented here have very low energy densities but operate at relatively low temperature ( $\approx 90^\circ\text{C}$ ). **Zeolites** offer significantly higher storage densities than silica gels even if charging temperature range is higher. **Chemical reaction materials** are ruled out for lifetime and charging temperature issues.

**Composite materials** are good candidates for rather high heat storage densities with acceptable temperature range and repeatable cycles. Nevertheless, there often is a great difference between theoretical and experimental performances of composite materials. [Hongois \(2011\)](#) has for example shown energy density of 13X-zeolite impregnated with magnesium sulfate (ZM10) is not higher than that of pure 13X-zeolite. A lot of researches are still ongoing to develop high energy performance composite materials, but in most cases, it goes through experimental investigations instead of numerical modeling. Indeed, it is very complicated to set up a numerical model that would take into account all transfers and chemical mechanisms at a microscopic scale. It would require a great deal of effort and computing resources. Research on composite materials is then promising but lies outside the scope of this thesis.

**Absorption heat storage** has several advantages such as low charging temperatures and good storage densities. But the main drawback of absorption heat storage remains in the low temperature drop on discharge compared to adsorption or chemical processes.

### I.1.3 Why is this thesis focusing on adsorption heat storage?

Several storage technologies have been investigated for long-term heat storage applications. **Geothermal heat storage** projects are mainly interesting for large scale operations and request wide surfaces to reach good storage capacities. It is then not really suitable for individual dwellings or downtown projects. **Latent heat storage** systems are interesting for short term heat storage applications (on a daily scale), but are not suitable for long-term heat storage because of sensible losses. **Pure chemical heat storage** are currently not applicable over several cycles due to

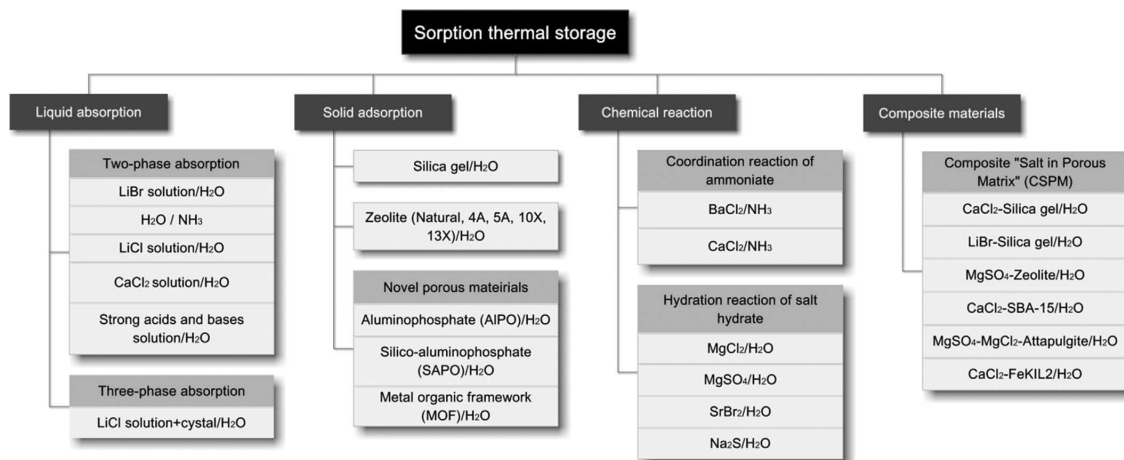


Figure I.3 – Sorption materials classification ([Yu et al., 2013](#), figure 8)



## I.2 Adsorption heat storage systems: a state of the art

### I.2.1 Adsorption principle

Adsorption is a process in which atoms or molecules move from a bulk phase (that may be solid, liquid, or gas) onto a solid or liquid surface (Bent, 2012). Attractive interactions occur between the surface (*adsorbent*) and molecules being adsorbed (*adsorbate*). An equilibrium point is reached when attractive and repulsive (Pauli) forces compensate each other. Lennard-Jones potential describes this equilibrium (equation I.6 and figure I.5).

$$V_{LJ}(r) = 4\epsilon \left[ \left( \frac{\sigma}{r} \right)^{12} - \left( \frac{\sigma}{r} \right)^6 \right] \quad (I.6)$$

$\sigma$  is the distance at which the potential is zero and  $\epsilon$  is the depth of the potential well. The higher  $\epsilon$  is, the more energy is released with adsorption (and required for desorption). This exothermic/endothermic process is used to release/store heat. The magnitude of the potential

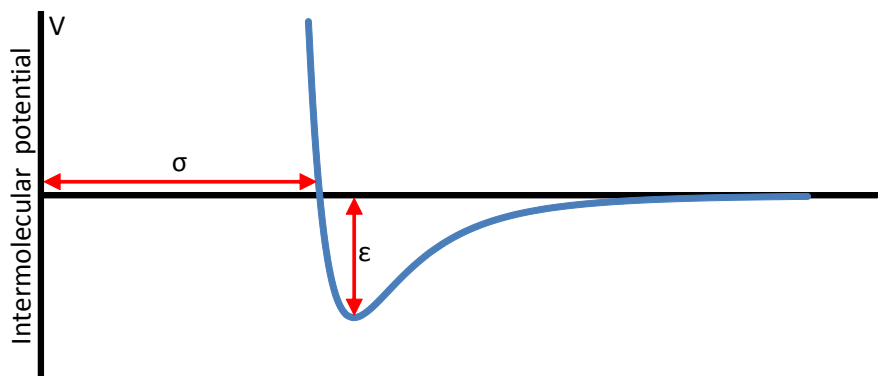


Figure I.5 – Lennard Jones potential

varies from 8 to 800 kJ mol<sup>-1</sup>, similarly to interactions found between atoms and molecules in bulk phase. Weak interactions (< 40 kJ mol<sup>-1</sup>) are referred to as **physisorption** and strong interactions (> 40 kJ mol<sup>-1</sup>) are referred to as **chemisorption**. Even if potential energy (and consequently heat storage density) is higher in chemisorption, this thesis focuses only on physisorption.

Physisorption is mainly due to Van der Waals interaction forces. Adsorbed molecules remain intact and the process is fully reversible. The extent of adsorption depends on intrinsic properties of material in use such as the adsorbent specific surface area and the affinity of the couple adsorbent/adsorbate. It also depends on operating conditions such as temperature, pressure and concentration in the bulk phase. High pressures, high concentrations, high surface areas, high affinities and low temperatures generally foster adsorption process.

### I.2.2 Adsorption Materials

Rigorously all solids are adsorbents but only those with a high specific surface area are interesting for sorption applications. A few adsorbent families are quickly presented in the following section.

### I.2.2.1 Activated carbon

Activated carbons are the most widespread adsorbents in industrial applications. It is mainly used in gas purification processes. Common activated carbons are non-polar and may be used for water purification. They are thereby not used in heat storage applications due to their low affinity for water. Activated carbons have a wide distribution of pore sizes and consequently don't have a good selectivity for adsorption of molecules of different sizes. A specific preparation process (cracking or polymerization of benzene for instance) can yet produce activated carbons with a narrower pores distribution. These molecular sieves are commonly used for gas separation. (Sun and Meunier, 2003)

### I.2.2.2 Silica gel

Silica gel is a porous form of silicon dioxide made synthetically from sodium silicate. Its chemical composition can be expressed as  $\text{SiO}_2 \cdot n\text{H}_2\text{O}$ . A careful control of synthesis conditions (pH and presence of cations) enable a control of pores size. Its high specific surface area (from  $600$  to  $800 \text{ m}^2 \text{ g}^{-1}$ ) and its hydrophilic properties makes it a very good desiccant all the more since it has a very high adsorption capacity at quite low pressures and temperatures. Once saturated with water, the gel can be regenerated at a quite low temperature ( $120^\circ\text{C}$ ) for a few hours. It reveals a low differential heat of sorption that is a strong limitation for heat storage applications.

### I.2.2.3 Zeolites

Zeolites are porous crystalline materials made of an assemblage of silicon Si, aluminum Al and oxygen O atoms. Each Si or Al atom is connected to four oxygen atoms in tetrahedral arrangements ( $\text{SiO}_4$  and  $\text{AlO}_4$ ). Each oxygen atom is shared with another tetrahedra which links Si or Al atoms to one another. This has two direct consequences:

- Angles between atoms are precisely defined which confers a very regular distribution in pores size. This is a particularity of zeolites (compared to other microporous adsorbents).
- Since each oxygen atom is shared between two tetrahedral Si or Al atoms, the stoichiometric composition of each tetrahedral unit is  $\text{SiO}_2$  or  $\text{AlO}_2$ .

The Si/Al ratio is at least 1.0 and there is no upper limit. Rich aluminum sieves show a high affinity for water since each Al atom introduces a negative charge in the material. Polar molecules such as water are sensitive to these charges which induce a hydrophilic behavior. Conversely, rich silicon sieves have an hydrophobic behavior. The transition between hydrophilic and hydrophobic behavior usually occurs at a Si/Al ratio between 8 and 10 (Ruthven, 1984). Adsorptive properties widely depend on framework structure and Si/Al ratio. There are several dozens of existing frameworks. Figure I.6 displays framework structures of four common commercial zeolites.

Sorbate diffusivity and hence adsorption kinetic depend on pore size. The smallest pores are accessible through a six-membered oxygen ring with a free diameter of about  $2.8 \text{ \AA}$  (sodalite). Chabazite, erionite or type A are restricted by a eight-membered oxygen ring ( $4.2 \text{ \AA}$ ). Large-pore

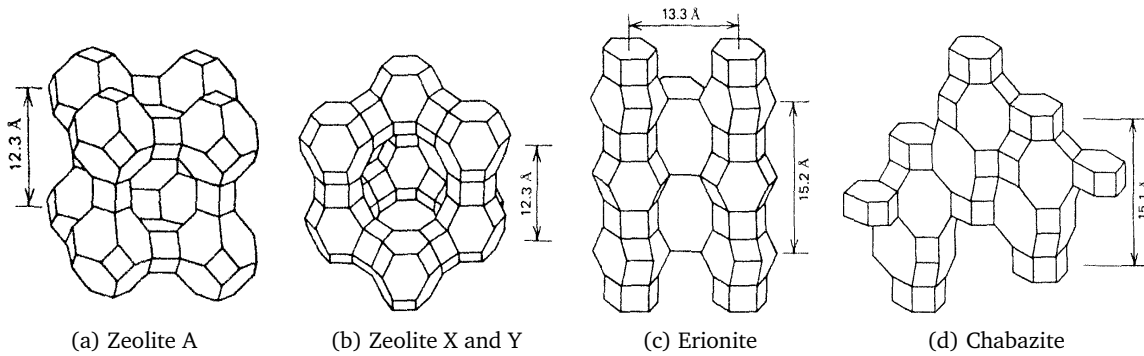


Figure I.6 – Schematic representation showing framework structures of different zeolites. A Si or Al is placed at each vertex and a O at or near the center of each line (Ruthven, 1984, figure 1.6).

zeolites such as X and Y frameworks are delimited by a twelve-membered oxygen ring ( $7.4 \text{ \AA}$ ). It facilitates mass transfers but reduce selectivity on adsorbed molecules. This is nonetheless not a concern in heat storage applications. Synthetic zeolites X and Y or their equivalent natural zeolite (faujasite) are good candidates for heat storage applications due to their large pores and their high affinity for water molecules. The difference between X and Y sieves lies in the Si/Al ratio which is higher for X (1-1.5) than for Y (1.5-3). Zeolites X hence present a higher affinity for water than zeolites Y. It is therefore a better candidate for heat storage applications. (Ruthven, 1984)

### I.2.3 Reactors types

Reactors can be classified into a lot of categories. A first distinction occurs between batch reactors and continuous reactors. **Batch reactors** are often characterized by a mechanical agitation, and a heating or cooling system that enables heat transfers. Mass transfers are limited to vapor discharge through the top of the vessel. No airflow is intended to cross the reactor. This is typically used in chemistry from laboratory scale to industrial scale.

**Continuous reactors** are more appropriate to heat and mass transfers applications. Continuous reactors are made of a vessel filled with small beads that can be a catalyst (in case of fluid-fluid reaction) or a reactant (in case of solid-fluid reaction). In adsorption heat storage, the bed is filled with adsorbent beads. There are numerous reactor types with different shapes and characteristics. In a general way, reactors are designed to enhance heat and mass transfers. Reactor design is often optimized for a given application. This is then not possible to achieve an exhaustive review of every existing solution. Nonetheless, a large distinction occurs between fixed bed reactors and fluidized bed reactors.

- **Fixed bed** reactors are commonly used in a wide range of applications. In adsorption heat storage, the solid reactant remains in the vessel while the fluid crosses the bed (figure I.7a). It ensures mass transfers between fluid and solid phases. The use of **baffles** can enhance fluid mixing and hence heat and mass transfers (figure I.7b).

Heat is either carried by the inlet fluid or transmitted to the reactor through a **heat ex-**

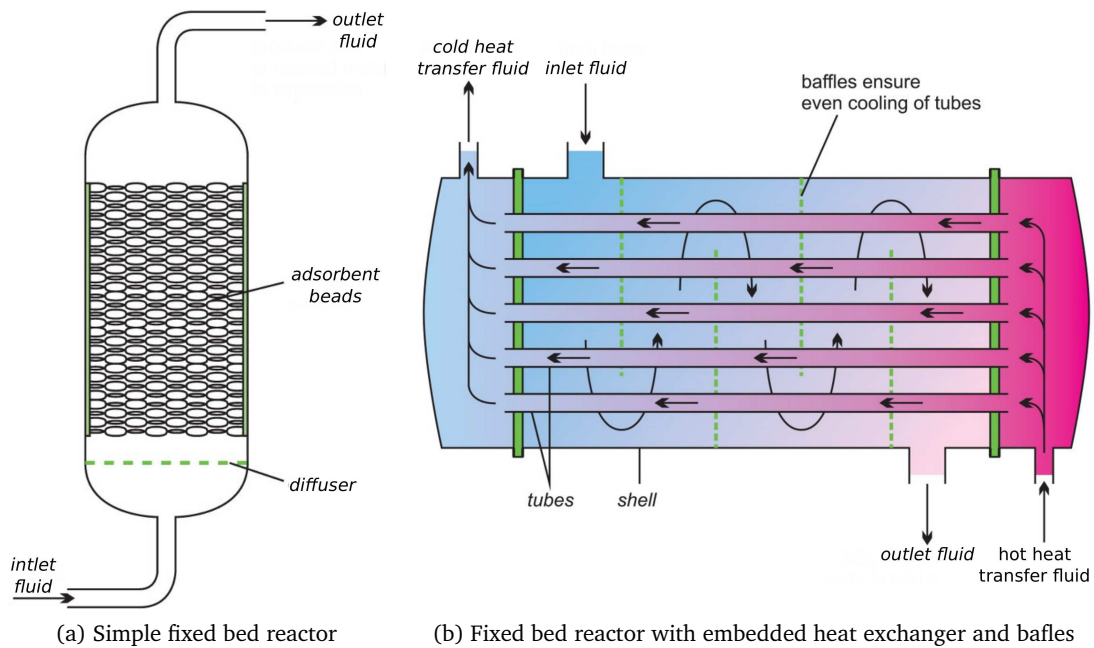


Figure I.7 – Two examples of fixed bed reactors (adapted from [The university of York \(2013\)](#))

**changer** that separates heat and mass carriers. In this case, the use of **fins** can ensure a good conduction within the adsorbent bed to carry heat from or to the heat transfer fluid, as illustrated in figure I.8 ([Makni, 2012](#)). [Guillemint et al. \(1993\)](#) propose an alternative solution to fins for heat transfers enhancement. They show it is possible to increase the bed thermal conductivity by an order of 100 by replacing pure adsorbent beads with a mixture containing a metallic foam in addition of zeolite powder. It can fairly reduce heat exchanger size and hence lead to more compact systems.

The decision to use an embedded heat exchanger (and where required, associated fins) is closely related to the system principle. Adsorption heat storage systems can mainly be divided into closed and open systems (this point is further developed in paragraph I.3.1 on systems typology). In **closed systems**, mass transfers occur in a closed loop between the adsorber, a condenser and an evaporator. Heat is thereby provided to or retrieved from the system through a heat transfer fluid that flows in an embedded heat exchanger.

In **open systems**, heat is generally carried with inlet flowrate and heat exchanger are then not necessary. Nonetheless, it could be interesting to use a heat exchanger in order to **preheat** the adsorbent bed, especially in winter, when high temperature heat is available on short periods. This would ensure that high temperature heat is mainly used for desorption purposes and not for material warm up. This idea is further developed in chapter 5.

- In **fluidized bed** reactors, solid particles are maintained in a fluid-like state. The inlet fluid flows from bottom to top and applies an upward force that compensate gravity force (figure I.9a). Particles movement ensures a very good mixing and enhance heat transfers. This is suitable for gas-gas reaction. It is also suitable when solid particles are playing an active part like in separation processes ([Seo et al., 2007](#)). No references have yet been found

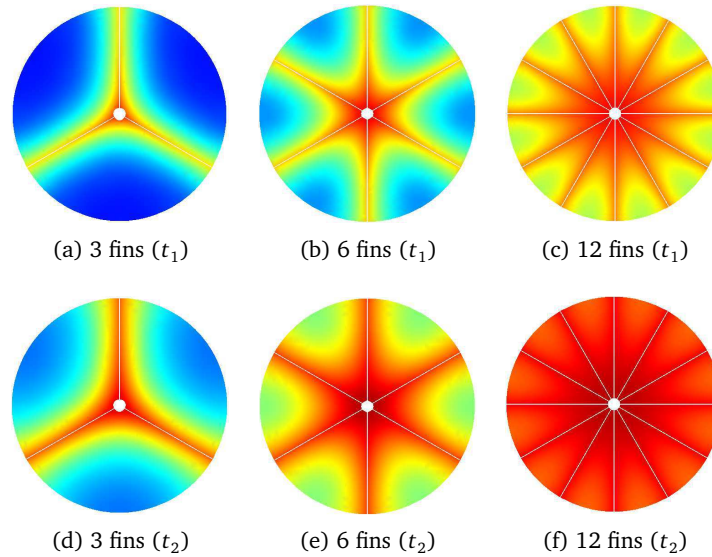


Figure I.8 – Effect of fins number on temperature profile in the adsorbent bed of a closed adsorption heat pump with heat transfer fluid flowing in a pipe embedded at the center of the cylindrical vessel (Makni, 2012)

in literature on the use of fluidized bed with adsorbent beads. Nevertheless, it would be interesting only if heat and mass transfers are limited by kinetics at the bed scale and not at the beads scale. A dimensionless analysis (see III.3) shows a fluidized bed would not necessarily be more efficient than a fixed bed reactor. Indeed, heat and mass transfers within the beads interstices do not seem to limit transfer kinetics.

Mette et al. (2014) propose a concept of external reactor in which the adsorbent particles storage tank and the reactor are dissociated. The objectives pursued by such design are to limit heat and mass transfers to a small part of the total storage material. It enables a reduction of heat losses (especially during the regeneration process) and a limitation of the amount of sensible energy required for material preheating during the regeneration process.

#### I.2.4 Existing prototypes: performance evolution and enhancement

Numerous research have been conducted on the development of adsorption heat storage technologies. Some researches focus on material development at a very small scale of a few hundred grams Whiting et al. (2013); Hongois (2011), while other projects came up with the development of laboratory scale or full scale experiments with 7 to 7000 kg of sorbent material. The present paragraph focuses on a few existing experimental setups. Important characteristics are summed up in table I.2 and some details are provided alongside.

In Munich (Germany), a very large 1350 kWh full scale experiment is conducted since 1997. This system is intended to fulfill heat demand of a 1625 m<sup>2</sup> school during peak demand hours at a maximum flow rate of 6000 m<sup>3</sup> h<sup>-1</sup>, and to cool-down an adjacent Jazz club with reasonable cooling loads. The 7000 kg of 13X zeolite loaded in the storage tank are charged at night, using

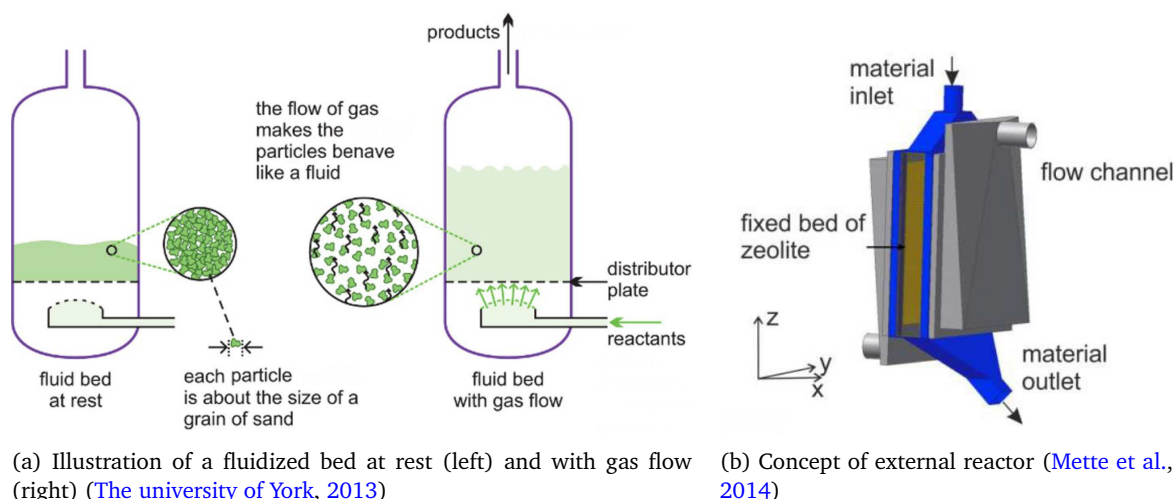


Figure I.9 – Illustration of a fluidized bed and of an external reactor

Table I.2 – Examples of solid adsorption heat storage prototypes performances

Project/ Institution	System type and material <i>O: Open, C: Closed</i>	Storage density $\text{kWh m}^{-3}_{\text{mat}}$	Outlet power $\text{W kg}^{-1}$	Charging temp. $^{\circ}\text{C}$	Estim. cost $\text{€ m}^{-3}$	Reference
ZAE Bayern	O Zeolite 13X	124	$18.6^{\diamond}$	$140^{\circ}\text{C}$	–	Hauer (2007)
Modestore	C Silica gel	50	$5^{\diamond}$	$88^{\circ}\text{C}$	4300	Bales et al. (2008)
SPF	C Zeolite 13X	180	$114^{\diamond}$	$180^{\circ}\text{C}$	2500	Bales et al. (2008)
Monosorp	O Zeolite 4A	160	21	$180^{\circ}\text{C}$	3000	Bales et al. (2008)
Flow-TCS	O Zeolite 4A	96	20	$180^{\circ}\text{C}$	–	Zettl et al. (2014)
E-hub	C Zeolite 5A	47	20	$103^{\circ}\text{C}$	–	Finck et al. (2014)
STAIID	O Zeolite 13X	104	27.5	$180^{\circ}\text{C}$	–	Johannes et al. (2015)

$^{\diamond}$ : Calculated value.

the district heating vapor steam at  $140^{\circ}\text{C}$ , and store up to  $124\text{kWh m}^{-3}$  of heat. It provides a nominal power of  $95\text{kW}$  and a maximal power of  $130\text{kW}$  ( $18.6\text{W kg}^{-1}$ ). (Hauer, 2007)

The EU-project MODESTORE (2003-2006), which is a follow-up of HYDES EU-project (1998-2001) (Hauer, 2007; Mette et al., 2012), was managed by Fraunhofer-ISE (Germany), but results presented here were obtained on a  $13\text{kWh}$ -prototype developed at AEE-INTECT (Austria). It is made of  $200\text{kg}$  of Silica gel,  $30\text{kg}$  of water,  $100\text{kg}$  of steel and  $50\text{kg}$  of copper. The volume of the prototype is about  $0.25\text{m}^3$  for a floor area of  $0.4\text{m}^2$  ( $32.5\text{kWh m}^{-2}$ ). A maximum outlet power of  $1000\text{W}$  is obtained, which lead to a very low power density of  $5\text{W kg}^{-1}$  (Bales et al., 2008). This is due to the storage tank design (figure I.11a) which maximizes compactedness (total prototype volume is as low as 1.5 times the material volume) to the cost of power performance.

At the Institut fuer Solartechnik (SPF) in Switzerland, a  $7\text{kg}$  13X zeolite closed prototype has been tested (Bales et al., 2008). It shows a good storage capacity of  $1\text{kWh}$  and more surprising,

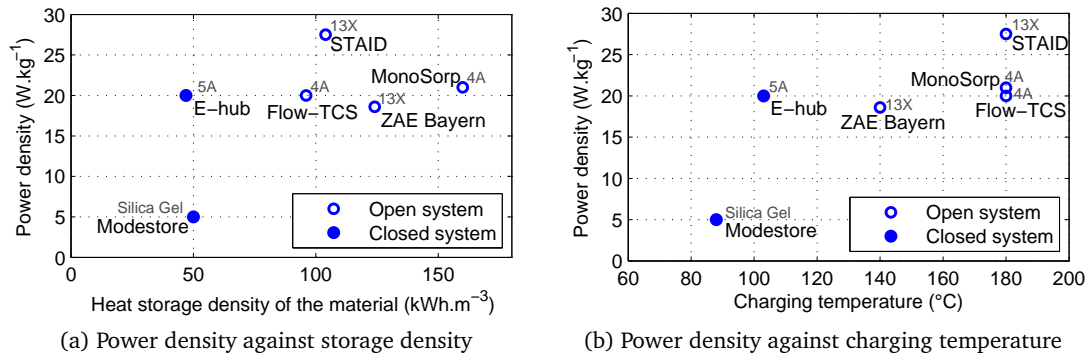


Figure I.10 – Performances achieved by projects presented in table I.2. Results from SPF are not presented in those graphs because the outlet power value (114W kg<sup>-1</sup>) is calculated from informations presented in Bales et al. (2008) and is considered as too high to be reliable without further details

an astonishing outlet power of 800W, which related to the sorbent mass comes up to 114 W kg<sup>-1</sup> (four times higher than all other prototypes found in literature). Two other interesting points are worth noting:

- A ratio of 1 to 3 is achieved from material volume to prototype volume which is not a very good compactedness.
- Storage capacity is a non-linear function of charging temperature. 57% of the 180°C-storage capacity is reached at 110°C while 94% is already reached at 150°C. This is a good point for solar applications since it states that a high charging temperature is not necessarily a strong requirement.

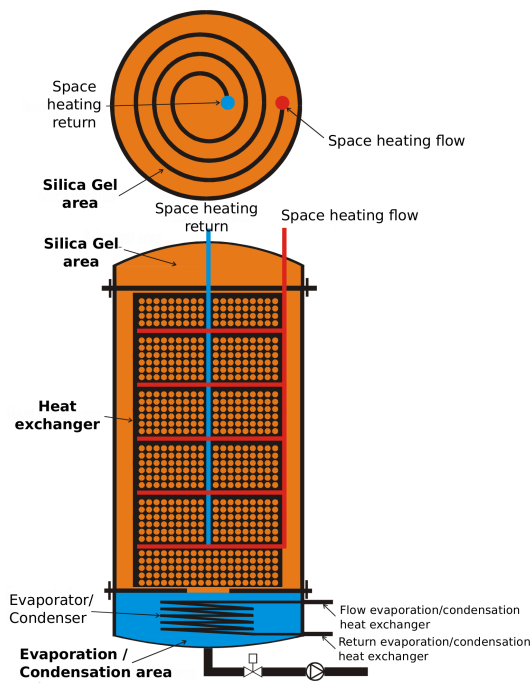
At the university of Stuttgart (Germany), ITW has built a 12 kWh-prototype in the framework of the MonoSorp project. It is made of 70 kg of 4A zeolite. The material shows a good storage density of 160 kWh m<sup>-3</sup> and a very good compactedness since a ratio of 3 to 4 is achieved between material volume and prototype volume. This is possible thanks to a very simple design, as shown in figure (I.12b). (Bales et al., 2008)

At the Austria solar innovation center (ASIC), a 12 kWh rotating prototype was experimented (figure I.12a). The moving reactor bed is supposed to enable a contribution of the whole bed to heat generation as opposed to fixed bed reactors where a sorption front is observed. This should allow an enhancement of outlet power. Maximum outlet power is 30 W kg<sup>-1</sup>, with an average power from 13 W kg<sup>-1</sup> to 20 W kg<sup>-1</sup>. A better control of the discharge process is also claimed by the authors. (Zettl et al., 2014)

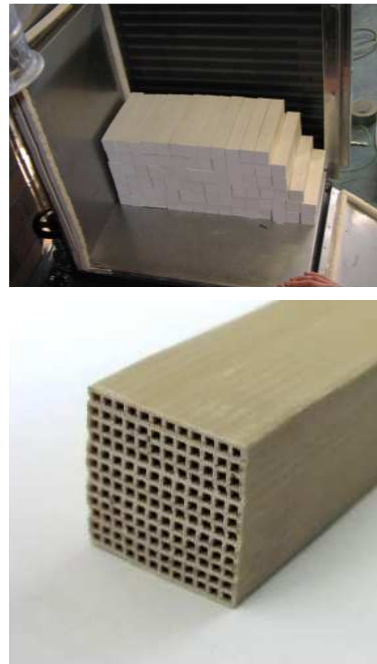
At the Netherlands organisation for Applied Scientific Research, a 3 kWh-prototype is developed with 41 kg of 5A zeolite. A maximum deliverable power of 971 W (24 W kg<sup>-1</sup>) is achieved thanks to 8 parallel heat exchangers. (Finck et al., 2014)

The STAID<sup>2</sup> project, led by CETHIL at INSA de Lyon (France), in coordination with EdF R&D, CETIAT, LOCIE and CNRS/IRCE Lyon, put emphasis on the maximization of outlet power. The

<sup>2</sup>Seasonal Thermochemical heAt storage In builDings

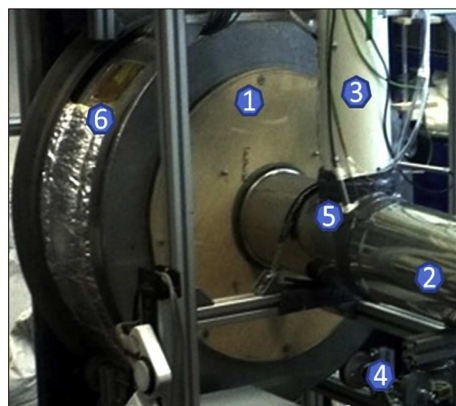


(a) Scheme of the second generation prototype of the Modestore project (Bales et al., 2008)

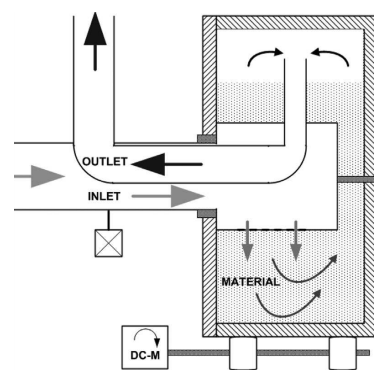


(b) Pictures of the MonoSorp project reactor (top), and detailed view on a monolith (bottom) (Bales et al., 2008)

Figure I.11 – Illustration of the shape of two existing prototypes



(a) Picture of the ASIC prototype: cylindrical rotating body part (1), air inlet (2), air outlet (3), roller bearings (4), temperature and humidity sensors (5), material door (6)



(b) Sketch of the ASIC prototype

Figure I.12 – Scheme of the ASIC rotating prototype (Zettl et al., 2014)



Figure I.13 – Picture of the STAID project prototype (Johannes et al., 2015)

specification requirements consisted in providing 2 kW for at least two straight hours. It came up to the construction of a prototype loaded with 80 kg of 13X zeolite into two vessels that can run in serial or in parallel (figure I.13). Results show a storage density of  $104 \text{ kWh m}^{-3}$  is achieved with a maximum outlet power of 2.2 kW ( $27.5 \text{ W kg}^{-1}$ ). (Johannes et al., 2015; Tatsidjodoung et al., 2016)

Finally, according to data concatenated by Yu et al. (2013, table 3), very high outlet power densities can be reached with closed composite sorption storage prototypes.

- At the Chiang Ma University, a 0.25 kg-prototype composed of  $\text{Na}_2\text{S} - \text{graphite}/\text{H}_2\text{O}$  provides a storage solution at  $2.24 \text{ kWh kg}^{-1}$  and a maximum outlet power of  $0.24 \text{ kW}$  ( $960 \text{ W kg}^{-1}$ !).
- At the ECN (Netherlands), a 3 kg-prototype composed of  $\text{Na}_2\text{S} - \text{cellulose}/\text{H}_2\text{O}$  stores heat at  $1.07 \text{ kWh kg}^{-1}$  with a maximum outlet power of  $0.70 \text{ kW}$  ( $233 \text{ W kg}^{-1}$ ).

Nevertheless, these very high power densities are observed on small scale prototypes. On bigger scale prototypes, values of power density are comparable to pure adsorption systems.

- At PROMES-CNRS, a 187 kg-prototype of  $\text{SrBr}_2 - \text{ENG}/\text{H}_2\text{O}$  reaches  $0.321 \text{ kWh kg}^{-1}$  energy density and outlet power density is  $21.4 \text{ W kg}^{-1}$ .
- At the ECN (Netherlands), a 17.2 kg-prototype made of  $\text{MgCl}_2/\text{H}_2\text{O}$  stores heat at a  $0.139 \text{ kWh kg}^{-1}$  density, and releases heat at a poor outlet power of  $8.7 \text{ W kg}^{-1}$ .

In conclusion, several lessons can be learned from this short review of existing adsorption heat storage prototypes,

- Simplest geometries are often the best since they allow a maximization of the material volume compared to the prototype volume. The MonoSorp project is a good example of high compactedness.
- Rotating prototypes or complex heat exchangers do not necessarily provide (yet)

expected enhancement in system performances.

- Closed composite sorption systems are very promising on small scale experiments but these results are not confirming (yet) on larger scale prototypes.

## I.3 Heat storage system description

### I.3.1 Systems typology

In literature, adsorption heat storage systems are usually classified into active/passive systems or open/closed systems which is about the same distinction. An active system is usually also an open system. In the same way, a passive system is often a closed system.

#### Active systems vs. passive systems

Active thermal storage systems are characterized by forced convection. The driven force is supplied to the system by a fan or a pump. Passive thermal storage systems are driven by a temperature, concentration or pressure gradient (Pinel et al., 2011).

#### Open systems vs. closed systems

Open thermal storage systems are characterized by a single vector (usually moist air) that carries both heat and mass (adsorbate) through the system. In closed systems two different vectors are used to carry heat and adsorbate. No adsorbate mass transfer occurs between the system and the surroundings.

Open/active systems and closed/passive systems use similar adsorption materials but different system architectures and working conditions as summed up in table I.3.

Table I.3 – Closed and open systems features

System typology	Closed/passive system	Open/active system
Gas	pure vapor	moist air
Pressure	vacuum	ambient
Heat exchange	indirect (2 fluids)	direct (1 fluid)
Driving force	temperature gradient and pressure gradient	forced convection
Main elements	heat source adsorber heat exchanger condenser evaporator	heat source adsorber heat exchanger fan

Michel et al. (2014) propose a numerical comparison of two system performances: a closed adsorption heat storage system and an open system, using both the same salt hydrate/water pair.

In closed systems, the bed thermal conductivity limits heat released to the heat transfer fluid. In open systems, bed permeability has a major influence on reaction kinetic.

### I.3.2 Adsorber geometry

Figures I.14 and I.15 detail adsorber geometry for an open and a closed system. Geometries presented here are cylindrical.

#### Adsorber geometry for an open system

An **open** system runs with moist air as a heat and mass carrier. Figure I.14 displays a schematic representation of the adsorber for a closed system.

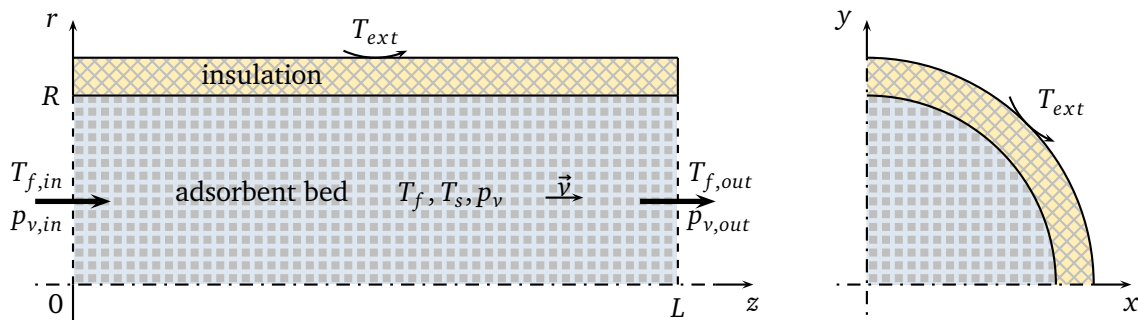


Figure I.14 – Schematic representation of an open adsorption heat storage tank

#### Adsorber geometry for a closed system

A **closed** system runs with pure water vapor as a mass carrier (connected to a condenser or an evaporator). Heat transfer fluid is physically separated from the adsorption material. Figure I.15 displays a schematic representation of the adsorber for a closed system.

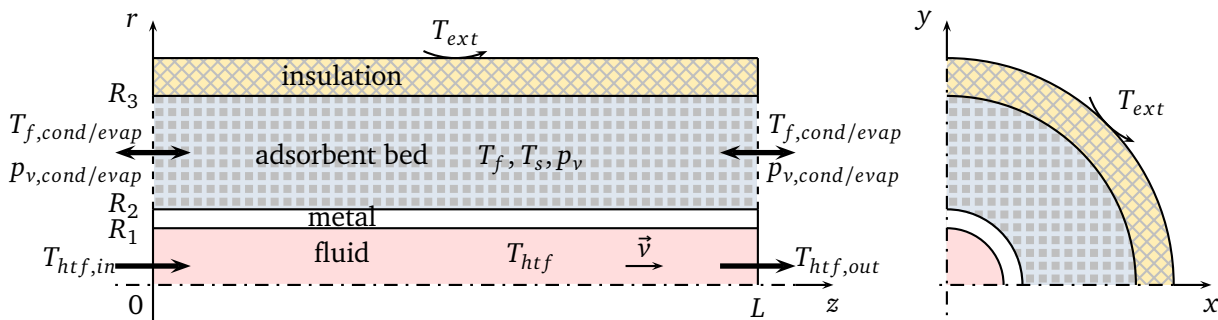


Figure I.15 – Schematic representation of the adsorber of a closed adsorption heat pump

### I.3.3 Case study definition

The main objective is to study heat and mass transfers within the adsorber.

### I.3.3.1 Numerical model vs. experiments

There are two complementary ways to study a system : experiments and numerical models. Numerical models require experimental data to be validated. Experiments often need complementary numerical tests, when a model exists. Numerical models can be complex to develop and to validate but they often are a good alternative (or even the only alternative) to experiments. Indeed, experiments can be time consuming, expensive, dangerous or at an inadequate scale (too small or too big to enable precise measurements) (Goncalves, 2005). Here, a numerical model seems to be more appropriate than experiments because several thousands of numerical experiments are intended to be run in order to better understand heat and mass transfers within the adsorbent bed, and to address the influence of material thermophysical properties and operating conditions on system performances. Hypothetical materials will be numerically tested, which would be unfeasible with experiments. Moreover, addressing the influence of different operating conditions would require at least two days for each experiment (to achieve a complete charge and discharge). This would be a serious limit to the number of experiments and to the number of configuration tested. These reasons plead, in the present case, for the development of a numerical model validated with experimental data.

### I.3.3.2 Numerical modeling specificities of open and closed systems

#### Equations formulation

Equations formulation is very similar for open and closed systems. In open systems, carrier gas is **moist air** and has to be split into two subspecies (pure water vapor and dry air). Furthermore, fluid velocity is set by **forced convection**. In closed systems, **pure water vapor** is the only gas. Numerical resolution is usually more complex due to more **two-dimensional solicitations** (heat transfer is mainly radial whereas mass transfer is mainly axial). Transient boundary conditions between heat transfer fluid and adsorbent bed tend to increase 2D behavior for low heat transfer fluid velocities. Furthermore, water vapor velocity is thermally-driven and calculated with Darcy's law which requires more computation.

#### Validation strategies

When developing a numerical model, it is very important to anticipate the validation strategy. Validation can be based on experimental data, if available. Analytic solutions can else be used in order to validate a model under very specific (simplifying) assumptions.

**Closed systems** Experimental data are not widespread for closed adsorption heat pumps. It is then complicated to set up a validation protocol. Sun et al. (1995) and Duquesne (2013) have based the validation of their adsorption heat pump numerical model on a simpler case with a known analytic solution.

**Open systems** Conversely, more experimental data on open systems are available. ANR<sup>3</sup> project STAID came up with a set of experimental data on an open adsorption heat storage system

---

<sup>3</sup>French national research agency

made of two reactors with 40 kg of zeolite beads, capable of running in serial or in parallel. In this project, the experimental plan was designed to investigate the influence of desorption temperature (120°C vs. 180°C), air flowrate (180 m<sup>3</sup> h<sup>-1</sup> vs. 90 m<sup>3</sup> h<sup>-1</sup> vs. 60 m<sup>3</sup> h<sup>-1</sup>), relative humidity in discharging mode (50% vs. 70%), bed length (20 cm vs. 10 cm) and interest of serial/parallel modes (Johannes et al., 2015).

### I.3.3.3 Open systems vs. closed systems

Closed systems have some interesting features such as the thermal driving force that does not require fans to run. It spares the system from auxiliary consumption that would lower global performances. But according to figure I.10 and table I.2, open systems enable better performances in terms of power density and storage density compared to closed systems, to the cost of higher charging temperatures (based on prototypes presented in this study). The first choice thus goes to open systems. It is then decided to develop a numerical model for an open system. Equations for a closed system are the same than for an open system. A closed system model can then be easily derived from the open system model by switching from moist air to water vapor. This is achieved by setting dry air density  $\rho_{da}$  to zero which comes back to remove dry air terms from the equations. In case of an external heat exchanger, it is easily taken into account in boundary conditions. If the heat exchanger is embedded in the adsorbent bed, modeling of heat transfers from the adsorbent bed to the heat exchanger becomes more complicated.

### I.3.3.4 Cylindrical vs. cartesian coordinates

Besides, cylindrical coordinates are much more natural than cartesian coordinates to describe cylindrical shapes usually found in adsorbers. But for sake of comprehension, in order to avoid useless writing complications due to cylindrical coordinates, equations are developed with cartesian coordinates. In practice, **both coordinate systems** (cartesian and cylindrical) **are implemented** so that different geometries can be treated.

It is decided to develop and validate a **numerical model** for an **open system**. Hence, equations for an open system will be fully developed in the next chapter.

## Chapter II

# Numerical model development of an adsorption heat storage system

### Contents

---

<b>II.1 Equations formulation</b> . . . . .	<b>32</b>
II.1.1 Definitions . . . . .	32
II.1.2 Numerical modeling of an heterogeneous medium . . . . .	32
II.1.3 Asumptions . . . . .	34
II.1.4 Energy conservation . . . . .	35
II.1.5 Mass conservation . . . . .	37
<b>II.2 Heat and mass transfers in porous media</b> . . . . .	<b>39</b>
II.2.1 A multi-scale approach . . . . .	39
II.2.2 Advection in porous media . . . . .	40
II.2.3 Diffusion in porous media . . . . .	41
II.2.4 Selected approach on kinetic modeling . . . . .	44
II.2.5 Numerical modeling of adsorption equilibrium . . . . .	45
II.2.6 Differential heat of adsorption $\Delta H$ . . . . .	52
<b>II.3 Numerical developments</b> . . . . .	<b>53</b>
II.3.1 Possible numerical methods for spatial discretization . . . . .	54
II.3.2 Model dimension and coordinate system . . . . .	55
II.3.3 Discretization operators . . . . .	57
II.3.4 Model implementation . . . . .	60
II.3.5 Coupled equations . . . . .	61

---

The present chapter aims at presenting necessary developments for the formulation of a numerical model describing heat and mass transfers in an adsorption heat storage tank. The derivation of the model starts from the formulation of heat and mass conservation laws. All choices and hypotheses are documented with technical references from literature, provided as the development goes along.

## II.1 Equations formulation

### II.1.1 Definitions

Before formulating conservation laws, it is necessary to set several definitions and to choose a strategy for modeling the adsorber's heterogeneous medium.

- $\epsilon_b$  is the **bed macroscopic porosity**. Zou and Yu (1995) propose a correlation to estimate bed porosity from bed diameter  $D_b$  and beads diameter  $d_p$ .

$$\left| \begin{array}{l} \epsilon_b = 0.372 + 0.002 \left( \exp \left( 15.306 \frac{d_p}{D_b} \right) - 1 \right), \text{ valid for } \frac{d_p}{D_b} \leq 0.256 \\ = 0.372, \text{ for } d_p = 1.8 \text{ mm and } D_b = 72 \text{ cm} \end{array} \right.$$

- $\epsilon_p$  is the **beads mesoscopic porosity**. Beads are made of conglomeration of smaller particles as schematically shown in figure II.4.

$$\left| \begin{array}{l} \epsilon_p = 0.32 \text{ (Sun et al., 1995)} \end{array} \right.$$

- $A$  is the **void fraction** inside the storage tank.

$$\left| \begin{array}{l} A = \epsilon_b + (1 - \epsilon_b) \epsilon_p \end{array} \right.$$

- $B_a$  is a **weighting factor for adsorption phenomenon**.

$$\left| \begin{array}{ll} & \text{if adsorption isotherm is measured...} \\ B_a = \begin{cases} 1 & \rightarrow \dots \text{ to the bed scale} \\ (1 - \epsilon_b) & \rightarrow \dots \text{ to the beads scale} \\ (1 - \epsilon_b)(1 - \epsilon_p) & \rightarrow \dots \text{ to the microparticules scale} \end{cases} \end{array} \right.$$

- $B_s$  is a **weighting factor for material thermophysical properties**.

$$\left| \begin{array}{ll} & \text{if material thermophysical properties are measured...} \\ B_s = \begin{cases} 1 & \rightarrow \dots \text{ to the bed scale} \\ (1 - \epsilon_b) & \rightarrow \dots \text{ to the beads scale} \\ (1 - \epsilon_b)(1 - \epsilon_p) & \rightarrow \dots \text{ to the microparticules scale} \end{cases} \end{array} \right.$$

- $\beta$  is a constant used in definition of **film temperature**  $T_{film}$ .

$$\left| \begin{array}{l} T_{film} = \beta T_s + (1 - \beta) T_f \end{array} \right.$$

### II.1.2 Numerical modeling of an heterogeneous medium

The storage reactor is filled with a porous material that can not be considered as an homogeneous medium as regards to numerical modeling. Two strategies are then applicable:

1. considering the reactor as **two homogeneous "phases"** (solid and gas) with their own temperature, material properties and governing equations,
2. considering the reactor as **one single homogeneous medium** with an homogeneous tem-

Table II.2 – Some correlations for equivalent thermal conductivity calculation

Serial network (min)	$\frac{1}{\lambda_{eq}} = \frac{\epsilon_b}{\lambda_f} + \frac{1-\epsilon_b}{\lambda_s} \Rightarrow \lambda_{eq} = \frac{1}{\frac{\epsilon_b}{\lambda_f} + \frac{1-\epsilon_b}{\lambda_s}}$
Parallel network (max)	$\lambda_{eq} = \frac{\lambda_f}{\epsilon_b} + \frac{\lambda_s}{1-\epsilon_b}$
Hsu et al. (1995)	$\frac{\lambda_{eq}}{\lambda_f} = \frac{2 \left( \frac{\lambda_s}{\lambda_f} \right)^2 (1-\epsilon_b) + (1+2\epsilon_b) \frac{\lambda_s}{\lambda_f}}{(2+\epsilon_b) \frac{\lambda_s}{\lambda_f} + (1-\epsilon_b)}$

perature and with averaged thermophysical properties representing effective conductivity, density, heat capacity, etc.

Both strategies have their own benefits and drawbacks.

**Homogeneous model: equivalent-temperature model**

Considering a single homogeneous medium requires one temperature variable and one energy balance for problem formulation. It **might seem simpler** at first but it calls for non-trivial **calculation of equivalent thermophysical properties**, such as thermal conductivity. There are several correlations proposing an estimation of thermal conductivity in heterogeneous medium composed of two materials. **Equivalent thermal conductivity** will always be in between two boundary values corresponding to a serial network and a parallel network. Table II.2 gives boundary values formulation and reproduces a correlation from **Hsu et al. (1995)**.

More detailed calculations can also be performed with numerical tools. *COMSOL Multiphysics*<sup>®</sup> provides this kind of feature as illustrated with figure II.1.

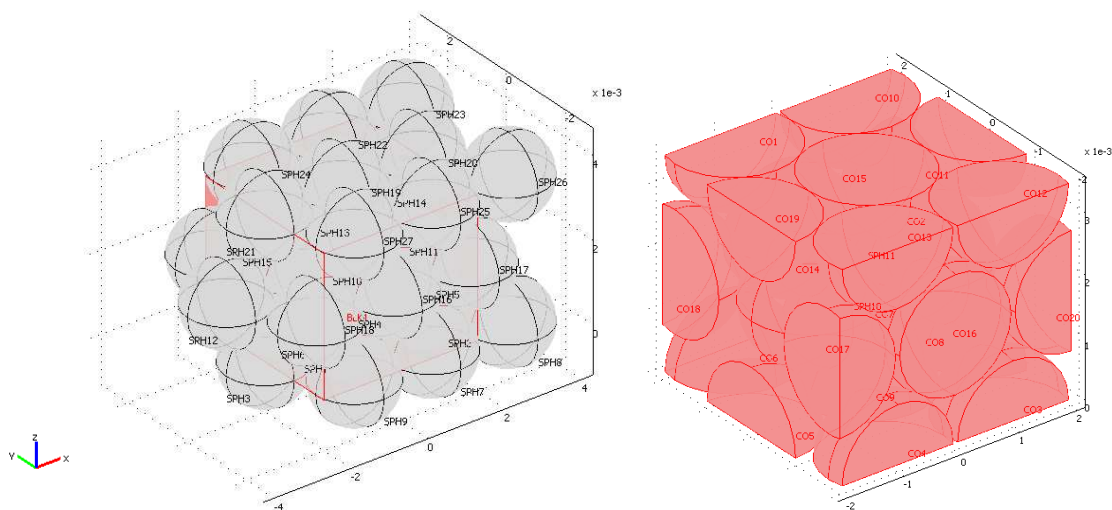


Figure II.1 – Illustration of equivalent thermal conductivity calculation with *COMSOL Multiphysics*<sup>®</sup> (Hongois, 2011))

### Heterogeneous model: 2-temperature model

Splitting the reactor into two "phases" (solid and gas) requires two energy balances and two temperature variables ( $T_f$  and  $T_s$  for fluid and solid). It also requires heat and mass transfers quantification between both phases. **Mass transfer rate** from solid to gas phase is governed by **adsorption kinetic**. **Heat transfer rate** from one phase to another has to be evaluated through a **convection heat transfer coefficient calculation**. It depends on beads diameter (i.e. specific surface area and bed porosity) and fluid velocity (or mass flow rate). Wakao and Kagei (1982, pp.292-294) propose a correlation that link Nusselt, Reynolds and Prandtl numbers (equation II.1 below).

$$\frac{h_{sf} D_b}{\lambda_f} = 2 + 1.1 Re^{0.6} Pr^{1/3} \quad \text{with} \quad \begin{cases} Re = \frac{\rho_g v D_b}{\mu_g} \\ Pr = \frac{C_p \mu}{\lambda} = 0.71(\text{air}) \end{cases} \quad (\text{II.1})$$

This correlation was fitted from numerous numerical or experimental data collected from twelve references, but is particularly less accurate for low Reynolds numbers ( $Re < 500$ ) which lies in the range of Reynolds numbers encountered in this work.

Kuwahara et al. (2001) propose a "numerical study of interfacial convective heat transfer coefficient in two-energy equation model for convection in porous media". Results came up to the following equation II.2 that is valid for a larger domain of bed porosity and Reynolds number.

$$\frac{h_{sf} D}{\lambda_f} = \left( 1 + \frac{4(1 - \epsilon_b)}{\epsilon_b} \right) + \frac{1}{2} (1 - \epsilon_b)^{1/2} Re^{0.6} Pr^{1/3} \quad (\text{II.2})$$

valid for  $0.2 < \epsilon_b < 0.9$

### Choice between 1-temperature and 2-temperature models

The choice between advantages and drawbacks of both strategies is not easy. But even if temperature difference between solid phase and gaz phase is not expected to be large, a 2-temperature formulation seems more natural. Thermal conductivity of each medium is known, and convection coefficient can be calculated or fitted from experimental results.

It is then decided to **develop** a numerical model with a **2-temperature approach**. Nonetheless, a **1-temperature** approach has **also been implemented**.

### II.1.3 Assumptions

The reactor tank is artificially split into solid medium and moist air. **Solid parts** are composed of **sorbent material** (referred to with subscript  $s$ ) and **adsorbed water** (referred to with subscript  $w$ ). **Fluid** (referred to with subscript  $f$ ) is composed of **dry air** (referred to with subscript  $da$ ) and **water vapor** (referred to with subscript  $v$ ). Several working hypotheses must be formulated as regard with calculation of **densities**, **volumetric heat capacities** and their **time derivatives**.

- Water vapor density  $\rho_v$ , is supposed to behave like an ideal gaz

$$\left| \begin{aligned} \rho_v &= \frac{p_v M_v}{R T_f} \Rightarrow \frac{\partial \rho_v}{\partial t} = \frac{\partial \rho_v}{\partial T_f} \frac{\partial T_f}{\partial t} + \frac{\partial \rho_v}{\partial p_v} \frac{\partial p_v}{\partial t} \\ &= -\frac{p_v M_v}{R T_f^2} \frac{\partial T_f}{\partial t} + \frac{M_v}{R T_f} \frac{\partial p_v}{\partial t} \end{aligned} \right.$$

- Volumetric heat capacity of moist air  $(\rho c_p)_f$

$$\left| \begin{aligned} (\rho c_p)_f &= \rho_{da} c_{pda} + \rho_v c_v \\ &= \rho_{da} c_{pda} + \frac{p_v M_v c_v}{R T_f} \Rightarrow \frac{\partial (\rho c_p)_f T_f}{\partial t} = \rho_{da} c_{pda} \frac{\partial T_f}{\partial t} + \frac{M_v c_v}{R} \frac{\partial p_v}{\partial t} \end{aligned} \right.$$

- Volumetric heat capacity of solid material  $(\rho c_p)_s$

$$\left| (\rho c_p)_s = B_s \rho_s c_s + B_a q c_a \Rightarrow \frac{\partial (\rho c_p)_s T_s}{\partial t} = (B_s \rho_s c_s + B_a q c_a) \frac{\partial T_s}{\partial t} + B_a c_a T_s \frac{\partial q}{\partial t} \right.$$

#### II.1.4 Energy conservation

An **elementary volume** of adsorbent bed is represented in figure II.2. **Energy fluxes** through the boundaries of this volume are represented. It may be divided into **heat conduction** and heat transportation through **advection**. Within the control volume, heat is also transmitted from one phase to another through **convection**. Finally, heat can be released or absorbed by the solid medium that acts as a **heat source** (in sorption mode) or a heat well (in desorption mode).

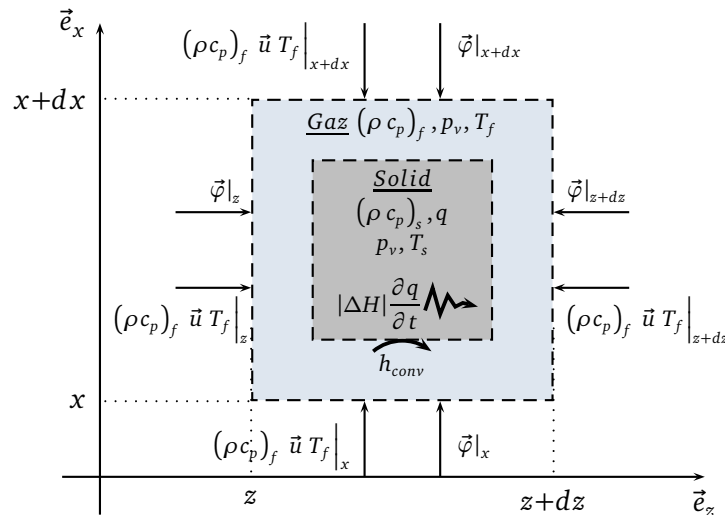


Figure II.2 – Energy balance on an elementary volume  $dV = dx dy dz$

As explained in paragraph II.1.2, two energy conservation laws must be written. One for the gas phase and one for the solid phase.

**Energy conservation in an elementary volume of gaz**

$$\begin{aligned}
 A \frac{\partial (\rho c_p)_f T_f}{\partial t} dx dy dz &= h_{conv} S_{exch} (T_s - T_f) \\
 &+ \left( \bar{\varphi}|_x + (\rho c_p)_f \bar{u} T_f \Big|_x - \bar{\varphi}|_{x+dx} - (\rho c_p)_f \bar{u} T_f \Big|_{x+dx} \right) dy dz \bar{e}_x \\
 &+ \left( \bar{\varphi}|_y + (\rho c_p)_f \bar{u} T_f \Big|_y - \bar{\varphi}|_{y+dy} - (\rho c_p)_f \bar{u} T_f \Big|_{y+dy} \right) dx dz \bar{e}_y \\
 &+ \left( \bar{\varphi}|_z + (\rho c_p)_f \bar{u} T_f \Big|_z - \bar{\varphi}|_{z+dz} - (\rho c_p)_f \bar{u} T_f \Big|_{z+dz} \right) dx dy \bar{e}_z
 \end{aligned} \tag{II.3}$$

Equation II.3 can be rearranged with the following form:

$$\begin{aligned}
 A \frac{\partial (\rho c_p)_f T_f}{\partial t} &= h_{conv} \frac{S_{exch}}{dx dy dz} (T_s - T_f) \\
 &+ \left[ \begin{aligned}
 &\frac{\bar{\varphi}|_x - \bar{\varphi}|_{x+dx}}{dx} + \frac{(\rho c_p)_f \bar{u} T_f \Big|_x - (\rho c_p)_f \bar{u} T_f \Big|_{x+dx}}{dx} \\
 &\frac{\bar{\varphi}|_y - \bar{\varphi}|_{y+dy}}{dy} + \frac{(\rho c_p)_f \bar{u} T_f \Big|_y - (\rho c_p)_f \bar{u} T_f \Big|_{y+dy}}{dy} \\
 &\frac{\bar{\varphi}|_z - \bar{\varphi}|_{z+dz}}{dz} + \frac{(\rho c_p)_f \bar{u} T_f \Big|_z - (\rho c_p)_f \bar{u} T_f \Big|_{z+dz}}{dz}
 \end{aligned} \right] \{\bar{e}_x, \bar{e}_y, \bar{e}_z\}
 \end{aligned} \tag{II.4}$$

Equation II.4 brings into play two developed forms of divergence operator. The same equation can be formulated with the following condensed form.

$$A \frac{\partial (\rho c_p)_f T_f}{\partial t} = h_{conv} \frac{S_{exch}}{V} (T_s - T_f) - \text{div} \left( (\rho c_p)_f \bar{u} T_f \right) - \text{div}(\bar{\varphi}) \tag{II.5}$$

The left hand side of the equation has been developed in the previous paragraph II.1.3. Volumetric heat capacity  $(\rho c_p)_f$  has also been formulated in this paragraph. Conductive heat flux  $\bar{\varphi}$  can be calculated with Fourier's law ( $\bar{\varphi} = -\lambda \overrightarrow{\text{grad}}(T)$ ). All these developments come up with the **strong formulation of energy conservation in gaz part** displayed with the following equation II.6.

$$\begin{aligned}
 [A \rho_{da} c_{pda}] \frac{\partial T_f}{\partial t} + \left[ A \frac{M_v c_v}{R} \right] \frac{\partial p_v}{\partial t} &= h_{conv} \frac{S_{exch}}{V} (T_s - T_f) \\
 - \text{div} \left( \left( \rho_{da} c_{pda} T_f + \frac{M_v c_v}{R} p_v \right) \bar{u} \right) + \text{div} \left( \lambda_f \overrightarrow{\text{grad}}(T_f) \right)
 \end{aligned} \tag{II.6}$$

**Energy conservation in an elementary volume of solid**

Figure II.2 also enables to write energy conservation in the solid part. Still, heat conduction in the solid medium is not depicted in this illustration since it is not obvious whether it has to be taken into account or not. **Conduction** occurs within a bead but **not much between beads** since contact

surface is very low. From the bed scale, heat transfer from one mesh to another essentially occurs through **convection/advection mechanism** rather than pure conduction. Conduction term is then neglected compared to advection. In this way, the solid parts within a control volume are not directly in contact with the boundaries of this control volume. Conduction is still a heat conveyor mechanism within a bead. A conductance  $U_b$  takes into account for convection at the bead surface and conduction inside the bead (developments and discussion are given in section II.2.4).

$$\frac{\partial (\rho c_p)_s T_s}{\partial t} dx dy dz = U_b S_{exch} (T_f - T_s) + B_a |\Delta H| \frac{\partial q}{\partial t} dx dy dz \quad (\text{II.7})$$

The left hand side of equation II.7 has been developed in paragraph II.1.3. It comes up with the **strong formulation of energy conservation in the solid part** displayed with equation II.8.

$$[B_s \rho_s c_s + B_a q c_a] \frac{\partial T_s}{\partial t} = U_b \frac{S_{exch}}{V} (T_f - T_s) + B_a (|\Delta H| - c_a T_s) \frac{\partial q}{\partial t} \quad (\text{II.8})$$

### II.1.5 Mass conservation

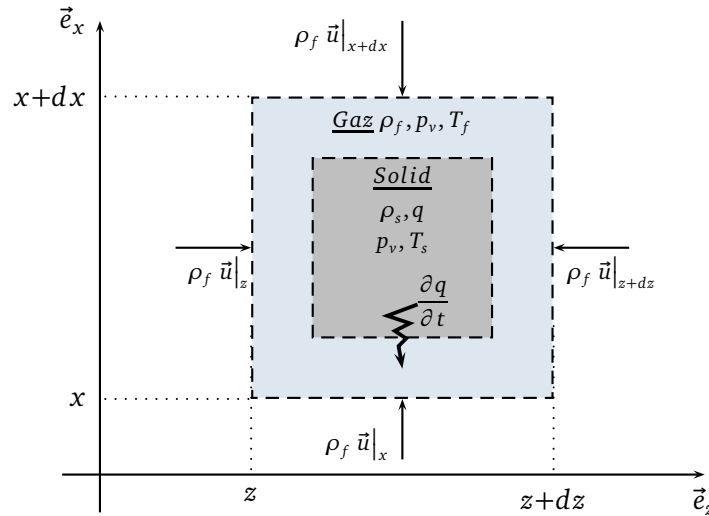


Figure II.3 – Mass balance on an elementary volume  $dV = dx dy dz$

#### Mass conservation of water vapor

Mass variation on a control volume is the product of density variation and volume (since density is the intensive property of mass).

$$\begin{aligned} A \frac{\partial \rho_v}{\partial t} dx dy dz = & -B_a \frac{\partial q}{\partial t} dx dy dz + (\rho_v \vec{u} \Big|_x - \rho_v \vec{u} \Big|_{x+dx}) dy dz \vec{e}_x \\ & + (\rho_v \vec{u} \Big|_y - \rho_v \vec{u} \Big|_{y+dy}) dx dz \vec{e}_y + (\rho_v \vec{u} \Big|_z - \rho_v \vec{u} \Big|_{z+dz}) dx dy \vec{e}_z \end{aligned} \quad (\text{II.9})$$

Equation II.9 can be rearranged with the following form:

$$A \frac{\partial \rho_v}{\partial t} = -B_a \frac{\partial q}{\partial t} + \frac{\rho_v \vec{u}|_x - \rho_v \vec{u}|_{x+dx}}{dx} \vec{e}_x + \frac{\rho_v \vec{u}|_y - \rho_v \vec{u}|_{y+dy}}{dy} \vec{e}_y + \frac{\rho_v \vec{u}|_z - \rho_v \vec{u}|_{z+dz}}{dz} \vec{e}_z \quad (\text{II.10})$$

Equation II.10 brings into play a developed form of divergence operator. The same equation can be formulated with the following condensed form.

$$A \frac{\partial \rho_w}{\partial t} = -B_a \frac{\partial q}{\partial t} - \text{div}(\rho_w \vec{u}) \quad (\text{II.11})$$

The left hand side of equation II.11 has been developed in paragraph II.1.3. It comes up with the **strong formulation of mass conservation of water vapor** formulated in the following equation II.12.

$$\left[ -A \frac{p_v M_v}{R T_f^2} \right] \frac{\partial T_f}{\partial t} + \left[ A \frac{M_v}{R T_f} \right] \frac{\partial p_v}{\partial t} = -\frac{M_v}{R} \text{div} \left( \frac{p_v}{T_f} \vec{u} \right) - B_a \frac{\partial q}{\partial t} \quad (\text{II.12})$$

### Adsorption kinetic

By definition, variation rate of adsorbed water density is the **time derivative**  $\partial q / \partial t$  of **adsorbed water density**  $q$ . Adsorption is a really fast process that adjusts adsorbed quantity quasi-instantly depending on temperature and partial pressure (or concentration) of adsorbate. But as porous materials are used to take a better advantage of adsorption phenomenon (by maximizing available surface), there might be a non-negligible temperature and pressure (or concentration) **gradient** between bed macroporosity and micropores of adsorbent material due to **diffusion process**. This can lead to differences between mean **instant adsorbed density**  $q$  and mean **equilibrium adsorbed density**  $q_e$  that *would be reached* under the same temperature and pressure conditions after complete diffusion.

Diffusion mechanisms and available alternatives for diffusion modeling are explained in section II.2.3. A good ratio between simplicity and precision has been chosen with a **LDF-like model** displayed in equation II.13 below.

$$\frac{\partial q}{\partial t} = k_m (q_e - q) \quad (\text{II.13})$$

## II.2 Heat and mass transfers in porous media

### II.2.1 A multi-scale approach

Adsorption is a molecular phenomenon that can be modeled to macroscopic or microscopic scale, which are two very different approaches in the modeling of adsorption. As adsorption depends on the surface area, porous materials are employed. It implies to take into account for mass transfers in porous media.

#### To the bed scale

Adsorbents often come as beads to the millimeter scale. Mass transfers occurs to the bed scale in the interstices in between beads that take up about 37% of the total tank volume ( $\epsilon_b = 0.37$  - (Zou and Yu, 1995)). This mass transfer mechanism is **advection**.

#### To the beads scale (macroscopic)

Mass transfer also occurs inside beads which are made of an agglomeration of microparticles (cf. figure II.4) with inter micro-particles porosity  $\epsilon_p$ . This is a transition between pure advection and pure diffusion. Fluid velocity to the beads scale is far lower than to the bed scale.

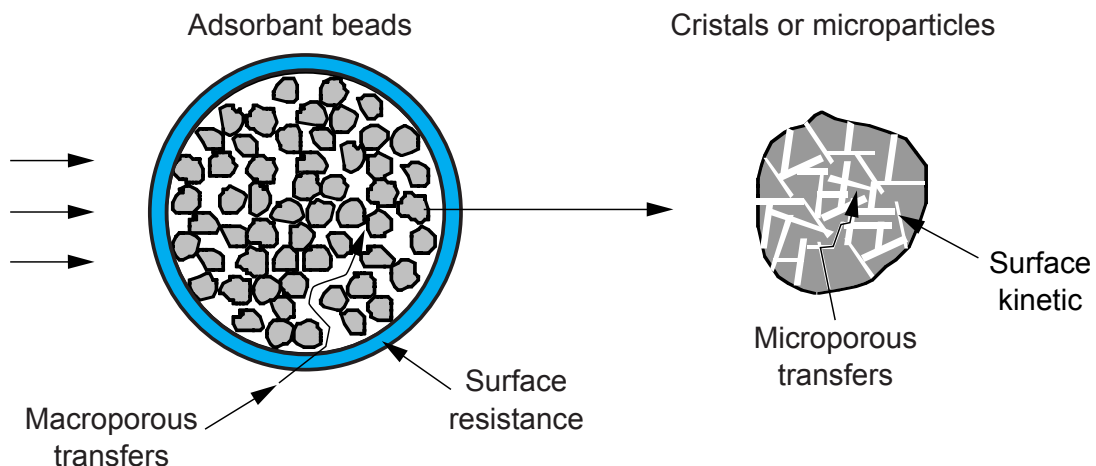


Figure II.4 – Adsorption kinetic mechanisms with a double porosity bead (translated from Sun and Meunier (2003)). The blue circle (left) has a 1.5 to 2 mm diameter. Each bead is composed of hundreds of smaller microparticles.

Most adsorption data are measured at a bead scale. Macroscopic adsorption models are then widely developed in literature (II.2.5.1). Such models use from two to dozens of fitting parameters set with experimental data (or microscopic models) to be adjusted. But these models are widespread because of the good trade-off between correctness and rapidity. A macroscopic scale model will be used within the framework of this thesis. Heat and mass transfers inside a bead (beyond the blue line of figure II.4) are accounted in a macroscopic way.

### To the pores scale (microscopic)

Detailed models at **microscopic scale** are aimed at describing adsorption process with **physical laws at molecular level**. This approach is the only way to predict adsorption properties of a material with only microscopic and thermophysical material properties as inputs. Experimental results are only required for validation purposes.

Microscopic scale models are beyond the scope of this Ph.D thesis. However, microscopic models are very interesting since they could be used at a pore scale to deeper understand and take into adsorption mechanisms. It would especially be useful to determine macroscopic models coefficients based on molecular and microscopic material properties such as pores shape and dimension, or Lennard-Jones potential (García et al., 2013).

However, even if adsorption mechanisms are not described to a molecular scale, diffusion mechanisms are still taken into account with a LDF-like model (paragraph II.2.3). It enables a satisfactorily reproduction of adsorption kinetic.

## II.2.2 Advection in porous media

Mass transfer to the bed scale is an advection process. Thus, fluid velocity must be carefully evaluated.

### II.2.2.1 Effective fluid velocity

Within a porous material, two definitions of fluid velocity are to be considered.

- The **superficial velocity**  $v_s$  that can be defined as the ratio of volume flow rate  $Q_v$  and cross section area  $S$ . This velocity definition is used for the evaluation of **global** values such as pressure drop or heat power.
- The **particle velocity**  $v_p$  that takes into account the length of the path followed by a fluid particle. It takes **tortuosity** into account. This is the *local* value of velocity.

Superficial fluid velocity depends on bed porosity and pressure drop across the bed. For Reynolds numbers lower than 10, fluid velocity is linear and can be estimated with Darcy's law (equation II.14, Darcy (1856), Gray and Miller (2004, eq. 6)) or Ergun equation (equation II.15, Ergun (1952)).

$$\vec{v}_s = -\frac{K}{\mu} \overrightarrow{\text{grad}}(p) \Rightarrow \|\vec{v}_s\| = \frac{K}{\mu} \frac{\Delta p}{L} \quad (\text{II.14})$$

$$v_s + b \rho_f v_s^2 = -\frac{K}{\mu} \Delta p_t \quad \text{with } b = \frac{3.5 r_p}{150 (1 - \epsilon)} \quad (\text{II.15})$$

Both equations use bed permeability  $K$  and dynamic viscosity  $\mu$ . For Reynolds numbers higher than 10, divergence from Darcy's law is observed. These nonlinearities were first attributed to turbulence. Another point of view attributes it to microscopic inertial effects or to the effects of increased microscopic drag forces on the pore walls (Hassanizadeh and Gray, 1987).

The fluid density  $\rho$  ( $1.2 \text{ kg m}^{-3}$ ), its dynamic viscosity  $\mu$  ( $1810^{-5} \text{ N s m}^{-2}$ ), velocity  $v$  and characteristic length  $l$  are used in the estimation of Reynolds number.

$$Re = \frac{\rho v l}{\mu} \quad (\text{II.16})$$

It is somehow complicated to estimate velocity and characteristic length with accurate values since it depends on local conditions. In the interstices between beads, velocity is greater so as characteristic length. It is the other way around within the beads. Hence, Reynolds number is maximal in the bed interstices. Characteristic length  $l$  in the bed interstices is hard to estimate but surely below beads diameter. Fluid velocity depends on airflow rate and tortuosity but is around  $0.1 \text{ m s}^{-1}$ . A very unfavorable estimation of Reynolds number would then estimate it at 10.6. Several over-estimations led to this value. It is then with good confidence that it is believed Reynolds numbers remain below 10 in the whole adsorbent bed. **Darcy's law is then chosen** for the calculation of fluid velocity in the remainder of the document.

### II.2.2.2 Bed permeability

Permeability is an intrinsic property of a porous material. It can be measured experimentally or evaluated theoretically with a correlation. Indeed, the **Kozeny-Carman** equation (Carman, 1956, eq. 1.40) establishes a relationship between pressure drop  $\Delta p$  of a fluid flowing across a packed bed.

$$\frac{\Delta p}{L} = \frac{180 \mu (1 - \epsilon_b)^2}{\Phi_s^2 d_p^2 \epsilon_b^3} v_s \quad (\text{II.17})$$

where  $\Phi$  is the **sphericity** of the particles in the packed bed,  $d_p$  the particles diameter and  $\epsilon_b$  the bed porosity.

A combination of equations II.17 and II.14 gives the following expression of bed permeability.

$$K = \frac{d_p^2 \epsilon_b^3}{180 (1 - \epsilon_b)^2} \quad (\text{II.18})$$

### II.2.2.3 Dynamic viscosity

The dynamic viscosity  $\mu$  of a fluid expresses its resistance to shearing flows. Dependence of air viscosity to temperature is not negligible in the range from  $20^\circ\text{C}$  to  $180^\circ\text{C}$  ( $\mu|_{T=180^\circ\text{C}}$  is 40% higher than  $\mu|_{T=10^\circ\text{C}}$ ). The correlation from equation II.19 is used for viscosity calculation.

$$\mu(T) = 4.564 \cdot 10^{-8} T + 4.745 \cdot 10^{-6} \quad (\text{II.19})$$

## II.2.3 Diffusion in porous media

Diffusion in porous materials is a really complex phenomenon. Ruthven (1984) explains that diffusion occurs in macropores and in micropores with completely different mechanisms.

### II.2.3.1 Macropore diffusion

Macropore diffusion is governed by four distinct transport mechanisms: molecular diffusion, Knudsen diffusion, Poiseuille flow and surface diffusion. The contribution of each mechanism depends on the details of **pore structure**.

- **Molecular diffusion** accounts for the resistance to mass transfer generated by collisions of diffused particles among themselves. It is the dominant transport mechanism when pore diameter is large relative to the mean free path of the gas (i.e., "*the average distance traveled between molecular collisions*" (Ruthven, 1984)).
- In **small pores** and at **low pressures**, the mean free path can become longer than the pore diameter. In this case, collisions with the pore walls are dominant which is known as **Knudsen diffusion**. There usually is a transition zone in which molecular diffusion and Knudsen diffusion coexist. The pressure range at which transition occurs depends on the sorbent material.
- For multilayer adsorption materials at relatively low temperatures, the thickness of the adsorbed layer is substantial. Thus, even if the mobility of the adsorbed phase is much smaller than that of the gas phase, the density is very high. **Surface diffusion** can then significantly contribute to mass diffusion.
- **Poiseuille flow** can contribute to total diffusion if there is a pressure drop across a particle. This is generally negligible in a packed bed at atmospheric pressure but it might be of greater significance under vacuum conditions.

### II.2.3.2 Micropore diffusion

Micropore diffusion is even of greater complexity and depends on the nature of the adsorbate-adsorbent pairs. This is then very complicated to come up with general correlations. Moreover, it is usually a rapid phenomenon that is complicated to capture experimentally. For sake of simplification, the resistance to mass transfers induced by micropore diffusion will then be neglected.

### II.2.3.3 Adsorption kinetics modeling

As explained earlier, diffusion can lead to a significant difference between the equilibrium state  $q_e$  calculated from the micropores' thermodynamic state and the adsorbate quantity  $q$  effectively adsorbed in micropores. It is then important to evaluate **adsorption kinetic**. This can be achieved through different approaches such as equilibrium models, diffusion models or linear driving force (LDF) models.

#### • Equilibrium model

It is reasonable to have recourse to an equilibrium model when **diffusion rate** of adsorbate within pores is **fast enough** to consider that there is an **equilibrium state** between adsorbate and adsorbent **at any time**. Variation rate of adsorbed water density is then given by the derivation of the adsorption equilibrium model (Duquesne et al., 2014).

$$q = q_e(T, p_v) \quad (\text{II.20})$$

$$\frac{\partial q}{\partial t} = \frac{\partial q_e(T, p_v)}{\partial t} = \frac{\partial q_e}{\partial T} \frac{\partial T}{\partial t} + \frac{\partial q_e}{\partial p_v} \frac{\partial p_v}{\partial t} \quad (\text{II.21})$$

#### • Diffusion model

As explained in paragraph II.2.3, diffusion is a complex phenomenon that calls for different mechanisms. It is then almost impossible to derive a diffusion model that takes all these mechanisms into account. The most widespread adsorption kinetic model is presented in equation II.22 below (Qiu et al., 2009).

$$\frac{\partial q}{\partial t} = \frac{D_s}{r^2} \frac{\partial}{\partial r} \left( r^2 \frac{\partial q}{\partial r} \right) \text{ with } \begin{cases} D_s, \text{ diffusion coefficient} \\ r, \text{ radial position} \end{cases} \quad (\text{II.22})$$

An equilibrium model is still needed to set conditions at the boundaries of a bead. Li and Yang (1999, eq.1-6) develop the solution of equation II.22 by integrating it over the whole particle volume and get the following infinite series:

$$\frac{\partial \bar{q}}{\partial t} = 6 q_e \sum_{n=1}^{\infty} \frac{D_s}{R_0^2} \exp\left(- (n\pi)^2 \frac{D_s t}{R_0^2}\right) \quad (\text{II.23})$$

This model (as other diffusion models) is more accurate than equilibrium model but also requires more computing resources which increases calculation time. The slow convergence of infinite series has motivated the development of simpler models (such as LDF) approximating this solution.

#### • Linear driving force (LDF) model

It seems that Lagergren (1898) was the first to propose a first-order equation describing kinetic of adsorption (for liquid-solid adsorption). Lagergren equation can be presented as follow.

$$\frac{\partial q}{\partial t} = \Psi (q_e - q) \text{ with } \begin{cases} q_e, \text{ ads. capacity at equilibrium} \\ \Psi, \text{ rate constant } [min^{-1}] \end{cases} \quad (\text{II.24})$$

Glueckauf (1955) estimates  $\Psi$  coefficient with a function of beads radius  $r_p$  and beads diffusivity  $D_s$ , which depends on temperature (Sun and Meunier, 2003).

$$\Psi = 15 \frac{D_s}{r_p^2} \text{ with } D_s = D_0 \exp\left(-\frac{E_a}{RT}\right) \quad (\text{II.25})$$

Ahn and Lee (2004, Eq. 11-12) propose a different correlation that is not temperature dependent. Their mass transfer coefficient  $k_m$  is an overall diffusion coefficient that depends on fluid velocity. Validation step (section III.2.2) shows this approach is to be preferred.

### II.2.4 Selected approach on kinetic modeling

**Equilibrium models** are known for **overestimating adsorption kinetic** whereas LDF models underestimate it for short time responses and give acceptable results at longer times (Sun and Meunier (2003); Qiu et al. (2009); Sircar and Hufton (2000) and figure II.5). **LDF models** have the other advantage to **estimate  $\partial q/\partial t$  with physical consideration** rather than a mathematical derivation of an equilibrium model that would use partial derivatives to estimate time derivatives.

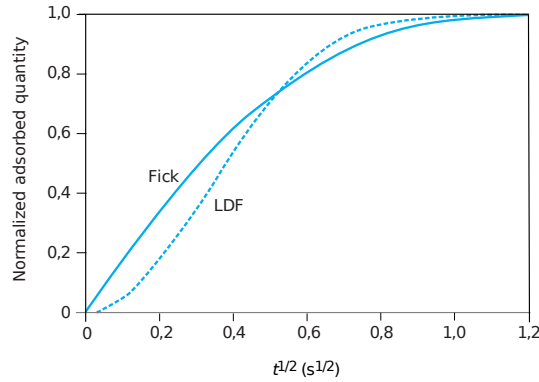
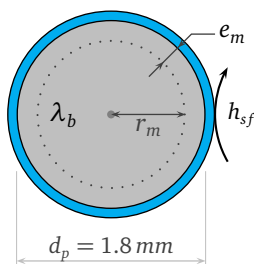


Figure II.5 – Comparison between dynamic responses from diffusion model (Fick) and LDF model (Sun and Meunier, 2003)

$$\underbrace{\frac{\partial q}{\partial t} = k_m (q_e - q)}_{\text{LDF-like model}} \text{ vs. } \underbrace{\frac{\partial q}{\partial t} = \frac{\partial q_e(p_v, T)}{\partial t} = \frac{\partial q_e}{\partial p_v} \frac{\partial p_v}{\partial t} + \frac{\partial q_e}{\partial T} \frac{\partial T}{\partial t}}_{\text{equilibrium model}} \quad (\text{II.26})$$

It is then decided to use a **LDF-like model**, at a larger scale than what is traditionally referred to as "LDF model" in litterature. This approach is reassured by conclusion of Sircar and Hufton (2000) on the consistency of LDF models. Mass transfer coefficient  $k_m$  is the sum of the contribution of diffusion at a pore scale and advection within beads. Its expression is of the form  $k_m = \Psi + k_{vs} \times v_s$ , with  $\Psi$  as formulated in equation II.25, and  $k_{vs}$  an experimentally determined coefficient. Final expression of  $k_m$  is given in equation III.1. A model for adsorption equilibrium is still required and will be developed in the following section.

This approach has also an influence on the evaluation of heat transfer coefficient, since heat transfer from a bead to the bed interstices must also be seen from a macroscopic point of view.



Heat is carried from/to the bead through conduction and transmitted to/from the fluid through convection. A global conductance  $U_b$  is defined as the sum of conductive and convective heat transfers.

$$U_b = \frac{1}{R_{conv} + R_{cond}} \quad (\text{II.27})$$

The convection heat transfer coefficient at the bead surface  $h_{sf} = 1/R_{conv}$  is given by equation

II.2 (Kuwahara et al., 2001). The conductive resistance  $R_{cond}$  depends on the bead conductivity  $\lambda_b$  and on the mean distance between any bead particle and the bead surface  $e_m$ . This distance is easily evaluated stating that, within the bead, volumes on either sides of the sphere of radius  $r_m = r_p - e_m$  are the same (eq. II.28). It comes up to an expression of the mean conductive resistance  $R_{cond}$  (eq. II.30).

$$\frac{4}{3}\pi r_m^3 = \frac{4}{3}\pi \left(\frac{d_p}{2}\right)^3 - \frac{4}{3}\pi r_m^3 \Rightarrow r_m = \frac{1}{\sqrt[3]{2}} \frac{d_p}{2} \quad (\text{II.28})$$

$$\Rightarrow e_m = \frac{d_p}{2} \left(1 - \frac{1}{\sqrt[3]{2}}\right) \simeq 0.21 \times \frac{d_p}{2} \quad (\text{II.29})$$

$$\Rightarrow R_{cond} = \left(1 - \frac{1}{\sqrt[3]{2}}\right) \frac{d_p}{2\lambda_b} \quad (\text{II.30})$$

A concatenation of equations II.2 and II.30 into equation II.27 gives the following expression of the mean heat conductance  $U_b$  between a bead and its surroundings.

$$\frac{1}{U_b} = \frac{D}{\lambda_f \left( \left(1 + \frac{4(1-\epsilon_b)}{\epsilon_b}\right) + \frac{1}{2}(1-\epsilon_b)^{1/2} Re^{0.6} Pr^{1/3} \right)} + \left(1 - \frac{1}{\sqrt[3]{2}}\right) \frac{d_p}{2\lambda_b} \quad (\text{II.31})$$

## II.2.5 Numerical modeling of adsorption equilibrium

### II.2.5.1 Macroscopic adsorption equilibrium models in literature

Most models evaluate **adsorption equilibrium** state as a function of temperature and adsorbate concentration or pressure. Adsorption data are commonly presented in the form of adsorption isotherms (more rarely isobaric diagrams). Brunauer have classified adsorption isotherms into five categories.

#### Brunauer classification of isotherms for adsorption equilibrium

Experimental measurement of adsorption equilibrium can be achieved with DVS (Dynamic Vapor Sorption) or TGA-DSC (ThermoGravimetric Analysis and Differential Scanning Calorimetry). Both methods can result in adsorption isotherm measurement if they are executed at constant temperature. Brunauer et al. (1940) proposed, in 1940, a classification of adsorption isotherms (figure II.6).

Ruthven (1984) gives detailed physical explanation of the five different shapes proposed by Brunauer.

- **Type I** is typical of microporous adsorbents in which pore sizes are not much larger than sorbate molecular diameter. Saturation is reached when all micropores are filled with one adsorbate molecule.
- **Types II and III** shapes are generally observed in adsorbent with a wide range of pore diam-

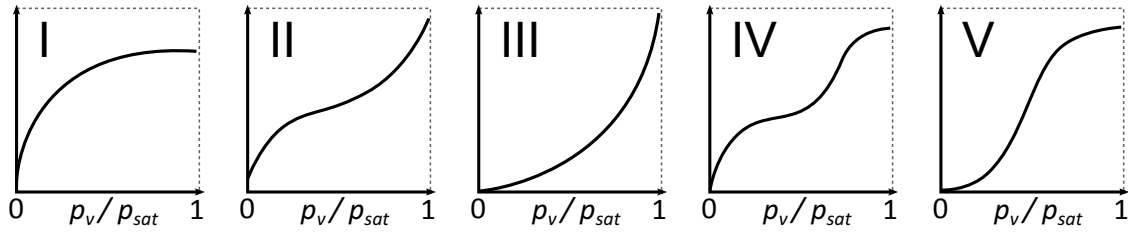


Figure II.6 – Brunauer classification of equilibrium isotherms

eters. Pore saturation occurs faster in small pores than in wider pores. There is a continuous loading from monolayer to multilayer adsorption. Capillary condensation occurs in largest pores at high pressures resulting in the increase of adsorption capacity.

In type III, interactions between adsorbate molecules are wider than interactions between adsorbent and adsorbate molecules.

- **Type V** is similar to Type I but is observed in case of high intermolecular attraction effects.

The formulation of a macroscopic model is often derived from physics. Nevertheless, these models require experimental data to fix their coefficients. Fitted coefficients are then only applicable to the adsorbent-adsorbate pair associated with experimental data used to fix the coefficients. Even if most adsorption isotherms can be related to one of the five types described above, detailed shape is different for each adsorbent. Different models have then been developed and refined for common adsorbents (such as activated carbon, zeolites, ...). [Furmaniak et al. \(2008\)](#) gives a complete overview of the evolution of adsorption modeling of water on carbons (figure II.7).

### Type I isotherms: Langmuir equation

Langmuir isotherm is the simplest theoretical model for monolayer adsorption. Basic assumptions on which the model is based are: ([Ruthven, 1984](#), p.49)

1. "Molecules are adsorbed at a fixed number of well-defined localized sites"
2. "Each site can hold one adsorbate molecule"
3. "All sites are energetically equivalent"
4. "There is no interaction between molecules adsorbed on neighboring sites"

Langmuir model derivation states there is, at equilibrium condition, an equality between adsorption rate and desorption rate.

$$\theta = \frac{q}{q_s} = \frac{b p}{1 + b p} \quad (\text{II.32})$$

with  $q_s$  the total number of adsorption sites,  $q$  the number of occupied sites,  $b$  a temperature dependent term and  $p$  the pressure.  $b$  follows a Vant Hoff equation.

$$b = b_0 \exp\left(\frac{-\Delta H_0}{R T}\right) \quad (\text{II.33})$$

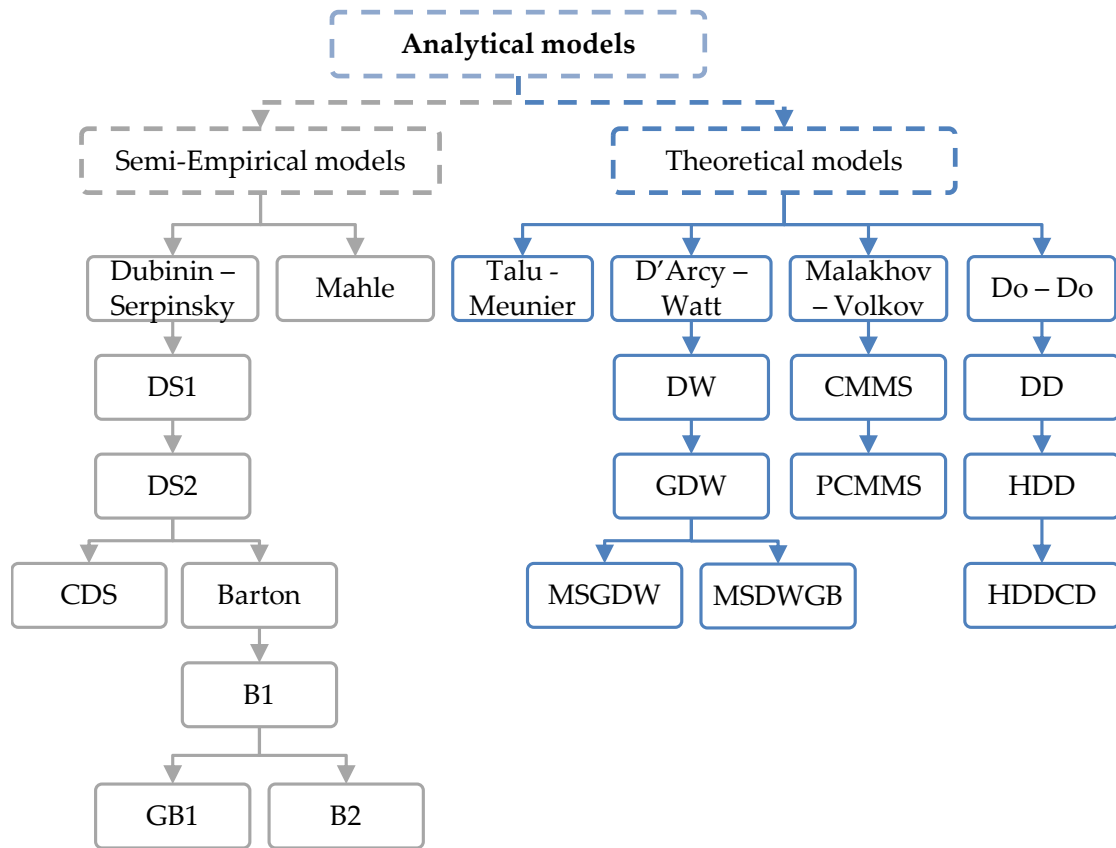


Figure II.7 – Derivation of models for water adsorption on carbons (reproduced from [Furmaniak et al. \(2008\)](#))

Langmuir equation satisfactorily reproduces Type I isotherms (monolayer adsorption - see figure II.8). Numerous models have been derived for monolayer adsorption. A few of them are enumerated below.

- **Langmuir-Freundlich model**

It is directly derived from Langmuir equation. It is used in case of adsorbent with heterogeneous surfaces ([Sun and Meunier, 2003](#), eq. 5).

$$q = q_s \frac{(b p^m)}{1 + (b p^m)} \quad (\text{II.34})$$

with  $m$  a constant describing interactions between adsorbate and adsorbent.  $m$  is generally below 1.

• **Dubinin-Radushkevich model**

This model fits type I isotherm with an exponential law (Dubinin, 1960; Sun and Meunier, 2003, eq. 7).

$$q = q_m \exp\left(-C \left(\frac{\epsilon_b}{\beta}\right)^2\right) \text{ with } \begin{cases} \epsilon_b = RT \ln\left(\frac{p_{sat}}{p}\right) \\ C, \text{ a constant} \\ \beta, \text{ a parameter} \end{cases} \quad (\text{II.35})$$

• **Dubinin-Astakhov model**

It introduces an additional parameter  $m$  that takes into account pores size distribution (Dubinin, 1960; Sun and Meunier, 2003, eq. 8).

$$q = q_m \exp\left(-C \left(\frac{\epsilon_b}{\beta}\right)^m\right) \quad (\text{II.36})$$

• **Toth model**

Toth model enables a good reproduction of pressure and temperature dependency of Type I isotherms with as low as five parameters (Wang and LeVan, 2009).

$$q = \frac{a p_v}{[1 + (b p_v)^t]^{\frac{1}{t}}} \text{ with } \begin{cases} a = a_0 \exp(E/T) \\ b = b_0 \exp(E/T) \\ t = t_0 + \frac{c}{T} \end{cases} \quad (\text{II.37})$$

**Type II isotherms**

For multilayer adsorption, more complicated models must be considered due to the shape of the adsorption curve (figure II.8).

• **Generalized Langmuir equation**

Generalized Langmuir equation sums up influences of different layers.

$$q = \sum_{i=1}^n q_{s_i} \frac{b_i p}{1 + b_i p} \text{ with } \begin{cases} q_{s_i} = \sum_{j=0}^3 \frac{a_{j,i}}{T^j} \\ b_i = b_{o,i} \exp\left(\frac{E_i}{T}\right) \end{cases} \quad (\text{II.38})$$

This model calls for  $4n$   $a_{j,i}$  fitting constants and  $n$   $b_i$  fitting constants. For instance, if  $n = 3$ , 15 constants must then be determined from experimental data. Sun et al. (1995) propose values for zeolite 13X-water and 13X-ammonia pairs.

- **BET theory**

Brunauer, Emmett and Teller (BET) have proposed a model that account for multilayer adsorption. It is still widely used to estimate monolayer capacity and specific surface area from experimental results. The first derivation of the BET equation stated an infinite number of layers (Ruthven, 1984).

$$q = q_m \frac{b \left( \frac{p}{p_{sat}} \right)}{\left( 1 - \frac{p}{p_{sat}} \right) \left( 1 - \frac{p}{p_{sat}} + b \frac{p}{p_{sat}} \right)} \quad (\text{II.39})$$

This model is only valid in the range  $0.05 < \frac{p}{p_{sat}} < 0.35$ . Its range of validity can be extended by considering a finite number of layers (Sun and Meunier, 2003).

$$q = q_m \frac{K_{BET} p_v}{1 - \frac{p_v}{p_{sat}}} \frac{1 - (m+1) \left( \frac{p_v}{p_{sat}} \right)^m + m \left( \frac{p_v}{p_{sat}} \right)^{m+1}}{1 - \frac{p_v}{p_{sat}} + K_{BET} p_v \left( 1 - \left( \frac{p_v}{p_{sat}} \right)^m \right)} \quad (\text{II.40})$$

with  $q_m$  the adsorption capacity of the first layer,  $K_{BET}$  a constant,  $p_v$  the partial pressure of sorbate,  $p_{sat}$  the saturation pressure and  $m$  the number of layers.

### Existing experimental databases on adsorptive material properties

There are several databases for experimental data on adsorption isotherms of numerous adsorbate-adsorbent pairs. Most are commercial tools that require user authentication, few are freely available. Three among the most widespread databases are quickly presented.

- **NIST Adsorbents database<sup>1</sup>**

This database is dedicated to adsorption data. The search engine enables queries formulated with names or chemical formula of adsorbent and/or adsorbate. It is also possible to set a filter on isotherm(s) temperature(s). This database embeds a plotting tool and also proposes to fit coefficients of Langmuir, Langmuir-Freundlich and Freundlich adsorption models with experimental data (fitting is applied isotherm by isotherm not across several isotherms). NIST adsorbents database can be seen as an aggregator and plotter of experimental data available in literature.

<sup>1</sup>NIST adsorbents database is available online at [adsorbents.nist.gov](http://adsorbents.nist.gov) (open-access)

- **Reaxys<sup>2</sup>**

Reaxys is a web-based tool developed and edited by *Elsevier*<sup>®</sup> and not accessible in open-access. The scope of Reaxys is very large since its development is based on former Beilstein database. It retrieves all available data from literature and patents regarding chemical and physical properties from 1771 to now. It includes adsorption data, if available. Reaxys' search engine embeds so much fields and filters possibilities that it is more complicated to use than NIST database. Moreover, it seems adsorption isotherms data are only available through their original articles which is less handy than NIST database.

- **Springer materials<sup>3</sup>**

Springer material database is also a database for chemical and thermophysical material properties. It is edited by *Springer*<sup>®</sup> and based on Landolt-Bornstein database, first published in 1883. Search engine is freely accessible but charts and data download is not open-access.

These databases, and especially the one from NIST, are a good attempt to share data with the whole scientific community. However it is not always easy to find good queries to get expected data. Moreover, literature seems to be extensive on pollutants adsorbates (since adsorption process is firstly used for separation purposes) but not extensive when the adsorbate is water.

Extensive time has been spent on the choice and development of adsorption equilibrium model. This work ended up at the following thoughts:

- The choice of an equilibrium model is strongly correlated to the set of experimental data to be fitted.
- The challenging part in the development of an adsorption model consists in fitting with the same coefficients several isotherms curves within a range of temperature.
- There is a lack of standard to measure adsorption properties. It is thus complicated, even with access to material databases, to get adsorption isotherm data:
  - for a given adsorbent/water pair,
  - at more than two different temperatures,
  - from the same measurement protocole.
- Available experimental isotherms generally lack of data in the low relative humidities. Unfortunately it is the most important range in our experiments.
- Adsorption isotherms are generally measured with very small samples whereas adsorption capacities seem to be lower in larger scale experiments ([Hongois, 2011](#)).

It is then decided to build the shape of an adsorption model based on data from [Ahn and Lee \(2003\)](#), which gives the most promising results with a BET model. Final coefficients used in the

---

<sup>2</sup>Reaxys database is available online at [www.elsevier.com/solutions/reaxys](http://www.elsevier.com/solutions/reaxys) (registration required)

<sup>3</sup>Springer material database is available online at [materials.springer.com](http://materials.springer.com) (registration required for accessing data)

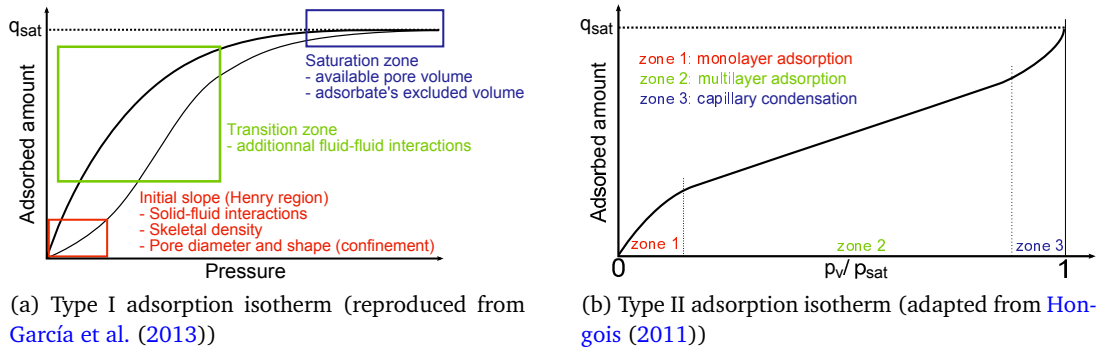


Figure II.8 – Schematic representation of types I and II isotherms

simulation are adjusted with some data coming from experimental results (remaining experimental data are used for validation purposes only).

### II.2.5.2 Equilibrium model development

Most macroscopic adsorption models are a function of temperature and vapor pressure (or relative humidity or concentration). Model fitting is a step that therefore requires data for several pressures and temperatures. Adsorption isotherms are good inputs for models calibration. It is however somewhat difficult to find in literature or in existing databases such data at more than two different temperatures, with the same measurement protocol and instrumentation. Concatenating data from different sources would be acceptable but is often not possible due to lack of consistency between data sets. It is then necessary to deal with existing data for want of anything better.

Several set of data from Ahn and Lee (2004); Wang and LeVan (2009); Bales et al. (2005a) have been fitted and numerically experimented. The best results were obtained with a BET model set with data from Ahn and Lee (2004). It enables a good prediction of step temperature and step duration. The transient falling edge at the end of the discharging phase was however not satisfactorily reproduced. Investigations have shown it is due to a lack of precision of the BET model at very low relative humidities. It is then decided to build an adsorption equilibrium model with a sharper evolution at low relative humidities.

The adsorption model is made of a sum of three terms:

- a **Langmuir isotherm**, that is dominant in low relative humidities,
- a **linear function** that is dominant in the transition region,
- a **term of BET model** that is dominant in high relative humidities (capillary condensation).

$$q_e = \underbrace{q_n \frac{b \varphi}{1 + b \varphi}}_{\text{Henry's region}} + \underbrace{a \varphi}_{\text{transition zone}} + \underbrace{q_{cap} \frac{\varphi}{1 - \varphi}}_{\text{capillary condensation}} \quad (\text{II.41})$$

Fitting coefficients for adsorption isotherms displayed on figure II.9 are shown in table III.4

(page 72). Consistency between fitted model and original data is very good. Adsorbent beads used by Ahn and Lee (2004) to get these adsorption isotherms may be slightly different from those used within the experiments of STAID project<sup>4</sup>, whose data are used for validation purposes. Besides, the temperature range (298K - 318K) is quite narrow compared to what is done in the experiments (293K - 453K). It is then fairly possible that temperature dependence is to be adjusted with experimental data. That is why some validation data are used in order to refine this model with a wider range of validity as explained in section III.2.2.

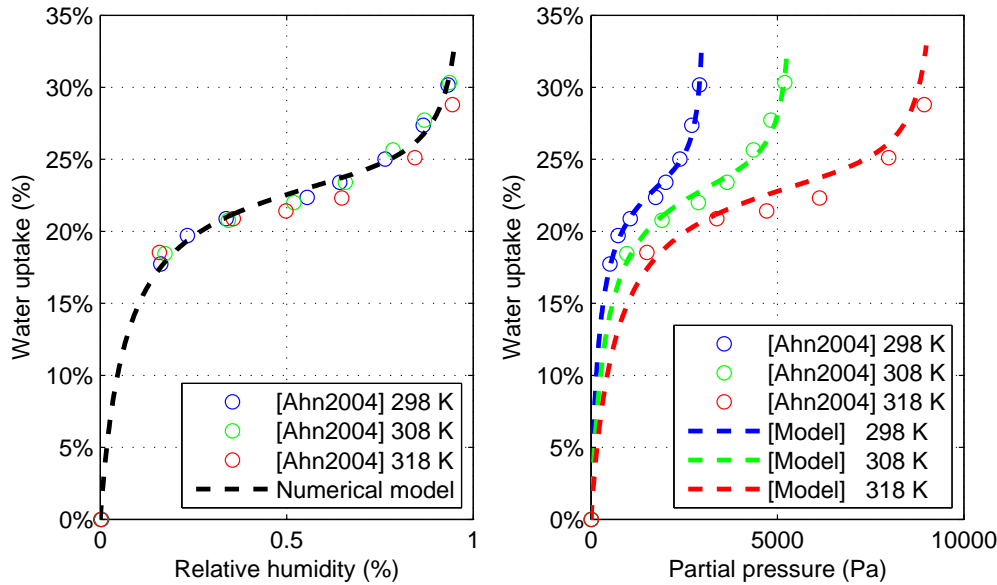


Figure II.9 – Experimental data (Ahn and Lee, 2004) and numerical model of water uptake displayed for three temperatures as a function relative humidity (left) and partial pressure (right)

### II.2.6 Differential heat of adsorption $\Delta H$

Differential enthalpy of adsorption  $\Delta H$  depends on water uptake. More energy is released when the adsorbent material is dry. In other words, adsorption occurs in priority on adsorption sites with a lower energy of activation, which release more energy to the surroundings. Figure II.10 shows the influence of water uptake on differential energy of adsorption for various adsorbent materials.

The following correlation is used to get the differential enthalpy of adsorption  $\Delta H$  of zeolite 13X as a function of water uptake  $\Delta m_w$ . It comes from the polynomial fitting of zeolite 13X curve of figure II.10.

$$\Delta H = 7.59 \times 10^{-4} \Delta m_w^5 - 5.34 \times 10^{-2} \Delta m_w^4 + 1.12 \Delta m_w^3 - 2.38 \Delta m_w^2 - 186.8 \Delta m_w + 4984 \quad (\text{II.42})$$

This correlation is restricted to a lower bound of  $2800 J/g_w$  and to an upper bound of  $4800 J/g_w$ .

<sup>4</sup>Design and development of a 2-kWh adsorption heat storage reactor (Johannes et al., 2015).

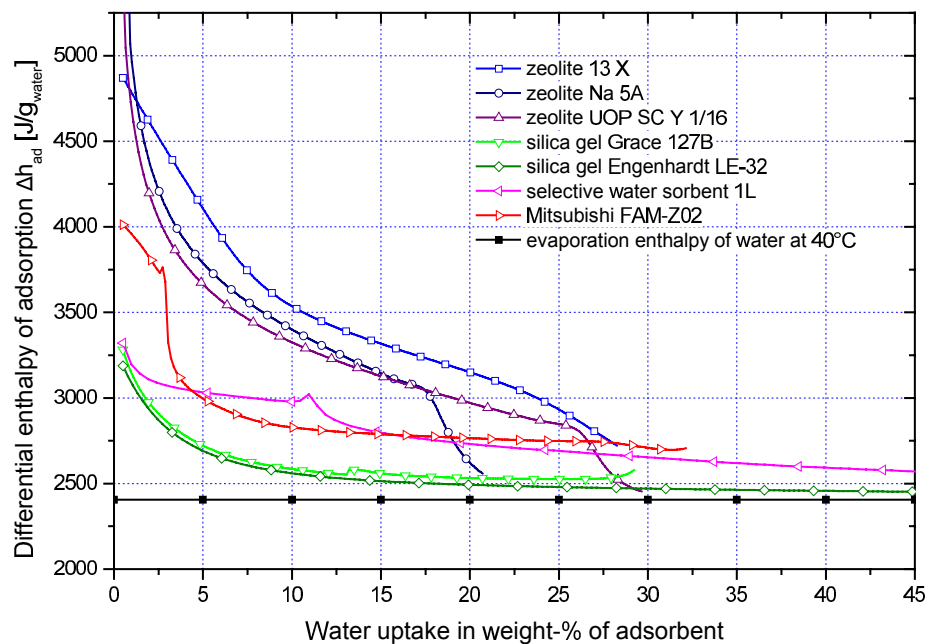


Figure II.10 – Differential heat of adsorption, at 40°C (from Bales et al. (2005a, fig. 5))

## II.3 Numerical developments

There are three steps in the computational modeling of a physical process. The first step is **problem definition**. Relevant quantities such as temperature, concentration or pressure are defined. It leads to an idealization of the problem of interest. The goal is to get a **well-posed** problem, in which a given set of parameters and operating conditions leads to one - and only one - numerical solution. This step has been treated in I.3.

The second step consists in the definition of a **mathematical model** that represents the physical phenomena. In fluid dynamics, a set of **governing equations** is often obtained with the formulation of conservation laws (energy, mass and momentum). The mathematical problem is then usually described by **partial differential equations (PDEs)** written in the **strong form**. A strong formulation invokes partial derivatives for any point of the domain. For sake of convenience, **simplifying assumptions** must generally be considered. At this step it is important to weigh up the pros and cons of each assumption. Reducing the complexity of the mathematical model mostly simplify problem resolution at the cost of accuracy. The mathematical model development has been done in section II.1 as general equations are concerned, and in previous section II.2.5 as regards to adsorption model.

Few problems are simple enough to be solved analytically (i.e. the solution can be formulated as an analytic function of space and time). In most cases, the problem must then be **solved computationally**.

A mathematical model represents the continuum of a physical phenomenon in space and time while computers only deal with discrete objects. The strong formulation of governing equations must then be discretized in space and time.

### II.3.1 Possible numerical methods for spatial discretization

Three classical methods have been developed in literature: finite difference methods (FDM), finite volume methods (FVM) and finite element methods (FEM). Each method uses a different approach with its own benefits and drawbacks. It leads to a discrete problem involving a **weak formulation** of the equations that does not call upon partial derivatives anymore. The partial differential equations are then turned into **ordinary differential equations (ODEs)**.

The three next paragraphs quickly introduce basics concepts of FEM, FDM and FVM and explains why FVM seems to be more suitable to the context of this work.

#### Finite elements method (FEM)

FEM is based on a variational formulation of the problem. The basic idea is to subdivide the whole domain into simpler parts, called finite elements, and to express the problem with an error function (the difference between the real solution and the approximate discrete solution). FEM then consists in minimizing this error function.

FEM has the advantage of being robust (many theoretical results on convergence) and suitable to any shapes. It is widely used in solid mechanics where many commercial tools are based on FEM (*ANSYS*<sup>®</sup>, *CADDS*<sup>®</sup>, *CATIA*<sup>®</sup>, *Abaqus*<sup>®</sup>...). *COMSOL Multiphysics*<sup>®</sup> is also developed with finite element analysis and computes mechanical, fluid dynamics, electrical and chemical calculations. Nevertheless, FEM might be harder to develop than FVM for fluid dynamics, and requires a larger amount of computer resources (higher calculation time and memory use).

#### Finite differences method (FDM)

FDM is historically the first method that was developed. Partial derivatives of the strong formulation are evaluated with Taylor series at each point of the discrete domain. FDM requires a rectilinear grid (but not necessarily a constant step) and is then limited to simple geometries. It was initially developed for 1D steady-state problems but it has been generalized to multidimensional domains since then (allowing 2D, 3D and/or unsteady calculations). Yet, it is complicated to set Neumann boundary conditions with FDM ([Goncalves, 2005](#)).

#### Finite volume method (FVM)

FVM is a discretization method based on integral formulation of equations. The calculation domain is subdivided into smaller subdomains called **control volumes**. Weak formulations are obtained by the integration of the strong formulation over each of these volumes. The quantities assigned at the center of each volume are then not an approximation of the local value but an averaged value over the whole control volume. This method has the strong advantage to conserve energy, mass and momentum locally but does not conserve fluxes for high orders.

FVM is widely used in fluid dynamics since this is the most natural development of conservation laws. A wide majority of CFD tools use FVM like the widespread proprietary tools *Ansys Fluent*<sup>®</sup> and *STAR-CCM+*, or the more specific *KIVA*<sup>®</sup> developed at the Los Alamos National Laboratory for numerical simulation of chemical reaction, heat transfers and fluid flow in engines. Several GNU-GPL licensed tools are also available like *OpenFOAM* or *Code Saturne* developed since 1997 at EdF R&D ([Archambeau et al., 2004](#)).

In the present research work, it seems important to fully control all the inputs, outputs, parameters and operating conditions, and to entirely understand and control all simplifying assumptions and their consequences. A choice has been made to manually implement a spatial discretization of the set of equations in *Matlab*<sup>®</sup> with the **finite volume method**, which is more suitable for conservation laws formulation, and to use an **ordinary differential equation (ODE) solver** to achieve the numerical integration of time derivatives.

### II.3.2 Model dimension and coordinate system

Numerical modeling requires to split a continuous calculation domain into a finite number of discrete points or volumes. Computer resources limit the total number of discrete elements considered in the calculation because of calculation time and memory issues (figure II.11 illustrates the evolution of calculation time against mesh number).

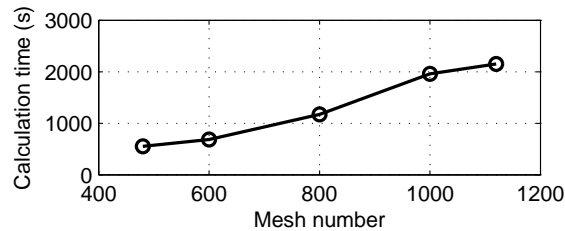
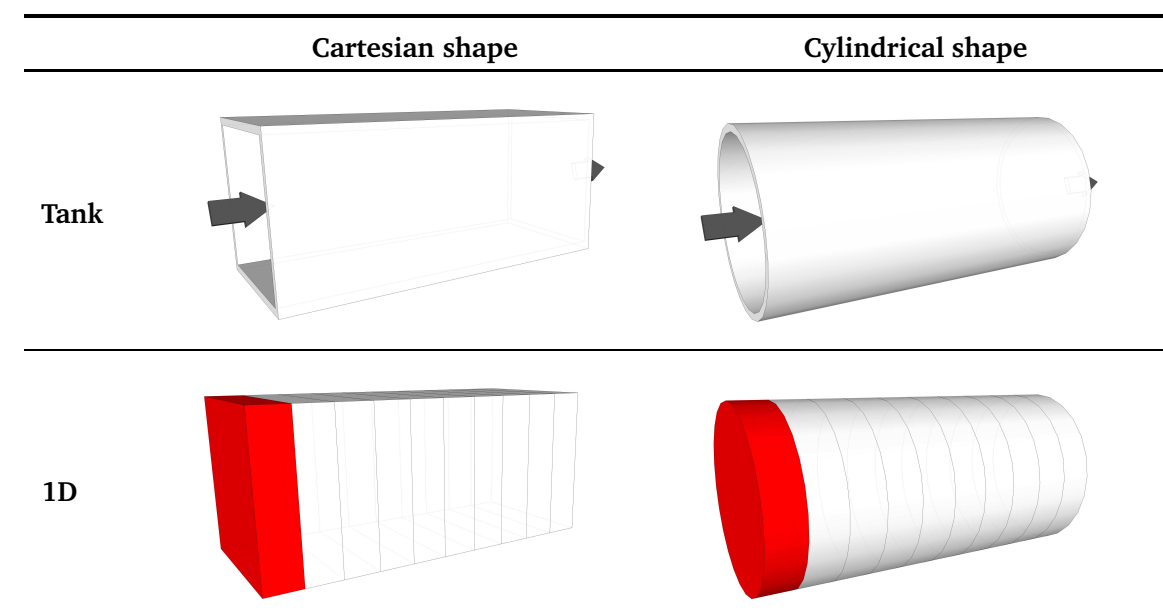
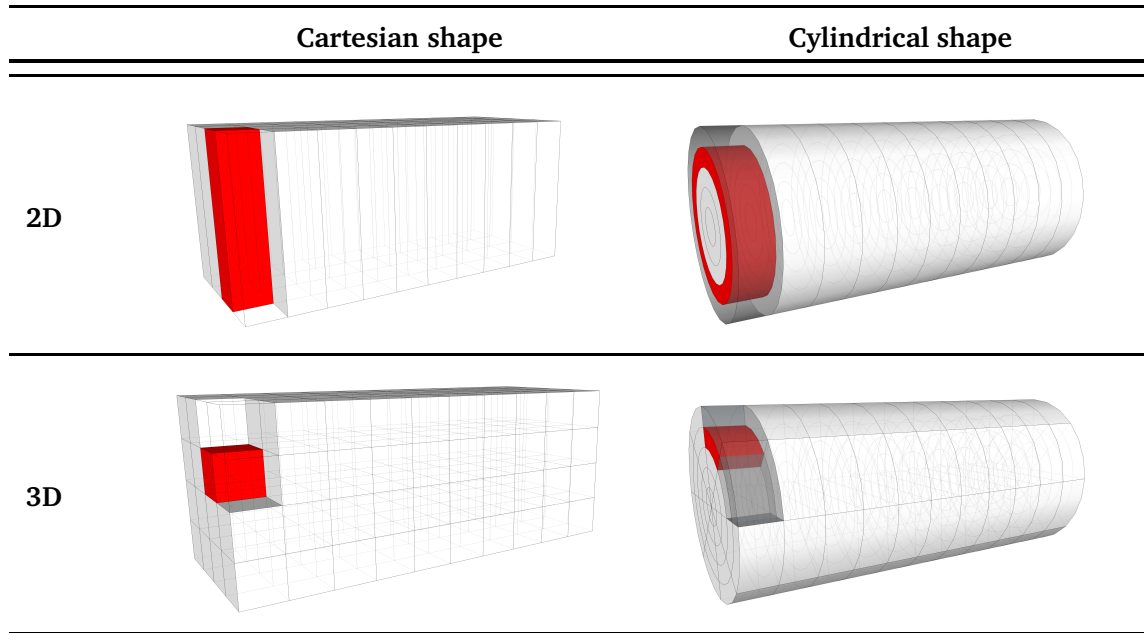


Figure II.11 – Example of the influence of mesh number on calculation time (data extracted from (Duquesne, 2013, Table 3.2))

To reach a compromise between calculation time and details or precision of results, it is sometimes necessary and justified to formulate some simplification assumptions enabling to consider 1D or 2D models instead of 3D models. In this work, a reactor tank with one opening on each of two opposite sides has to be discretized.





### II.3.2.1 1D models

One dimensional models assume **flow pattern is uniformly distributed** along any cross section of the tank. Liu et al. (2014) have numerically studied flow maldistribution in a small-scale axial adsorber. Results show pressure and velocity profiles may widely depend on radial position near the reactor entrance. Radial dependency decreases rapidly along the bed except along the walls of the reactor because of inhomogeneity in beads distribution near walls (fig. II.12). Homogeneity of flow distribution is then an hypothesis reasonably justifiable.

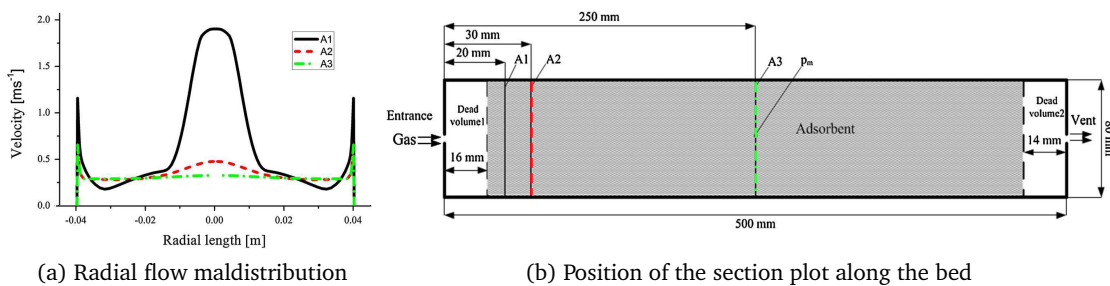


Figure II.12 – Radial velocity distribution along the bed (adapted from Liu et al. (2014))

Regarding heat transfers, 1D model states temperature distribution is uniform along any cross section of the tank. In other words, there is **no radial temperature gradient** in the reactor. This condition is rigorously justified if (1) flow is unidirectional and uniformly distributed, (2) tank walls are adiabatic, (3) internal heat sources diffuse heat uniformly in a cross section. In practice, a well insulated tank is sufficient to complete condition (2).

### II.3.2.2 2D models

2D models are not widely used for cartesian shapes unless there is specific boundary conditions justifying a 2D distribution of velocity, pressure or temperature. Two-dimensional models are however widely used for cylindrical shapes since it only states a symmetry of revolution ( $\theta$ -independent distribution). This is generally true when the influence of gravity on the system behavior can be negligible.

### II.3.2.3 3D models

3D models are used when one or several assumptions enabling to use 1D or 2D models are not reasonably acceptable. When computational resources or calculation time is limiting mesh number, it is important to refine mesh distribution along the coordinate where temperature and/or pressure gradients will be the highest. This is generally along the main flow direction (for forced convection systems) or perpendicular to the hottest or coldest surface (for thermally driven systems).

The numerical model has been developed to easily enable a switch in model dimension and/or coordinate system. **Fictive nodes** are used to deal with boundary conditions. It has the strong advantage of being **independent of model dimension**. A 1D-model with  $N$  volume nodes will for instance be treated as a 3D-model with  $3 \times 3 \times (N + 2)$  nodes. The numerical model calls upon **strong formulation of conservation laws**, and discretizes it afterwards along the mesh grid with the **selected discretization operators** (which depend on the system coordinate). The choice of discretization operators is done accordingly to system coordinate and model dimension.

## II.3.3 Discretization operators

The volume of the storage tank is subdivided into meshes. Figure II.13 provides information on subscript notations.

### II.3.3.1 Gradient operator

Gradient discretization is achieved with a second order formula.

$$\begin{array}{c}
 \leftarrow \Delta x \rightarrow \quad \bullet \quad \bullet \quad \bullet \\
 \quad \quad \quad u_{i-1} \quad u_i \quad u_{i+1}
 \end{array}
 \quad \frac{\partial u}{\partial x} \Big|_i = \frac{u_{i+1} - u_{i-1}}{2 \Delta x} \quad (\text{II.43})$$

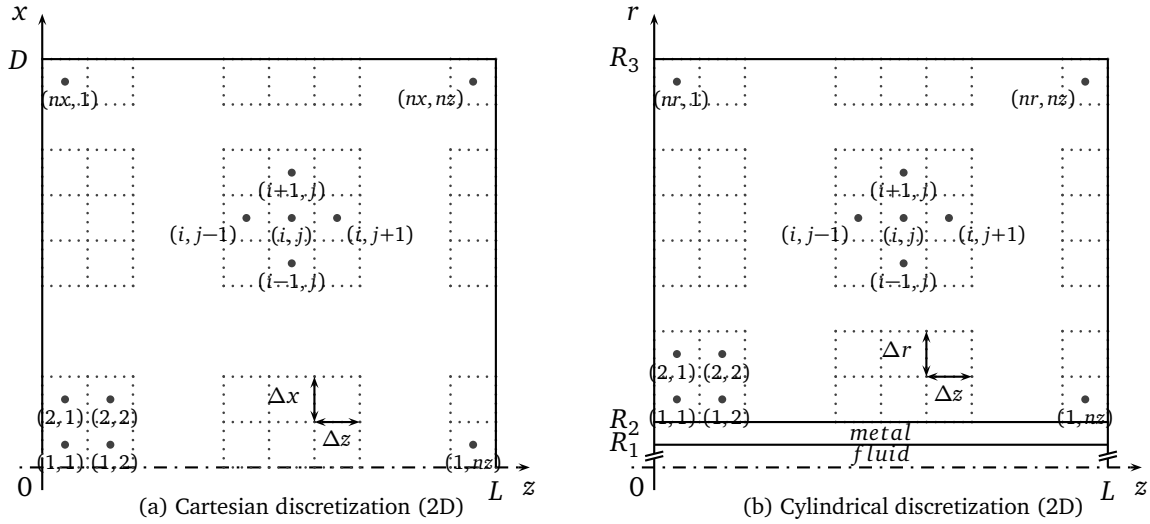


Figure II.13 – Subscripts notation for spatial discretization of the adsorbent bed

### II.3.3.2 Divergence operator

#### Cartesian coordinates

$$\begin{aligned} \operatorname{div}(\vec{u})|_{i,j,k} &= \frac{\partial u_x}{\partial x} + \frac{\partial u_y}{\partial y} + \frac{\partial u_z}{\partial z} \\ &= \frac{u_x|_{i+\frac{1}{2},j,k} - u_x|_{i-\frac{1}{2},j,k}}{\Delta x} + \frac{u_y|_{i,j+\frac{1}{2},k} - u_y|_{i,j-\frac{1}{2},k}}{\Delta y} + \frac{u_z|_{i,j,k+\frac{1}{2}} - u_z|_{i,j,k-\frac{1}{2}}}{\Delta z} \end{aligned} \quad (\text{II.44})$$

#### Cylindrical coordinates

$$\begin{aligned} \operatorname{div}(\vec{u})|_{i,j} &= \frac{1}{r} \frac{\partial (r u_r)}{\partial r} + \frac{\partial u_z}{\partial z} \\ &= \frac{u_z|_{i,j+\frac{1}{2}} - u_z|_{i,j-\frac{1}{2}}}{\Delta z} + \frac{1}{r_{i,j} \Delta r} \left( \left( r_{i,j} + \frac{\Delta r}{2} \right) u_r|_{i+\frac{1}{2},j} - \left( r_{i,j} - \frac{\Delta r}{2} \right) u_r|_{i-\frac{1}{2},j} \right) \end{aligned} \quad (\text{II.45})$$

### II.3.3.3 Laplace operator

#### Cartesian coordinates

$$\begin{aligned} \Delta u_{i,j,k} &= \frac{\partial^2 u}{\partial x^2} \Big|_{i,j,k} + \frac{\partial^2 u}{\partial y^2} \Big|_{i,j,k} + \frac{\partial^2 u}{\partial z^2} \Big|_{i,j,k} \\ &= \frac{u_{i-1,j,k} - 2u_{i,j,k} + u_{i+1,j,k}}{\Delta x^2} + \frac{u_{i,j-1,k} - 2u_{i,j,k} + u_{i,j+1,k}}{\Delta y^2} + \frac{u_{i,j,k-1} - 2u_{i,j,k} + u_{i,j,k+1}}{\Delta z^2} \end{aligned} \quad (\text{II.46})$$

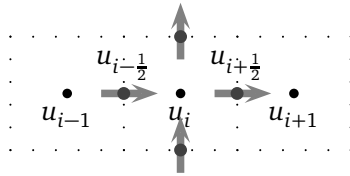
### Cylindrical coordinates

$$\begin{aligned}\Delta u_{i,j} &= \left. \frac{\partial^2 u}{\partial r^2} \right|_{i,j,k} + \frac{1}{r} \left. \frac{\partial u}{\partial r} \right|_{i,j,k} + \left. \frac{\partial^2 u}{\partial z^2} \right|_{i,j,k} \\ &= \frac{u_{i+1,j} - 2u_{i,j} + u_{i-1,j}}{\Delta r^2} + \frac{1}{r_{i,j}} \frac{u_{i+1,j} - u_{i-1,j}}{2\Delta r} + \frac{u_{i,j-1} - 2u_{i,j} + u_{i,j+1}}{\Delta z^2}\end{aligned}\quad (\text{II.47})$$

Equation II.47 is the natural development of Laplace operator with second order formulas of first and second derivatives. Equation II.48 below is the natural development of  $\Delta u = \text{div}(\overrightarrow{\text{grad}} u)$ . Both equations are strictly identical.

$$\Delta u_{i,j} = \frac{1}{r_{i,j}} \left( \left( r_{i,j} - \frac{\Delta r}{2} \right) \frac{u_{i-1,j} - u_{i,j}}{\Delta r^2} + \left( r_{i,j} + \frac{\Delta r}{2} \right) \frac{u_{i+1,j} - u_{i,j}}{\Delta r^2} \right) + \frac{u_{i,j-1} - 2u_{i,j} + u_{i,j+1}}{\Delta z^2} \quad (\text{II.48})$$

#### II.3.3.4 Estimation of interface values



There are three kinds of interface values: velocities, fluid properties (temperature or pressure) and boundary values.

#### Fluid velocity calculation

Velocity calculation is needed for **advection terms** evaluation. Advection terms participate to heat and mass transfers from a given node to adjacent nodes (and the other way around). It therefore always appears in **divergence operators**, which are a measurement of the balance of all fluxes crossing the boundaries of a volume node. It then seems handy to directly evaluate velocities to the boundaries of a volume node. This is a **staggered grid**, that is strongly advised for stability purposes (Patankar, 1980). Equation II.14 becomes, for example, equation II.49 at interface defined with coordinates  $(i - \frac{1}{2}, j)$ .

$$\vec{v}_{i-\frac{1}{2},j} = -\frac{K}{\mu} \frac{P_{v_{i,j}} - P_{v_{i-1,j}}}{\Delta x} \vec{e}_x \quad (\text{II.49})$$

#### Variable evaluation

Evaluation of temperature, pressure, or any other relevant quantity **at an interface between two volumes nodes** is achieved with an **UpWind scheme**. An UpWind scheme look at the direction of the flow and set the interface value to the value of the "UpWind" node. If there is no velocity, a centered scheme is used.

$$u_{i-\frac{1}{2},j} = \begin{cases} u_{i-1,j} & \text{if } \vec{v} \cdot \vec{e}_x > 0 \\ (u_{i-1,j} + u_{i,j})/2 & \text{if } \vec{v} \cdot \vec{e}_x = 0 \\ u_{i,j} & \text{if } \vec{v} \cdot \vec{e}_x < 0 \end{cases} \quad (\text{II.50})$$

#### Boundary value definition

In case a volume node touches a border of the calculation domain, the value of the fictive node that is adjacent to this volume node must be calculated according to boundary conditions. There

are mostly two kind of boundary conditions:

- If the *value* of the variable is specified, it is a **Dirichlet boundary condition**. The value of the fictive node must then be set with equation II.51 so that the value *on* the boundary is correct.
- If the *first spatial derivative* of the variable is specified, it is a **Neumann boundary condition**. The value of the fictive node must then be set with equation II.52 so that the value *on* the boundary is correct.

$$u_{z=L} = \frac{u_{i,nz} + u_{i,nz+1}}{2} \Rightarrow u_{i,nz+1} = 2u_{z=L} - u_{i,nz} \quad (\text{II.51})$$

$$\left. \frac{\partial u}{\partial z} \right|_{z=L} = \frac{u_{i,nz+1} - u_{i,nz}}{\Delta z} \Rightarrow u_{i,nz+1} = \Delta z \left. \frac{\partial u}{\partial z} \right|_{z=L} + u_{i,nz} \quad (\text{II.52})$$

### II.3.4 Model implementation

#### Numerical solver for time integration

The numerical model is implemented on *Matlab*<sup>®</sup> software. Matlab provides different ordinary differential equations (ODE) solvers that allow to deal with most problems. The choice of a solver is influenced by problem formulation. If equations are formulated as in equation II.53 it does not require a mass matrix. If it is formulated as in equation II.54 it does require a mass matrix.

$$\frac{\partial y}{\partial t} = f(t, y) \quad (\text{II.53})$$

$$\underbrace{M(t, y)}_{\text{Mass matrix}} \frac{\partial y}{\partial t} = \underbrace{f(t, y)}_{\text{RHS}} \quad (\text{II.54})$$

It is more natural to formulate equations with a mass matrix when partial time derivatives of several variables appear in one conservation law. As summed up in section II.3.5, it is the case in equations II.6 and II.12.

Solver *ode15s* is chosen because of the system stiffness. Among other tested solvers, this is by far the fastest one. It proceeds to numerical integration with a **Gear's method** which is an **implicit method** using a **backward differentiation formula** (BDF). It is a **linear multistep method** that consists first in approximating the solution with values of already computed times.

#### Jacobian pattern

*Ode15s* performance is clearly enhanced if the pattern of the Jacobian matrix is provided to the solver. However, calculation time is not necessarily improved when the full analytic Jacobian matrix is provided. In fact, analytic Jacobian might be somewhat long to be evaluated whereas the Jacobian pattern provides enough information to avoid useless calculation.

**Code structure**

<b>Main.m</b>	
▼ Geometry	
	3D Cartesian.m
	2D Axisymmetric.m
▼ Equations	
	1T LDF.m
	2T LDF.m
▼ Adsorption model	
	Cethyl STAID.m
	Cethyl Ahn.m
	BET Ahn.m ...
▼ Validation case	
	STAID Case1.m
	STAID Case2.m ...

Care has been taken to develop a **clean and documented code** that is meant to be continuously **upgraded**. Functions have been gathered into **classes**. A **Class** is thus a group of functions specific to one characteristic of the numerical model (geometry, set of equations, adsorption model, validation case, set of variables, ...). One class must be selected in each group of classes so that the model can run. Several functions do not belong to any specific class and are available for every set of classes. The numerical model also requires definition functions (such as *mu.m* which calculates dynamic viscosity as a function of temperature) and post-processing functions (like results analysis and plotting functions).

**II.3.5 Coupled equations**

The set of partial differential equations spatially discretized (section II.3.3) and numerically integrated with *ode15s* (section II.3.4) is summed up in the following equation. It groups together four conservation equations : energy conservation in the gaz (eq. II.6) and in the solid (eq. II.8), mass conservation of water vapor (eq. II.12) and adsorbed water (eq. II.13).

$A \rho_{da} c_{pda}$	0	$A \frac{M_v c_v}{R}$	0	$\frac{\partial}{\partial t}$	=	$-\text{div}((\rho c_p)_f \vec{u} T_f)$	$+\lambda_f \text{div}(\vec{\text{grad}}(T_f))$	$+U_b S_{\text{exch}}/V (T_s - T_f)$		
0	$B_s \rho_s c_s$ $+B_a q c_a$	0	$B_a c_a T_s$ $-B_a  \Delta H $					$U_b S_{\text{exch}}/V (T_f - T_s)$		
$-A \frac{p_v M_v}{R T_f^2}$	0	$A \frac{M_v}{R T_f}$	$B_a$					$-\frac{M_v}{R} \text{div}\left(\frac{p_v}{T_f} \vec{u}\right)$		
0	0	0	1					$k_m (q_e - q)$		
<div style="border-top: 1px solid black; border-left: 1px solid black; border-right: 1px solid black; width: 100%; margin-top: -10px;"></div> <p>Mass matrix</p>						<div style="border-top: 1px solid black; border-left: 1px solid black; border-right: 1px solid black; width: 100%; margin-top: -10px;"></div> <p>Right Hand Side (RHS)</p>				

**Conclusion**

All developments required to set up a numerical model describing heat and mass transfers in an adsorption heat storage tank have been developed in the present chapter. In the next chapter, the consistency between numerical results and experimental data is investigated and enhanced with the adjustment of some parameters, mostly on the adsorption model.



## Chapter III

# Numerical model validation and reactor first analysis

### Contents

---

III.1 Mesh dependency . . . . .	63
III.2 Model validation . . . . .	66
III.2.1 Validation of the convection-diffusion model . . . . .	66
III.2.2 Validation of the complete model . . . . .	67
III.3 Dimensionless analysis . . . . .	81
III.3.1 Dimensionless variables . . . . .	81
III.3.2 Nondimensionalization of conservation equations . . . . .	82
III.4 Analysis of energy conversion efficiency . . . . .	87

---

Full development of the numerical model describing heat and mass transfers in an adsorption heat storage tank has been achieved in chapter 2. The present chapter is dedicated to the study of the model behavior and consistency. The first step consists in the study of the influence of mesh distribution on the quantity of interest (QOI). It enables to find the best trade off between results precision and simulation time and to choose accordingly the default mesh distribution. Then, a large section of this chapter is dedicated to model validation by a comparison between numerical results obtained from the present model and experimental results from the french ANR project STAID (Johannes et al., 2015; Tatsidjodoung et al., 2016). Once the detailed model is validated, a dimensionless analysis is carried out in order to investigate whether it is possible to consider equations simplification without affecting much results precision. Finally, an analysis of the energy conversion chain is conducted. It shows the system must be considered as an integrated system rather than a standalone component.

### III.1 Mesh dependency

The influence of mesh discretization is investigated by running a full factorial design on two parameters: mesh number in axial direction  $n_z$  and mesh number in longitudinal direction  $n_x$ .

Table III.1 – Mesh number and distribution used for the study of mesh number influence

<b>nx</b>	<b>nz</b>	<b>20</b>	<b>30</b>	<b>40</b>	<b>50</b>	<b>60</b>
<b>1</b>		20	30	40	50	60
<b>2</b>		80	120	160	200	240
<b>4</b>		320	480	640	800	960
<b>6</b>		720	1080	1440	1800	2160
<b>8</b>		1280	1920	2560	3200	3840
<b>10</b>		2000	3000	4000	5000	6000

Other parameters are kept to their default value. Different levels are selected. Longitudinal mesh numbers  $n_x$  and  $n_y$  are simultaneously varied from 2 to 10 (step: 2), and axial mesh number  $n_z$  is varied from 20 to 60 (step: 10). Each possible combination is investigated as shown in table III.1.

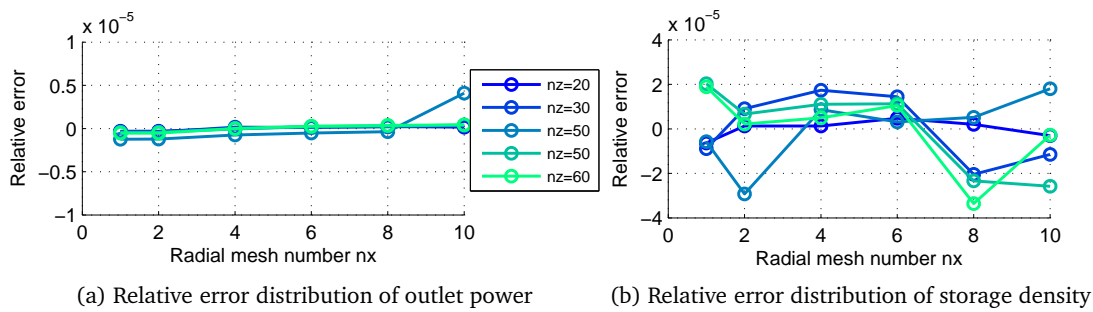


Figure III.1 – Influence of radial mesh number  $n_x$  on outlet power and energy storage densities

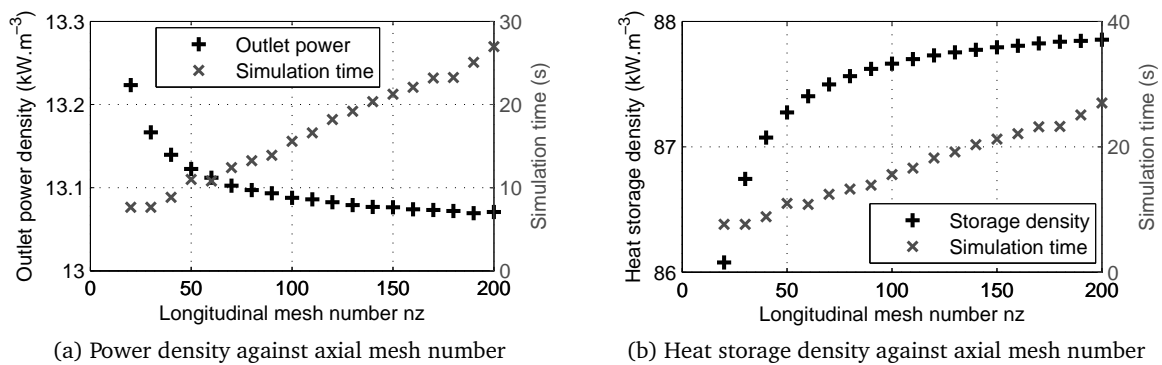
The investigations are worn on deviation of maximum outlet power density and energy storage density. As shown in figure III.1, deviation from mean is very negligible for a given  $n_z$  ( $< 0.01\%$ ). Results dependency on  $n_x$  and  $n_y$  values is then really negligible. This doesn't mean temperature and pressure fields are homogeneous on a cross-section. It only means that, given the solicitations of the system, few 2D or 3D effects are noticed. Actually, only heat losses through the walls of the adsorbent bed are supposed to introduce perturbations in heat and mass transfers in the axial flow pattern. With a high fluid velocity uniformly distributed, it is not surprising that heat and mass transfers through diffusion are negligible compared to advection. With a non uniform flow pattern at the inlet of the adsorbent bed or a lower velocity, results could have been somewhat different though mean value at the outlet of the reactor might remain unchanged. Here, what is important is to correctly represent heat and mass transfers inside the adsorbent bed in order to evaluate instant and integral quantities at the outlet of the adsorbent bed.

Results depend more on mesh distribution along axial direction. Figure III.2 displays the evolution of outlet power density and heat storage density as a function of mesh number  $n_z$ . It shows a convergence for  $n_z$  value of about 200 with a 20 cm bed length. It is then advised to ideally design mesh grid with 10 meshes/cm in axial direction. Table III.2 provides the relative

Table III.2 – Deviation observed from asymptotic value on outlet power and energy storage density results for different axial mesh numbers

Axial mesh number $nz$	20	40	60	80	100	120	200
Outlet power variation	+1.17%	+0.53%	+0.32%	+0.20%	+0.13%	+0.09%	ref.
Storage density variation	-2.02%	-0.89%	-0.51%	-0.33%	-0.22%	-0.14%	ref.

error distribution as a function of the longitudinal mesh number (with  $nz = 200$  as a reference). Default value ( $nz = 40$ ) was 5 times lower than specification. It leads to a 0.5% overestimation of outlet power density and a 0.9% underestimation of heat storage density, with a simulation time 3.5 times faster.

Figure III.2 – Influence of axial mesh number  $nz$  on outlet power and energy storage densities

As a conclusion, mesh grid design must trade off results precision and simulation time. For a single run, simulation time is usually not the main decision factor. For parametric runs or sensitivity analysis, it is important to limit simulation time and volume of results data under acceptable ranges. It often remains acceptable for 1D models unless the reactor bed is very long. But for 3D models, mesh number and hence simulation time fastly become very high. Figure III.3 shows simulation time is **quasi-linear** against mesh number for 1D and 3D configurations of table III.2. These simulations were made on a 6-hour charging phase and a 18-hour discharging phase. Ratio between simulated time and simulation time varies from 12000 to 130 with 8500 in default conditions. Nevertheless, timestep is adaptive. Simulation goes much faster once a steady-state is reached than during charging and discharging phases. This ratio will then be much lower under non stable boundary conditions. It can then not be extrapolated to yearly simulations since that would definitely last for more than several hours.

As a conclusion to this study on the influence of mesh distribution on QOI, few 2D or 3D solicitations are encountered in the present case. A 1D model then provides very acceptable results. It is then decided to work with a 1D model in the remainder of the document. As demonstrated in the next section, validation work provides confidence in the consistency of this choice. A longitudinal mesh number of 500 meshes  $m^{-1}$  (i.e. 100 in the default conditions, with a bed length of 20 cm) is chosen as results are in the asymptotic convergence

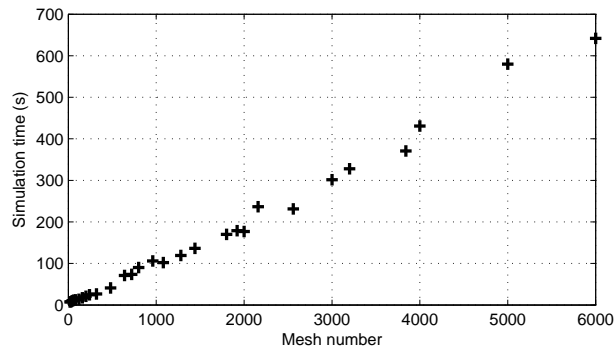


Figure III.3 – Simulation time against mesh number

domain (figure III.2)

## III.2 Model validation

The complexity of the model development and validation remains in two very different blocking points. Adsorption modeling is definitely one of them. Numerous PhD thesis and research articles have dealt in recent years with the modeling of adsorption heat storage tank (Hongois, 2011; Michel et al., 2012; Metchueng Kamdem et al., 2012; Duquesne et al., 2014; Tatsidjodoung, 2014; Fopah Lele et al., 2015, among many others). None of them use nor the same adsorption model neither the same data to fit their model. This shows that adsorption modeling is still a challenging research area since there has been no decisive breakthrough yet.

The second blocking point, which is more a technical issue than a lack of scientific developments, is the modeling of coupled heat and mass transfer. It introduces non-linear differential equations which call for very different numerical methods than when equations are linear.

Validation of the numerical model is then achieved in two steps. First, adsorption phenomenon is put aside. Thus, only the convection-diffusion part of the numerical model is tested. Then, once there is no more doubt on the model architecture and numerical methods used for the resolution of convection-diffusion problems, the entire model is tested, including adsorption.

### III.2.1 Validation of the convection-diffusion model

The Center for Energy and Thermal sciences of Lyon (CETHIL) has an **experimental test bench** of adsorption heat storage. It is made of an insulated air duct inside an insulated box. Boundary conditions (temperature, relative humidity and airflow rate) at the inlet of the duct are controlled. Temperature of the surroundings  $T_{box}$  may also be controlled and is measured with a thermocouple. As displayed on figure III.4, the air duct is roughly subdivided into three zones. The first half of the duct is the laminarisation zone. It contains no material. The next quarter is the material zone where adsorbent or glass beads are located. The last quarter is free of material and ensure

there is no turbulence inside the material zone.

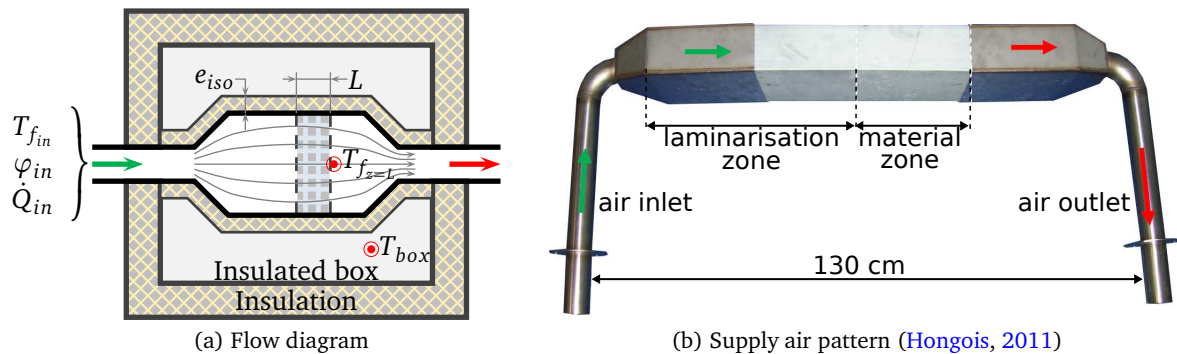


Figure III.4 – Model validation with glass beads (no adsorption)

In order to validate the numerical model without adsorption, it is decided to replace adsorbent beads with glass beads of the same diameter. Experimental setup is done without insulating the duct ( $e_{iso} = 0$ ). The dynamic response of the glass beads bed is plotted on figure III.5a. Absolute error between numerical and experimental data remains below  $1^\circ\text{C}$  (as shown on figure III.5b). These results are considered as satisfactorily enough to validate the convection-diffusion model and the assumptions on conduction.

### III.2.2 Validation of the complete model

As explained in section II.2.5.2, data from STAID project (Johannes et al., 2015) are used in order to validate the full model under dynamic operating conditions. This project was aimed to design and develop a 2 kWh adsorption heat storage tank. The prototype is made of two separated reactors that can be connected in serial or in parallel, in order to test advantages and constraints of each configuration. Each reactor is a cylinder of 72 cm diameter, with a bed length of 20 cm. Moist air flows vertically inside the reactor. A sketch of the prototype and a picture of the experimental setup is displayed on figure III.6.

The plan of experiments has been developed in order to address, with a minimum of tests, the influence of:

- desorption temperature ( $120^\circ\text{C}$  vs.  $180^\circ\text{C}$ ),
- air flowrate ( $180\text{ m}^3\text{ h}^{-1}$  vs.  $90\text{ m}^3\text{ h}^{-1}$  vs.  $60\text{ m}^3\text{ h}^{-1}$ ),
- relative humidity in discharging mode (50% vs. 70%),
- bed length (20 cm vs. 10 cm),
- serial/parallel configurations.

Configuration of all eight tests is displayed in table III.3. Experiments 2 and 4 have been used to assess the influence of temperature in real conditions and to fix accordingly the adsorption model parameters. Experiments 2 and 3 have been used in order to investigate the influence of airflow rate  $\dot{Q}_v$  on adsorption. It is shown that mass transfer coefficient  $k_m$  and heat transfer coefficient  $U_b$  depend on superficial velocity  $v_s$ . Experiments 1, 5, 6, 7 and 8 are used only for validation purposes.

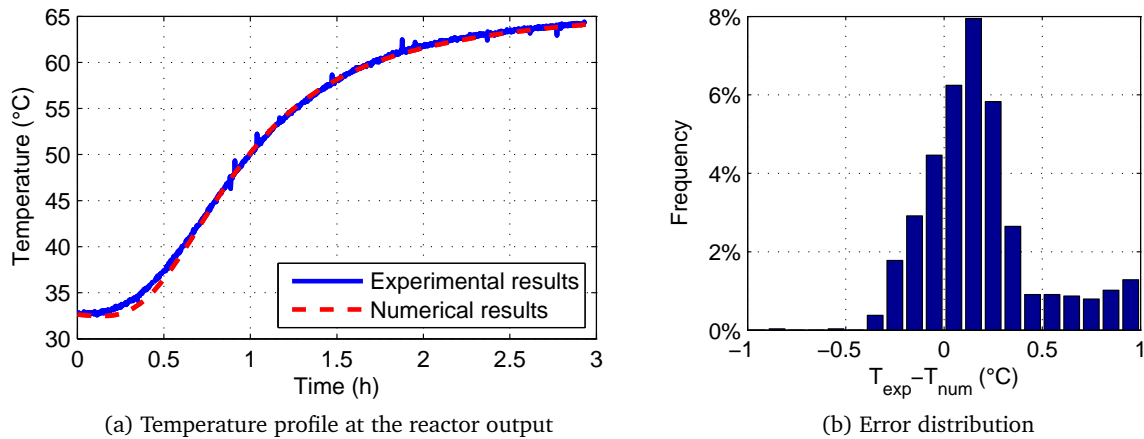


Figure III.5 – Experimental setup used for convection-diffusion validation

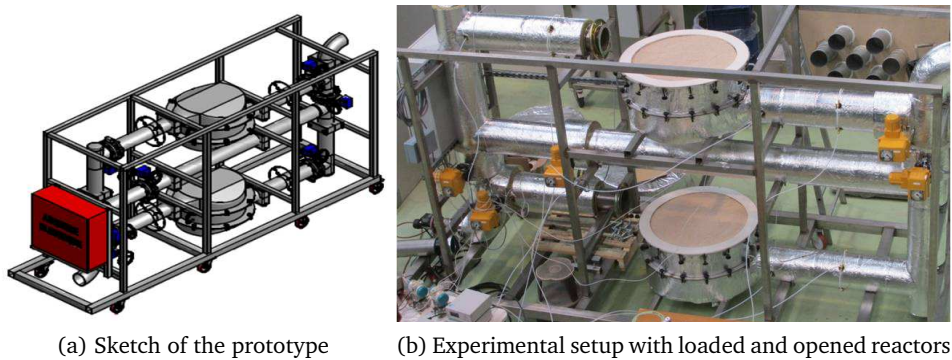


Figure III.6 – Experimental setup used in STAID project

### III.2.2.1 Coefficients adjustments according to validation data

#### Adjustments made on mass transfer coefficient $k_m$

Mass transfer coefficient  $k_m$  is seen as a global mass transfer coefficient at a bead scale. It describes both diffusion at the pore scale and advection at the bead scale. Diffusion term depends only on temperature and parameters evaluated at a microscopic scale. Advection term of  $k_m$  coefficient must be scaled experimentally.

$$k_m = \frac{15 D_0}{d_p^2} \exp\left(\frac{-E_a}{RT_f}\right) + k_{vs} v_s \text{ with } D_0 = 4 \times 10^{-7}, E_a = 4 \times 10^4, k_{vs} = 0.032 \quad (\text{III.1})$$

Experiments 2 and 4 enabled to set  $D_0$  and  $E_a$  coefficients. A comparison between test cases 2 and 3 enabled an evaluation of  $k_{vs}$  coefficient. The shape of  $k_m$  evolution over possible operating conditions is displayed on figure III.10a.

#### Adjustments made on heat transfer coefficient $U_b$

In the same way as  $k_m$  is a global mass transfer coefficient,  $U_b$  is seen as a global heat transfer coefficient. It describes not only heat exchange at the interface between beads surface and inter-

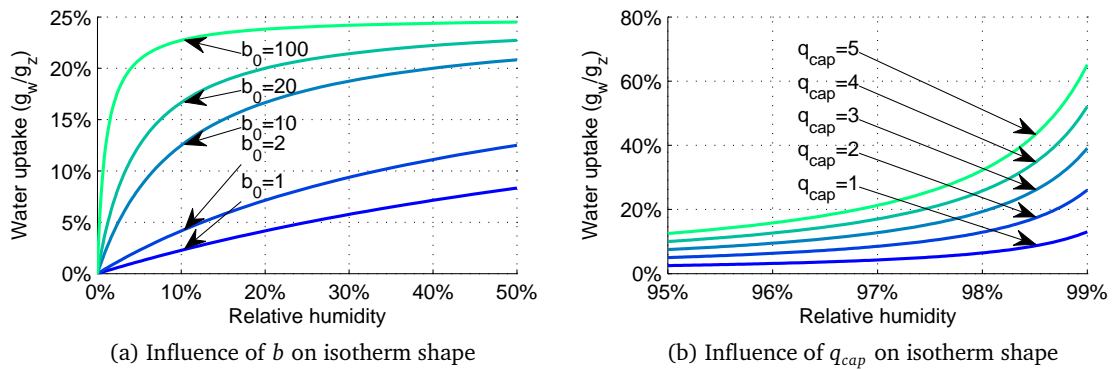
Table III.3 – Configurations of STAID project experiments

Configuration			Desorption (charge)			Adsorption (discharge)			
S: Serial	$m_{adsorbent}$		Ref.	$T_{fin}$	$\dot{Q}_{vin}$	Ref.	$T_{fin}$	$\varphi_{in}$	$\dot{Q}_{vin}$
P: Parallel	$kg_z$			$^{\circ}C$	$m^3 h^{-1}$		$^{\circ}C$	%	$m^3 h^{-1}$
1	1	40	1H	180	180	1D	20	70	180
2	2P	40	2H	180	90	2D	20	70	90
3	2P/2S	40	3H	180	180	3D	20	70	180
4	2P	40	4H	120	90	4D	20	70	90
5	2P	40	5H	120	90	5D	20	50	90
6	2S	40	6H	120	180	6D	20	70	180
7	1	20	7H	180	180	7D	20	70	180
8	2P	40	8H	180	60	8D	20	70	60

stitial fluid, but it describes also a mean heat transfer resistance at a bead scale. This takes into account heat transfers through convection and conduction, from the deepest pores to the bead surface, as stated in equation II.31. This coefficient did not required to be scaled. The shape of  $U_b$  evolution over possible operating conditions is displayed on figure III.10b.

#### Adjustments made on adsorption model coefficients $b$ and $q_{cap}$

Two parameters were identified as being very sensible on results shape. Parameter  $b$  in Langmuir equation influences the shape of adsorption isotherm in low relative humidity range (fig. III.7a). Parameter  $q_{cap}$  is the scaling coefficient for capillary condensation (fig. III.7b).

Figure III.7 – Influence of model coefficients  $b$  and  $q_{cap}$  on isotherm shape

$b$  has a strong influence on the rising-edge slope of the charging curve. It also slightly influences the duration of the intermediate step (fig. III.8a). On discharge, it influences the falling-edge slope of the temperature profile (fig. III.8b), and it strongly determines the sharpness of the temperature drop at the end of the high temperature stage. The evolution of coefficient  $b$  follows Vant Hoff equation (eq. II.33 and III.2). Analysis of test cases 2 and 4 enabled to set coefficients  $\Delta H_m$  and  $b_0$ . Moreover, the shape of  $b$  evolution as a function of temperature is displayed on

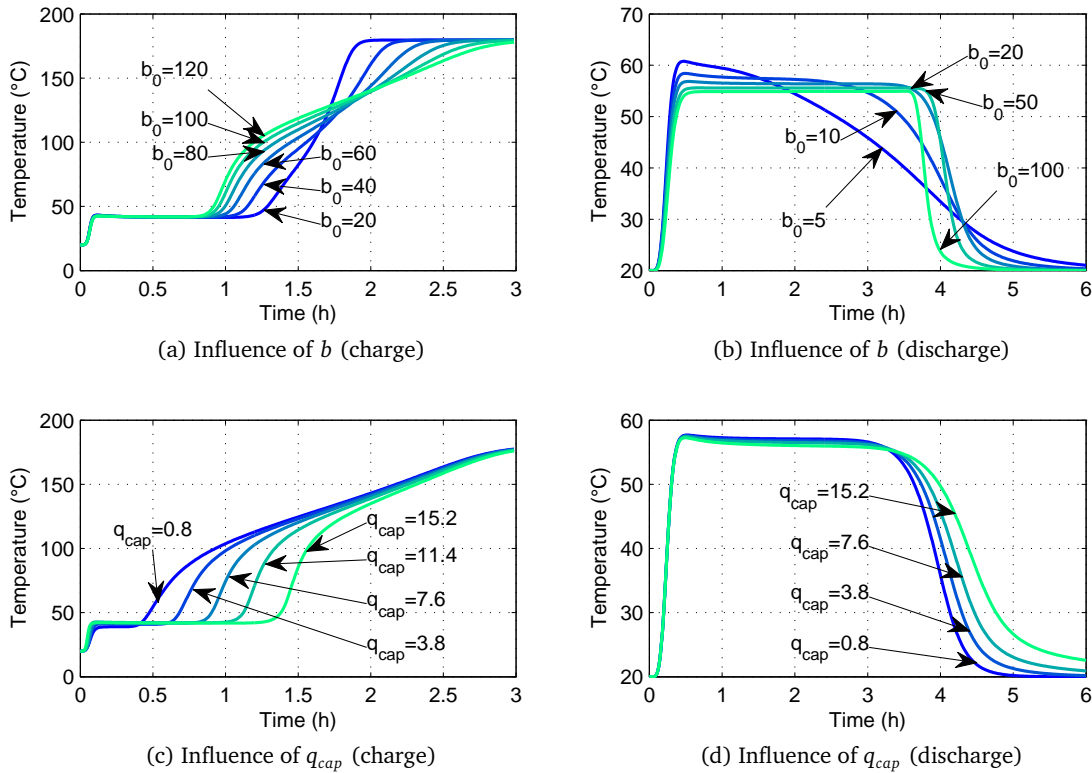

 Figure III.8 – Influence of  $b$  and  $q_{cap}$  on the shape of temperature profile on charge and discharge

figure III.10c.

$$b = b_0 \exp\left(-\frac{\Delta H_m M_v}{R T_f}\right) \text{ with } b_0 = 5.0 \times 10^4, \Delta H_m = 1.2 \times 10^6 \quad (\text{III.2})$$

Capillary condensation coefficient  $q_{cap}$  mainly influences the duration of the intermediate step (fig. III.8c). On discharge (adsorption), it also influences the falling-edge slope of the temperature profile (fig. III.8d) but it has no effect on the step duration.

Analysis of experiments 2 and 4 has shown a dependency of  $q_{cap}$  on charging temperature  $T_{in,charge}$  and operating temperature  $T_{in}$ . This behavior is obviously not ideal.  $q_{cap}$  should only depend on local instant temperature  $T$ . The following correlation is proposed for a better behavior.

$$q_{cap} = q_{cap,1} \cdot T_{in,charge} + q_{cap,2} \cdot T_{in} + q_{cap,3} \quad (\text{III.3})$$

with  $q_{cap,1} = 7.4 \times 10^{-2}$ ,  $q_{cap,2} = -4.7 \times 10^{-5}$ ,  $q_{cap,3} = -3.9 \times 10^{-3}$

The shape of  $q_{cap}$  evolution as a function of charging temperature and operating temperature is displayed on figure III.10e.

### Adjustments made on parameter $q_n$ on the shape of temperature profile

$q_n$  represents the adsorption capacity of the first layer which is the limit value of a Langmuir isotherm. Given the adsorption model construction, and contrary to all three other coefficients, a

small variation on  $q_n$  leads to a wide variation of water uptake average value over the whole pressure and temperature domain. Results' sensitivity to this parameter is large. Figure III.9 shows the influence of  $q_n$  on the shape of temperature profile in charge and discharge configurations.

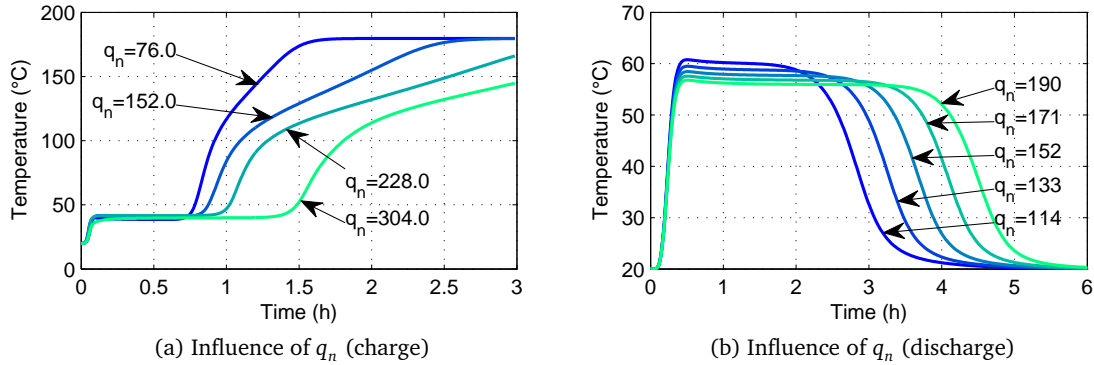


Figure III.9 – Influence of  $q_n$  on the shape of temperature profile on charge and discharge

A higher adsorption capacity  $q_n$  naturally leads to a longer desorption time (fig. III.9a) since more adsorbate particules must be desorbed. The same observation is valid for discharge: a longer time is required in order to saturate the adsorbent material. The high temperature stage will then last longer with a higher adsorption capacity  $q_n$  (fig. III.9b).

Analysis of test cases 2 and 4 has shown  $q_n$  depends on charging temperature  $T_{in,charge}$ . As noticed for  $q_{cap}$ , this behavior is not ideal.  $q_n$  should ideally be an intrinsic parameter of the adsorbent material or should only depend on local instant temperature  $T_f$ . But such relationship has been investigated and lead to about a 30% error on high temperature stage duration on discharge on test case 2. Consequently, and for want of a more logical behavior of the model, the following correlation is implemented.

$$q_n = q_{n,1} \cdot T_{in,charge} + q_{n,0} \text{ with } q_{n,1} = 8.4 \times 10^{-1}, q_{n,0} = -1.98 \times 10^2 \quad (\text{III.4})$$

The shape of  $q_n$  evolution as a function of charging temperature is displayed on figure III.10d.

### Resulting adsorption model coefficients and heat and mass transfer coefficients

Table III.4 gives an overview of the original coefficients of the adsorption model (fitted in section II.2.5 on isotherm data from [Ahn and Lee \(2004\)](#) with a narrow temperature range from 25°C to 45°C). It also refers to equations used in the final model in order to evaluate final coefficients (obtained with experimental data at full-scale, on a wider temperature range from 20°C to 180°C).

Figure III.10 displays the values of mass transfer coefficient  $k_m$  (III.10a), heat transfer coefficient  $U_b$  (III.10b), Langmuir adsorption isotherm coefficients  $b$  (III.10c) and  $q_n$  (III.10d), and capillary condensation coefficient  $q_{cap}$  (III.10e) over the temperature range and airflow range used within STAID experiments.

### Resulting adsorption model shape

Equation III.3 shows that the behavior of  $q_{cap}$  depends on operating temperature  $T_{in}$ . As operating

Table III.4 – Coefficients used in the equilibrium adsorption model

Exp. Data	$q_n$ $\text{kg}_w \text{m}^{-3}$	$b$	$a$ $\text{kg}_w \text{m}^{-3}$	$q_{cap}$ $\text{kg}_w \text{m}^{-3}$	$k_m$ $\text{m}^2$	$U_b$ $\text{W m}^{-2} \text{K}^{-1}$
Ahn and Lee (2004)	185.2	14.87	9.067	3.608	-	-
STAID	eq. III.4	eq. III.2	3.04	eq. III.3	eq. III.1	eq. II.31
min	114	8	-	2	1.4	1
max	183	160	-	15	4.0	7

temperature is different in charge (from 100°C to 180°C) and in discharge (about 20°C), it necessarily leads to an hysteresis effect at high relative humidities. Figure III.11 shows the shape of adsorption isotherm curves for three different temperature within the temperature range in use. The slope of the curve mainly differs from one temperature to another at low and high relative humidities. This hysteresis effect is not necessarily related to a physical hysteresis effect but more likely to a difference in adsorption kinetics between charge and discharge that is not correctly taken into account with the overall mass transfer coefficient  $k_m$ .

### III.2.2.2 Validation indicators

A comparison between numerical data and experimental data is achieved. Besides temperature profile plots, several indicators are defined in order to quantify the accuracy of the fitting between the numerical model and the experiments:

- $T_{f_0}$ , is the initial temperature,
- $T_{f_{max}}$ , is the maximum temperature reached during a charge or discharge run,
- $t_0$ , is the initial time,
- $t_1$  (resp.  $t_2$ ), is the time when  $T_f$  reaches 63% (resp. 95%) of  $T_{f_{max}}$  (rising-edge),
- $t_3$  (resp.  $t_4$  and  $t_5$ ), is the time when  $T_f$  reaches 95% (resp. 37% and 5%) of  $T_{f_{max}}$  (falling-edge, discharge only),
- $t_{step}$ , is the duration of the high-temperature stage:  $t_{step} = t_3 - t_2$ ,
- $|\overline{T_{f_{exp}} - T_{f_{num}}}|$ , is the averaged temperature difference between experimental and numerical results. It is calculated only over transient periods (meaning from  $t_0$  to  $t_2$  for charge, and from  $t_0$  to  $t_5$  for discharge),
- $E_{sens}$ , is the sensible energy absorbed (charge) or released (discharge) during the run.

Table III.5 provides charge, discharge and overall average values for all these indicators. Mean error remains below 15% for all indicators and below 5% for three among the four most important ones (maximum temperature, mean temperature difference and sensible energy). Only the high temperature stage duration is not entirely satisfactorily reproduced, mainly due to bad results of test case 8 (low flowrate) on this indicator, probably because of assumptions made on advection.

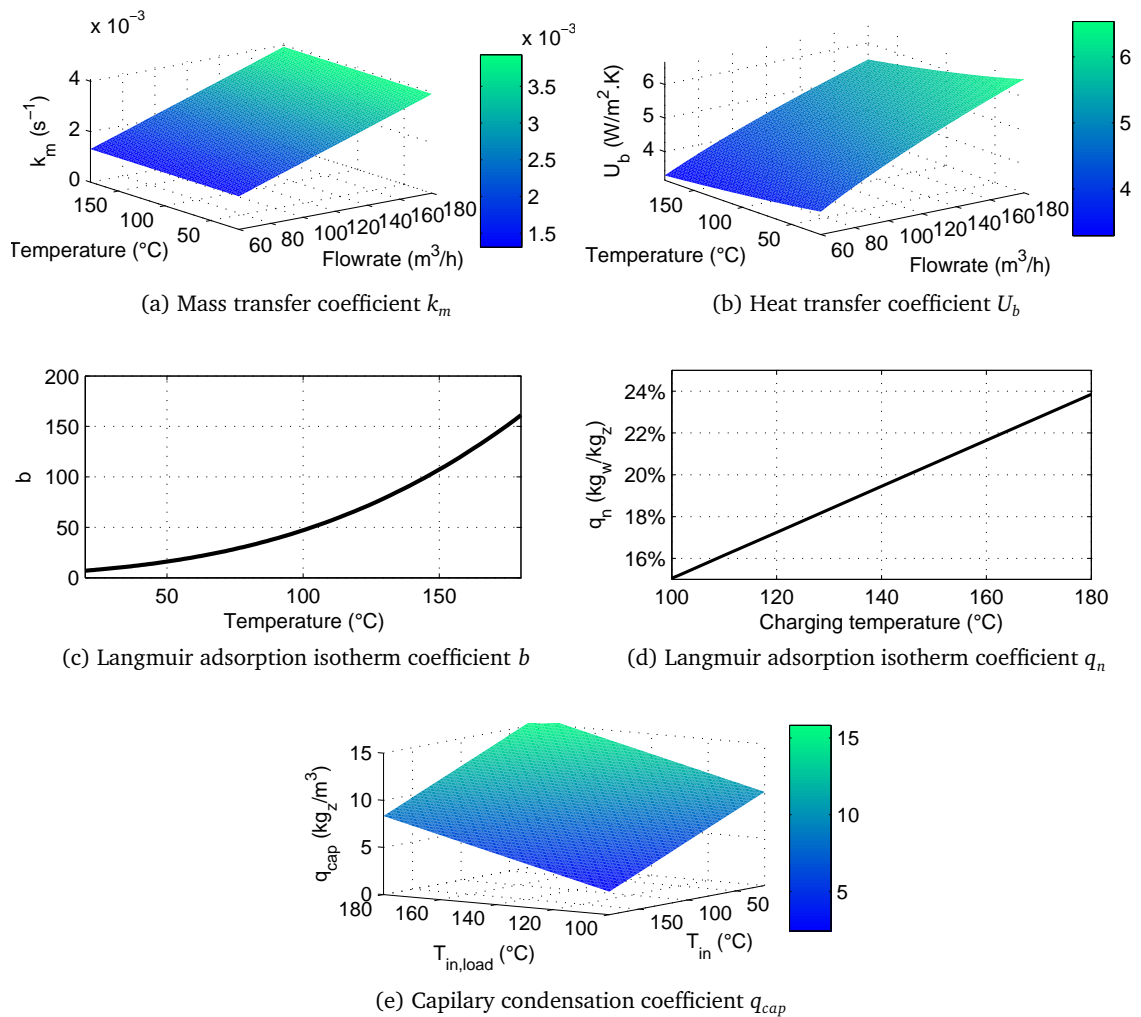


Figure III.10 – Comparison between charge and discharge values of  $k_m$ ,  $U_b$ ,  $b$ ,  $q_n$  and  $q_{cap}$

Most important indicators are **maximum temperature**  $T_{f_{max}}$  (that is evaluated with a good precision:  $1.7^\circ\text{C}$ , 1.6% on average,  $12.2^\circ\text{C}$ , 8.5% maximum), **mean temperature difference**  $|\overline{T_{f_{exp}} - T_{f_{num}}}|$  ( $4.0^\circ\text{C}$ , 5.3% on average,  $9.6^\circ\text{C}$ , 6.2% max), **high temperature stage duration**  $t_{step}$  ( $36'22''$ , 13.1% on average, with a maximum at  $2h58'$ , 45.6% that increases significantly average values), and **sensible energy** absorbed or released  $E_{sens}$  (0.41 kWh, 4.6% on average, 1.6 kWh, 8.3% max).

These values seem acceptable to consider the full numerical model as validated. More details on model behavior under different solicitations are given in the remainder of this chapter.

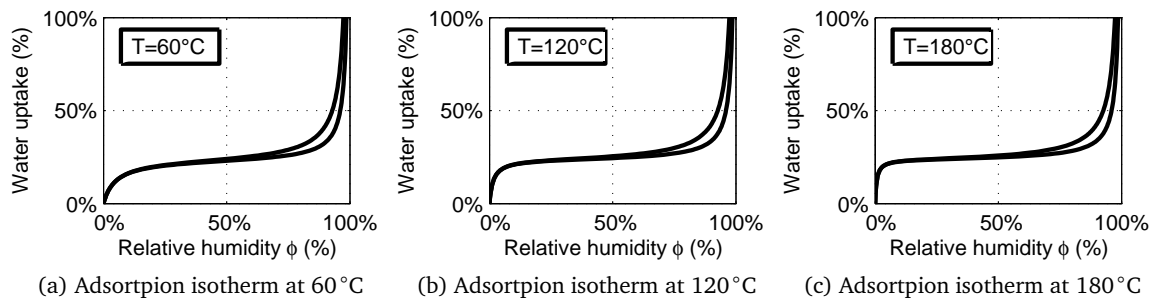


Figure III.11 – Adsorption isotherm at three different temperature (60 °C, 120 °C, 180 °C)

Table III.5 – Mean error on charge and discharge for each validation indicator

	$T_{f_{max}}$ °C	$\overline{ T_{f_{exp}} - T_{f_{num}} }$ °C	$t_1$	$t_2$	$t_3$	$t_4$	$t_5$	$t_{step}$	$E_{sens}$ kWh
<b>Charge</b>	2.73	5.68	11'22''	37'53''	-	-	-	-	0.47
	1.9%	4.5%	9.2%	18.0%	-	-	-	-	3.3%
<b>Discharge</b>	0.72	2.25	3'19''	19'04''	22'56''	16'15''	1h54'	36'22''	0.35
	1.3%	6.2%	15.6%	23.3%	8.0%	4.9%	30.6%	13.1%	6.0%
<b>Overall</b>	1.73	3.97	7'21''	28'28''	22'56''	16'15''	1h54'	36'22''	0.41
	1.6%	5.3%	12.4%	20.6%	8.0%	4.9%	30.6%	13.1%	4.6%

### III.2.2.3 Validation data

**Note:** In the following section, validation charts and data are not displayed in the same order than in table III.3. For each of the eight confrontation between numerical results and experiments (figures III.12 to III.19), profiles of experimental and numerical outlet temperatures are displayed for both charge(a) and discharge(b). A bar plot also provides information on the distribution of temperature difference between experimental and numerical results for both charge (c) and discharge (d). Finally, main numeric values of fitting indicators are provided for charge (table e) and discharge (table f).

### Validation of model behavior under different temperature conditions

Experiments 2 and 4 are realized under the exact same operating conditions on charge and discharge, except for charging temperature (180 °C versus 120 °C). Figures III.12 and III.13 show that the numerical model correctly takes into account these two different desorption temperatures.

The shape of the experimental outlet temperature is correctly reproduced for both charge and discharge. The average temperature difference is lower than 5% on charge and about 6% on discharge for both experiments. The high temperature stage duration is slightly underestimated by 12 (at 180 °C) and 14 minutes (at 180 °C), which are respectively a 3.3% and 6.4% error. Sensible energy released by the adsorbent bed on charge is underestimated up to 4.4% (which

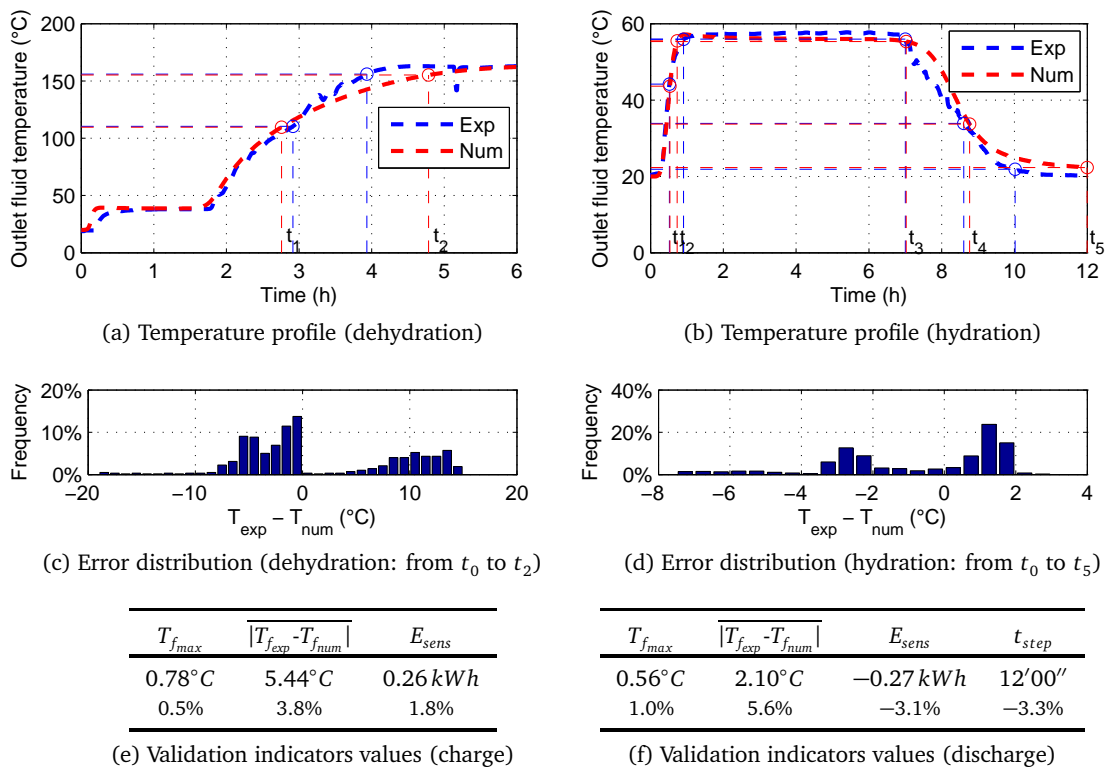


Figure III.12 – Validation of test case 2

means absorbed energy is overestimated). It is in accordance with the overestimation of released energy on discharge (by 3.1% at 180 °C and 12.4% at 120 °C which is not entirely satisfactory).

### Validation of model behavior under different airflow rate conditions

Experiments 1, 2 and 8 are realized under the same operating conditions on charge and discharge, except for airflow rate ( $180 \text{ m}^3 \text{ h}^{-1}$ ,  $90 \text{ m}^3 \text{ h}^{-1}$  and  $60 \text{ m}^3 \text{ h}^{-1}$ ). Figures III.14, III.12 and III.15 show that the numerical model correctly takes into account these three different airflow rates. Charging time correctly decreases with airflow from 7h17' at  $60 \text{ m}^3 \text{ h}^{-1}$  to 2h27' at  $180 \text{ m}^3 \text{ h}^{-1}$  (4h43' at  $90 \text{ m}^3 \text{ h}^{-1}$ ). Discharging high temperature stage lasts longer with a smaller flow rate (9h30' at  $60 \text{ m}^3 \text{ h}^{-1}$  versus 3h02' at  $180 \text{ m}^3 \text{ h}^{-1}$ ) which is consistent with the expected behavior and with experimental results.

Nevertheless, temperature drop at the end of discharge of case 8H ( $60 \text{ m}^3 \text{ h}^{-1}$ ) is less accurate. On this validation case, the average temperature difference error is 11.4% which is the worst accuracy encountered. The high temperature stage duration is also not correctly reproduced, since it is overestimated by 46%. It shows the discharge model tends to overestimate the influence of fluid velocity at low airflow rates. This inaccuracy leads to an overestimation of sensible energy absorbed (charge) and released (discharge). But this is overestimated by only 7.3% which sounds acceptable compared to others indicators. On discharge, it can be explained by the fact that the maximum temperature underestimation and the high temperature stage duration overestimation compensate each other in terms of sensible energy released.

In conclusion, the model is more satisfactory at high fluid velocities than at low velocities.

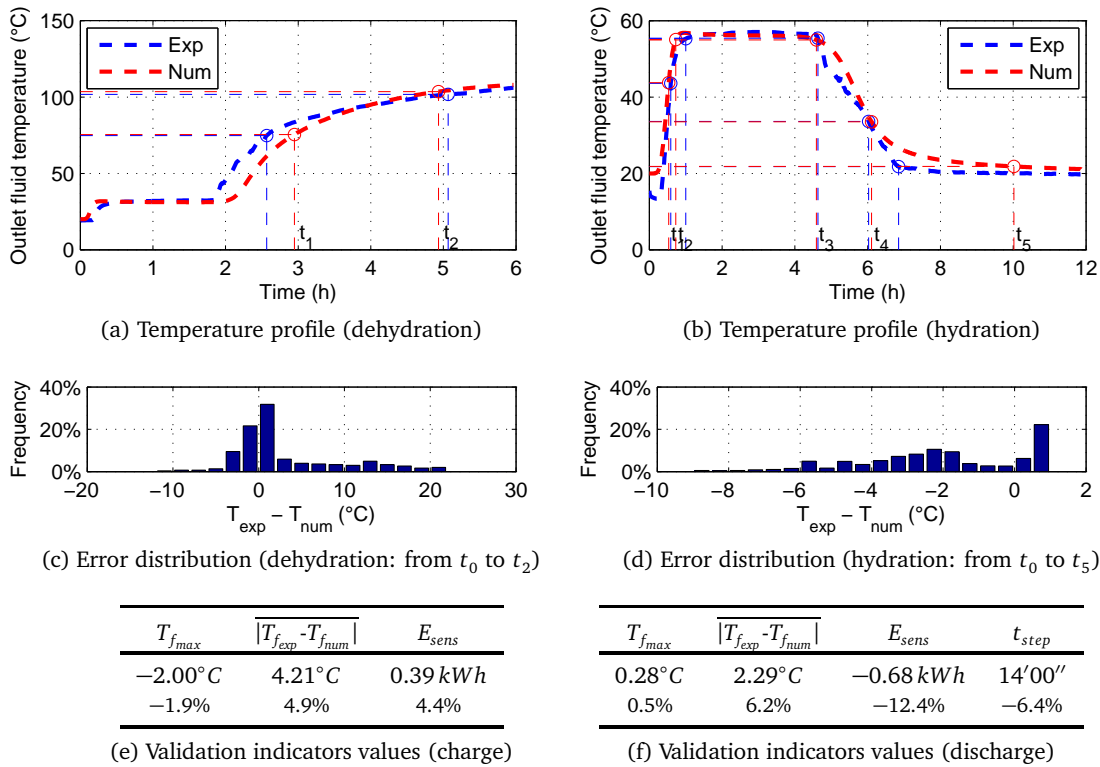


Figure III.13 – Validation of test case 4

The model is thus validated on the full investigated range (from  $60 \text{ m}^3 \text{ h}^{-1}$  to  $180 \text{ m}^3 \text{ h}^{-1}$ ) but great care is required in the model exploitation for velocities under  $60 \text{ m}^3 \text{ h}^{-1}$ .

### Validation of model behavior under different relative humidity conditions

Comparison between test cases 4 and 5 allows a validation of the discharge model under different relative humidities. With 70% relative humidity at the inlet, discharging temperature is about  $57^\circ C$  in both experimental and numerical results (test case 4, fig. III.13). With 50% relative humidity at the inlet, discharging temperature falls to  $48.3^\circ C$  in numerical results (versus  $46.5^\circ C$  in experiment, 4.0% relative error) which seems satisfactorily enough (test case 5, fig. III.16).

The lower inlet charging humidity does not introduce any restriction in the model validation since all indicators are evaluated with a good precision. The error on maximum temperature remains below 1% on both charge and discharge while the average temperature difference is under 4%. Besides, the bar plots of figures III.16c and III.16d show the error distribution is correctly centered around zero.

### Validation of model behavior under a different bed geometry

All experiments except one (test case 7) are conducted with the same bed geometry. The adsorbent bed is a cylinder of  $72 \text{ cm}$  diameter and  $20 \text{ cm}$  length, which corresponds to  $40 \text{ kg}$  of zeolite beads. In test case 7 (fig. III.17), only  $20 \text{ kg}$  of zeolite beads are loaded into the reactor which tallies with a bed length of  $10 \text{ cm}$ . A comparison between experiments 1 and 7, which are achieved with the exact same conditions (except the bed length), enables a first validation of the model

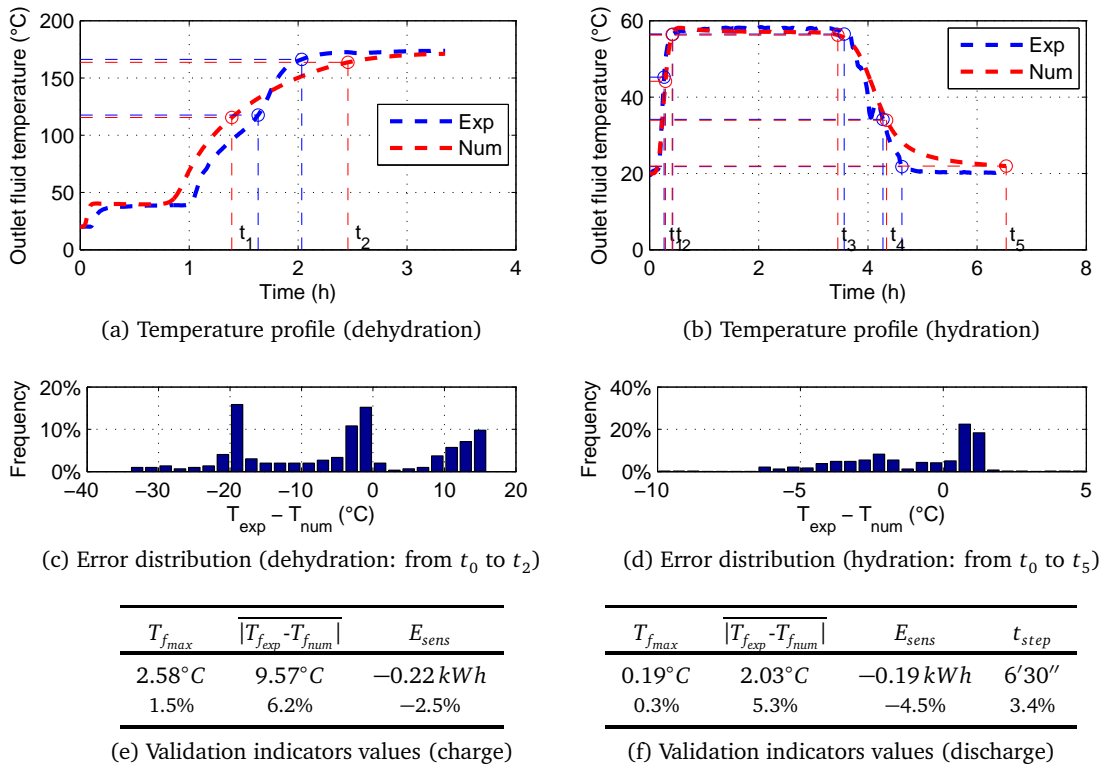


Figure III.14 – Validation of test case 1

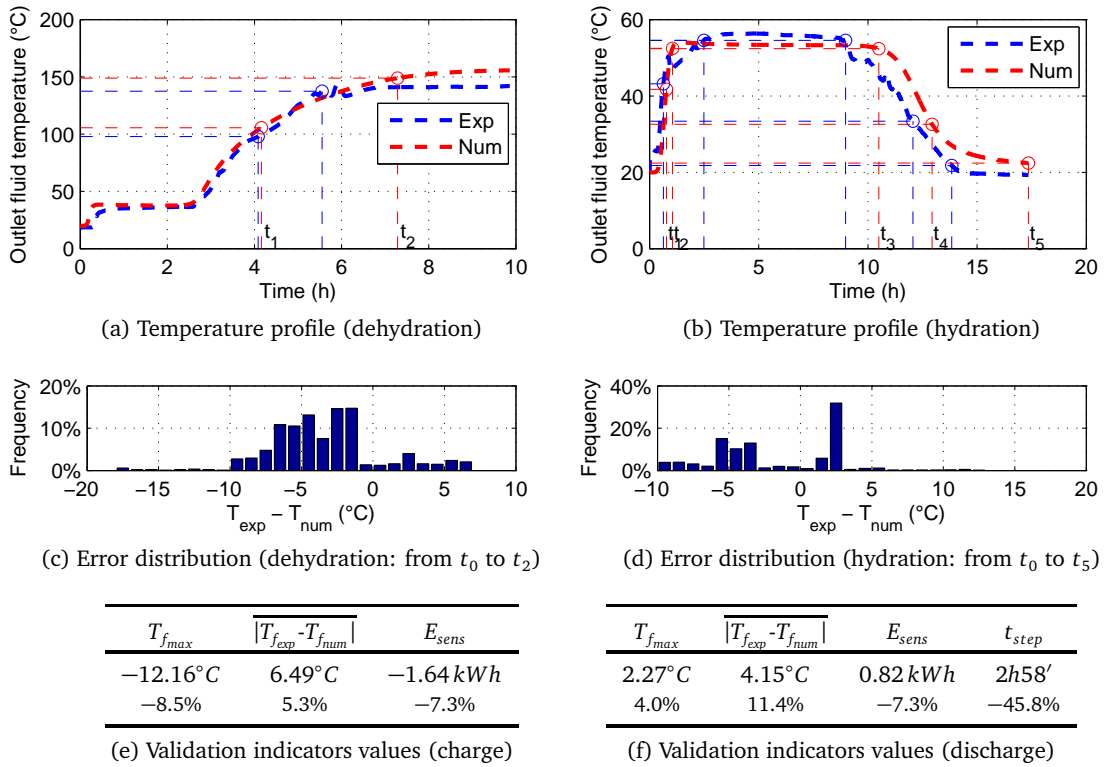


Figure III.15 – Validation of test case 8

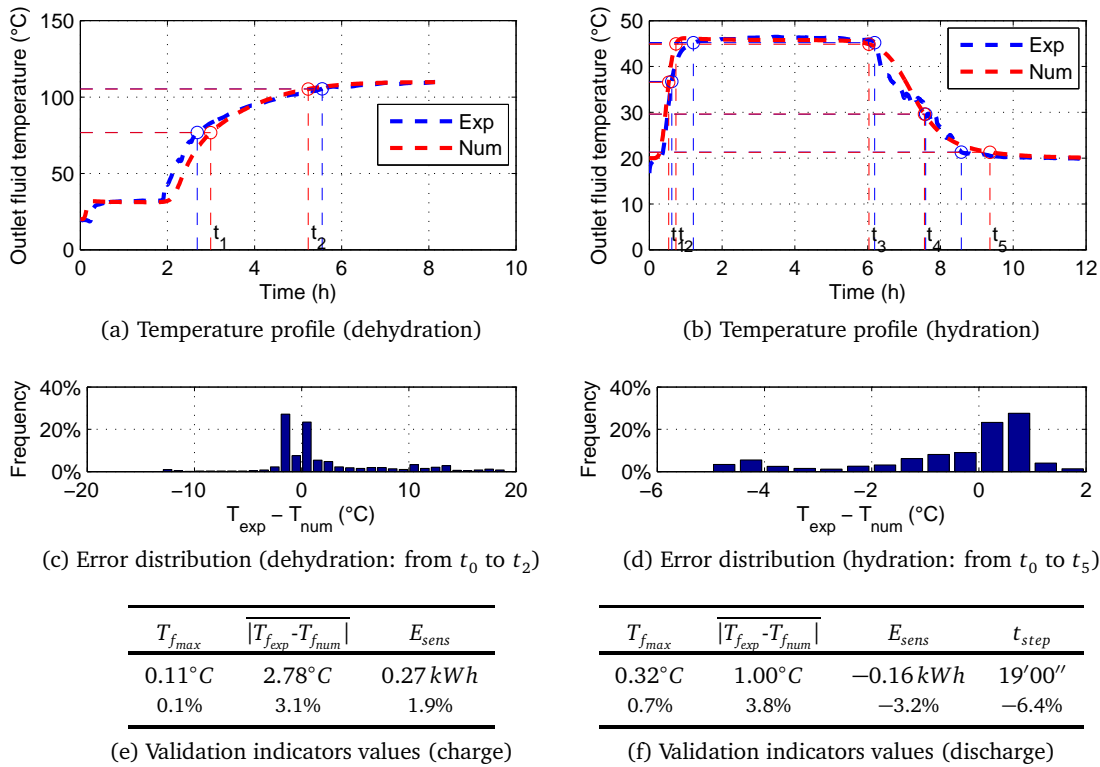


Figure III.16 – Validation of test case 5

behavior under different surface/length ratios.

On charge, the transient behavior is really accurate. The average temperature difference from  $t_0$  to  $t_2$  (95% of the temperature drop) is under 4°C (2.6% relative error). The charging time (11' overestimation) and the asymptotic temperature (0.7% overestimation) are also correctly reproduced so is the sensible energy absorbed (1.9%).

Results are also very good on discharge since the errors on maximum temperature and released energy evaluations remain around 1%. The high temperature stage duration is correctly evaluated with an error under 5 minutes (4.9%). And the average temperature difference is acceptable (6.2%) with a distribution correctly centered around zero and few extreme values (figure III.17d).

### Cross validation temperature/airflow rate

The two last available test cases are achieved at temperature, airflow rate and relative humidity already tested in others cases (but not with the same set of operating conditions).

In test case 6 (figure III.18), the fitting between experimental and numerical results is also satisfying for the charging process (all indicators remain under 4% of error). On discharge, the shape of the curve is good, but the high temperature stage duration is not satisfactorily predicted since it is strongly underestimated (43' absolute and 27.6% relative errors).

Test case 3 is charged under the same conditions that test case 1. Discharge is achieved by connecting the two reactors in serial. Results presented on figure III.19 only concern the first

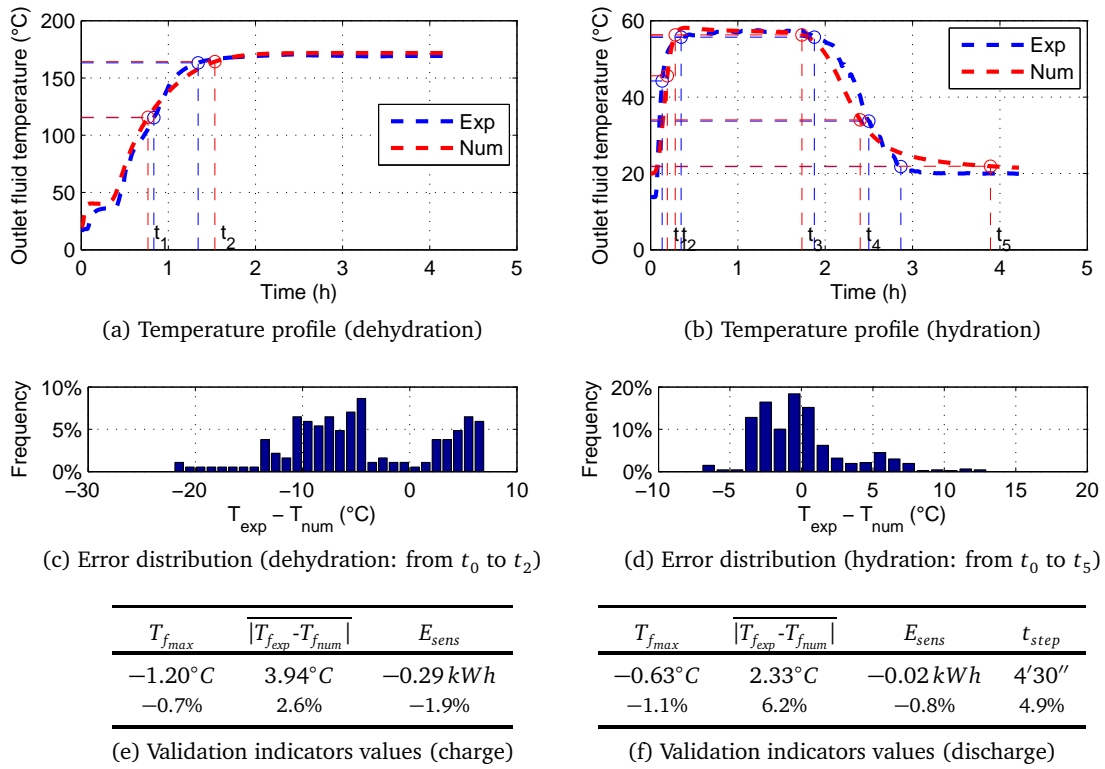


Figure III.17 – Validation of test case 7

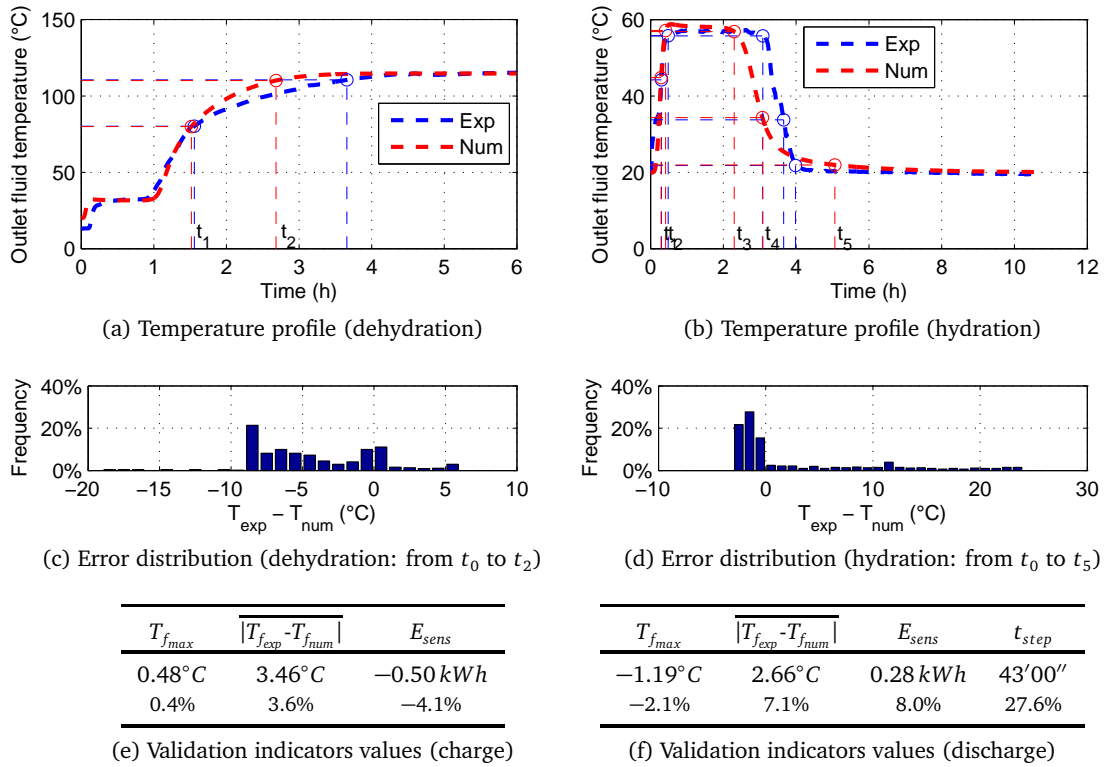


Figure III.18 – Validation of test case 6

reactor. Figures III.19a and III.19c show there are strong divergence between numerical and experimental results in the charging process. But, as this charge is achieved under the exact same conditions than for test case 1D, the shape of experimental results should be identical to figure III.14a. This is obviously not the case. It is interpreted as an inconsistency in experimental results in test case 3D (since test case 1D is in better accordance with the others test cases).

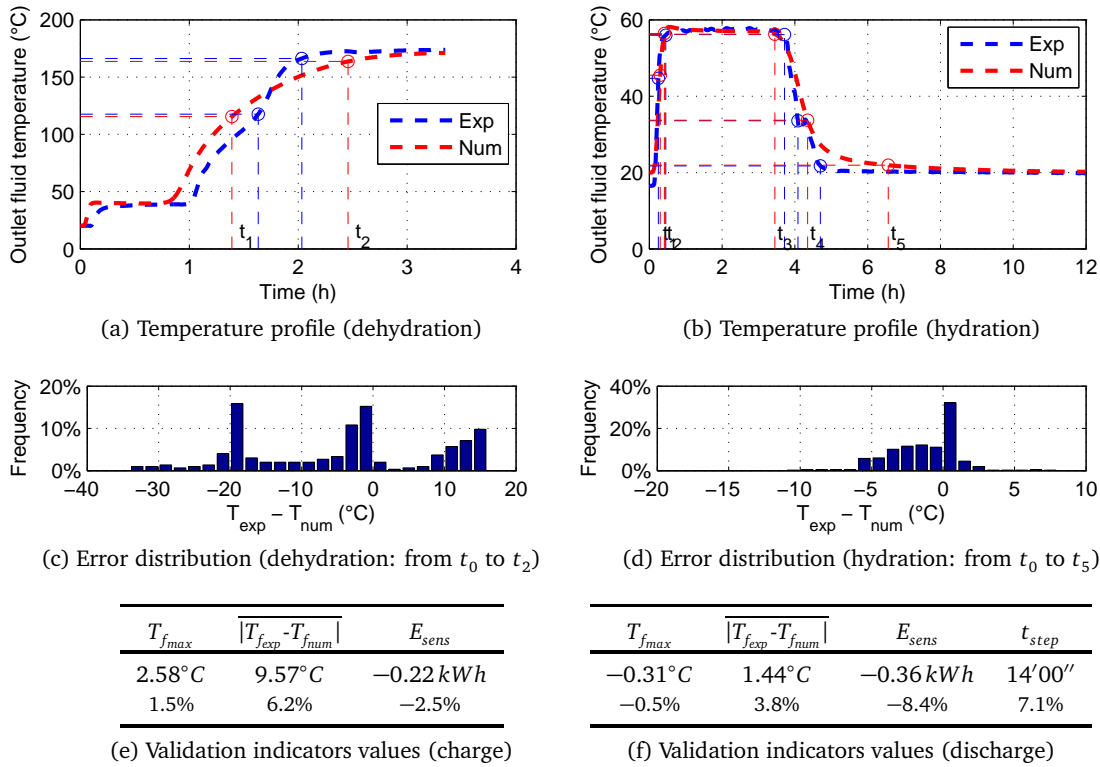


Figure III.19 – Validation of test case 3

## Conclusion

Given the good accordance between experimental and numerical results just described, the model is considered as fully validated in the following range of operating conditions:

- charging temperature from 120°C to 180°C,
- inlet humidity on charge of 30% at 20°C,
- inlet humidity on discharge from 50% at 70% at 20°C, with a great response of the model allowing confidence for a wider range of operation,
- inlet fluid velocity from 0.01 m s<sup>-1</sup> at 0.03 m s<sup>-1</sup>, with a warning on lower inlet fluid velocities.

The full model has thus demonstrated its capability of satisfactorily describing heat and mass transfers in the adsorbent bed. The next section develops a dimensionless analysis which is

achieved with two goals. First, it compares the weight of each term in the governing equations in order to assess if a simplification of one or several terms is possible, or not. Second, it enables a reflection on the relative influence of each term on outlet power maximization.

### III.3 Dimensionless analysis

In the field of model analysis and system optimization, it is somehow important to formulate equations in dimensionless form or, failing that, intensive properties. For instance, absolute power (W) is not a good response variable but power density ( $\text{W m}^{-3}$ ) is more relevant. In the same way, bed length (m) is an extensive property while the ratio between cross section surface and bed length is intensive ( $\text{m}^2 \text{m}^{-1}$ ). Temperature, pressure or velocity variables are already intensive properties, but can be formulated as dimensionless variables varying from 0 to 1, if upper and lower limit values can be expressly defined. Dimensionless form of equations brings out dimensionless numbers. A comparison between dimensionless numbers can highlight the preponderance of some terms on others and hence provides a guideline for model simplification or performance enhancement. The first step consists in the definition of dimensionless variables.

#### III.3.1 Dimensionless variables

The following dimensionless variables are used for nondimensionalization process. These dimensionless numbers call for limit values or reference values, that are summed up in table III.6.

$$t^* = \frac{u_{max}}{L} t \quad \Rightarrow t = \frac{L}{u_{max}} t^* \quad (\text{III.5})$$

$$T_f^* = \frac{T_f - T_{min}}{T_{max} - T_{min}} \quad \Rightarrow T_f = \Delta T (T_f^* + T_{min}^*) \quad \text{with } T_{min}^* = \frac{T_{min}}{\Delta T} \quad (\text{III.6})$$

$$T_s^* = \frac{T_s - T_{min}}{T_{max} - T_{min}} \quad \Rightarrow T_s = \Delta T (T_s^* + T_{min}^*) \quad \text{with } T_{min}^* = \frac{T_{min}}{\Delta T} \quad (\text{III.7})$$

$$p_v^* = \frac{p_v - p_{v_{min}}}{p_{v_{max}} - p_{v_{min}}} \quad \Rightarrow p_v = \Delta p_v (p_v^* + p_{v_{min}}^*) \quad \text{with } p_{v_{min}}^* = \frac{p_{v_{min}}}{\Delta p_v} \quad (\text{III.8})$$

$$u^* = \frac{u}{u_{max}} \quad \Rightarrow u = u_{max} u^* \quad (\text{III.9})$$

$$q^* = \frac{q - q_{min}}{q_{max} - q_{min}} \quad \Rightarrow q = \Delta q (q^* + q_{min}^*) \quad \text{with } q_{min}^* = \frac{q_{min}}{\Delta q} \quad (\text{III.10})$$

Table III.6 – Lower and upper limits used for equations nondimensionalization

Variable	Lower limit	Upper limit (or reference value)	Difference
$T_f, T_s$	$T_{min} = 293.15 \text{ K}$	$T_{max} = 453.15 \text{ K}$	$\Delta T = T_{max} - T_{min}$
$p_v$	$p_{v_{min}} = 500 \text{ Pa}$	$p_{v_{max}} = 5000 \text{ Pa}$	$\Delta p_v = p_{v_{max}} - p_{v_{min}}$
$u$	$u_{min} = 0 \text{ m s}^{-1}$	$u_{max} = 0.05 \text{ m s}^{-1}$	
$q$	$q_{min} = q_e(T_{max}, p_{v_{min}})$	$q_{max} = q_e(T_{min}, p_{v_{max}})$	$\Delta q = q_{max} - q_{min}$

### III.3.2 Nondimensionalization of conservation equations

#### III.3.2.1 Dimensionless form of energy conservation equation for the fluid part

Energy conservation equation in the fluid part is displayed in equation II.6 on the form:

$$\begin{aligned} & \left[ A \rho_{da} c_{p_{da}} \right] \frac{\partial T_f}{\partial t} + \left[ A \frac{M_v c_v}{R} \right] \frac{\partial p_v}{\partial t} = -div \left( \left( \rho_{da} c_{p_{da}} T_f + \frac{M_v c_v}{R} p_v \right) \vec{u} \right) \\ & + U_b \frac{S_{exch}}{V} (T_s - T_f) + div \left( \lambda_f \overrightarrow{grad}(T_f) \right) \end{aligned}$$

By replacing  $T_f, T_s, p_v$  and  $u$  variables by their dimensionless form (equation III.5), it comes up to the following developed expression.

$$\begin{aligned} & A \rho_{da} c_{p_{da}} \frac{\Delta T u_{max}}{L} \frac{\partial T_f^*}{\partial t^*} + A \frac{M_v c_v}{R} \frac{\Delta p_v u_{max}}{L} \frac{\partial p_v^*}{\partial t^*} \\ & = -u_{max} div \left( \left( \rho_{da} c_{p_{da}} \Delta T (T_f^* + T_{f_{min}}^*) + \frac{M_v c_v}{R} \Delta p_v (p_v^* + p_{v_{min}}^*) \right) \vec{u}^* \right) \quad (III.11) \\ & = U_b \frac{S_{exch}}{V} \Delta T (T_s^* - T_f^*) + \Delta T div \left( \lambda_f \overrightarrow{grad}(T_f^* + T_{f_{min}}^*) \right) \end{aligned}$$

This expression can be reduced to the following form:

$$\begin{aligned} & A \frac{\partial T_f^*}{\partial t^*} + A \frac{\Delta p_v M_v c_v}{\rho_{da} c_{p_{da}} R \Delta T} \frac{\partial p_v^*}{\partial t^*} = -L div \left( \left( (T_f^* + T_{f_{min}}^*) + \frac{\Delta p_v M_v c_v}{\rho_{da} c_{p_{da}} R \Delta T} (p_v^* + p_{v_{min}}^*) \right) \vec{u}^* \right) \\ & + \frac{L S_{exch}}{V} \frac{U_b}{u_{max} \rho_{da} c_{p_{da}}} (T_s^* - T_f^*) + \frac{\lambda_f}{L u_{max} \rho_{da} c_{p_{da}}} L^2 div \left( \overrightarrow{grad}(T_f^* + T_{f_{min}}^*) \right) \quad (III.12) \end{aligned}$$

It brings Peclet and Stanton numbers into play. Peclet number is a ratio between advection and conduction heat transfers within the bed. The Stanton number,  $St$ , is a dimensionless number that measures the ratio of heat transferred into a fluid to the thermal capacity of fluid.

There also is another dimensionless number, stated as  $\chi_{v,da}$ , which is sort of a ratio between vapor and dry air volumetric heat capacities. Finally, the product  $\Xi$  between exchange surface

density and bed length quantifies exchange surface available for convection heat transfers.

$$Pe = \frac{L u_{max} \rho_{da} c_{pda}}{\lambda_f} = \frac{L u_{max}}{D_f} \text{ with } D_f = \frac{\lambda_f}{\rho_{da} c_{pda}} \quad (\text{III.13})$$

$$St = \frac{U_b}{u_{max} \rho_{da} c_{pda}} \quad (\text{III.14})$$

$$\chi_{v,da} = \frac{\Delta p_v M_v C_{p_v}}{\rho_{da} c_{pda} R \Delta T} \quad (\text{III.15})$$

$$\Xi = \frac{L S_{exch}}{V} \quad (\text{III.16})$$

A replacement of dimensionless terms by their according dimensionless numbers comes to the following equation (III.17) that is the dimensionless form of energy conservation in the fluid part.

$$\begin{aligned} A \frac{\partial T_f^*}{\partial t^*} + A \chi_{v,da} \frac{\partial p_v^*}{\partial t^*} = & -L \operatorname{div} \left( \left( (T_f^* + T_{fmin}^*) + \chi_{v,da} (p_v^* + p_{vmin}^*) \right) \vec{u}^* \right) \\ + \Xi St (T_s^* - T_f^*) + \frac{1}{Pe} L^2 \operatorname{div} \left( \vec{\operatorname{grad}} (T_f^* + T_{fmin}^*) \right) \end{aligned} \quad (\text{III.17})$$

This dimensionless equation shows fluid temperature  $T_f$  and vapor pressure  $p_v$  are coupled, which was already noticed in chapter 2. If maximizing outlet power is the main objective, the time derivative of fluid temperature has to be maximized. On the left hand side of the equation, a minimization of  $A$  would lead to an increase of time derivatives values (if right hand side (RHS) of the equation remains constant in the same time). This would plead for a low porosity.

The RHS of equation III.17 is a sum of three terms. The first term is heat transport through advection. This is a **purely heat transport term**, that has to be high enough to carry heat out of the adsorbent bed but this is **not a source term**. The second term stands for heat exchange between the solid and the fluid part. Maximizing  $\Xi St$  won't necessarily increase outlet power since heat transfer will soon be limited by the temperature difference between solid and gas parts. Finally, the third and last term of the RHS is a diffusion term. Stating  $\frac{1}{Pe} \simeq 2 \times 10^{-3} \ll 1$ , this term is negligible compared to advection term, when advection occurs (i.e. when the reactor is opened). When the reactor is closed, advection is not mechanically driven anymore but thermally driven, which means  $u^* \ll 1$  and diffusion can influence results again. Since diffusion term does not require much computational resources to be calculated, it seems relevant, simpler and safer to keep this term.

In conclusion, a maximization of outlet power in the fluid part get through a study of energy conservation in the solid part.

### III.3.2.2 Dimensionless form of energy conservation equation for the solid part

Equation II.8 states energy conservation in the solid part. It is formulated in the following form.

$$[B_s \rho_s c_s + B_a q c_a] \frac{\partial T_s}{\partial t} = U_b \frac{S_{exch}}{V} (T_f - T_s) + B_a (|\Delta H| - c_a T_s) \frac{\partial q}{\partial t}$$

Replacing  $T_f$ ,  $T_s$ ,  $p_v$ ,  $u$  and  $q$  variables by their dimensionless form of equation III.5 brings the following developed expression.

$$\begin{aligned} [B_s \rho_s c_s + B_a \Delta q (q^* + q_{min}^*) c_a] \frac{\Delta T u_{max}}{L} \frac{\partial T_s^*}{\partial t^*} &= U_b \frac{S_{exch}}{V} \Delta T (T_f^* - T_s^*) \\ + B_a (|\Delta H| - c_a \Delta T (T_s^* + T_{min}^*)) \frac{\Delta q u_{max}}{L} \frac{\partial q^*}{\partial t^*} & \end{aligned} \quad (III.18)$$

Last formulation can be rearranged to the following more condensed formulation.

$$\begin{aligned} \left[ B_s + B_a \frac{\Delta q c_a}{\rho_s c_s} (q^* + q_{min}^*) \right] \frac{\partial T_s^*}{\partial t^*} &= \frac{U_b}{u_{max} \rho_s c_s} \frac{L S_{exch}}{V} (T_f^* - T_s^*) \\ + B_a \frac{\Delta q c_a}{\rho_s c_s} \left( \frac{|\Delta H|}{\Delta T c_a} - (T_s^* + T_{min}^*) \right) \frac{\partial q^*}{\partial t^*} & \end{aligned} \quad (III.19)$$

This brings into play the same Stanton number  $St$  and exchange surface ratio  $\Xi$  as for dimensionless form of energy conservation in the fluid part. A dimensionless number  $\chi_{w,s}$ , similar in construction to  $\chi_{v,da}$ , is defined as the ratio between adsorbed water volumetric capacity and solid volumetric heat capacity. Finally, a new dimensionless number  $\Gamma$  is introduced. It represents the ratio between the profit and the cost of adsorption in terms of specific energy. In others words, it is the ratio between specific energy released through differential heat of adsorption and specific heat required to change water state from gas to adsorbed phase.

$$\chi_{w,s} = \frac{\Delta q c_a}{\rho_s c_s} \quad (III.20)$$

$$\Gamma = \frac{|\Delta H|}{\Delta T c_a} \quad (III.21)$$

A replacement of dimensionless terms by their according dimensionless numbers brings the following dimensionless form of energy conservation in the solid part.

$$[B_s + B_a \chi_{w,s} (q^* + q_{min}^*)] \frac{\partial T_s^*}{\partial t^*} = -St \Xi (T_s^* - T_f^*) + B_a \chi_{w,s} (\Gamma - (T_s^* + T_{min}^*)) \frac{\partial q^*}{\partial t^*} \quad (III.22)$$

As stated earlier, a maximization of outlet power requires a maximization of time derivative of solid's temperature  $T_s$ . A minimization of left hand side of equation III.22 would lead to an increase of solid temperature time derivative. This can be achieved with a low  $\chi_{w,s}$  number. Increasing the right hand side (RHS) of the equation will also lead to an increase of time derivative.

RHS is made of the sum of two terms. The first term is the heat exchange term between solid and fluid part. A minimization of  $St\Xi$  would effectively lead to an increase in solid temperature but at the cost of a decrease of heat transfer rate between solid and fluid. This would not increase the total energy available in the system but only differ its propagation. On the other side, the second term is a source term. It is the only lever to increase heat available in the system. An increase of  $\Gamma$  and/or  $\chi_{w,s}$  would increase the source term and hence increase energy released in the system. In others words, higher  $|\Delta H|$  or  $\Delta q$  values will provide better outlet power, which is relevant but not innovative.

### III.3.2.3 Dimensionless form of water vapor mass conservation equation

Equation II.12 states water vapor mass conservation in the following form.

$$\left[ -A \frac{p_v M_v}{R T_f^2} \right] \frac{\partial T_f}{\partial t} + \left[ A \frac{M_v}{R T_f} \right] \frac{\partial p_v}{\partial t} = -\frac{M_v}{R} \text{div} \left( \frac{p_v}{T_f} \vec{u} \right) - B_a \frac{\partial q}{\partial t}$$

This equation can be nondimensionalized, in the same way as for energy conservation equations, to turn to the following developed form.

$$\begin{aligned} & \left[ -A \frac{\Delta p_v (p_v^* + p_{v_{min}}^*) M_v u_{max}}{L R \Delta T (T_f^* + T_{min}^*)^2} \right] \frac{\partial T_f^*}{\partial t^*} + \left[ A \frac{M_v \Delta p_v u_{max}}{L R \Delta T (T_f^* + T_{min}^*)} \right] \frac{\partial p_v^*}{\partial t^*} \\ & = -\frac{\Delta p_v M_v u_{max}}{R \Delta T} \text{div} \left( \frac{p_v^* + p_{v_{min}}^*}{T_f^* + T_{min}^*} \vec{u}^* \right) - B_a \frac{\Delta q u_{max}}{L} \frac{\partial q^*}{\partial t^*} \end{aligned} \quad (\text{III.23})$$

Last expression can be rearranged to the following form. Both expressions are of course strictly equivalent.

$$-A \frac{(p_v^* + p_{v_{min}}^*)}{(T_f^* + T_{min}^*)^2} \frac{\partial T_f^*}{\partial t^*} + \frac{A}{(T_f^* + T_{min}^*)} \frac{\partial p_v^*}{\partial t^*} = -L \text{div} \left( \frac{p_v^* + p_{v_{min}}^*}{T_f^* + T_{min}^*} \vec{u}^* \right) - B_a \frac{R \Delta T \Delta q}{\Delta p_v M_v} \frac{\partial q^*}{\partial t^*} \quad (\text{III.24})$$

It brings up a new dimensionless number,  $\Upsilon$ , that is sort of a ratio between adsorbed water density variation and water vapor density variation. This definition would be rigorously true if water vapor density was not a function of two variables  $T_f$  and  $p_v$ .

$$\Upsilon = \frac{R \Delta T \Delta q}{\Delta p_v M_v} \quad (\text{III.25})$$

After a replacement of dimensionless terms by their according dimensionless numbers, last equation becomes the following dimensionless form of mass conservation equation.

$$-A \frac{p_v^* + p_{vmin}^*}{(T_f^* + T_{min}^*)^2} \frac{\partial T_f^*}{\partial t^*} + \frac{A}{T_f^* + T_{min}^*} \frac{\partial p_v^*}{\partial t^*} = -L \operatorname{div} \left( \frac{p_v^* + p_{vmin}^*}{T_f^* + T_{min}^*} \vec{u}^* \right) - B_a \Upsilon \frac{\partial q^*}{\partial t^*} \quad (\text{III.26})$$

Equation III.26 shows that an increase in adsorbed water quantity will lead to a temperature increase and a vapor pressure decrease. This behavior is logical since adsorption retrieves water from the gas phase and releases energy. The first term of the right hand side (RHS) equation stands for mass transport through advection. The second term is a water vapor source/sink. An increase of  $\Upsilon$  would lead to an increase in mass exchange from the gas to the solid which would increase heat released to (or retrieve from) the system. This also pleads for a high adsorption variation range value,  $\Delta q$ .

### III.3.2.4 Dimensionless form of adsorption kinetics equation

Adsorbed water mass conservation is displayed on the following form in equation II.13.

$$\frac{\partial q}{\partial t} = k_m (q_e - q)$$

This equation can be turned into a dimensionless equation by replacing variables  $q$  and  $t$  by their dimensionless expressions.

$$\frac{\Delta q u_{max}}{L} \frac{\partial q^*}{\partial t^*} = k_m \Delta q (q_e^* - q^*) \quad (\text{III.27})$$

It brings up a new dimensionless number  $k_m^* = \frac{k_m L}{u_{max}}$  which is defined as a ratio between diffusion and advection time constants.

$$\frac{\partial q^*}{\partial t^*} = k_m^* (q_e^* - q^*) \quad (\text{III.28})$$

A high  $k_m^*$  value insures a good transition from instant adsorption value  $q^*$  to equilibrium value  $q_e^*$ . This tends to use an equilibrium model with a numerical evaluation of time derivative of  $q$ , under the assumption of a high diffusion rate within adsorption pores.  $k_m^*$  value is actually (strongly) influencing results while it remains the limiting factor. Once  $k_m^*$  is high enough to ensure close  $q^*$  and  $q_e^*$  values, an increase of  $k_m^*$  value is no longer influencing results.  $(q_e^* - q^*)$  then becomes the limiting factor in equation III.28.

### III.3.2.5 Dimensionless form of coupled conservation equations

Equations III.17, III.22, III.26 and III.28 are grouped together into the following matricial form. Dimensionless numbers used in these coupled equations are summed up in table III.7.

$A$	$0$	$A \chi_{v,da}$	$0$	$\frac{\partial}{\partial t}$	$=$	$T_f^*$	$\Xi St (T_s^* - T_f^*) + \frac{L^2}{Pe} \Delta (T_f^* + T_{fmin}^*)$ $-L \operatorname{div} \left( \left( \begin{array}{c} \chi_{v,da} (p_v^* + p_{vmin}^*) \\ + (T_f^* + T_{fmin}^*) \end{array} \right) \vec{u}^* \right)$
$0$	$B_s + B_a \chi_{w,s}$ $\times (q^* + q_{min}^*)$	$0$	$(T_s^* + T_{min}^* - \Gamma)$ $\times B_a \chi_{w,s}$			$T_s^*$	$St \Xi (T_f^* - T_s^*)$
$\frac{-A (p_v^* + p_{vmin}^*)}{(T_f^* + T_{min}^*)^2}$	$0$	$\frac{A}{T_f^* + T_{min}^*}$	$B_a \Upsilon$			$p_v^*$	$-L \operatorname{div} \left( \frac{p_v^* + p_{vmin}^*}{T_f^* + T_{min}^*} \vec{u}^* \right)$
$0$	$0$	$0$	$1$			$q^*$	$k_m^* (q_e^* - q^*)$
$\underbrace{\hspace{15em}}_{\text{Mass matrix}}$						$\underbrace{\hspace{15em}}_{\text{Right Hand Side (RHS)}}$	

Dimensional analysis reached few tangible results in terms of outlet power optimization or model simplification. It was nonetheless interesting for equations understanding to compare the relative weight of each term and each dimensionless number.

The next step towards the understanding of the system behavior and the enhancement of its performances is to focus on the energy conversion chain from the heat source (charge) to the heat release (discharge). It will provide guidelines for the improvement of the energy efficiency of the system.

### III.4 Analysis of energy conversion efficiency

It is important when designing a heat storage system to be aware of heat fluxes entering and leaving the reactor at every step of charging and discharging processes. Indeed, experiments from STAID project and numerical simulations both show that a non negligible amount of energy provided to the storage tank is not stored or not retrieved on discharge. Thermal energy provided to the system is thus not entirely converted into sorption storage potential. The goal of the following study is to deeper understand energy conversion mechanisms and enhance system performances. The question raised is why sensible energy provided to the system in charging phase is not completely turned back into sensible energy during the discharging phase. The best way to address this problem and visualize energy conversion chain is to draw a Sankey diagram from heat generated by the heat source on charge to sensible heat released by the reactor on discharge.

Several definitions and equations must be set in order to collect or generate all data required for this study. All equations are summed up in table III.9. A specific nomenclature is provided in table III.8 to specify subscript notations used in table III.9.

Table III.7 – Summary of dimensionless numbers formulation, default value and physical meaning

Number	Formulation	Default	Log <sub>10</sub>	Physical significance (ratio)
1	$A = \epsilon_b + (1 - \epsilon_b) \epsilon_p$	0.56	-0.3	Void fraction in the adsorbent bed, which depends on bed macroporosity $\epsilon_b$ at the interstices between beads, and beads porosity $\epsilon_p$ at the interstices between particules.
2	$Pe = \frac{L u_{max} \rho_{da} c_{pda}}{\lambda_f}$	$4.7 \times 10^2$	2.7	Advection heat transfer over conduction heat transfer in the fluid
3	$St = \frac{U_b}{u_{max} \rho_{da} c_{pda}}$	$3.0 \times 10^{-2}$	-1.5	Conduction-convection heat transfer over advection heat transfer
4	$\chi_{v,da} = \frac{\Delta p_v M_v C_{p_v}}{\rho_{da} c_{pda} R \Delta T}$	$1.0 \times 10^{-1}$	-1.0	Water vapor volumetric heat capacity over dry air volumetric heat capacity
5	$\chi_{w,s} = \frac{\Delta q c_a}{\rho_s c_s}$	$5.5 \times 10^{-1}$	-0.3	Adsorbed water volumetric heat capacity over solid volumetric heat capacity
6	$\Xi = \frac{L S_{exch}}{V}$	$4.9 \times 10^2$	2.7	Characterization of exchange surface available for convection heat transfer.
7	$\Gamma = \frac{ \Delta H }{\Delta T c_a}$	$1.1 \times 10^1$	1.0	Heat released on adsorption over heat required for adsorption state change
8	$\Upsilon = \frac{R \Delta T \Delta q}{\Delta p_v M_v}$	$4.1 \times 10^3$	3.6	Adsorbed water density variation over water vapor density variation
9	$k_m^* = \frac{k_m L}{u_{max}}$	$6.4 \times 10^{-3}$	-2.2	diffusion time constant over advection time constant

**Note:**  $B_s$  and  $B_a$  are dimensionless numbers that are not used for sizing purposes. It is scaling numbers that are respectively used to adapt solid density and adsorption properties values according to the scale at which measurements were achieved. For instance, if solid density was measured at a bed scale, it already takes into account for porosity and  $B_s = 1$  but if it was measured at a bead scale it has to account for bed macro-porosity and  $B_s = 1 - \epsilon_b$ .

Thermal energy is generated in a **heat source**. The heat source can either be a solar source (solar heat collectors), or wasted heat from energy production power plants (or industrial processes), or generated from an electrical heater. The heat source generates a given amount of thermal energy  $E_s$  (equation III.29) that is intended to flow in the storage tank. From this amount, a part  $E_{dlc}$  is wasted through conduction within the duct walls and convection (**distribution losses** - equation III.31) and a useful part  $E_p$  is finally provided to the reactor (equation III.30). Figure III.20a displays temperature profile at the inlet and at the outlet of the adsorbent bed. Total thermal energy provided to the tank can be divided into two parts:

- **Heat  $E_{sc}$  absorbed** by the adsorbent bed, which is represented by the integral between inlet and outlet temperature profile.
- **Heat  $E_{olc}$  retrieved at the outlet** of the adsorbent bed which is wasted in the sense that it is not retained by the storage tank. But this amount of heat is necessary to the charging process. However, it can be minimized with a good monitoring of the charging process. Indeed, the reactor is fully charged once the outlet temperature is equal to the inlet tem-

Table III.8 – Nomenclature for energy conversion analysis

$t_{0,c}$	:	charging phase start time	(h)	<b>Subscripts</b>
$t_{f,c}$	:	charging phase final time	(h)	$s$ : source
$t_{0,d}$	:	discharging phase start time	(h)	$b$ : adsorbent bed
$t_{f,d}$	:	discharging phase final time	(h)	$in$ : inlet condition
$\dot{Q}_{v,in}$	:	inlet volume flow rate	( $m^3 h^{-1}$ )	$out$ : outlet value
$T$	:	fluid temperature	( $m^3 h^{-1}$ )	

perature. Once this point is reached, all energy that flows in the reactor is lost at the outlet. It is then important not to keep on charging vainly. Moreover, outlet thermal energy losses can cleverly be used for thermal application (heating or domestic hot water generation) or as an inlet of the thermal source (in case of a closed loop). It is then really important to consider the storage system as a part of a fully integrated system. These considerations are developed in chapter V.

Only a certain amount  $E_{sd}$  of heat absorbed by the bed in charging process will be released in discharging phase. Heat  $E_q$  stored as an **adsorption potential** can be calculated with equation III.34. This potential is slightly lower than the total amount of heat retained by the storage tank. The difference is commensurate with sensible energy stored in the gas phase of the reactor, which participates to adsorption equilibrium but is invisible to the calculation of storage potential.

From the amount of potential energy  $E_q$ , a part is **lost in sensible energy**. Indeed, at the end of the charging phase, the whole reactor is at high temperature. Even if the reactor is insulated, the adsorbent bed slowly cools down to come back to ambient temperature conditions. Cool-down losses occur through the storage tank walls. At this stage, the amount of water within the reactor is kept constant since no mass exchange occurs with the surroundings. Nonetheless, temperature change leads to adsorption equilibrium change. A lower temperature tends to increase the amount of water molecules adsorbed in the sorbent pores. Adsorption process releases thermal energy that is lost until a final equilibrium is reached. This explains differences between adsorption heat storage potential  $E_q$  at the end of the charging phase, and final thermal energy potential at the end of the cool-down process. Finally, a given amount  $E_{ld}$  of heat is lost during the discharge process. It is partly interpreted as energy losses through bed walls. But most of this share is due to a **lower mass of water** in the adsorbed bed at the end of the discharge process compared to initial conditions (at the beginning of the charging phase).

A **Sankey diagram** is drawn in figure III.20c with the set of default settings parameters. It illustrates all steps of energy conversion and heat losses under a full charge-discharge cycle. Amount of energy are provided in intensive ( $kWh m^{-3}$ ) and relative (%) units. Percentages are calculated relatively to the amount of sensible heat absorbed by the reactor. All heat shares are calculated on **95 % of the temperature drop**, as displayed on figure III.20b. Arrows width are proportional to the related amount of thermal energy. Moreover, numbers provided refer to equations of table III.9.

This diagram shows that about 70% of absorbed energy is converted into useful heat released on discharge. It also underlines the fact that about the same amount than absorbed energy is

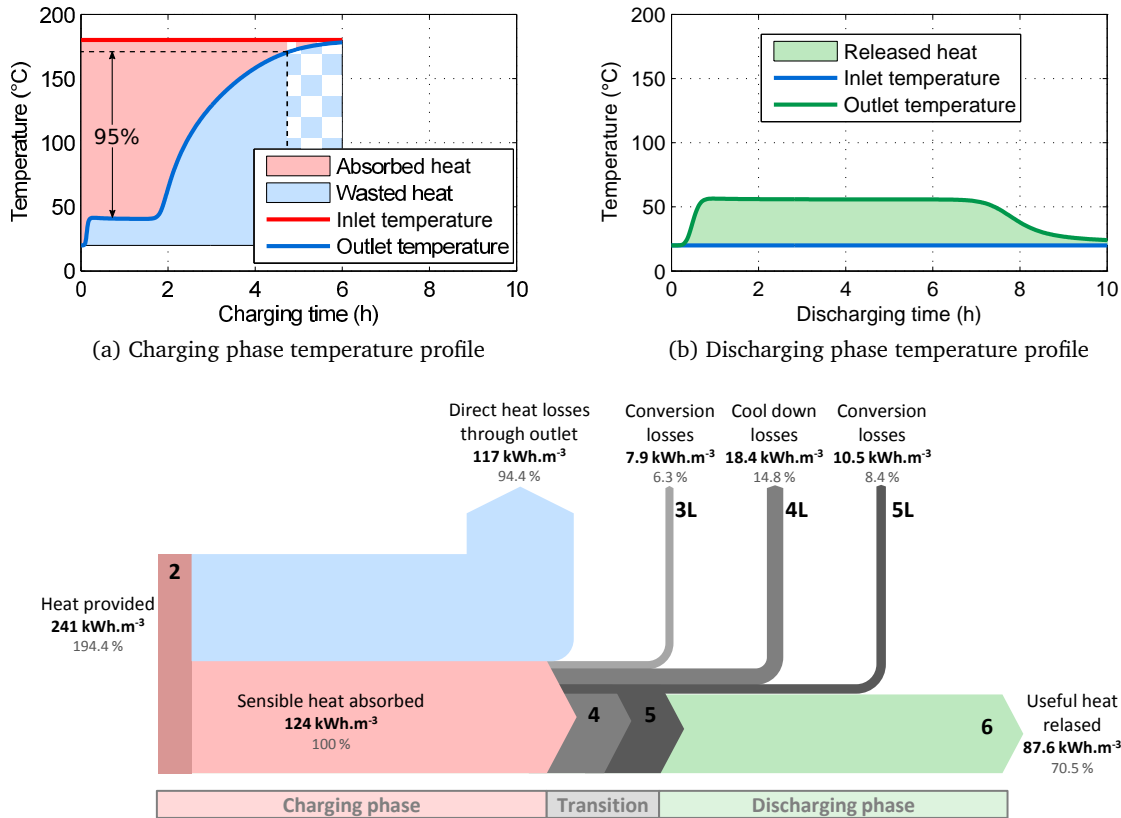


Figure III.20 – Illustration of absorbed, wasted and released sensible heat on a full charge-discharge cycle with default setting conditions

directly lost at the outlet of the adsorbent bed. Global heat conversion and losses mechanisms are described in the next chapter that addresses the influence of material properties on system performances. It is nonetheless interesting to point out the influence of key thermophysical properties, operating conditions and system geometry on conversion efficiency. Results from sections IV.2 and IV.3 are used in order to address this question. For each of the eight physical properties, five operating conditions and two geometrical parameters investigated, differences in heat losses and conversion ratio mean values of low-level and high-level sets of results are calculated. Detailed results are displayed in table 8 of appendix B.

Some parameters are influencing much more conversion efficiency than others. Interpretations and illustrations of figures III.21 and III.22 focus on most influencing parameters.

- Figure III.21a illustrates that highest conversion ratio are all obtained with high-level  $|\Delta H|$  value (+31.4% from 50% to 150% of default value). As explained in section IV.2, a higher differential heat of adsorption  $|\Delta H|$  increases heat absorbed and heat released by the system in about the same proportions. Consequently, the ratio between heat released and heat absorbed rises with  $|\Delta H|$ .
- A similar approach provides similar results on adsorption equilibrium function  $q_e$ .

- Solid density has a strong influence on sensible heat storage in the storage tank. As illustrated in figure III.21b, a lower  $\rho_s$  enables to reach higher conversion ratio values (+18.2% from  $1500 \text{ kg m}^{-3}$  to  $600 \text{ kg m}^{-3}$ ). Less thermal energy is used to warm up the material and is lost during cool-down phase.
- Charging temperature  $T_{in,charge}$  has a noteworthy importance, as illustrated in figure III.21c. It shows highest conversion ratios are obtained with low charging temperature. Indeed, with a lower maximum value, cool-down losses are also lower (−39.7% from  $180^\circ\text{C}$  to  $110^\circ\text{C}$ ) to the cost of storage density. Direct energy losses through the outlet are also reduced by 27.0% on the same variation range.
- As shown on figure III.21d, high values of inlet relative humidity on discharge  $\varphi_{in,discharge}$  also provide higher conversion ratios (+28.1% from 50% to 80% of inlet relative humidity). This is explained by a very strong diminution of discharge losses. As stated earlier, a negative water mass difference is observed with default setting conditions between the beginning and the end of a full charge-discharge cycle (about  $-1.5 \text{ kg}_v \text{ m}^{-3}$  out of water densities of  $12 - 13 \text{ kg}_v \text{ m}^{-3}$ ). This underlines a lack of humidity in discharging conditions to reach back initial conditions. With a higher inlet relative humidity on discharge (80% vs. default 70%), the water mass difference is compensated.

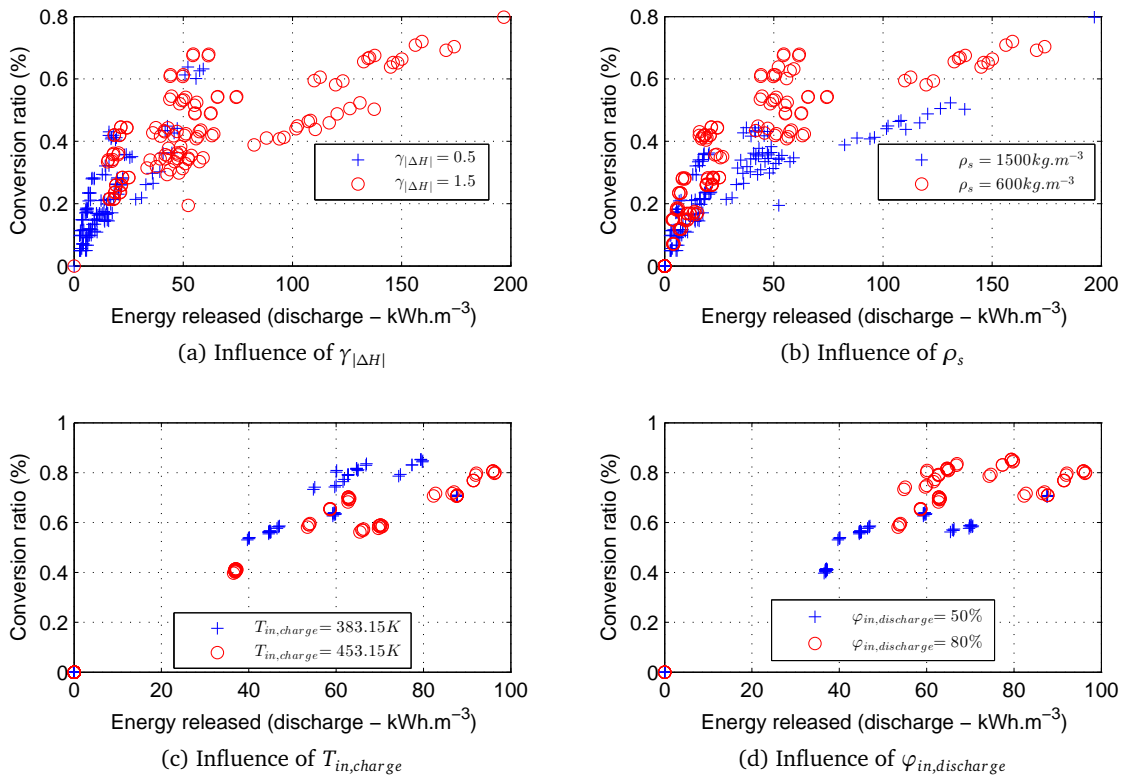


Figure III.21 – Heat conversion ratio against energy released for some of most influencing parameters ( $\gamma_{|\Delta H|}$ ,  $\rho_s$ ,  $T_{in,charge}$  and  $\varphi_{in,discharge}$ )

Two parameters provide results that deserve additional plots to be analyzed (figure III.22).

- According to the comparison between short beds (10 cm) and long beds (50 cm) behavior, a longer bed enables sensible reductions in the share of direct losses through the outlet. This is actually a matter of system autonomy. Figure III.22a displays inlet and outlet temperature profiles for three different bed lengths. As explained in part IV.2, system autonomy is proportional to bed length. Energy absorbed (and hence released) is then also proportional to bed length. If charging process is stopped as soon as outlet temperature reaches a target point for each experiment (say for instance 95% of inlet temperature), amount of wasted energy is comparable from one experiment to another. Curve slope is slightly sharper for a shorter bed which tends to minimize wasted heat. But wasted heat is globally bed length independent. Ratio of wasted heat against absorbed heat is then clearly in favor of longer beds.
- Inlet flowrate on charge also has an influence on temperature profile (figure III.22b) and charging time but few influence on conversion efficiency. At high inlet flowrates, amount of energy absorbed (and released) is slightly greater (+2.3% and +2.9% for absorbed and released heat from  $60 \text{ m}^3 \text{ h}^{-1}$  to  $250 \text{ m}^3 \text{ h}^{-1}$ ) and conversion ratio is also improved (1.3 pt). But these slow improvements are achieved to the cost of heat losses. Indeed, a higher fluid velocity generates more direct losses through the outlet during charging process (+17.6% on the same variation range). Figure III.22b shows in case of high velocities, integral of absorbed energy tends to reduce faster than integral of wasted energy (see figure III.20a for a graphical definition of absorbed and wasted heat).

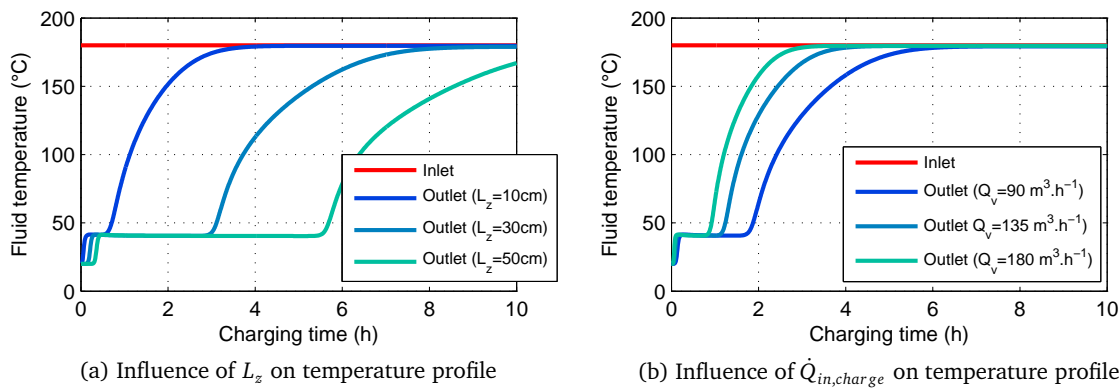


Figure III.22 – Temperature profiles on charge for three different values of  $L_z$  and  $\dot{Q}_{in,charge}$ . It illustrates the influence of these parameters on the ratio between direct losses and absorbed thermal energy.

In conclusion, this short analysis of energy conversion and energy losses is offering a wealth of information. It enables a deeper understanding and a deeper control of heat losses throughout a full charge-discharge process. It brings out formal definition of heat conversion chain. It also underlines key thermophysical properties and parameters that must be controlled in order to maximize conversion ratio from charge to discharge.

Some parameters are more playing with numbers than offering real solutions ( $|\Delta H|$ ,  $T_{in,charge}$ ) but others are providing real specification requirements. The following guideline tends to improve heat conversion efficiency.

- a low solid density  $\rho_s$ ,
- a low inlet flow rate  $v_{in,charge}$ ,
- a high bed length  $L_z$  (a trade off must be found with pressure drop increase across the bed which tends to increase fan power consumption),
- a high inlet relative humidity on discharge ( $\varphi_{in,discharge}$ ).

These requirements must match those from system performance analysis (in terms of outlet power and storage density maximization) performed in chapter 4. It is also important to underline that besides the quantification of heat losses, the improvement of energy efficiency requires a distinction between low temperature and high temperature outlets. Indeed, high temperature outlet fluxes can be used for more qualitative use than low temperature fluxes. This point is addressed in chapter 5.

But besides the results, the Sankey diagram and its analysis show there are two very different and complementary ways of improving system performances:

- A reflection at the **reactor scale** (or even at the material scale) to enhance heat and mass transfers within the storage tank. This is achieved in the following chapter 4.
- A reflection at a **system scale** on the integration of the storage system into the heating and ventilating system of a building in order to create synergies between the HVAC system and the storage system. It will enable a clever use of heat losses (2L) for other heating applications. This is achieved in the last chapter (page 123).

Chapters 4 and 5 are hence completely independent one another.

Table III.9 – Equation formulation for the study of energy conversion within the whole heat storage process

Denomination		Equation formulation
1	Energy generated by the heat source Charge <i>Not evaluated</i>	$E_s = \int_{t=t_{0c}}^{t_{fc}} \dot{Q}_{v_{in}} \rho_{da} C_{p_{da}} (T_{out,s} - T_{in,s}) dt \quad (III.29)$
2	Energy provided to the adsorbent bed Charge	$E_p = \int_{t=t_{0c}}^{t_{fc}} \dot{Q}_{v_{in}} \rho_{da} C_{p_{da}} (T_{in,b} - T_{in,s}) dt \quad (III.30)$
1L =1-2	Distribution losses Charge losses <i>Not evaluated</i>	$E_{dlc} = \int_{t=t_{0c}}^{t_{fc}} \dot{Q}_{v_{in}} \rho_{da} C_{p_{da}} (T_{out,s} - T_{in,b}) dt \quad (III.31)$
3	Sensible energy absorbed by the reactor Charge	$E_{sc} = \int_{t=t_{0c}}^{t_{fc}} \dot{Q}_{v_{in}} \rho_{da} C_{p_{da}} (T_{out,b} - T_{in,b}) dt \quad (III.32)$
2L =2-3	Heat losses through outlet Charge losses	$E_{olc} = \int_{t=t_{0c}}^{t_{fc}} \dot{Q}_{v_{in}} \rho_{da} C_{p_{da}} (T_{out,b} - T_{0,b}) dt \quad (III.33)$
4	Adsorption potential after charge Charge	$E_q = \int_{t=t_{0c}}^{t_{fc}} \left( \iiint_V B_a \frac{\partial q}{\partial t}  \Delta H  dV \right) dt \quad (III.34)$
3L +4L	Cool-down losses Transition losses	$E_{cdl} = B_s \rho_s c_s \left( \overline{T}_s _{t_{fc}} - \overline{T}_s _{t_{0d}} \right) + A \rho_{da} C_{p_{da}} \left( \overline{T}_f _{t_{fc}} - \overline{T}_f _{t_{0d}} \right) + A \frac{M_v C_{p_v}}{R} \left( \overline{p}_v _{t_{fc}} - \overline{p}_v _{t_{0d}} \right) \quad (III.35)$
5 =3-3L	Remaining energy storage potential after cool-down losses Transition	$E_r = E_{sc} - E_{cdl} \quad (III.36)$
6	Sensible useful energy released on discharge Discharge	$E_{sd} = \int_{t=t_{0d}}^{t_{fd}} \dot{Q}_{v_{in}} \rho_{da} C_{p_{da}} (T_{out,b} - T_{in,b}) dt \quad (III.37)$
5L =5-6	Conversion and dynamic losses on discharge Discharge	$E_{ld} = E_r - E_{sd} \quad (III.38)$

## Chapter IV

# Detailed analysis of the system: towards material selection and system optimization

### Contents

---

IV.1	Definition of quantities of interest . . . . .	96
IV.2	Study of thermophysical properties influence . . . . .	96
IV.2.1	Selection of factors, levels and variation ranges . . . . .	97
IV.2.2	Optimization of model parameters . . . . .	97
IV.2.3	Conclusion on the influence and optimization of material properties . . . . .	105
IV.3	Optimization of operating conditions and system geometry . . . . .	106
IV.3.1	Influence of inlet relative humidity $\varphi_{in}$ (on both charge and discharge) . . . . .	107
IV.3.2	Influence of inlet fluid velocity $v_{in}$ (on both charge and discharge) . . . . .	108
IV.3.3	Influence of charging inlet temperature $T_{in,charge}$ . . . . .	110
IV.3.4	Influence of bed length $L_z$ and cross section area $S$ . . . . .	112
IV.3.5	Conclusion on the influence and optimization of operating conditions . . . . .	115
IV.4	Development of a metamodel . . . . .	116

---

Now that the numerical model is developed (chapter 2) and validated (chapter 3), numerical experimentations are conducted in order to understand the behavior of the storage tank under different solicitations. The influence of thermophysical properties on system performance is investigated. It enables a deeper comprehension of heat and mass transfers within the adsorbent bed. Then, the influence of operating conditions and system geometry is addressed. It leads to some specifications for outlet power control and enhancement. Finally, a metamodel is developed in order to quickly predict storage density, outlet power and system autonomy under a set of seven control parameters.

## IV.1 Definition of quantities of interest

A detailed study on model behavior is to be performed. Objectives pursued at this step are to assess the influence on results of model parameters such as thermophysical properties, operating conditions or system geometry. Some inputs are controllable (like operating conditions or system geometry) whereas others are uncontrollable, such as thermophysical properties or adsorption model parameters (although they may be controllable for the purposes of sensitivity analysis or optimization of material properties). Investigations on controllable inputs address the optimization of operating conditions whereas uncontrollable parameters study provides information towards material selection. In any case, it is necessary to be able to quantify system response to a given set of variables. Indeed, raw outputs of each simulation is on the form of temperature, pressure and adsorbed quantity fields that are displayed for numerous timesteps. But optimization function requires a single output called **response variable**.

Several response variables can be considered but only one at a time can be investigated. Quantities of interest are outlet power and energy density. But response variables better have to be relative to system dimensions or material weight. Two response variables are then defined as **maximum outlet power density**  $P_{d,max}$  ( $\text{W m}^{-3}$ ) and **heat storage density**  $Q_d$  ( $\text{kWh m}^{-3}$ ). Other interesting response variables concern time characteristics of both charge and discharge phases. Charging time  $t_c$  and discharging time  $t_d$  formulations take over notations  $t_0$ ,  $t_2$  and  $t_3$  defined in part III.2.2.2. Calculation of  $P_{d,max}$ ,  $Q_d$ ,  $t_c$  and  $t_d$  are achieved according to following equations.

$$P_{d,max} = \frac{\dot{Q}_v \rho_{da} C_{pda}}{3600 \times S L_z} (T_{f,max} - T_{f_0}) \quad (\text{IV.1})$$

$$Q_d = \frac{\dot{Q}_v \rho_{da} C_{pda}}{3600 \times S L_z} \int_{t_0}^{t_5} (T_f|_{z=L_z} - T_f|_{z=0}) dt \quad (\text{IV.2})$$

$$t_c = t_2 - t_0 \quad (\text{IV.3})$$

$$t_d = t_3 - t_2 \quad (\text{IV.4})$$

Two independent works are conducted in sections IV.2 and IV.3 on thermophysical properties on the one hand, system geometry and operating conditions on the other hand.

## IV.2 Study of thermophysical properties influence

Thermophysical properties and model parameters describing material properties and intrinsic behavior of the storage tank are too numerous to consider all possible interactions between variables. A filtering step has to be performed first in order to select most influencing parameters. A **one at a time (OAT)** parametric analysis is thus performed on model thermophysical properties. This step enables to rank parameters from the most influencing to the less influencing. Selection of influencing parameters is done according to a mathematical quantification of **main effects**. No

interaction effect between factors is taken into account at this step.

### IV.2.1 Selection of factors, levels and variation ranges

The definition of variation range is the most delicate and arbitrary step. Sensitivity analysis focuses on a small variation domain around a selected set of default parameters. This can lead to an erroneous interpretation of parameters influence. Indeed, some parameters can have a dominant behavior under a given variation range and not influence results anymore outside this variation range.

For instance, and as stated in paragraph III.3.2.4, a low value of mass transfer coefficient  $k_m$  limits mass transfers.  $k_m$  is then a limiting factor for the system behavior. A small variation of this parameter implies a sensible variation of results. On the contrary, if  $k_m$  is large enough, mass transfers are limited by the potential difference between local adsorbed quantity  $q$  and equilibrium adsorbed quantity  $q_e$  at the bed interstices conditions. Under these circumstances, a small variation of  $k_m$  has no tangible effect on results. The same restrictions are observed for several parameters whose influence is not varying linearly. This is typically the case of heat transfer coefficient  $U_b$  which behavior is analog to mass transfer coefficient  $k_m$ . Dimensionless analysis has shown conduction term is not dominant compared to advection term under forced convection. This might change for a high conduction value or under lower forced convection.

A consequence to these thoughts is that optimization and material selection purposes require a wider variation range than sensitivity analysis. The whole domain has to be investigated in order to find an optimum value or in order to correctly assess the influence of each parameter. A list of main factors under study is provided in table IV.1 with default values and variation ranges considered for the analysis. A parametric design is set up with three levels (minimum, default, maximum value) for each of the 21 parameters selected at this stage. As explained earlier, only main effects are investigated. 63 configurations are run with 43 original sets of parameters and 20 duplications of the default set. Duplications enable to check the consistency of the parametric run algorithm. Indeed, if results differ for one or several default set, it reveals an algorithm dysfunction. Results are presented in the same table IV.1 and parameters are ranked from the most influencing to the less influencing.

Results from table IV.1 show the seven most influencing parameters (overall) are also the seven most influencing parameters for both outlet power density and heat storage density. The seventh parameter accounts respectively for 0.9% of mean square sum for power density ( $\lambda_b$ ), and 1.6% of mean square sum for storage density. The eighth parameter  $\epsilon_b$  still accounts for 0.5% of mean square sum on storage density while all other parameters accounts for less than 0.05% on both power and energy densities. It then seems relevant and cautious enough to keep "only" the top eight most influencing parameters from table IV.1 to go to the next step.

### IV.2.2 Optimization of model parameters

This step consists in running a numerical experiment based on the eight parameters selected in the previous paragraph. Given the number of parameters and the simulation time, it is worth con-

Table IV.1 – List of thermophysical properties inventoried with default, minimum and maximum values, and influence weight on maximum outlet power density and energy storage density

Rank	Physical property	Units	Values			Power density		Storage density	
			Default	Min	Max	Mean Sq.	Rank	Mean Sq.	Rank
1	$\gamma_{ \Delta H }$	% default value	100%	50%	150%	41.19	53.3%	2680.6	34.8%
2	$M_v$	kg mol <sup>-1</sup>	0.018	0.012	0.040	23.3	30.2%	3020.6	39.2%
3	$\gamma_{q_e}$	% default value	100%	50%	150%	3.52	4.6%	1344.2	17.4%
4	$c_a$	J kg <sup>-1</sup> K <sup>-1</sup>	2000	1000	4180	3.22	4.2%	218.3	2.8%
5	$C_{p_v}$	J kg <sup>-1</sup> K <sup>-1</sup>	2000	1000	4000	2.49	3.2%	179.5	2.3%
6	$\rho_s$	kg m <sup>-3</sup>	760	600	1500	2.69	3.5%	99.2	1.3%
7	$\lambda_f$	W m <sup>-1</sup> K <sup>-1</sup>	0.025	0.025	1.00	0.72	0.9%	122.2	1.6%
8	$\epsilon_b$	—	0.37	0.32	0.40	0.0003	0.0%	42.55	0.6%
9	$c_s$	J kg <sup>-1</sup> K <sup>-1</sup>	1200	500	1500	0.040	0.1%	0.00	0.0%
10	$\lambda_b$	W m <sup>-2</sup> K <sup>-1</sup>	0.10	0.02	0.50	0.024	0.0%	0.49	0.0%
11	$\gamma_{k_m}$	% default value	100%	50%	150%	0.020	0.0%	0.04	0.0%
12	$C_{p_{da}}$	J kg <sup>-1</sup> K <sup>-1</sup>	1000	700	1300	0.0022	0.0%	0.54	0.0%

**Note:** Others investigated parameters are the beads diameter  $d_p$ , particles porosity  $\epsilon_p$ , dry air density  $\rho_{da}$ , heat transfer coefficient  $U_b$  (which value is probably to high to lie in a range with tangible effects), moist air dynamic viscosity  $\mu_f$  and insulation properties such as insulation thickness  $e_i$ , conductivity  $\lambda_i$  and convective heat transfer coefficient on the inner and outer wall  $h_{conv,int}$  and  $h_{conv,ext}$ . Mean square values for all of these 9 coefficients are very low for both outlet power density ( $\leq 0.0007$ ) and storage density ( $\leq 0.11$ ).

sidering a  $2^k$  full factorial design. It means that all possible combinations between two levels (low and high) of each of the eight parameters are run. In others words, 256 charge/discharge cycles are run with either the low or the high value of each parameter. Each run takes 18 seconds on average. The  $2^8$  full factorial design is then intended to last for little less than 1h20 which is very acceptable. These simulation results are analyzed by three different complementary approaches.

- A full factorial design enables to watch the influence of main effects (as in the previous step) but also the influence of all interaction effects between groups of two variables. This can technically be achieved on *Matlab*<sup>®</sup> by using the N-way analysis of variance function *anovan* from the Statistics Toolbox, with the *interactions* model. Results are displayed in table IV.2.
- A graphical approach is also achieved in figures IV.1 to IV.6. Scatter plots are drawn for each factor under investigation. They display storage density against outlet power on the one hand, and charging time against discharging time on the other hand. Sets of low level and high level values are highlighted by two different colors. This enables to quickly see if a trend emerges. Red circles are always representing the value of interest (either low or high) for power and storage densities maximization. Gray solid points represent the intersection of all selected criteria already presented. From one figure to the next one, the number of

gray points is then divided by two (starting from 128 in figure IV.1 to 1 in figure IV.6), while the number of red circles and blue crosses remains constant (128 each).

- These trends are numerically confirmed by the calculation of mean differences between sets of low level and high level values. Absolute and relative results are provided in table IV.3 for outlet power and storage densities, and for charging and discharging times.

### Analysis of variance

Results from analysis of variance are displayed in table IV.2. They are ranked by order of influence. Mean square value of each factor (and factors combinations) is compared to the overall mean square values sum into a weighting term. The overall weight value is calculated by averaging weight values on outlet power density and storage density. Not all possible interactions are shown on this table but only most influencing ones. The leftover weight is calculated as the sum of remaining terms.

Table IV.2 – Analysis of variance on outlet power density and heat storage density, for selected thermophysical properties

Rank	Num.	Factor	Power density		Energy density		Overall weight	Left over
			Mean Sq.	Weight	Mean Sq.	Weight		
1	1	$\gamma_{\Delta H}$	2742.8	54.8%	131392.9	28.0%	41.4%	58.6%
2	2	$M_v$	741.9	14.8%	127006.1	27.1%	20.9%	37.7%
3	3	$\gamma_{q_e}$	65.7	1.3%	104919.2	22.4%	11.8%	25.8%
4	1x2	$\gamma_{ \Delta H } \times M_v$	567.7	11.3%	29627.8	6.3%	8.8%	17.0%
5	2x3	$M_v \times \gamma_{q_e}$	252.3	5.0%	21780.0	4.6%	4.8%	12.2%
6	1x3	$\gamma_{ \Delta H } \times \gamma_{q_e}$	0.2	0.0%	20768.1	4.4%	2.2%	9.9%
7	4	$c_a$	148.5	3.0%	6713.7	1.4%	2.2%	7.7%
8	5	$C_{p_v}$	145.7	2.9%	5616.9	1.2%	2.1%	5.7%
9	2x6	$M_v \times \rho_s$	138.3	2.8%	166.8	0.0%	1.4%	4.3%
10	3x7	$\gamma_{q_e} \times \rho_s$	87.2	1.7%	604.6	0.1%	0.9%	3.4%
11	6	$\lambda_f$	10.1	0.2%	6291.1	1.3%	0.8%	2.6%
12	2x5	$M_v \times C_{p_v}$	39.8	0.8%	2231.6	0.5%	0.6%	1.9%
13	2x4	$M_v \times c_a$	31.6	0.6%	1822.8	0.4%	0.5%	1.4%
14	2x6	$M_v \times \lambda_f$	3.0	0.1%	2281.9	0.5%	0.3%	1.2%
15	7	$\rho_s$	19.0	0.4%	36.4	0.0%	0.2%	1.0%
16	1x6	$\gamma_{ \Delta H } \times \lambda_f$	0.4	0.0%	1528.5	0.3%	0.2%	0.8%
17	8	$\epsilon_b$	0.7	0.0%	1408.2	0.3%	0.2%	0.6%

Please notice that in table IV.2, weights can only be compared by column (from one factor to another), not on rows. For instance, the higher weight on power density than on storage density does not mean the influence of  $|\Delta H|$  on power is stronger than the influence on storage density. It

Table IV.3 – Mean difference on outlet power density, heat storage density, charging time and system autonomy between sets of maximum and sets of minimum physical parameters value

Factor	Mean performance				Mean time difference			
	Power density		Stor. Density		on charge		on discharge	
	kW m <sup>-3</sup>	%	kWh m <sup>-3</sup>	%	abs.	rel.	abs.	rel.
1 $\gamma_{ \Delta H }$	3.2	39.7%	22.6	47.4%	43'59"	28.6%	08'18"	5.4%
2 $M_v$	1.7	21.2%	22.6	47.3%	1h01'25"	39.9%	2h02'42"	79.4%
3 $\gamma_{q_e}$	0.5	5.6%	20.2	42.3%	35'50"	23.3%	1h06'22"	43.0%
4 $c_a$	-0.8	-10.0%	-5.8	-12.0%	-10'42"	-7.0%	-03'41"	-2.4%
5 $C_{p_v}$	0.7	8.6%	4.7	9.8%	11'04"	7.2%	01'44"	1.1%
6 $\lambda_f$	-0.3	-4.0%	0.4	0.8%	14'42"	9.6%	02'19"	1.5%
7 $\rho_s$	-0.3	-3.1%	-5.0	-10.4%	-02'15"	-1.5%	1h12'18"	-46.8%
8 $\epsilon_b$	-0.1	-0.9%	-2.7	-5.7%	-08'06"	-5.3%	-08'29"	-5.5%

only reveals fewer contributions of others parameters in the case of power density. Table results are not extensively discussed here but are discussed factor by factor in following paragraphs with scatter plots analyses.

#### IV.2.2.1 Influence of differential heat of adsorption $|\Delta H|$

Strong influence of differential heat of sorption  $|\Delta H|$  on both storage density and power is more than expected. The highest  $|\Delta H|$  is, the more heat is released within the reactor. This directly influences maximum temperature and thus outlet power density and storage density. Figure IV.1a confirms this, by displaying heat storage density against outlet power density for all 256 simulations achieved at this stage. Among these 256 simulations, half were carried on with a low  $|\Delta H|$  value while the other half was carried with the high  $|\Delta H|$  value. A discrimination between low and high values clearly shows the influence of  $|\Delta H|$ . Table IV.3 shows there is a 39.7% increase in outlet power when  $|\Delta H|$  change from 50% to 150% of its default value. Increase in storage density is even greater (+47.4%).

A similar discussion can be held on time considerations. Figure IV.1b plots charging time against system autonomy (discharging time). This shows that, as expected, a higher  $|\Delta H|$  value also increases charging time (+28.6%) since more energy has to be provided to each adsorption site. At a constant inlet flowrate and inlet temperature, it necessarily takes longer to provide heat to the reactor. Same considerations are, however, not true for system discharge. In discharge mode, inlet flowrate provides water vapor to the system and retrieves heat. A higher  $|\Delta H|$  releases more heat without requiring more water vapor. Inlet vapor rate is then not affecting system performances. System autonomy then increases only by +5.4%, which means outlet flowrate is almost sufficient to carry additional heat away from the adsorbent bed.

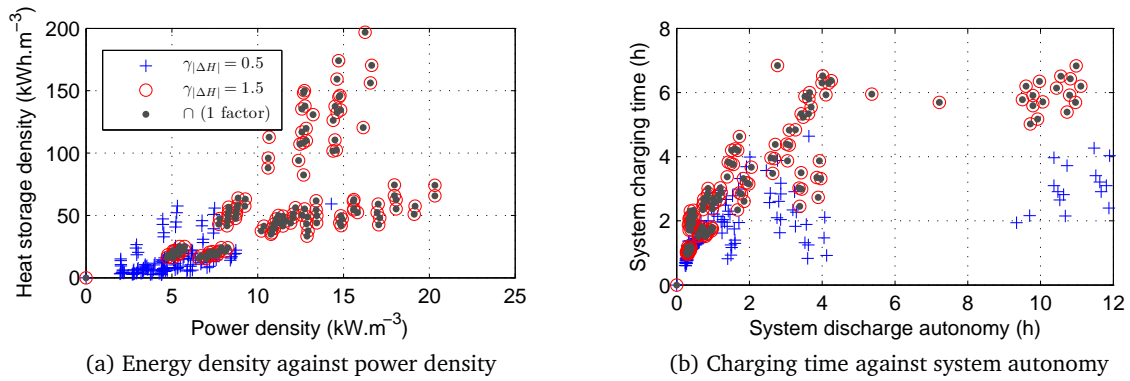


Figure IV.1 – Illustration of the influence of differential heat of adsorption  $|\Delta H|$  on energy storage density, outlet power density, charging time and system autonomy

#### IV.2.2.2 Influence of vapor molar mass $M_v$

The second most influencing parameter is vapor molar mass  $M_v$ . This parameter is very well known, precisely measured in literature and therefore not intended to vary if water is used as a fluid. But this parameter is used in the calculation of water vapor density  $\rho_v$ . It thus shows that vapor density strongly influences results. Figure IV.2a states high vapor density value increases power density by 21.2% and storage density by 47.3%. Figure IV.2b shows time characteristics also speak in favor of a high density value. Nevertheless, these considerations are very theoretical since molar mass of water is unchangeable, and another fluid can have some unpredictable behavior (starting from different adsorption properties) not taken into account in this thought. But again, the goal here is not to draw the ideal profile of hypothetical materials but only to point out what matters and what does not.

Gray points on figures IV.2a and IV.2b underline simulations results that were obtained with high heat of adsorption  $|\Delta H|$  and low vapor molar mass  $M_v$ . In others words, it is the intersection between best options for the first two factors under study.

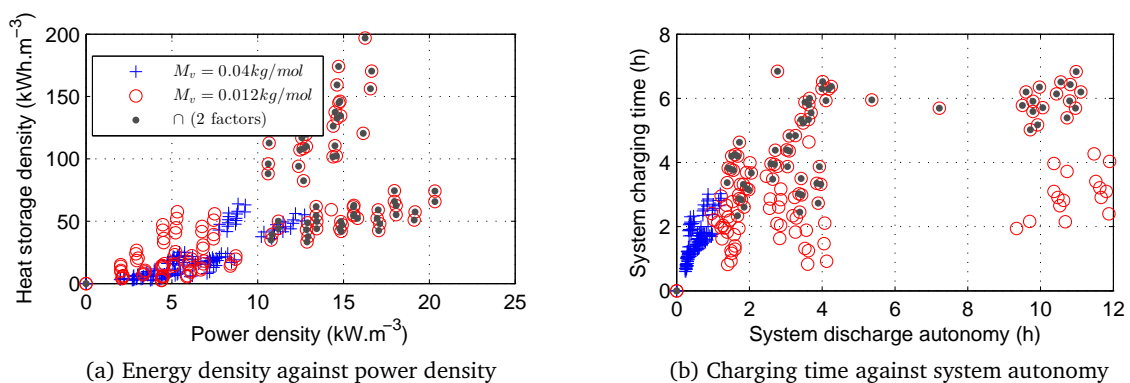


Figure IV.2 – Illustration of the influence of vapor molar mass  $M_v$  on energy storage density, outlet power density, charging time and system autonomy

### IV.2.2.3 Influence of adsorption equilibrium $\gamma_{q_e}$

Adsorption equilibrium is a function of fluid temperature and pressure. This is then not a direct parameter. In order to assess the influence of high or low equilibrium values on results, a weighting factor is used to artificially modify  $q_e$  value. Table IV.3 shows  $q_e$  has a stronger influence on storage density (+42.3% when  $q_e$  change from 50% to 150% of its default value) than on outlet power (+5.6%). Figure IV.3a confirms power density values are well distributed while the split on storage density values is quite clear. As stated in the dimensionless analysis (III.3), outlet power depends on the source term of energy conservation equation in the solid part (eq. II.8).

$$\text{Source term} = B_a (|\Delta H| - c_a T_s) \frac{\partial q}{\partial t} \quad (\text{IV.5})$$

$$= B_a (|\Delta H| - c_a T_s) k_m (\gamma_{q_e} q_e - q) \quad (\text{IV.6})$$

Multiplying  $q_e$  value by a factor  $\gamma_{q_e}$  will lead to a multiplication of instant adsorption ( $q$ ) average value with about the same amplitude. But this variation is slowed down by  $k_m$  value resulting in a lower amplitude in the variation of  $\frac{\partial q}{\partial t}$ . In others words, if  $\gamma_{q_e} > 1$ , the amplitude of variation of  $q$  is greater but happens in a greater amount of time, releasing more heat in the system in the end but not necessarily at a significantly faster rate. A direct consequence to greater amount of heat released at the same outlet power is a lengthening of discharging time. Figure IV.3b illustrates that high discharging times all occur for high  $q_e$  values. Moreover, a correlated effect to the increase of average  $q$  value is an increase in the  $\rho C_p|_s$  value, which also tends to limit solid temperature elevation by storing more heat within the material. This also works the other way around. With  $\gamma_{q_e} < 1$ , the diminution of  $\rho C_p|_s$  value combined with similar  $\frac{\partial q}{\partial t}$  values lead to high outlet power density values with very low storage capacities.

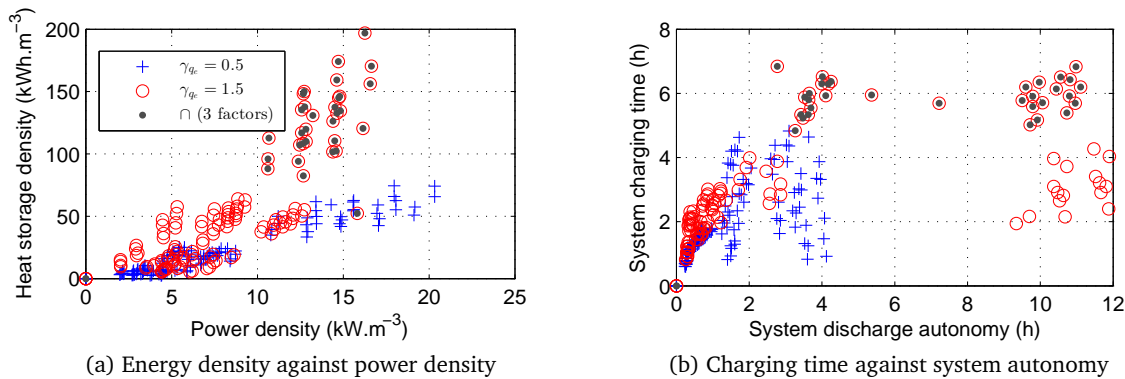


Figure IV.3 – Illustration of the influence of adsorption equilibrium value  $q_e$  on energy storage density, outlet power density, charging time and system autonomy

### IV.2.2.4 Influence of adsorbed layer heat capacity $c_a$

As stated in dimensionless analysis,  $c_a$  has a strong influence on heat releasable to the system. Indeed, a quantity  $|\Delta H|$  is released on adsorption. But this reaction requires to turn a water molecule from vapor to adsorbed state. Energy contained in the vapor phase is proportional to

the product between vapor heat capacity  $C_{p_v}$  and fluid temperature  $T_f$  while energy contained in the adsorbed layer is proportional to adsorbed layer heat capacity  $c_a$  and solid temperature  $T_s$ . An amount  $c_a T_s - C_{p_v} T_f$  has then to be provided to the water vapor to turn it into adsorbed phase. In others words, the net amount of heat released on adsorption is  $|\Delta H| - (c_a T_s - C_{p_v} T_f)$ . Consequently, the higher  $c_a$  is, the more energy is required to trigger adsorption reaction, the lower is net heat released. This is the sense of  $\Gamma$  dimensionless number in table III.7.

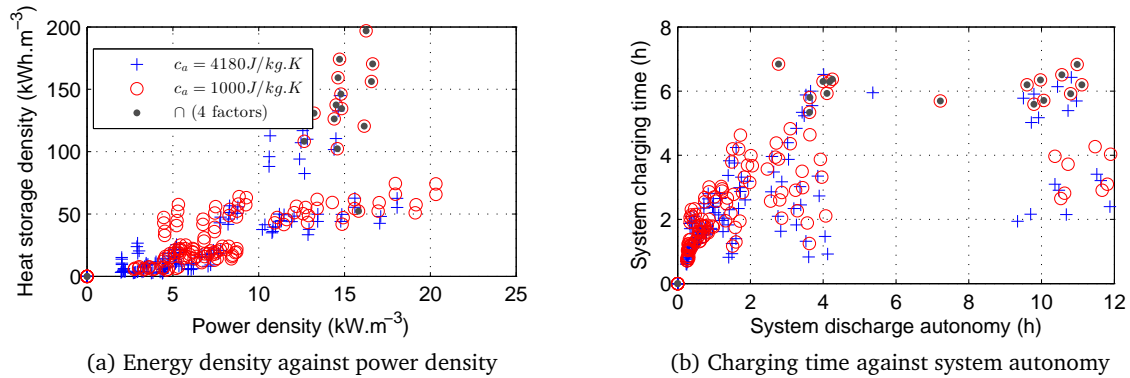


Figure IV.4 – Illustration of the influence of adsorbed layer heat capacity  $c_a$  on energy storage density, outlet power density, charging time and system autonomy

Figure IV.4a shows a lower  $c_a$  value is beneficial to both storage density (+12.0% from  $c_a = 4180 \text{ J kg}^{-1} \text{ K}^{-1}$  to  $c_a = 1000 \text{ J kg}^{-1} \text{ K}^{-1}$ ) and outlet power (+10.0%). Figure IV.4b shows the counterpart to more efficiency on energy conversion is a slightly longer charging time. It does not sound logical at first, but it actually is. On charging phase, heat provided to the storage tank is converted into desorption. The same energy gap  $|\Delta H|$  is required to desorb one molecule but this desorption will come up with more (high  $c_a$ ) or less (low  $c_a$ ) heat released to the system. This amount of useless heat is turned into useful heat by preheating downstream material. When more energy is given back, charging time is then shorter.

#### IV.2.2.5 Influence of water vapor heat capacity $C_{p_v}$

Experiments are carried on with a low value of  $C_{p_v} = 1000 \text{ J kg}^{-1} \text{ K}^{-1}$  and a high value of  $C_{p_v} = 4000 \text{ J kg}^{-1} \text{ K}^{-1}$ . The same comment than for water molar mass is necessary: the goal here is not to address the influence of small changes in water vapor mass to evaluate, for instance, the importance of taking into account its variation to temperature changes. The goal is to address the influence of fluid heat capacity in order to investigate the opportunity to use another fluid.

Results from table IV.3 and figure IV.5 show vapor heat capacity influences energy storage density (+9.8%) and outlet power (8.6%). The same considerations than for the interpretation of adsorbed layer heat capacity influence are relevant. With a higher  $C_{p_v}$  value and the same inlet temperature, energy gap from vapor to adsorbed phase is lower. Net heat released on adsorption is consequently greater.

It also influences charging time (+7.2%) without changing much discharging time (+1.0%). The same interpretation than for  $M_v$  seems relevant. A more efficient energy conversion retains

more energy in the adsorbent material in charging mode. As heat is provided at the same rate, charging time is increased. On discharge, the same amount of water vapor is required to release more heat, which explains why energy storage and power performances are enhanced without impacting system autonomy.

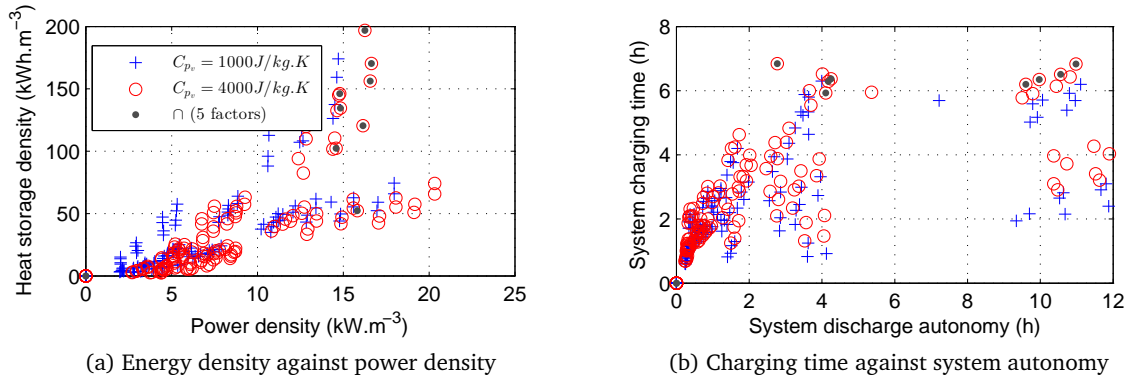


Figure IV.5 – Illustration of the influence of water vapor heat capacity  $C_{pv}$  on energy storage density, outlet power density, charging time and system autonomy

#### IV.2.2.6 Influence of fluid thermal conductivity $\lambda_f$

In this study, fluid thermal conductivity was exaggeratedly varied from a very low ( $0.025 \text{ W m}^{-1} \text{ K}^{-1}$ ) to a very high value ( $1.0 \text{ W m}^{-1} \text{ K}^{-1}$ ). This very wide variation does not lead to significant changes in outlet power or storage densities. As explained in the sensitivity analysis, two heat transport mechanisms are coexisting. Diffusion, that does not require mass transport and that is proportional to  $\lambda_f$ , and advection that rely on mass transport (and hence fluid velocity). On charging or discharging modes, advection term is about 500 times greater than diffusion. This is then not surprising that it does not influence much results ( $-4.0\%$  on power and  $+0.8\%$  on storage density with a high level value 40 times bigger than the low level value).

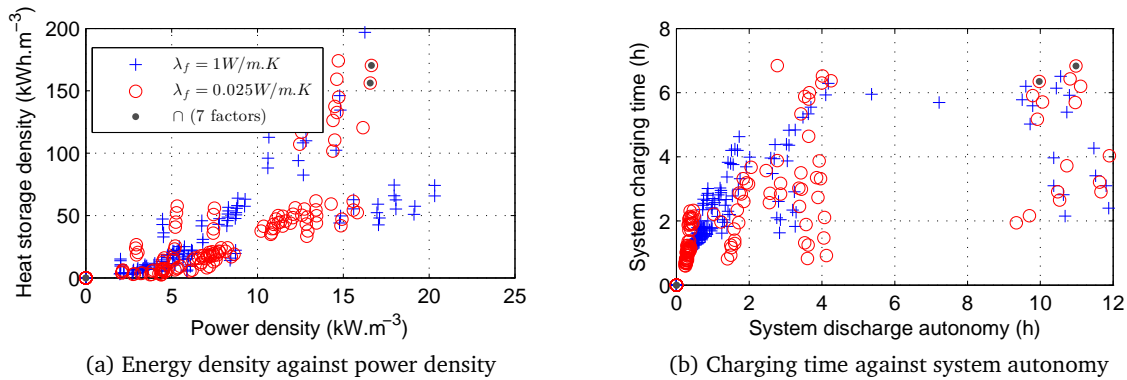


Figure IV.6 – Illustration of the influence of fluid thermal conductivity  $\lambda_f$  on energy storage density, outlet power density, charging time and system autonomy

### IV.2.2.7 Influence of solid density $\rho_s$

Investigations on the solid density influence have been conducted with a low level value of  $600\text{kg m}^{-3}$  and a high level value of  $1500\text{kg m}^{-3}$ . Table IV.3 shows  $\rho_s$  has a quiet low influence on outlet power ( $-3.1\%$  from low level to high level value) but has a stronger influence on storage density ( $-10.4\%$ ). A greater solid density tends to limit the temperature drop within the solid and hence the temperature drop within the fluid. This explains why outlet power is limited by high solid densities. For what energy density is concerned, solid density influences the charging phase. Indeed, for a given inlet fluid temperature, a higher solid density limits temperature drop within the solid. A lower temperature leads to a lower desorption state and hence to a lower charging state.

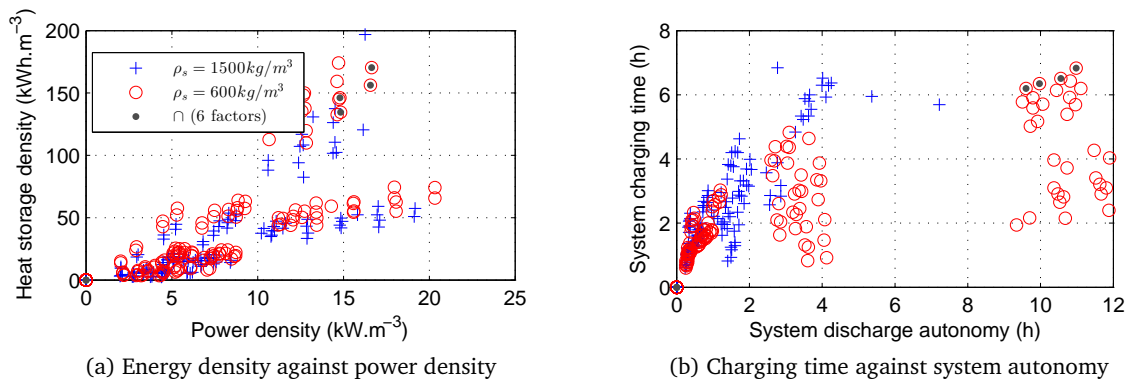


Figure IV.7 – Illustration of the influence of solid density  $\rho_s$  on energy storage density, outlet power density, charging time and system autonomy

### IV.2.2.8 Influence of bed porosity $\epsilon_b$

Bed porosity influence is investigated with low level value  $\epsilon_b = 0.32$  and high level value  $\epsilon_b = 0.40$ . Table IV.3 and figure IV.8a show that the influence of  $\epsilon_b$  on outlet power is quiet negligible ( $-0.9\%$ ) while it is more important on storage density ( $-5.7\%$ ).  $\epsilon_b$  has a direct influence on fluid/solid volume ratio, and also on the exchange surface between fluid and solid. A higher  $\epsilon_b$  value tends to lower exchange surface, to increase fluid volume and to decrease solid volume. As the number of adsorption sites is proportional to solid density (to the bed scale), an increase in  $\epsilon_b$  naturally leads to a decrease in system performances. Since less adsorption sites are available, a shorter charging time ( $-5.3\%$  and a shorter system autonomy ( $-5.5\%$ ) is relevant.

## IV.2.3 Conclusion on the influence and optimization of material properties

Influence of eight physical parameters on outlet power, energy storage density and system autonomy have been addressed. Interpretation of model behavior shows results seem consistent. It tends to strengthen trust in this numerical model. Parameters have been ranked by order of influence. The following conclusions can be listed.

- Differential heat of sorption  $|\Delta H|$  is to be maximized.

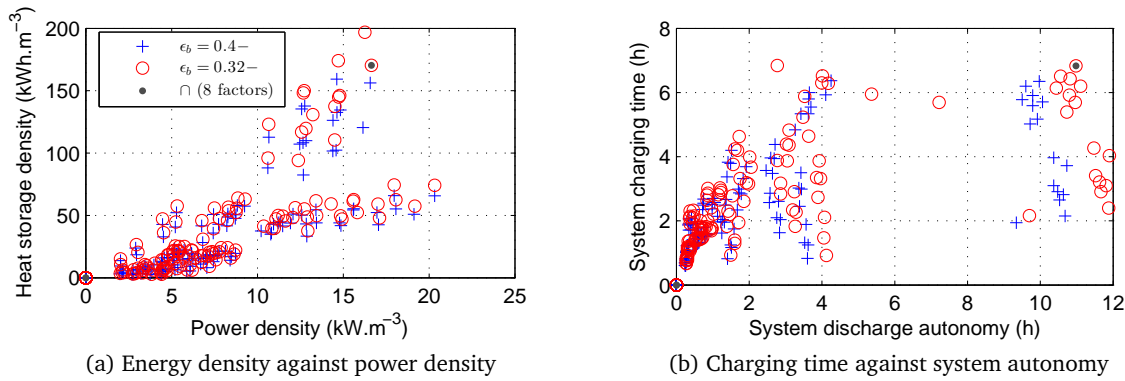


Figure IV.8 – Illustration of the influence of bed porosity  $\epsilon_b$  on energy storage density, outlet power density, charging time and system autonomy

- Fluid density is also to be maximized for power, energy storage and system autonomy enhancement.
- Adsorption capacity  $q_e$  is of course a key parameter that is also to be maximized. Nevertheless, as  $|\Delta H|$  decreases with adsorbed capacity (see figure II.10), highest outlet power densities are obtained at low  $q_e$  values to the detriment of storage density.
- The difference between vapor heat capacity  $C_{p_v}$  and adsorbed layer heat capacity ( $c_a$ ) is to be minimized.
- Solid density  $\rho_s$  is to be minimized if it is not to the detriment of adsorption properties.
- A lower bed porosity enhance solid proportion and exchange surface and is thereby beneficial to system performances.

### IV.3 Optimization of operating conditions and system geometry

Operating conditions are all controllable parameters that define the adsorbent bed boundary conditions. Five parameters have been identified as important operating conditions:

- inlet flowrate on charge  $\dot{Q}_{in,charge}$  (and hence fluid velocity  $v_{in,charge}$ ),
- inlet flowrate on discharge  $\dot{Q}_{in,discharge}$  (and hence fluid velocity  $v_{in,discharge}$ ),
- charging temperature  $T_{in,charge}$ ,
- charging humidity ratio  $\varphi_{in,charge}$ ,
- discharging humidity ratio  $\varphi_{in,discharge}$ ,

Besides, volume and shape of the adsorbent bed necessarily have an influence on energy density, power density and system autonomy. It seems coherent to carry out operating conditions study and geometrical study together, since it can influence one another. Influences of bed length  $L_z$  and cross section area  $S$  are thus also investigated.

A  $2^7$  full factorial design is conducted. It leads to 128 numerical simulations. Results are tapped by three possible ways.

- Analyse of variance, which provides information on factor ranking and dependence to one another (table IV.4).
- A factor-by-factor analyse with scatter plots and numerical calculation of mean differences between sets of results obtained with the low value and the high value (table IV.5 and figures IV.9 to IV.11).
- A statistical study of results in order to come up with a regression model that enable a quick estimation of the objective function. This part of the work is developed in the next section IV.4.

Furthermore, some additional experiments can be conducted if a specific point has to be addressed and  $2^k$  factorial design is not able to provide any answer.

Results of the analyses of variance are displayed in table IV.4 in ranked order. The main outcome of this step is to rank parameters influence for the next step. Results analyses are provided alongside analyses of scatter plots drawn for each factor.

### IV.3.1 Influence of inlet relative humidity $\varphi_{in}$ (on both charge and discharge)

Inlet relative humidity has a strong influence on results on both charge and discharge phases. As explained in the first chapter, an adsorption heat storage system does not store heat directly but store an hydration potential. In charge, the objective is to dehydrate the porous medium as far as possible. In discharge, it is to hydrate it as far as possible. Heat releasable is directly correlated to the gap between full dehydration state and full hydration state. A decrease in inlet humidity ratio on charge (or an increase on discharge) will increase the gap and then naturally lead to a higher storage capacity and higher heat power. Figures IV.9a (charge) and IV.9c (discharge) confirm heat storage density is clearly correlated to inlet relative humidity. Table IV.5 provides numerical estimation, for each factor under study, of the mean difference between results obtained with the high value and results obtained with the low value. In the present case, it states respectively a  $13.2 \text{ kWh m}^{-3}$  (17.9%) and  $12.4 \text{ kWh m}^{-3}$  (16.8%) storage density difference for charge and discharge inlet relative humidity. Outlet power density is also changed in about the same proportions (12.5% on charge and 17.9% on discharge).

Nevertheless, it is important to notice that relative humidity is at once a practical units and a source of confusion. Indeed, it is defined as the ratio between partial vapor pressure and saturated vapor pressure, which strongly depends on temperature.

$$\varphi = \frac{P_v}{P_{v_{sat}}(T_f)} \quad (\text{IV.7})$$

A 30% relative humidity at  $20^\circ\text{C}$  is, for instance, the same absolute humidity (or partial vapor pressure) than 0.07% relative humidity at  $180^\circ\text{C}$ . It means inlet relative humidity is to

Table IV.4 – Analysis of variance on outlet power density and heat storage density, for different operating conditions

Factor			Power density		Energy density		Overall weight	Left over
			Mean Sq.	Weight	Mean Sq.	Weight		
1	1	$\varphi_{in,charge}$	1187.9	1.5%	22256.1	43.9%	22.7%	77.3%
2	2	$\varphi_{in,discharge}$	4467.8	5.5%	19706.2	38.8%	22.2%	55.1%
3	3	$L_z$	28697.4	35.6%	534.1	1.1%	18.3%	36.8%
4	4	$v_{in,discharge}$	28782	35.7%	342.9	0.7%	18.2%	18.6%
5	3x4	$L_z \times v_{in,charge}$	10752.4	13.4%	51.4	0.1%	6.7%	11.9%
6	1x5	$\varphi_{in,charge} \times T_{f,in,charge}$	91.7	0.1%	4342.1	8.6%	4.3%	7.5%
7	5	$T_{f,in,charge}$	1198.8	1.5%	1847.7	3.6%	2.6%	5%
8	2x4	$\varphi_{in,discharge} \times v_{in,charge}$	1670.8	2.1%	274.8	0.5%	1.3%	3.7%
9	2x3	$\varphi_{in,discharge} \times L_z$	1667.5	2.1%	40.2	0.1%	1.1%	2.6%
10	3x5	$L_z \times T_{f,in,charge}$	529.6	0.7%	82.3	0.2%	0.4%	2.2%
11	1x3	$\varphi_{in,charge} \times L_z$	496.7	0.6%	87	0.2%	0.4%	1.8%
12	6	$v_{in,charge}$	3.5	0.0%	337.4	0.7%	0.3%	1.5%
13	3x6	$L_z \times v_{in,discharge}$	3.3	0.0%	331.4	0.7%	0.3%	1.1%
14	4x5	$v_{in,charge} \times T_{f,in,charge}$	442.1	0.5%	34.3	0.1%	0.3%	0.8%
15	2x5	$\varphi_{in,discharge} \times T_{f,in,charge}$	48.3	0.1%	268.4	0.5%	0.3%	0.5%
16	1x6	$\varphi_{in,charge} \times v_{in,charge}$	446.1	0.6%	0.3	0.0%	0.3%	0.2%
21	7	$S$	0.1	0.0%	0.5	0.0%	0.0%	0.0%

be compared at the same temperature in order to feel the humidity difference between charge and discharge. But representing humidity as a percentage of vapor saturation is also practical to check for consistency and for limit values.

Besides, figures IV.9b shows inlet humidity on charge influences both charging and discharging time, while figure IV.9d shows inlet relative humidity on discharge influences only discharging time. Since numerical experiments are conducted on a charge-discharge cycle, this statement is not surprising. Lower relative humidity on charge leads to longer charging time since boundary conditions are further from initial conditions. More time is then required to reach steady-state. Drying out the inlet charging fluid from 0.5% to 0.1% increases system autonomy by 11.8% on average. Humidifying inlet fluid on discharge from 50% to 80% increases system autonomy by 18.1% on average. It also increases outlet power density (+24.2% and storage density (+16.8%)

### IV.3.2 Influence of inlet fluid velocity $v_{in}$ (on both charge and discharge)

Inlet fluid velocity is an operating condition that has a strong influence on system behavior and can be easily adjusted.

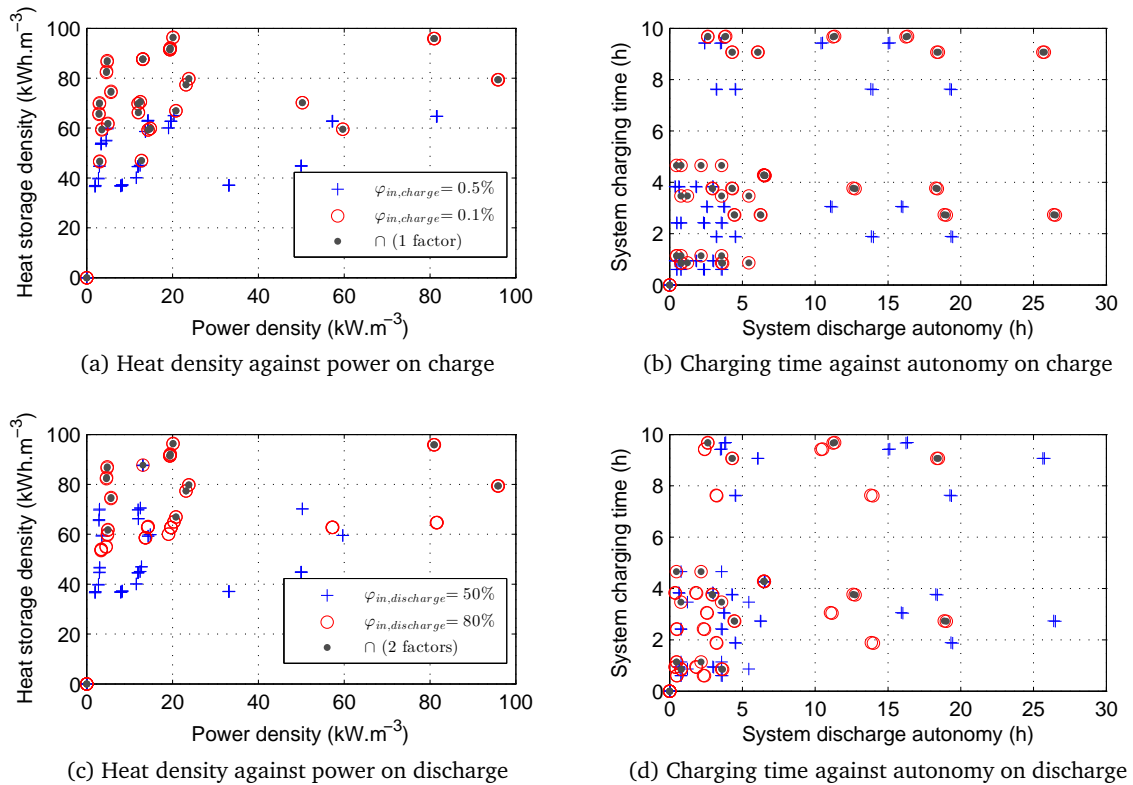


Figure IV.9 – Illustration of the influence inlet relative humidity on energy storage density, outlet power density, charging time and system autonomy

Table IV.5 – Mean difference on outlet power density, heat storage density, charging time and system autonomy between sets of maximum and sets of minimum operating conditions parameter value

Factor	Mean performance difference				Mean time difference			
	Power density		Stor. density		on charge		on discharge	
	$\text{kW m}^{-3}$	%	$\text{kWh m}^{-3}$	%	abs.	rel.	abs.	rel.
1 $\varphi_{in,charge}$	-3.0	-12.5%	-13.2	-17.9%	-20'52"	-8.5%	-43'17"	-11.8%
2 $\varphi_{in,discharge}$	5.9	+24.2%	12.4	+16.8%	0"	0.0%	1h06'23"	+18.1%
3 $L_z$	-15.0	-61.3%	-2.0	-2.8%	1h49'58"	+45.0%	4h10'28"	+68.1%
4 $v_{in,discharge}$	15.0	+61.4%	1.6	+2.2%	0"	+0.0%	3h'49'25"	-62.4%
5 $T_{in,charge}$	-3.1	-12.5%	3.8	+5.1%	-29'23"	-12.0%	1h02'07"	+16.9%
6 $v_{in,charge}$	0.17	+0.7%	1.6	+2.2%	2h11'59"	-54.1%	7'23"	+2.0%
7 $S$	0.02	+0.1%	0.07	+0.1%	24"	+0.2%	-1'51"	-0.5%

- Figure IV.10a displays the influence of  $v_{in,charge}$  on storage characteristics with a set of results at  $0.04\text{ m s}^{-1}$  and a set at  $0.17\text{ m s}^{-1}$  (which is respectively equivalent to  $60\text{ m}^3\text{ h}^{-1}$  and  $250\text{ m}^3\text{ h}^{-1}$  in default conditions). It shows that the inlet fluid velocity influence is quite negligible on both energy storage density (+2.2%) and power (+0.7%). This slight positive influence is nonetheless explained by an increase in mass transfer coefficient with velocity increase, which tend to enhance full charging state.
- Furthermore, figure IV.10b shows that the charging time strongly depends on  $v_{in,charge}$ . It means inlet velocity is a limiting factor to global heat and mass transfer. Increasing inlet fluid velocity increases heat provided to the system and also increases the capacity to retrieve water molecules from the system. This mainly has an impact at a bed scale (within beads interstices) but it also enhances heat and mass transfer within beads. This leads to a slightly better charging state. Indeed, as shown in table IV.5, a higher inlet fluid velocity on charge also increases storage density (+2.0%), outlet power (+0.7%) and system autonomy (+2.0%).
- Figure IV.10c displays the influence of  $v_{in,discharge}$  on storage characteristics. It shows outlet power is strongly influenced by fluid velocity (+61.4% from  $60\text{ m}^3\text{ h}^{-1}$  to  $250\text{ m}^3\text{ h}^{-1}$  equivalent). The same mechanisms than for charging phase are evoked. An increase in inlet fluid velocity on discharge increases the amount of water vapor in the system. As reaction kinetic is fast enough and bed long enough to adsorb all incoming water molecules, adsorption sites are filled at a faster pace, and more heat is retrieved from the reactor. It has nonetheless no great influence on storage capacity (+2.2% due to heat and mass transfer enhancement in macropores). Heat is then retrieved at a faster pace without changing much the total amount of heat releasable. This has necessarily a great influence on discharging time, as confirmed by figure IV.10d. An increase in inlet fluid velocity leads to a decrease in system autonomy in the same proportions than power increase (−62.4%).

These results are in scope with experimental observations made during the STAID project [Johannes et al. \(2015\)](#).

### IV.3.3 Influence of charging inlet temperature $T_{in,charge}$

Adsorption equilibrium depends on temperature and vapor pressure. At high temperature, molecular agitation is higher, and adsorbed layer density lower. Inlet temperature on charge has then a strong influence on adsorption equilibrium and hence system charge. A higher charging temperature is expected to allow a dryer final charging state. This tends to increase the water molecules gap from charge to discharge and hence increases storage density and system autonomy. Figure IV.11c displays heat storage density and outlet power density against charging temperature for 15 points ranging from  $110\text{ }^\circ\text{C}$  to  $180\text{ }^\circ\text{C}$ . It shows heat storage density linearly increases by +61.5% within this temperature range. Outlet power density is also slightly increasing (+3.2%), but not linearly. An asymptotic behavior is observed from  $160\text{ }^\circ\text{C}$ . The variation is anyway negligible and is exaggerated with a rescale of the right axis of figure IV.11c. Increasing inlet temperature also

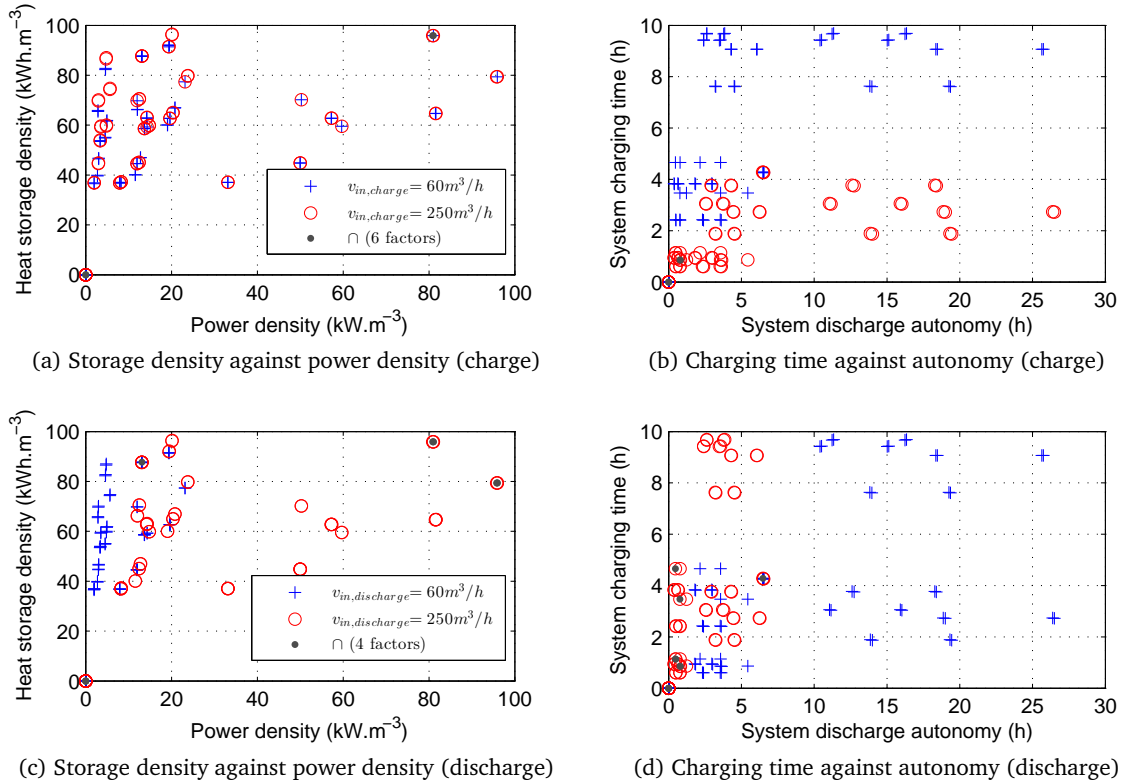


Figure IV.10 – Illustration of the influence of inlet fluid velocity  $v_{in}$ , on energy storage density, outlet power density, charging time and system autonomy

reduces charging time ( $-12\%$  from  $110^\circ\text{C}$  to  $180^\circ\text{C}$ ) while increasing system autonomy ( $+86.2\%$  in default conditions) according to figure IV.11d).

Nevertheless, what is observed with default conditions (except charging temperature) in figures IV.11c and IV.11d is surprisingly different from observations from figures IV.11a and IV.11b and from table IV.5. A closer look to axis scales shows default conditions are limited to the 20% lower values of power density and system autonomy values of figures IV.11a and IV.11b. System behavior looks different with a different set of parameter. It confirms information from table IV.4 that states that factor interactions have a strong influence on results. In others words, influence of charging temperature is not only directly predictable but also depends on others parameters values.

For instance, according to table IV.4, interaction between  $\varphi_{in,charge}$  and  $T_{f,in,charge}$  has a stronger influence on results than charging temperature alone. This is actually more a mathematical issue than a physical one. In the  $2^k$  full factorial design, inlet conditions that are varied are relative humidity  $\varphi$  and inlet temperature  $T_{f,in}$ . Setting both  $\varphi_{in}$  and  $T_{in}$  introduces a constraint on vapor pressure value  $p_{v,in}$ .

$$\varphi_{in} = \frac{p_{v,in}}{p_{v,sat}(T_{in})} \Rightarrow p_{v,in} = \varphi_{in} \times p_{v,sat}(T_{in}) \quad (\text{IV.8})$$

Saturating vapor pressure is a non linear function of temperature. A change in temperature will have non linear repercussion on inlet vapor pressure to maintain relative humidity to its setting

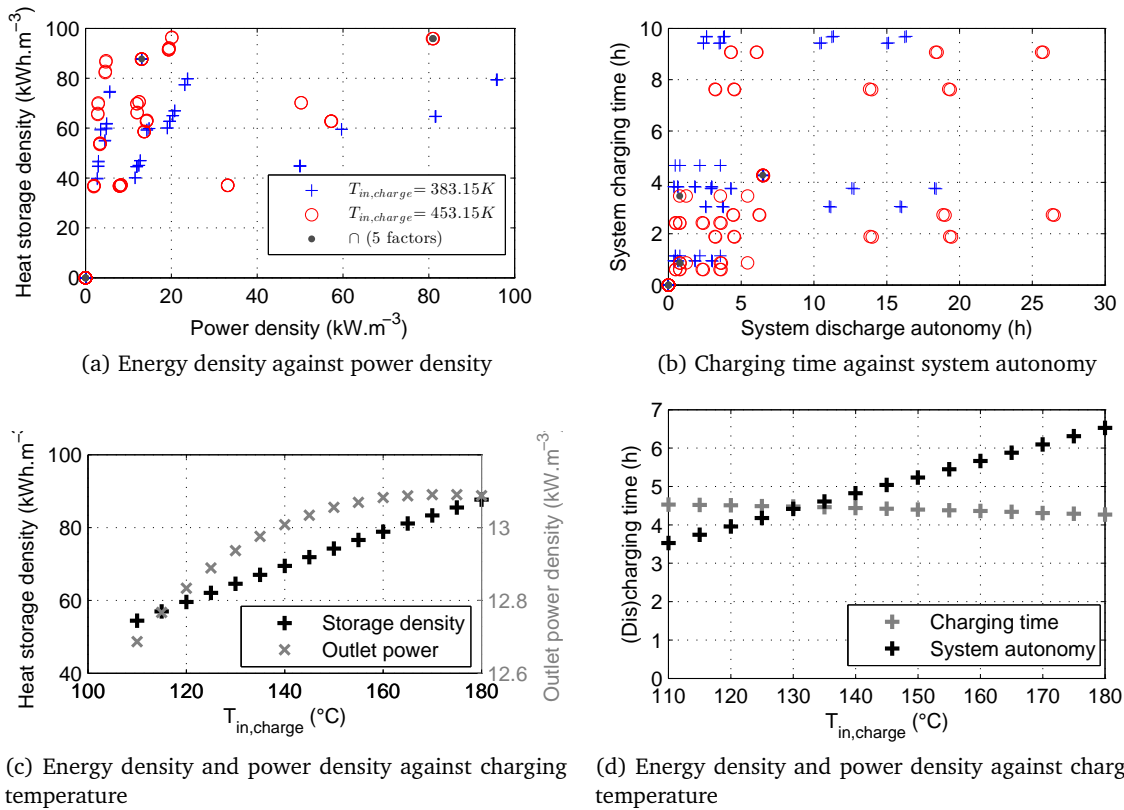


Figure IV.11 – Illustration of the influence of inlet fluid temperature  $T_{in,charge}$  during charge, on energy storage density, outlet power density, charging time and system autonomy

value. The main contribution of  $T_{in}$  is then not sufficient to describe effects on results which explains why interaction contribution is high.

Why then, is there a linear dependence of storage density to inlet temperature in figure IV.11c? Because in this case, all parameters are set to their default value except inlet temperature. There is only one linear variation in inlet boundary conditions, that besides seems to produce linear consequences on results.

As a conclusion, if the results on the influence of inlet temperature seem to lack of consistency, it is only due to nonlinear solicitations that follow the use of relative humidity as a setting parameter in place of absolute quantities such as vapor pressure or humidity ratio.

### IV.3.4 Influence of bed length $L_z$ and cross section area $S$

Bed geometry, defined with bed length  $L_z$  and cross section area  $S$ , is investigated jointly for sake of coherence.

- Figure IV.12a displays storage density against power density for a short bed ( $L_z = 10$  cm) and for a long bed ( $L_z = 40$  cm). Results clearly show a strong correlation between bed length and outlet power density. A shorter bed provides higher power density (+61.3% from 40 cm to 10 cm). Influence on heat storage density is only 2.8%.
- Figure IV.12c displays storage density against power density for a narrow bed ( $S = 0.2$  m<sup>2</sup>)

and for a large bed ( $S = 0.8\text{m}^2$ ). Results show, and numerical results of tables IV.4 and IV.5 confirm, that cross section area has no influence at all on results. Please note at this step that velocity conditions are imposed. Volume airflow rate is then set according to cross section area and velocity.

These observations enable the following conclusions. Outlet power density varies a lot with bed length and doesn't vary at all with cross section area. But a change on these two geometrical parameters introduces a change in volume conditions. It then means that the volume change caused by bed length change is not compensated by a change on absolute outlet power. In others words, outlet power is not sensible to bed length variation. On the contrary, a change in volume caused by a change on cross surface area is compensated by a change in absolute outlet power so that outlet power density remains constant. It means outlet power density is directly proportional to cross section area.

The same argument construction is developed to show that a constant heat storage *density* on volume variation means heat storage *capacity* (kWh) is directly proportional to the storage tank volume.

Besides, important observations can also be made on time characteristics.

- Figure IV.12b displays charging time against system autonomy for two different bed lengths. It shows that a longer adsorbent bed (40 cm vs. 10 cm) strongly increases both charging time (+45%) and system autonomy (+68.1%).
- Figure IV.12d displays the same graph for two different values of cross section area. It shows changing cross section area has no influence on neither charging time (+0.2%) nor system autonomy (−0.5%). Again, it is important to notice that volume airflow rate is calculated accordingly to set fluid velocity under a given cross section area.

These observations show system autonomy does not depend on adsorbent bed volume but only on its length. This is quite understandable when it is stated that adsorption or desorption occurs on a sharp front.

Observations tells autonomy depends on bed length, power on cross section area and storage capacity on storage tank volume. But it is still unknown if these variations are linear or not. To answer this question, a set of experiments was conducted under different geometries. Bed length was varied from 10 cm to 50 cm (step 10 cm). Cross section area was varied from  $0.2\text{m}^2$  to  $0.8\text{m}^2$  (step  $0.1\text{m}^2$ ). All 35 possible combinations were run. Results are displayed in figure IV.13.

- Figure IV.13b shows energy storage capacity is directly proportional to storage tank volume, which is logical since flow pattern is uniformly distributed. No dead zones are introducing asymmetry in the use of the entire bed volume.
- Figure IV.13a states outlet power is directly proportional to cross section area. Again, the assumption of a uniformly distributed flow pattern amplify this observation. But it is generally true if wall effects are neglected.

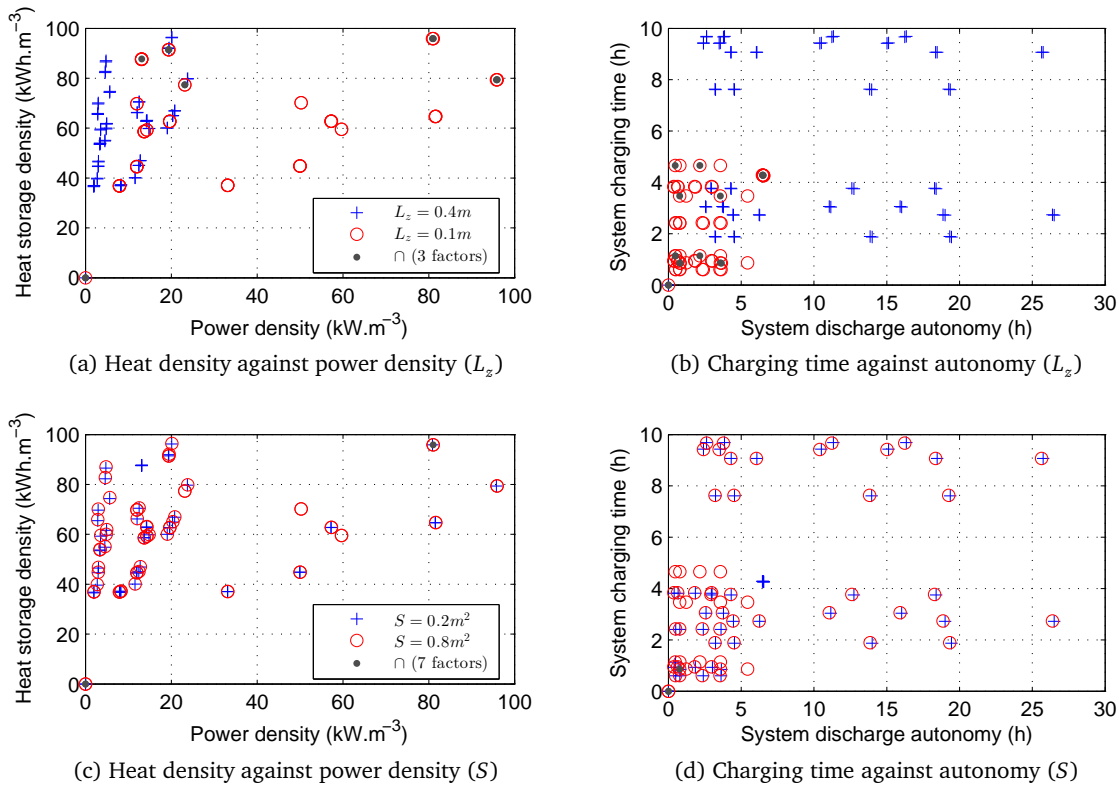


Figure IV.12 – Illustration of the influence of bed length  $L_z$  and cross section area  $S$  on energy storage density, outlet power density, charging time and system autonomy

- Figures IV.13c and IV.13d state a linear dependence of charging and discharging time to bed length. It confirms that adsorption and desorption occur on a sharp front otherwise side effect would be noticed for very short bed length.
- Figure IV.13d also provides an estimation of pressure drop across the bed, as a function of bed length. Increasing bed length linearly increases pressure drop. This is leading to over-consumption of fan devices. It is thus probably smarter to reach system autonomy by considering a multiplication of parallel modules than a prolongation of bed length.

Important conclusions are drawn from the study of system response to different geometries.

- **Outlet power** is directly proportional to **cross section area**,
- **Heat storage capacity** is directly proportional to **storage tank volume**,
- **System autonomy** is directly proportional to **bed length**.

These observations show that it is therefore appropriate to talk about heat storage density (unit:  $\text{kWh m}^{-3}$ ) in system performance specifications. Outlet power density (unit:  $\text{kW m}^{-3}$ ) is less relevant than outlet power surface density (unit:  $\text{kW m}^{-2}$ ) to compare system performances from one to another. In the same way, system autonomy (unit: s) would better be expressed relatively to bed length as lineic autonomy (unit:  $\text{s m}^{-1}$ ).

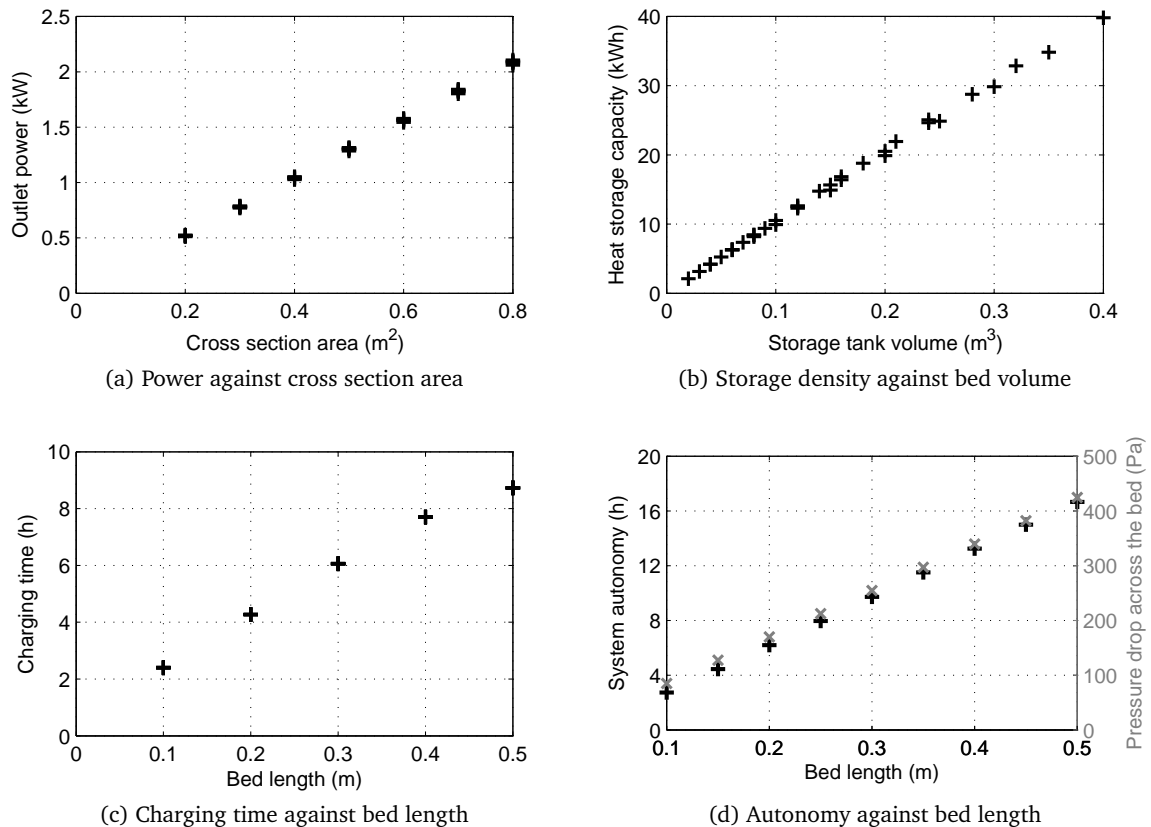


Figure IV.13 – Linear distributions of outlet power against cross section area, heat storage capacity against storage tank volume, and charging time and autonomy against bed length

### IV.3.5 Conclusion on the influence and optimization of operating conditions

The influence of operating conditions on system performances have been investigated and provide the following guideline.

- The difference between **inlet relative humidity** on charge and discharge is to be maximized to enhance outlet power, energy density and system autonomy. Indeed, it maximizes the water uptake between full charge and full discharge.
- The **inlet fluid velocity** has obviously a great influence on time characteristics. A greater fluid velocity on charge mostly reduce the charging time. A greater fluid velocity on discharge strongly increases outlet power to the cost of system autonomy, with a negligible improvement of storage capacity.
- The **charging temperature** has a strong influence on storage density and system autonomy while the influence on outlet power and charging time is negligible.

## IV.4 Development of a metamodel

Metamodeling techniques have been developed from many different disciplines as surrogate of the expensive simulation process, in order to improve the overall computation efficiency. They are then found to be a valuable tool to support design optimization. Different metamodels exist: polynomial, splines, multivariate adaptive regression splines, Kriging, artificial neural network, etc (Kuznik et al., 2015a). Here, a polynomial model has been chosen. Coefficients are calculated from numerical results of a  $2^k$  full factorial design.

A  $2^k$  factorial design comes up with a  $n$ -by- $k$  solicitation matrix  $X$  of  $k$  predictors (or variables) and  $n$  observations (or runs), and with a  $n \times 1$  vector of responses  $y$ . Of course, vector  $y$  can take different values depending on the response variable under study.

For instance, if there are three variables  $x_1$ ,  $x_2$  and  $x_3$ , the  $2^3$  full-factorial design provides the following solicitation plan  $X$ . Results of the eight experiments are concatenated into vector  $y$ .

$$X = \begin{matrix} & \begin{matrix} x_{1i} & x_{2i} & x_{3i} \end{matrix} \\ \begin{matrix} -1 & -1 & -1 \\ -1 & -1 & 1 \\ -1 & 1 & -1 \\ -1 & 1 & 1 \\ 1 & -1 & -1 \\ 1 & -1 & 1 \\ 1 & 1 & -1 \\ 1 & 1 & 1 \end{matrix} & \end{matrix} \quad (\text{IV.9})$$

$$y = \begin{matrix} y_i \\ y_1 \\ y_2 \\ y_3 \\ y_4 \\ y_5 \\ y_6 \\ y_7 \\ y_8 \end{matrix} \quad (\text{IV.10})$$

It is possible to find a polynomial function with  $2^k$  coefficients and  $2^k$  independent variables that fits the  $2^k$  response values  $y_i$ . This polynomial is of the form:

$$y_i = \sum_{j=1}^{2^k} \alpha_j x_{ji} \quad (\text{IV.11})$$

where  $x_{ji}$  are:

- $k$  main factors  $x_{1i}, x_{2i}, \dots, x_{ki}$ ,
- cross interactions between two factors  $x_{1i} \times x_{2i}, \dots, x_{1i} \times x_{ki}$ ,
- cross interactions between three factors  $x_{1i} \times x_{2i} \times x_{3i}, \dots, x_{1i} \times x_{(k-1)i} \times x_{ki}$ ,
- ...,
- 1 cross interaction between  $k$  factors  $x_{1i} \times x_{2i} \times \dots \times x_{ki}$ .

The  $2^k (= n)$  coefficients can be determined by solving a system of  $n$  equations with  $n$  un-

knowns.

$$\begin{cases} y_1 = \sum_{j=1}^{2^k} \alpha_j x_{j1} \\ y_2 = \sum_{j=1}^{2^k} \alpha_j x_{j2} \\ \dots \\ y_n = \sum_{j=1}^n \alpha_j x_{jn} \end{cases} \quad (\text{IV.12})$$

The *fit* function of *LinearModel* class from *Matlab*<sup>®</sup> Statistics Toolbox enables a calculation of the  $n$  coefficients  $\alpha_j$  configuring a **linear regression model**. With  $k = 3$  it gives the following model of eight coefficients (equation IV.13).

$$y_i = \alpha_1 + \alpha_2 x_{1i} + \alpha_3 x_{2i} + \alpha_4 x_{3i} + \alpha_5 x_{1i} \times x_{2i} + \alpha_6 x_{1i} \times x_{3i} + \alpha_7 x_{2i} \times x_{3i} + \alpha_8 x_{1i} \times x_{2i} \times x_{3i} \quad (\text{IV.13})$$

These fitting models are very good tools for sizing purposes. But it is not very convenient to use a  $n$ -coefficient polynomial. For sake of simplification, it is possible to reduce the fitting model to most influencing coefficients without affecting much prediction precision.

The model error can be defined as the sum (over the  $n$  runs) of the squared differences between the metamodel and the numerical response. For the full model with  $n$  coefficients, the error is null, by definition (equation IV.14).

$$\epsilon_n^2 = \sum_{i=1}^n \left( \sum_{j=1}^n \alpha_j x_{j,i} - y_i \right)^2 = 0 \quad (\text{IV.14})$$

If only  $m$  terms among the  $n$  initial terms are kept ( $m < n$ ), an error is made by the fact that  $n - m$  terms are disregarded.

$$\epsilon_m^2 = \sum_{i=1}^n \left( \sum_{j=1}^m \alpha_j x_{j,i} - y_i \right)^2 \quad (\text{IV.15})$$

$$= \sum_{i=1}^n \left( y_i - \sum_{j=m+1}^n \alpha_j x_{j,i} - y_i \right)^2 \quad (\text{IV.16})$$

$$= \sum_{i=1}^n \left( \sum_{j=m+1}^n \alpha_j x_{j,i} \right)^2 \quad (\text{IV.17})$$

Starting from this definition of truncated error, it is possible to demonstrate that  $\epsilon_m^2 \geq \epsilon_{m+1}^2$  by playing with the properties of a  $2^k$  full factorial design made of  $-1$  and  $1$ . For instance,  $\sum_{i=1}^n x_{j,i}$  is null for any value of  $j$  ( $1 \geq j \geq n$ ). The basic idea consists in expressing  $\epsilon_m^2$  as a function of  $\epsilon_{m+1}^2$ , and to show that the remainder term is positive.

$$\begin{aligned}\epsilon_m^2 &= \sum_{i=1}^n \left( \sum_{j=m+1}^n \alpha_j x_{j,i} \right)^2 \\ &= \sum_{i=1}^n \left( \alpha_{m+1} x_{m+1,i} + \sum_{j=m+2}^n \alpha_j x_{j,i} \right)^2\end{aligned}\quad (\text{IV.18})$$

$$= \sum_{i=1}^n \left( (\alpha_{m+1} x_{m+1,i})^2 + 2 \alpha_{m+1} x_{m+1,i} \sum_{j=m+2}^n \alpha_j x_{j,i} + \left( \sum_{j=m+2}^n \alpha_j x_{j,i} \right)^2 \right)\quad (\text{IV.19})$$

$$= \sum_{i=1}^n (\alpha_{m+1} x_{m+1,i})^2 + 2 \alpha_{m+1} \sum_{i=1}^n \left( x_{m+1,i} \sum_{j=m+2}^n \alpha_j x_{j,i} \right) + \sum_{i=1}^n \left( \sum_{j=m+2}^n \alpha_j x_{j,i} \right)^2\quad (\text{IV.20})$$

$$= \underbrace{\sum_{i=1}^n (\alpha_{m+1} x_{m+1,i})^2}_{\geq 0} + 2 \alpha_{m+1} \underbrace{\sum_{j=m+2}^n \alpha_j \sum_{i=1}^n (x_{m+1,i} x_{j,i})}_{=0} + \underbrace{\sum_{i=1}^n \left( \sum_{j=m+2}^n \alpha_j x_{j,i} \right)^2}_{\epsilon_{m+1}^2}\quad (\text{IV.21})$$

$$\Rightarrow \boxed{\epsilon_m^2 \geq \epsilon_{m+1}^2}\quad (\text{IV.22})$$

This derivation shows each additional term contributes to reduce the error of the statistical function. But among the  $n$  terms, a few of them are providing the main contribution to the response construction and most of them have a negligible influence on the response variable. In order to simplify the metamodel, coefficients are sorted in descending order. An analysis is then achieved in order to assess the error profile as a function of the number of terms. Results are displayed in figure IV.14 for three different response variables:

- outlet power,
- storage density,
- system autonomy.

It is chosen to present a dimensionless form  $\epsilon_m^*$  of the sum of squared differences  $\epsilon_m$ . So that the different response variables are comparable to one another, the sum is divided by the mean squared value.

$$\epsilon_m^* = \frac{\epsilon_m}{y_i}\quad (\text{IV.23})$$

Results of figure IV.14a show that the storage density response converges much faster than outlet power or system autonomy. A zoom on lowest values (figure IV.14c) shows the dimensionless sum is lower than 1<sup>1</sup>:

- for metamodels with more than 10 coefficients as far as storage density is concerned,

---

<sup>1</sup>This threshold value is chosen arbitrarily

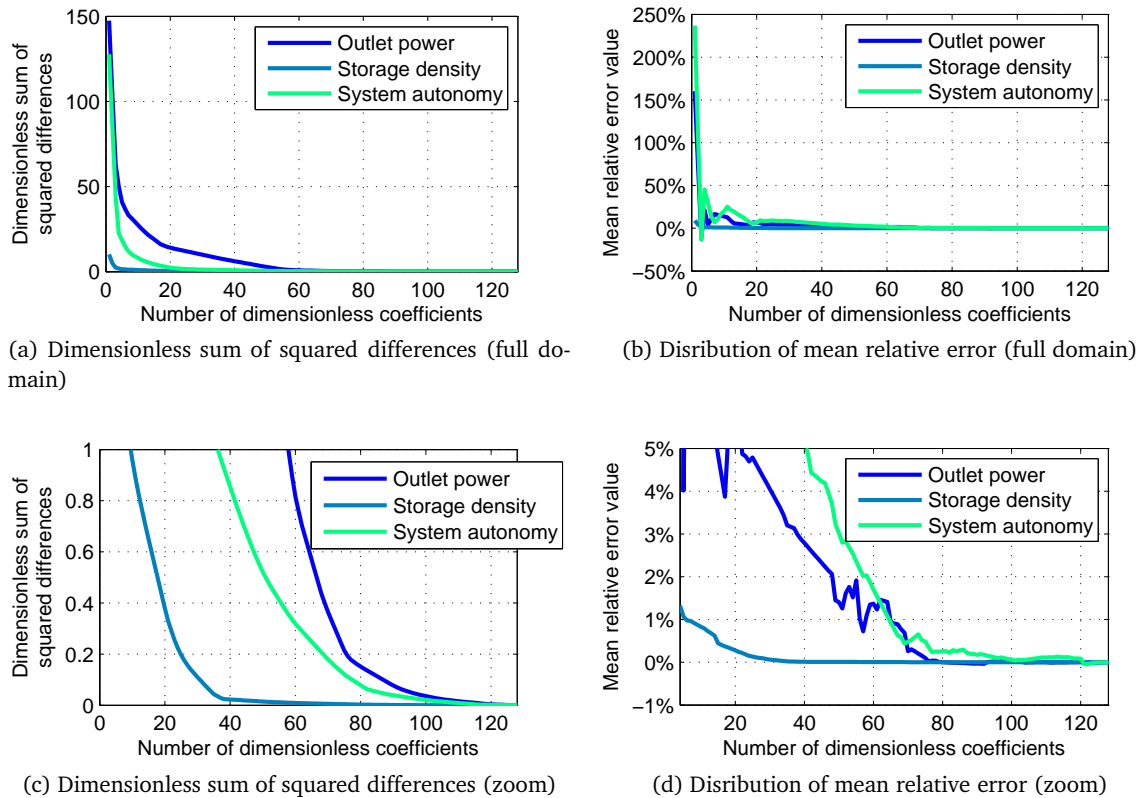


Figure IV.14 – Distribution of the dimensionless sum of squared differences and mean relative error against the number of coefficients in the metamodel for three different response variables (power, storage capacity and system autonomy)

- for metamodels with more than 36 coefficients as far as system autonomy is concerned,
- for metamodels with more than 58 coefficients as far as outlet power is concerned.

A closer look at figure IV.14d shows the mean relative error remains below 1% for a metamodel describing outlet power density with as few as 5 coefficients. 22 coefficients are necessary to reach a 5% mean relative error in outlet power prediction whereas 41 coefficients are required to achieve the same precision in system autonomy prediction.

The correspondence between coded variables (-1 or 1) and physical variables is provided in table IV.6 page 120. Minimum and maximum values are provided, so are default values and corresponding coded variable used for the metamodel validation.

Given the number of coefficients required to reach a satisfying precision, detailed results are provided in appendix (tables 1 to 6, starting from page 165).

Tests of the full metamodel on default values (that differ from the center point with only zeros) is achieved for each response variable under study. Results are barely satisfying on outlet power with a predicted value of  $14.4 \text{ W m}^{-3}$  to be compared to the numerical result of  $13.1 \text{ W m}^{-3}$  (+9.9%), and storage density prediction with a statistical value of  $86.2 \text{ kWh m}^{-3}$  against  $87.6 \text{ kWh m}^{-3}$  for the numerical model (-1.6%). Results are however very poor on system autonomy since 9.9 h are predicted while the numerical model comes up with an autonomy of only 6.5 h (+51.4% for

Table IV.6 – Minimum, maximum and default values of physical variables and corresponding coded variable

Physical variables	Min	Max	Default	Coded default
$L_z$	0.1 m	0.5 m	0.2 m	-0.333
$S$	0.2 m <sup>2</sup>	0.8 m <sup>2</sup>	0.407 m <sup>2</sup>	-0.309
$\varphi_{in,charge}$	0.1 %	0.5 %	0.08 %	-1.124
$\varphi_{in,discharge}$	50 %	80 %	70 %	0.333
$v_{in,charge}$	60 m <sup>3</sup> h <sup>-1</sup>	250 m <sup>3</sup> h <sup>-1</sup>	90 m <sup>3</sup> h <sup>-1</sup>	-0.684
$v_{in,discharge}$	60 m <sup>3</sup> h <sup>-1</sup>	250 m <sup>3</sup> h <sup>-1</sup>	90 m <sup>3</sup> h <sup>-1</sup>	-0.684
$T_{in,charge}$	110 °C	180 °C	180 °C	1

the predicted value).

These linear metamodels are then good tools under certain conditions. It could be relevant to look for higher order coefficients ( $x_i^2$  for instance).

## Conclusions

Influence of eight physical parameters, five operating conditions and two geometric characteristics on outlet power, energy storage density and system autonomy have been addressed. The following guideline must be followed for material development, system design and control strategy optimization.

- Differential **heat of sorption**  $|\Delta H|$  is obviously to be maximized.
- **Fluid density** is also to be maximized for power, energy storage and system autonomy enhancements.
- **Adsorption capacity**  $q_e$  is of course a key parameter that is also to be maximized. Nevertheless, highest outlet power densities are obtained at low  $q_e$  values to the detriment of storage density.
- The difference between **vapor heat capacity**  $C_{p_v}$  and **adsorbed layer heat capacity** ( $c_a$ ) is to be minimized.
- Solid density  $\rho_s$  is to be minimized if it is not to the detriment of adsorption properties.
- A **lower bed porosity** enhances solid proportion and exchange surface and is beneficial to system performances.
- The difference between **inlet relative humidity** on charge and discharge is to be maximized. Indeed, it maximizes the water uptake between full charge and full

discharge.

- The **inlet fluid velocity** has obviously a great influence on time characteristics. A greater fluid velocity on charge mostly reduces the charging time. A greater fluid velocity on discharge strongly increases outlet power to the cost of system autonomy.
- The **charging temperature** has a strong influence only on storage density and system autonomy.
- **Outlet power** is directly proportional to **cross section area**,
- **Heat storage capacity** is directly proportional to **storage tank volume**,
- **System autonomy** is directly proportional to **bed length**.

Furthermore, for a better comparison between one storage system and another, it is suggested to refer to system performances by talking about heat **storage density** (unit:  $\text{kWh m}^{-3}$ ), **outlet power surface density** (unit:  $\text{kW m}^{-2}$ ) and **lineic autonomy** (unit:  $\text{s m}^{-1}$ ).



## Chapter V

# Integration of the storage system in its building environment and sizing methodology

### Contents

---

<b>V.1 Sizing methodology</b> . . . . .	<b>124</b>
V.1.1 Thermal energy needs and maximal power estimations using heating degree-hours . . . . .	124
V.1.2 Detailed design information for a long-term energy storage system . . . . .	129
V.1.3 Conclusion on the sizing methodology . . . . .	136
<b>V.2 Storage system integration in a building context</b> . . . . .	<b>137</b>
V.2.1 Possible system operation strategies . . . . .	137
V.2.2 Integrated system design . . . . .	139
V.2.3 Command laws . . . . .	141
<b>V.3 Operating strategies for partial charges optimization</b> . . . . .	<b>143</b>
V.3.1 Influence of initial temperature on system charge . . . . .	143
V.3.2 Enhancement of the full system: utility of an internal heat exchanger . . . . .	145
V.3.3 Cascaded use of heat for system performances increase . . . . .	146
V.3.4 Charging strategy for parallel reactors . . . . .	147

---

A general context of this thesis as been developed in the first chapter. It has enabled a focus on adsorption heat storage and a more precise definition of a case study. A numerical model of this case study have been developed in the second chapter and validated in the third one. The fourth chapter proposed numerical experiments on the model, at the reactor (or material) scale, in order to assess the influence of material properties, operating conditions and system geometry on system performances. These investigations were performed in a context of a single and full charge-discharge solicitation. But system performances can also be improved with a reflection to the **system scale**. And few researchers have addressed adsorption heat storage from

an integrated system point of view. The present chapter thus broaches the wide topic of heat storage system integration in its buildings environment. The objective is to raise solutions that enable a **reduction of system volume without affecting its performances**.

It first proposes a **sizing methodology** (V1) that aims at estimating **design power** and **storage capacity** based on sizing criteria such as weather data, system operation, heat coverage fraction and desired storage autonomy. This step is important to carefully define the **specification requirements**. In a second part, sketches of material elements and connections, required to operate an adsorption heat storage system in solar heated buildings, are proposed and discussed. This step is clearly related to the choice of **system operation** and **control strategy**. Finally, some investigations on the system behavior under **partial charges** are presented. Operating strategies and **system enhancement** are also proposed to optimize the use of the solar resource available in winter (V3).

## V.1 Sizing methodology

**Foreword:** The present section on sizing methodology is part of a work published in *Energy Conversion & Management* in 2014 under the title "Specification requirements for inter-seasonal heat storage systems in a low energy residential house" (Gondre et al., 2014) reproduced in appendix, from page 176.

Volume and cost of heat storage systems are among the most important issues for user acceptance. The volume can either be estimated from material energy density or from kinetic considerations. Energy to be stored or maximum power to be delivered will then be sizing variables. First studies show that energy density is rarely the limiting factor while deliverable power is (Hongois, 2011). This section aims at providing detailed sizing information for the design process of a thermal storage system intended to partially cover energy needs and power demand of a low energy residential house<sup>1</sup>. Correlations between heating degree-days (*HDD*) and thermal energy consumption or maximum power consumption are first established (V.1.1). A detailed study then provides specification requirements for the sizing of a thermal storage system designed to partially cover energy needs and power demand of a low energy residential house (V.1.2).

### V.1.1 Thermal energy needs and maximal power estimations using heating degree-hours

Building heating consumption mainly depends on weather conditions, building energy performances and internal gains. Several methods have been developed in order to quickly predict building heating demand (Jaffal et al., 2009; Zhao and Magoulès, 2012). Heating Degree Days (*HDD*) is one of those methods and it depends only on weather conditions. A clear correlation

---

<sup>1</sup>As regards with the French thermal regulation RT2005 (Ministère de l'emploi, de la cohésion sociale et du logement, 2006). More details and others definitions may be found in (European commission, 2009)

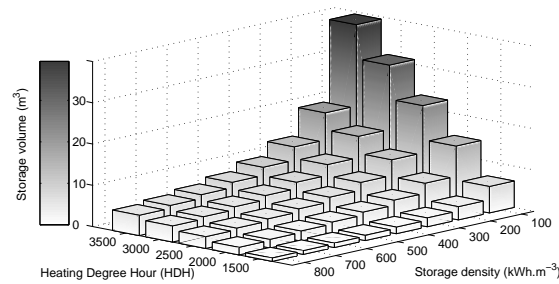


Figure V.1 – Storage volume of a TES system covering full annual thermal energy needs of a 100 m<sup>2</sup> low energy residential house as a function of its energy storage density and climate (given by HDH value - see equation V.2 below for more details)

between building energy needs and *HDD* can then be found only if building energy performance and internal gains remain constant. As stated in the introduction part, storage volume is an important issue for user acceptance. It is shown in (Pinel et al., 2011) that reasonable storage volume can be achieved only with chemical heat storage which also has the advantage to be low time dependent. Energy densities of 250 kWh m<sup>-3</sup> are mentioned in (N'Tsoukpoe et al., 2009) for adsorption processes and up to 780 kWh m<sup>-3</sup> for chemisorption. Potential materials suitable for chemical heat storage in residential applications are listed in (Tatsidjoudoung et al., 2013) but research in this field is still at an early stage and there are large differences between theoretical energy densities and experimental results (Hongois et al., 2011). In this section, the building energy performance is designed to meet low-energy buildings requirements. Reasonable seasonal heat storage is indeed possible only if building energy needs are low. Figure V.1 displays storage volume of a TES system covering full annual thermal energy needs of a 100 m<sup>2</sup> low energy residential house. It shows storage volume may already be higher than an acceptable value considering the climate harshness and the thermal energy storage density of the system. For that reason, this sizing methodology only focuses on low energy residential buildings. Figure V.1 also illustrates why it is important to be able to design a TES system that is aimed at providing only a partial coverage of annual thermal energy needs.

Indeed, it shows the system volume is already an issue if the volume calculation is based on energy storage capacity. But as kinetics considerations appears to be even more limiting than energy storage density (Hongois, 2011), volume issues will be higher when using heating power demand as a sizing factor unless the system is not intended to be able to provide maximum power demand. In this case, it is interesting to correlate energy and power so that the design of the system can reach the best trade off between minimum volume and maximum heating coverage.

### V.1.1.1 Methodology

#### Building thermal energy needs estimation

The software Trnsys 17 is used for all simulations (TESS, 2008). Simulation time step and time base (used for wall transfer functions calculation in the multizone building component (type 56)) are both set to 15 minutes in order to accurately estimate heat power demand. The test case of

Table V.1 – Wall layout and material properties

Wall Type	Material	Thickness	Thermal cond.	Density	Heat capacity	U-value
		mm	$\text{W m}^{-1} \text{K}^{-1}$	$\text{kg m}^{-3}$	$\text{J/kg}^{-1} \text{K}^{-1}$	
External wall	Concrete	150	0.740	800	648	0.163
	Insulation	200	0.035	12	840	
	Concrete	150	0.740	800	648	
Ground floor	Insulation	250	0.029	15	880	0.114
	Hollow slab	160	1.23	1 300	648	
	Concrete	40	1.75	2 400	880	
Attic	Insulation	400	0.035	12	840	0.087
	Plasterboard	13	0.320	850	799	
Intern. floor	Concrete	220	1.75	2 400	880	7.95

this study is a two-story residential house of  $100 \text{ m}^2$  (Spitz et al., 2012). Wall layout and material properties used in the simulation are described in table V.1.

Each floor is described by a rectangular cuboid of 6.5 m by 7.5 m by 2.7 m. Windows have a U-value of  $1.29 \text{ W m}^{-2} \text{ K}^{-1}$  and a frame fraction of 15 %. Wall surfaces and glazing ratios are described in table V.2. The south oriented facade is over-hanged by a balcony on the ground floor and by the roof on the first floor.

Table V.2 – Wall surfaces and glazing ratios

Orientation	Wall area ( $\text{m}^2$ )	Glazing ratio	
		Ground floor	First floor
South	20.25	51.0%	30.0%
North	20.25	4.3%	4.3%
East	17.55	5.7%	7.5%
West	17.55	20.0%	13.0%

The construction is designed for a four-member family with three bedrooms, a bathroom upstairs and a living room downstairs including a kitchen. Occupancy profiles and internal gains are arbitrarily defined to represent the thermal load generated by this family. A sensible heat load of 80 W per person is taken into account. Appliances run mainly in the early morning and in the evening and account for all electronic devices used in the house. The same appliances profile is repeated every day while two different occupancy profiles are used for weekdays and weekends as shown in figure V.2. A value of  $10 \text{ W m}^{-2}$  is considered for lighting loads when occupancy is planned and total solar radiation ( $IT$ ) is too low. Lights are turned on when  $IT$  is lower than  $120 \text{ W m}^{-2}$  and turned off when  $IT$  is higher than  $200 \text{ W m}^{-2}$  defining a hysteresis effect which describes user behavior.

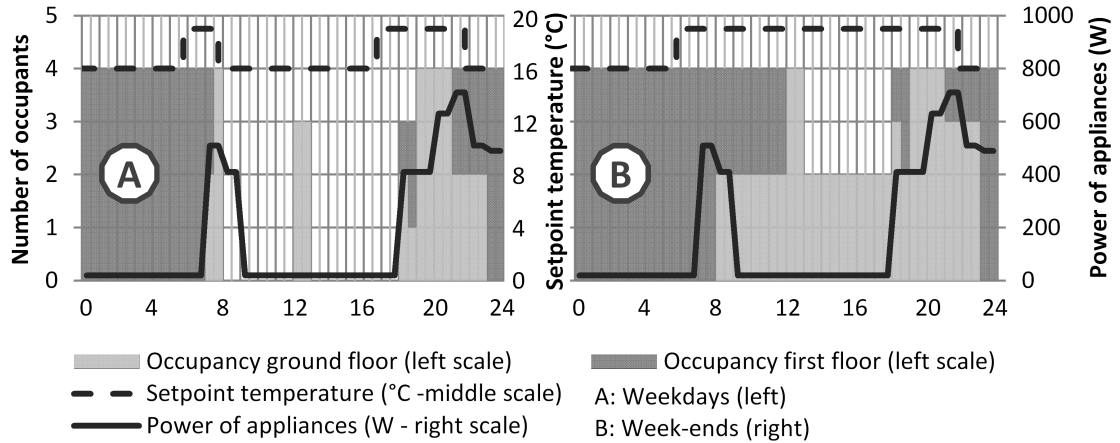


Figure V.2 – Occupancy schedules, internal gains and setpoint temperatures for weekdays and weekends as a function of time

Table V.3 – List of cities included in the study

Agen (FRA)	Budapest (HUN)	London (GB)	Rennes (FRA)
Amsterdam (NLD)	Carpentras (FRA)	Macon (FRA)	Riga (LVA)
Berlin (DEU)	Copenhagen (DNK)	Moscow (RUS)	Stockholm (SWE)
Bern (DEU)	Dublin (IRL)	Nancy (FRA)	Trappes (FRA)
Brussels (BEL)	Helsinki (FIN)	Nice (FRA)	Vienna (AUT)
Bucharest (ROU)	La Rochelle (FRA)	Prague (CZE)	Warsaw (POL)

An ideal heating system calculates at each timestep the exact amount of heat to be supplied to the house in order to reach a given setpoint temperature. Setpoint temperature is changed on schedule : 19°C when occupants are home without sleeping and 16°C when occupants are not home or are supposed to sleep.

Simulations have been carried out for the twenty-four European cities listed in table V.3 and representing most European climates according to the Köppen-Geiger classification (Markus Kottek et al., 2006). For each simulation, energy needs and heat power requirements have been monitored and linked to the *HDD*.

### Calculation of heating degree-day (HDD)

Annual Heating Degree-Day (*HDD*) is a measurement designed to reflect the energy needs of a building. *HDD* are usually defined as:

$$HDD = \sum_{k=1}^{365} \max \left[ \left( T_b - \frac{T_{k,max} - T_{k,min}}{2} \right) \times 24; 0 \right] \times \delta_k \quad (V.1)$$

with  $T_b$  the base temperature,  $T_{k,max}$  the maximum temperature of the  $k^{th}$  day,  $T_{k,min}$  the mini-

imum temperature of the  $k^{th}$  day and  $\delta_k$  a boolean operator (1 during heating season, 0 else).

Definition of  $\delta_k$  may vary from a reference to another. The base temperature  $T_b$  is set as a constant for the whole calculation. It is linked to the setpoint temperature reduced by the average contribution of solar gain (generally 3 °C). For a setpoint temperature of 21 °C, the corresponding base temperature is 18 °C. The principle of the *HDD* method lies in the fact that daily heating needs are proportional to the temperature difference between  $T_b$  and  $T_{mean}$  (daily average temperature). But as the setpoint temperature used in the simulation is not constant, it is not relevant to use a constant base temperature. A better correlation is found between energy needs (or power) and *HDD* with a variable base temperature. The calculation is not based on a one-day scale anymore but on an hourly scale. The index thus defined can be named Heating Degree-Hour (*HDH*).

$$HDH = \sum_{k=1}^{8760} \max[(T_{sp,k} - 3) - T_k; 0] \times \delta_k \quad (V.2)$$

with  $T_{sp,k}$  the setpoint temperature of the  $k^{th}$  hour,  $T_k$  the temperature of the  $k^{th}$  hour and  $\delta_k$  the same boolean operator (1 during heating season, 0 else).

As Europe is in northern hemisphere,  $\delta_k$  will be set to 1 at the calculation beginning (January). It will change to 0 at the end of the heating season and finally change back to 1 at the beginning of the next heating season. Since different climates are tested, heating season must be mathematically defined. Four days are chosen as constants:  $D_{we}$  (March 15<sup>th</sup>),  $D_{sb}$  (June 15<sup>th</sup>),  $D_{se}$  (August 15<sup>th</sup>),  $D_{wb}$  (November 15<sup>th</sup>).

- In the range  $[D_{wb}; D_{we}]$ ,  $\delta_k = 1$  (heating season for all climates).
- In the range  $[D_{sb}; D_{se}]$ ,  $\delta_k = 0$ .
- In the range  $[D_{we}; D_{sb}]$ ,  $\delta_k$  may change from 1 to 0 if  $T_{max,k} > 18$  and  $T_{sp,mean} - 3 - T_{mean} \leq 2$ .
- Conversely,  $\delta_k$  may change from 0 to 1 in the range  $[D_{se}; D_{wb}]$ , if  $T_{max,k} < 18$  and  $T_{sp,mean} - 3 - T_{mean} \geq 2$ .

### V.1.1.2 Results

Results show a clear correlation between annual thermal energy needs  $Q_y$  and *HDH* but also between maximal power consumption  $P_{max}$  and *HDH* (figure V.3) for climates with *HDH* above 1000. *HDH* under 1000 have been excluded from the correlation since they correspond to very mild climates where the installation of a TES system is not profitable.

These results can be used for a rough estimation of thermal energy needs and maximum power consumption of low energy residential houses similar to the present case-study and for all kind of climates (at least in Europe) with a *HDH* above 1000. A linear correlation between annual heating needs  $Q_y$  and *HDH* (equation V.3) is found with a correlation factor of 98.1 %. A

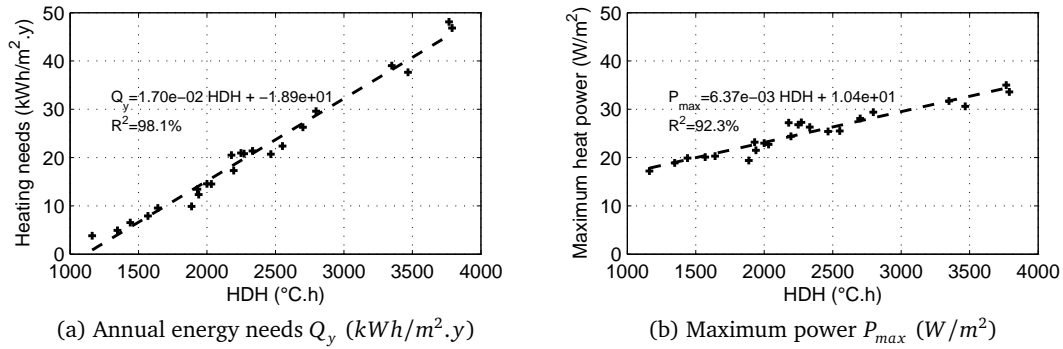


Figure V.3 – Annual energy needs and maximal power as a function of HDH

similar correlation between maximum power demand  $P_{max}$  and  $HDH$  (equation V.4) provides a correlation factor of 92.3 %.

$$Q_y = 1.705 \times 10^{-2} \times HDH - 18.95 \quad (V.3)$$

and

$$P_{max} = 6.365 \times 10^{-3} \times HDH + 10.41 \quad (V.4)$$

As explained in the introduction of the current section, these two variables depend on climate but also on building performance and internal gains. These results may then not be extended to residential houses with different energy performances or too different internal gains. But the method may be reproduced easily in particular in buildings with lower energy standards ( $> 50 kWh m^{-2} y^{-1}$ ). Indeed, the HDH method is a good estimation of heat losses while internal gains and solar gains tend to modify the results. A building with a lower energy performance will have a higher share of heat losses and then the correlation between  $HDH$  and heating demand will be better.

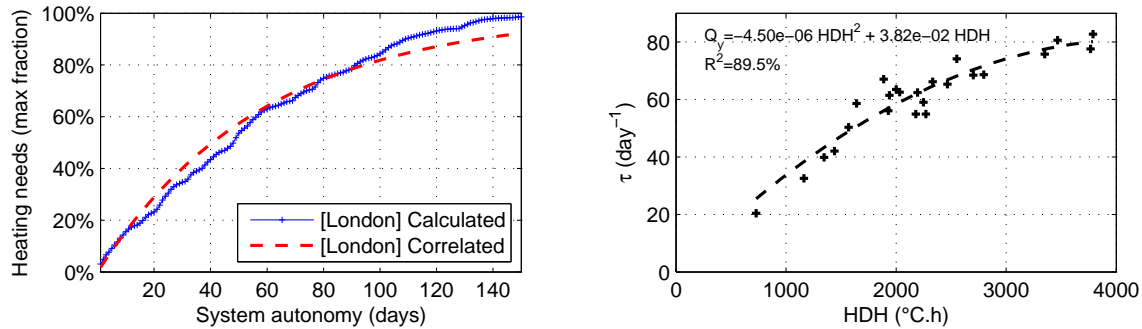
The same kind of correlation can also be found for a partial coverage of the energy needs. Results can for instance be exploited for the twenty or forty coldest days. It may also be focused on a specific part of the day when the overall domestic energy demand is the highest. These detailed results may be interesting for the design of a thermal inter-seasonal storage system that is not bound to provide the whole heating needs but that only aims at reducing power peak demand.

## V.1.2 Detailed design information for a long-term energy storage system

### V.1.2.1 Design based on heating energy needs

A long-term energy storage system is not necessarily designed to fulfill annual thermal energy needs of a building. It may be designed to work only under certain conditions as mentioned previously. The system might work only during the coldest days or only during a specific part of the day. It may also use, in addition, partial charge and store energy in mid-season or even in winter. In order to design the system for a shorter period of time than the entire heating season, it

is interesting to calculate the maximum possible energy needs to be provided over a given period of time. In other words, the goal is to find - for a given autonomy (in the range of 1 to 150 days) - the worst series of days as regard to energy consumption and express this amount of energy to be provided as a percent value of the overall annual energy needs. One example is given in figure V.4a for the city of London (UK).



(a) Yearly fraction of heating needs over a given period of consecutive days (for the city of London)

(b) Decay constant trend as a function of  $HDH$

Figure V.4 – Heat coverage fraction calculation as a function of system autonomy

Figure V.4a displays the maximum fraction  $R_{max}^{[t]}$  of annual thermal energy needs over a given period of time  $t$  (expressed in consecutive days). This evolution follows an exponential law:

$$R_{max}^{[t]} = 1 - \exp\left(\frac{-t}{\tau}\right) \quad (V.5)$$

where  $\tau$  is the time constant of evolution (expressed in  $day^{-1}$ ). It characterizes the distribution of heating needs during increasingly longer periods of consecutive coldest days. The time constant value is equal to the duration of the shortest (and coldest) period of consecutive days when 63 % of the annual needs are required to meet comfort requirements.  $\tau$  is the only correlation parameter and is set in order to minimize the root mean square (rms) difference between calculated and correlated values. The method is repeated for each of the twenty-four cities studied. The overall shape of the calculation curve is always the same. The time constant  $\tau$  can then be calculated for each city. The  $\tau$  values are correlated to the  $HDH$  values as shown in figure V.4b.

Correlated values of  $\tau$  are calculated using equation V.6 which is a result from figure V.4b.

$$\tau = -4.50 \times 10^{-6} \times HDH^2 + 3.82 \times 10^{-2} \times HDH \quad (V.6)$$

The use of correlated values of  $\tau$  instead of calculated values increases the rms difference between correlated and calculated values of  $R_{max}^{[t]}$  from 0.270 to 0.371 (for 150 values) but does not change the standard deviation (4.26 % vs. 4.24 %). Then, it is satisfying to use correlated values of  $\tau$  in order to estimate  $R_{max}^{[t]}$  values (even if the coefficient of determination  $R^2$  is only 89.5 %). It means that  $R_{max}^{[t]}$  values depend only on  $HDH$  as expressed in equation V.5 and equation V.6.

Since it is possible to assess the annual thermal energy needs of a low energy residential house only by knowing the  $HDH$  of its climate (see equation V.2), it is then also possible to estimate the

energy  $Q_{st}^{[t]}$  to be stored by a thermal storage system by setting its autonomy and by knowing the *HDH* of the place where it will be used (equation V.7).

$$Q_{st}^{[t]} = \left(1 - \exp\left(\frac{-t}{\tau}\right)\right) \times (1.705 \times 10^{-2} \times HDH - 18.95) \quad (V.7)$$

$$\text{with } \tau = -4.50 \times 10^{-6} \times HDH^2 + 3.82 \times 10^{-2} \times HDH$$

Equation V.7 enables to draw the sizing chart of figure V.5. The sizing chart is a very fast way to get a rough idea of the size of a storage system used in a low energy residential house.

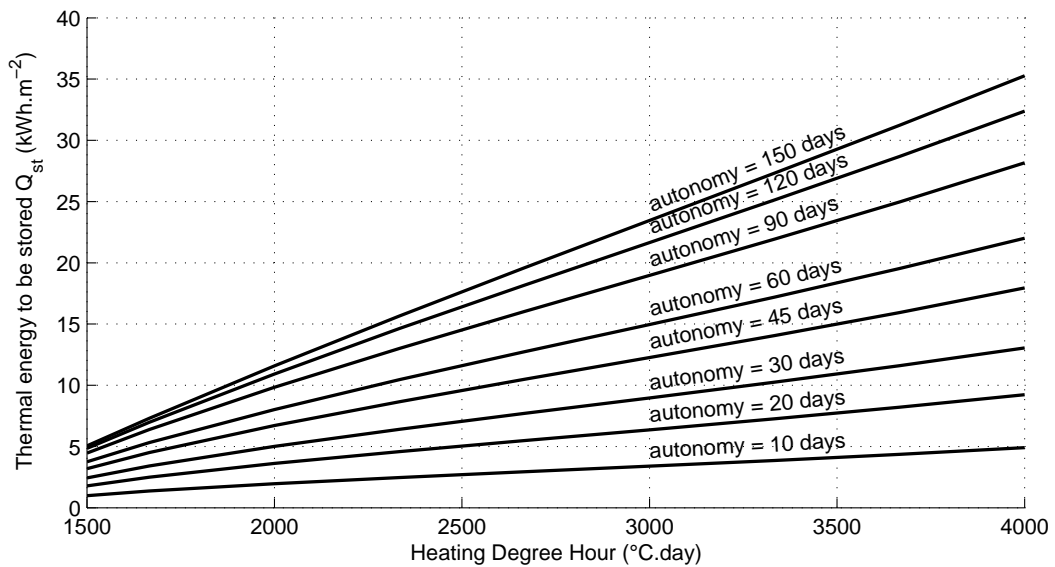


Figure V.5 – Energy to be stored as a function of HDH and system autonomy

### V.1.2.2 Design based on maximum power

The same kind of considerations can be carried out on maximal power. In order to size a storage system, the energy to be stored will not necessarily be the limiting factor. Even in low energy buildings, thermal power involved to heat the building can be large. As thermal power developed by a thermal storage system is often an issue (Hongois, 2011), such systems are not always designed to meet maximum power demand. This section presents a study on power demand distribution and establishes a correlation between *HDH* and power demand distribution.

Maximum power values obtained from Trnsys simulations are high compared to literature (Thullner, 2010). But a detailed analysis shows that less than 5 % of the values are higher than expected. Three combined factors can explain these differences. First, the setpoint temperature is not constant along the day, second the maximal power is set to an unlimited value in Trnsys and third the time step is 15 minutes. A sudden change in setpoint temperature from 16 °C to 19 °C leads to a peak demand. As the power is unlimited, it is calculated so that the setpoint temperature is reached within one time step. It leads to significant differences between a one-hour time step calculation and a 15-minute time step calculation. Power values obtained in first instance are

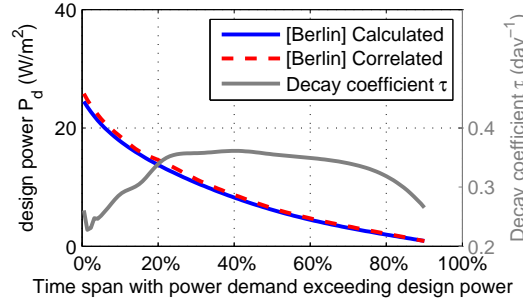


Figure V.6 – Decay coefficient formulation and illustration of its meaning, with results for the city of Berlin

then over-estimated (Ghiaus, 2013). Average power demand  $\bar{P}_k$  and standard deviation  $\sigma_{P,k}$  are calculated for each city. Only values lower than  $\bar{P}_k + 2 \times \sigma_{P,k}$  are considered in the remainder of the study which is, on average, 95 % of the non-zero initial values.

Filtered power demand results are then sorted in decreasing order. Sorted power values follow an exponential decay with a variable decay coefficient (see figure V.6). The decay coefficient is calculated on different points in order to get a correlated curve that fit the exponential decay curve. Figure V.6 shows for instance that power demand is below  $15 \text{ W m}^{-2}$  about 80 % of the time for the city of Berlin. At each point, the decay variable value  $\tau_k(x)$  is given by equation V.9.

$$P_k(x) = P_{max,k} \times \exp\left(\frac{-x}{\tau_k(x)}\right) \quad (\text{V.8})$$

$$\Rightarrow \tau_k(x) = \frac{-x}{\ln\left(\frac{P_k(x)}{P_{max,k}}\right)} \quad (\text{V.9})$$

For Berlin climate, figure V.6 gives  $P_{max} = 25.8 \text{ W.m}^{-2}$  and  $P_d = 14.6 \text{ W.m}^{-2}$  at  $x = 20\%$  which leads to  $\tau_k(20\%) = 0.34 \text{ day}^{-1}$ .

The decay coefficient variation can be interpolated by a polynomial of degree 5 for each of the twenty-four cities studied (equation V.10). The shape of the curve is the same except for the cities of Nice ( $HDH < 1000$ , excluded from the calculations) and La Rochelle (oceanic climate).

$$\tau_k = \sum_{i=0}^5 c_{i,k} \times x^i \quad \text{for } k = \{1, 2, \dots, 24\} \quad (\text{V.10})$$

The series  $\{c_{5,1}, c_{5,2}, \dots, c_{5,23}\}$ ,  $\{c_{4,1}, c_{4,2}, \dots, c_{4,23}\}$ , ...,  $\{c_{0,1}, c_{0,2}, \dots, c_{0,23}\}$  depend on  $HDH$  value. For each of the six coefficients of equation V.10, a linear interpolation is done based on the results of the twenty-three cities considered. An average expression  $\bar{c}_i$  of each of the six coefficients is then proposed (equation V.11).

$$\bar{c}_i(HDH) = a_i \times HDH + b_i \quad \text{for } i = \{0, 1, \dots, 5\} \quad (\text{V.11})$$

It enables to get a mean expression of  $\tau$  as a function of  $x$  and  $HDH$  (equation V.12).

$$\bar{\tau}(x, HDH) = \sum_{i=0}^5 (a_i \times HDH + b_i) \times x^i \quad (V.12)$$

If the city of Nice ( $HDH < 1000$ ) is excluded, the use of a mean distribution leads to a relative error of 6.4% in average (and 13.5% maximum for the Dublin climate) which seems acceptable. The standard deviation of the relative errors distribution is 3.2%.

Equation V.12 is used in order to calculate a correlated distribution of power values. The maximum power value is estimated according to the  $HDH$  value (see equation V.4). It is then possible to estimate a design power  $P_d$  according to  $HDH$  value and to the ratio of time  $x$  when the power value will be higher than  $P_d$  (over a year).

$$P_d(x, HDH) = \exp\left(\frac{-x}{\bar{\tau}(x, HDH)}\right) \times (6.365 \times 10^{-3} \times HDH + 10.41) \quad (V.13)$$

Equation V.13 is used in order to draw a power sizing chart (figure V.7). This chart is a good engineering tool to estimate the maximum power to be delivered by a thermal storage system installed in a low energy residential house.

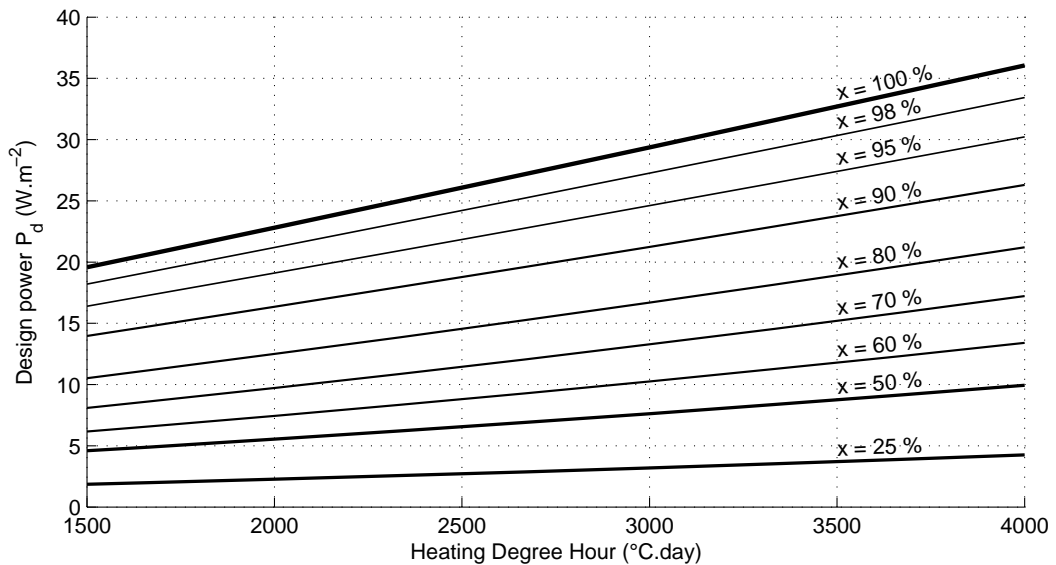


Figure V.7 – Power sizing chart - Design power value to choose in order to meet power demand in  $x$  percent of the heating time with respect to  $HDH$  value

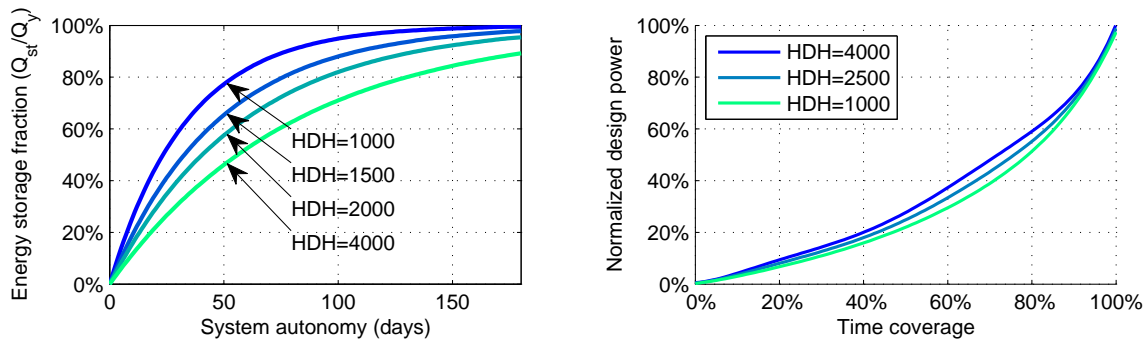
### V.1.2.3 Design based on both energy needs and power

Sections V.1.2.1 and V.1.2.2 provide information for system sizing based on the energy storage capacity or on the maximum delivering power. But it is not possible to link those two results yet. That is the purpose of the following section.

The design can be done at first either on energy storage capacity or on deliverable power.

Once one of these two parameters is fixed using figure V.8a (if energy storage capacity is the designing factor) or figure V.8b (if deliverable power is the designing factor), the second one can be optimized using figure V.10.

Figure V.8a presents a relationship between normalized storage capacity ( $\frac{Q_{st}}{Q_y}$ ), system autonomy (expressed in consecutive days, see section V.1.2.1 for more details) and heating degree-hour (*HDH*). For instance, the city of Lyon has a calculated *HDH* of 1741 (as regards with equation V.2 and with setpoint temperature profile defined in figure V.2). Figure V.8a then shows that heating demand for the 60 coldest consecutive days will represent 68 % of the annual heating needs  $Q_y$ .



(a) Heat storage fraction as a function of system autonomy, for different HDH

(b) Normalized design power  $P_d/P_{max}$  as a function of daily coverage, for different HDH

Figure V.8 – Trend of storage fraction and power fraction as a function of sizing parameters (autonomy and daily coverage)

If the design is primarily done on deliverable power then figure V.8b is used instead of figure V.8a. Figure V.8b shows the normalized design power ( $\frac{P_d}{P_{max}}$ ) as a function of time percentage when power will be sufficient for different values of *HDH*. In Lyon (*HDH* = 1741), a design power  $P_d$  of only 50% of the maximum power  $P_{max}$  is sufficient for about 78% of the heating time.

Once one ratio is defined (either  $\frac{Q_{st}}{Q_y}$  or  $\frac{P_d}{P_{max}}$  depending on which one is supposed to be the limiting factor), the second ratio can be optimized so that both ratios are sized to be system limiting factors. There are three ways to consider the link between heating needs and deliverable power. It depends on the control strategy of the system. A TES system can indeed be used either on base-mode (the TES system is used as soon as heat is required - see figure V.11b) or on load shedding-mode (the TES system is used only above a given threshold i.e. for peak demand). In this case, it can either be used in order to smooth heating demand (a base production is always provided by an auxiliary heater - see figure V.11d) or to reduce peak energy cost (the TES system is used in order to provide most of the heat share during peak demand, when energy is the most expensive - see figure V.11c). The choice between these three strategies will be done according to the TES system strengths and weaknesses. If deliverable power is the limiting factor, the first strategy will be better. If heat storage capacity is the limiting factor, the second strategy will be more appropriate. If deliverable power and energy needs are well balanced, the third strategy could be the most relevant for economic profitability of the system. But in 2013, most of seasonal heat storage systems are more limited by their deliverable power than by their heat storage

density. That is the reason why the following results are presented in base-mode (1). It is easy to deduce results for the second strategy from the first one. Results for the third strategy are not presented here.

In the case where none of the three different control strategies presented is excluded because of system constraints, the choice would probably depends on two main factors: the system owner and the electricity pricing policy. If the TES system is purchased by an individual, he will expect an economic profitability. If electricity pricing is constant, the best economic profitability will be reached with the first control strategy (which maximizes the use of renewable intermittent energy sources integrated to the building). If electricity pricing depends on demand, the third control strategy will be more profitable for the individual since he will avoid using electricity from the network when it is the most expensive. Now if the TES system is installed or subsidized by the network manager or by the government, it will aim at smoothing peak demand. The second control strategy will better fit if the system is widely diffused but the third one will be more relevant if it remains more confidential (so that one TES system installed in one individual house can offset several non-equipped houses during peak demand).

The relationship between the normalized storage capacity and the normalized design power depends on the system autonomy. If the autonomy is set for instance to 30 days, the energy to be stored  $Q_{st}$  will be lower than if the autonomy is set to 90 days whereas annual heating needs  $Q_y$  remains constant.

Figure V.9 gives results for a complete seasonal storage (i.e. the autonomy is sufficient to provide heat for the entire heating season). For each of the twenty-four cities of the study, the normalized storage capacity  $Q_{st}$  is calculated for different values of the normalized design power as expressed in equation V.14 below.

$$Q_{st,m} = \sum_{i=1}^{8760 \times 4} \min\left(P_i, P_{max} \times \frac{m}{10}\right) \quad (\text{V.14})$$

with  $m = \{1, 2, \dots, 10\}$

Figure V.9 displays one curve for each of the twenty-four cities studied and one mean curve (dashed line). If the cities of Nice and La Rochelle are excluded from the mean curve calculation, the average standard deviation between the mean curve and the calculated curves is no more than 0.5 %.

The same graph can be drawn for different autonomies. The set of curves is then more dispersed than for figure V.9 but the average standard deviation between the mean curve and the calculated curves is 3.8 % (maximum 6.0 % for an autonomy of 90 days). Figure V.10 displays the mean curves for different autonomies.

**Example of application** A thermal storage system has to be installed near Lyon, in France, in a  $100 \text{ m}^2$  residential house. The system is designed for an autonomy of 90 days and the deliverable power has to be sufficient for at least 80 % of the time. Heating needs capacity will be optimized so that it is neither over-sized nor limiting.

Lyon has an *HDH* of 1741. Equations V.3 and V.4 give annual energy needs of  $10.7 \text{ kWh m}^{-2} \text{ y}^{-1}$

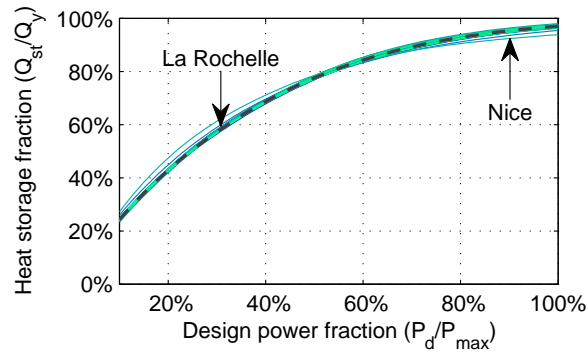


Figure V.9 – Relationship between normalized storage capacity and normalized design power for the twenty-four cities studied and mean curve (dashed line) for a complete seasonal storage

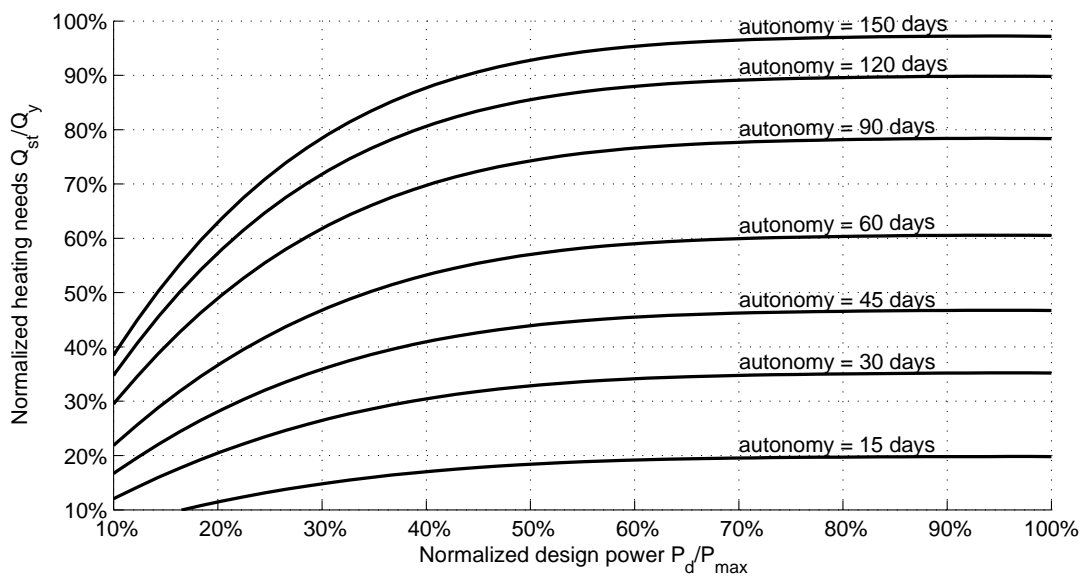


Figure V.10 – Average relationship between normalized storage capacity and normalized design power for different system autonomies (15, 30, 60, 90, 120 days and the whole heating season)

and maximum power of  $21.5 \text{ W m}^{-2}$  which lead to  $1070 \text{ kWh y}^{-1}$  and  $2.15 \text{ kW}$ . Design power is chosen according to figure V.8b to 53% of the  $P_{max}$  :  $P_d = 1.15 \text{ kW}$ . Figure V.10 is then used in order to find the best normalized heating capacity. A normalized design power of 53% and an autonomy of 90 days give a  $\frac{Q_{st}}{Q_y}$  ratio of 60%. The TES system will then need to store  $644 \text{ kWh}$ , which is about  $6.2 \text{ m}^3$  considering an average storage density of  $104 \text{ kWh m}^{-3}$ .

### V.1.3 Conclusion on the sizing methodology

A sizing methodology was presented. It enables an estimation of annual thermal energy needs and maximum power consumption for most European climates characterized by their heating degree hour (*HDH*). It also gives detailed information for the design of a thermal storage system that does not aim at providing 100% of heating needs. It is then possible to assess the required storage capacity of a thermal storage system as a function of the desired autonomy. It is also

possible to determine the design power based on time coverage considerations. This methodology is developed for low energy residential buildings. Results are then only applicable to this kind of buildings which is the best application for thermal storage systems. However the same methodology can be easily applied for other building types.

This step was necessary to optimize the design on both storage capacity and power. It provides guidelines for **coverage fraction optimization** with a given storage volume. But playing on system autonomy and coverage fraction is not the single way to find the best trade off between system performances and volume. As shown in the energy conversion analysis (page 87), reflections must be conducted to find the best way to **integrate** the storage system into the full heating, ventilation and air conditioning (**HVAC**) system. It is the only way to **create synergies** between the storage system and the heating system that will **enhance global performances**.

## V.2 Storage system integration in a building context

Integration of the storage tank into a full system integrated to the building and to the heat source requires to develop simultaneously:

- the system **operation strategy**: what are the objectives pursued and when is the system intended to run?,
- the system **design**: what are the material elements needed to get the system work and how are these elements connected to each other?,
- the system **control strategy**: what are the command laws that activate fans and valves?.

These questions are addressed in the following part.

### V.2.1 Possible system operation strategies

System volume and ground surface are strong issues for user acceptance (sizing methodology part (V.1), starting from page 124, provides detailed information on this statement). Basically, it is **not reasonable** to design a storage system that would **cover the whole yearly heating needs** of a building. In order to optimize heat coverage fraction and storage volume, it is relevant to consider that the heat storage system is not necessarily intended to be charged only in summer. [Rathgeber et al. \(2015\)](#) have shown that an increase of charge-discharge cycles lowers the investment cost. Indeed, it reduces the volume of storage material that is necessary to cover energy needs. Partial recharges can be contemplated with a solar heat source, even in winter. In this case, it is particularly important to address the system behavior under partial charge-discharge cycles. This step is developed in section V.3 and will enable to refine the control strategy by providing some information on minimum charging time and temperature requirements.

However, it still seems complicated to reach a 100% fraction coverage. The storage system must then be managed in collaboration with an auxiliary heater that will cover the remainder of heat loads. The control strategy that will give priority to either the auxiliary heater or a storage system discharge is preponderant in system sizing and performances.

### V2.1.1 Charging strategy

The charging strategy is closely related to the heat source. Four possible solutions are briefly evoked.

1. Heat used for system charge can be generated by **industrial processes**. Few flexibility is then accorded to charging control strategy. System is charged when heat is available at a sufficiently high temperature.
2. Heat can be generated from a **solar collector**. Again, few flexibility is then accorded to charging control strategy, and solar sources are not very foreseeable. In summer, long charging phases at high temperature are expected. In winter, fewer charging phases are expected, at lower temperatures. The goal of the control strategy is then to optimize the use of the solar resource in order to provide heat at sufficiently high temperatures and for sufficiently long times.
3. One could consider using an **hybrid solar-auxiliary heat source**. The solar source could be supplemented by an auxiliary heater in order to use solar resource at sufficiently high temperature. The amount of auxiliary heat provided to the system could be (partly) recovered at the storage tank outlet, as seen in energy conversion analysis (see figure III.20a of section III.4). Heat recovered could be used for direct building heating. In a way, the auxiliary heater would then *lend* high temperature heat to get back low temperature heat.
4. Finally, heat can be fully generated by an auxiliary (electrical) source. Objective pursued in this case is to reduce peak demand and heating cost. The control strategy must then be closely related to energy prices. Moreover, it is mandatory to recover heat losses for direct heating otherwise the ratio between heat provided (in low cost period) and heat released (in high cost period) would be too high to be compensated by cost differences.

### V2.1.2 Discharging strategy

The decision to proceed to a storage tank discharge can be made on **time, load and/or economic indicators**. It depends on the objectives pursued by the use of a thermal energy storage system.

1. If the goal is to **optimize the solar fraction** in building heating, the thermal storage will better be used on time criteria, preferentially **at night**, when there is no chance to use direct solar heating (fig. V.11a).
2. Now if the goal is to **optimize the storage fraction in building heating**, the system will better be used as a **base production** running as soon as heat demand exists, without necessarily reaching high instant coverage fraction (fig. V.11b).
3. Finally, if **economical criteria** are driving decisions, heat store will be used as soon as **energy cost is above a threshold value**. High energy cost is more likely coinciding with peak demand, but could also differ depending on local climate, building internal loads and insulation. The TES system is then only used above a given threshold i.e. for peak demand.

In this case, load management strategies propose two different options that depend on TES system strengths and weaknesses:

- If deliverable power is the limiting factor, a partial load shedding is used in order to smooth heating demand, but a base production is always provided by an auxiliary heater as shown on figure V.11d.
- If heat storage capacity is the limiting factor (but deliverable power is not), a full load shedding is more appropriate. The whole heating needs are then provided by the storage system while heating demand is above the threshold, as shown on figure V.11c.

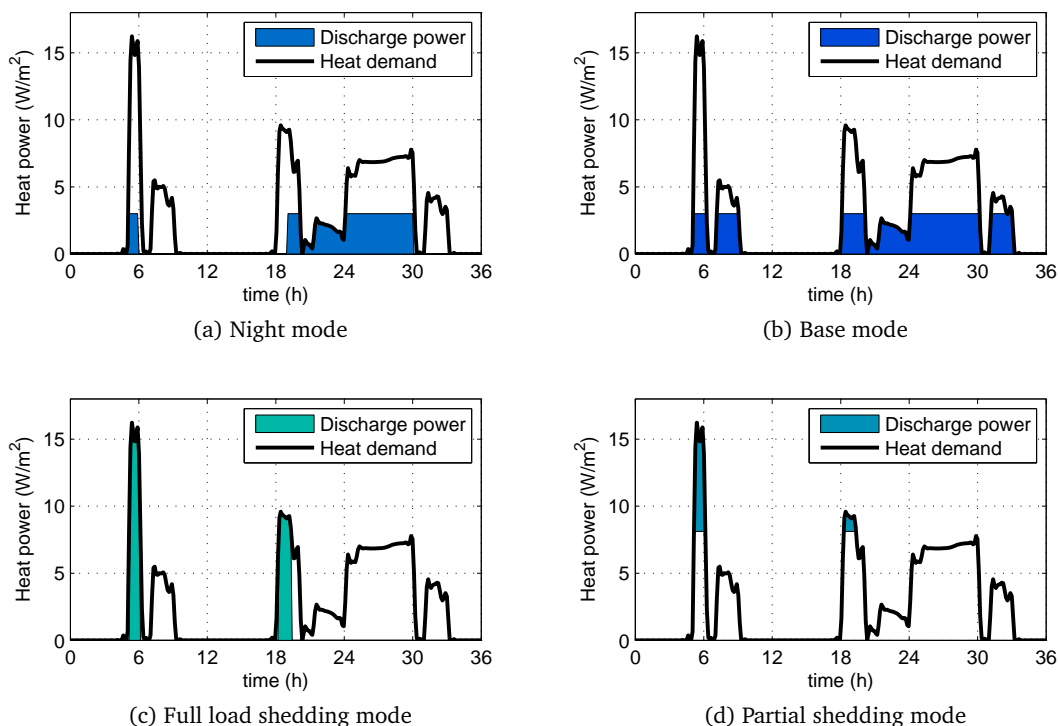


Figure V.11 – Four different possible control strategies

## V.2.2 Integrated system design

Whatever is the heat source and the discharge strategy, several elements must be connected to the storage tank in order to include it in an integrated storage system. As explained earlier, a **heat source** (solar collector and/or auxiliary heater) is required to provide heat to the adsorption heat storage system. At least one **heat exchanger** is also mandatory during discharge, in order to warm the inlet fresh air with heat retrieved from the store. This heat exchanger can cleverly be used for **heat recovery** purposes in the remainder of the time to reduce building load (as in winter to retain heat as in summer to keep cold). It is then a good investment that participates not only in the heat storage system but also in the building energy efficiency.

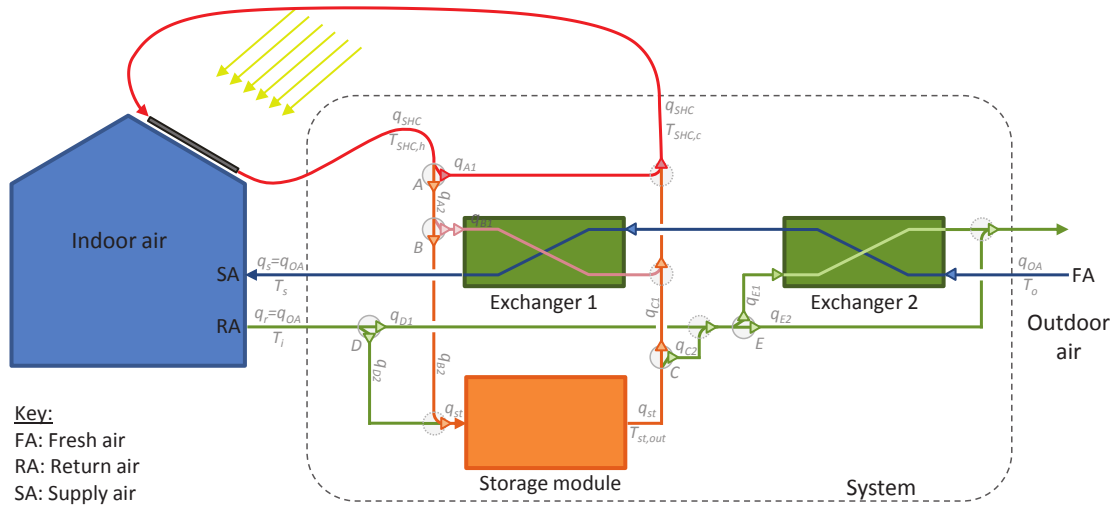


Figure V.12 – Sketch of the storage system integration to its building environment

Table V.4 – Possible configurations

Configuration	W1	W2	W3	W4	W5	S1	S2	S3
Heat recovery	✓	✓	✓	✓	✓	✓	✓	
Direct solar heating		✓		✓				
Heat storage charge			✓	✓			✓	
Heat storage discharge					✓			
Free-cooling								✓
Related figure	2a	1a	2b	1b	1c	2a	2b	2c

It can be worth considering a **second heat exchanger**, and even compulsory in case of a solar heat source. Indeed, outlet temperature of solar panels is, most of the time, not high enough to consider a heat store charge. But outlet power can be sufficiently high to consider **direct solar heating applications** (heat loads or domestic hot water). In a general way, direct use of heat resources provides better efficiency ratios than an intermediate storage. But economical and statistical considerations can prevent a clever control strategy to run only on efficiency bases. This is discussed in the next paragraph (V.2.3).

A third heat exchanger might be required in case of a solar heat source running with a liquid heat transfer fluid. It is indeed mandatory to provide the storage system with a dry and hot gas fluid in charging mode. The third heat exchanger would then ensure heat transfer from the solar panel liquid loop to the storage tank air loop. It is nevertheless necessary to investigate whether a liquid loop can provide sufficiently high temperatures in winter to be considered.

A fully integrated solar storage system is sketched on figure V.12. It displays connections between a solar heat collector, the storage module, the building and two heat exchangers. Numerous configurations are possible in winter as in summer. They are summed up in table V.4. The last row refers to figures in appendix that display used and unused pipes in each configuration.

Table V.5 – Control values of each valve and airflow rates in each branch of the system described on figure V.12

	W1=S1		W2		W3=S2		W4		W5		S3	
	C	q	C	q	C	q	C	q	C	q	C	q
A1	1	$q_{SHC}$	0	0	0	0	0	0	1	$q_{SHC}$	1	$q_{SHC}$
A2	0	0	1	$q_{SHC}$	1	$q_{SHC}$	1	$q_{SHC}$	0	0	0	0
B1	1	0	1	$q_{SHC}$	0	0	0.1	$0.1 q_{SHC}$	1	0	1	0
B2	0	0	0	0	1	$q_{SHC}$	0.9	$0.9 q_{SHC}$	0	0	0	0
C1	1	0	1	0	1	$q_{SHC}$	1	$0.9 q_{SHC}$	0	0	1	0
C2	0	0	0	0	0	0	0	0	1	$q_{OA}$	0	0
D1	1	$q_{OA}$	1	$q_{OA}$	1	$q_{OA}$	1	$q_{OA}$	0	0	1	$q_{OA}$
D2	0	0	0	0	0	0	0	0	1	$q_{OA}$	0	0
E1	1	$q_{OA}$	1	$q_{OA}$	1	$q_{OA}$	1	$q_{OA}$	1	$q_{OA}$	0	0
E2	0	0	0	0	0	0	0	0	0	0	1	$q_{OA}$
$q_{st}$		0		0		$q_{SHC}$		$0.9 q_{SHC}$		$q_{OA}$		0

### V.2.3 Command laws

Command laws are developed based on considerations from operating strategies and system design. Each of the five valves (from A to E on figure V.12) are open at anytime on one of the two downstream duct sections. It requires five command laws (one for each valve). Besides, two command laws are required to control two fans (not represented on figure V.12). One fan controls fresh air supplied to the building. The other one is used to control airflow rate through the solar heat collector. Seven command laws are then required to control this system. Table V.5 sums up control values of each valve and airflow rates in each branch for all scenarios considered.

A set of command laws is proposed in table V.7. A specific nomenclature is also provided in table V.6. It defines heating season (and cooling season for night ventilation). The **setpoint temperature** is not necessarily constant but can vary along the day between a high setpoint temperature and a low setpoint temperature. **Setpoint temperature profile** is very important to ensure thermal comfort while limiting over-consumption. A consistent temperature profile can ensure energy savings up to 30% (Osello et al., 2013). Of course, it is correlated to the building occupancy.

- In case of a **residential building**, a good temperature profile avoids over-consumption at night or during working hours. Peak consumption is then more likely to occur early in the morning and late in the afternoon. If the solar resource is available, it can directly cover **afternoon heating needs**, either exclusively or **downstream a storage recharge**. This idea is already mentioned in paragraph III.4 on energy conversion analysis. The use of heat stored then preferentially happens in the early morning.
- In case of an **office building**, a good temperature profile especially avoids over-consumption after working hours and at night. Main heat power demand clearly occurs prior to the beginning of working hours where the use of stored heat seems particularly wise, if the storage system is intended to reach high solar fractions.

Table V.6 – Nomenclature for command laws

Command variables	Command settings
$T_i$ : indoor temperature	$T_s$ : supply air temperature
$T_{SHC}$ : solar heat collector temperature	$T_{set}$ : setpoint temperature
$T_{exc2,out}$ : outlet temperature of the 2 <sup>nd</sup> heat exchanger	$T_{ch,max}$ : maximum charging temperature
$t_{24}$ : day time (0h-24h)	$T_{ch,min}$ : minimum charging temperature
$t$ : year time (0h-8760h)	$t_{ch,max}$ : max start time for charge
$I_T$ : incident radiation	$t_{d0}$ : beginning of discharge span
$Q_H$ : heating needs	$t_{df}$ : end of discharge span
$q_{OA}$ : supply airflow rate	$t_{wb}$ : beginning of heating season
$q_{SHC}$ : solar heat collector airflow rate	$t_{we}$ : end of heating season
$St$ : Storage status	$t_{sb}$ : beginning of cooling season
$Sn$ : Season (-1:winter, 1:summer)	$t_{se}$ : end of cooling season

Heat storage can occur only above a minimum temperature  $T_{ch,min}$  to maintain performances, and under a maximum temperature  $T_{ch,max}$  to prevent the system from possible damages. Airflow rate  $q_{STC}$  through the solar heat collector is controlled by equation V.20. This equation **adjusts the flowrate** from a minimum to a maximum value in order to maximize occasions with **acceptable charging temperature**. But very short charging windows are not efficient and can even be detrimental to the charging state. It is nevertheless difficult to forecast whether it is worth starting a charging phase or not. The only predictable data is sunset hour. A limiting hour  $t_{ch,max}$  is then set to prevent the launching of any charging phase if sunlight is, for sure, not going to last long enough to ensure a proper charge. Ongoing charging process can, of course, be maintained after this time limit. It requires the definition of a state variable  $St$  that indicates whether a charge is going on ( $St = 1$ ) or not ( $St = 0$ ).

Discharge process is only possible during heating season ( $Sn = 1$ ), when heating needs are existing. Moreover, it is possible to restrain available discharge windows by setting a time span that allows discharge phases only from  $t_{d0}$  to  $t_{df}$ .

In the present proposition, fresh air continuously flows in the building at the same rate. It tends to increase heat consumption, even with a heat recovery device. A control of inlet fresh air flowrate with occupancy detection would lower energy consumption.

Table V.7 – Command laws

<b>A2</b>	$= (Sn = 1) \cdot (T_{SHC} > T_i) \cdot (t_{24} > t_{ch,max}) \cdot (St = 0) + (T_{SHC} > T_{ch,min}) \cdot ((t_{24} \leq t_{ch,max}) + (t_{24} > t_{ch,max}) \cdot (St = 1))$	(V.15)
<b>B2</b>	$= (T_{SHC} > T_{ch,min}) \cdot ((t_{24} \leq t_{ch,max}) + (t_{24} > t_{ch,max}) \cdot (St = 1))$	(V.16)
<b>C2</b>	$= D2$	(V.17)
<b>D2</b>	$= (Sn = 1) \cdot (Q_H > 0) \cdot \left( (t_{d0} < t_{df}) \cdot (t_{24} \geq t_{d0}) \cdot (t_{24} < t_{df}) + ((t_{24} \geq t_{d0}) + (t_{24} < t_{df})) \right)$	(V.18)
<b>E2</b>	$= (Sn = -1) \cdot (T_o < T_i)$	(V.19)
$q_{STC}$	$= (I_T > 0) \cdot \min \left( \max \left( \frac{T_{SHC} - T_{ch,min}}{T_{ch,max} - T_{ch,min}}, 0.1 \right), 1 \right)$	(V.20)

### V.3 Operating strategies for partial charges optimization

The present section addresses the system behavior under **short charging periods** and proposes solutions to optimize the use of available **solar resources** in **winter**.

#### V.3.1 Influence of initial temperature on system charge

Up to now, the initial temperature of the storage tank was supposed uniform and equal to 20°C. In real conditions, initial temperature depends on surrounding temperature. It can also be much higher than surrounding temperature if the storage tank is preheated.

Indeed, solar potential is not necessarily high enough in winter to provide sufficiently high temperatures for the charging process. In this case, heat generated by the solar collector can be used for different purposes.

- For solar heat concentration in a **short circuit** (the outlet of the solar panel is connected to its inlet),
- **direct heating** of the building,
- storage system **preheating** (with an internal heat exchanger),
- **cascaded** storage system **preheating** and **direct heating** of the building.

Intuition suggests that the **initial temperature** influences the **desorption phase performance**. Indeed, a part of the inlet heat is converted into sensible heat. High desorption states are reached at high temperatures and low relative humidities. The amount of energy from high temperature flow used to warm up the material is not used for advanced desorption. This intuition is confirmed with a numerical investigations of the influence of initial temperature on

partial charges (figure V.13). Each simulation starts with the same amount of water (17.04 kg<sub>v</sub>). The charging time and the initial temperature  $T_0$  are different from one simulation to another. Initial vapor pressure is determined accordingly to the initial temperature and the initial mass of water so that adsorption equilibrium fulfills mass conservation of water.

$$m_{H_2O} = m_{H_2O,v} + m_{H_2O,w} \quad (V.21)$$

$$m_{H_2O} = A \frac{p_v M_v}{R T_f} + q_e(p_v, T_{film}) \quad (V.22)$$

Default initial conditions are  $T_{0,d} = 20^\circ\text{C}$  and  $p_{v,0,d} = 2000\text{ Pa}$  (86% relative humidity). The new initial value  $p_{v,0}$  of vapor pressure must satisfy the following balance equation.

$$A \frac{p_{v,0} M_v}{R T_{f,0}} + q_e(p_{v,0}, T_{film,0}) = A \frac{p_{v,0,d} M_v}{R T_0} + q_e(p_{v,0,d}, T_0) \quad (V.23)$$

Charging time varies from 20 to 240 minutes (4 hours) in order to reproduce the wide range of charging windows that can be encountered in realistic conditions.

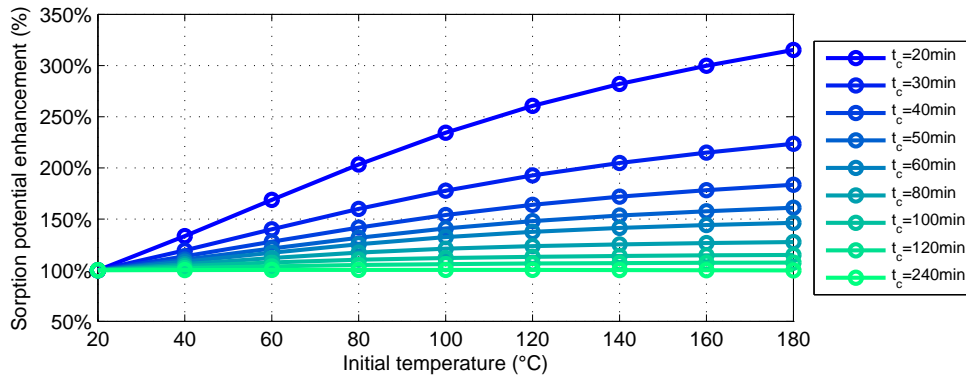
Results displayed in figure V.13 are derived from the calculation of the theoretical amount of energy  $E_q$  stored within the material as a sorption potential. It is calculated according to equation III.34, reproduced here:

$$E_q = \int_{t=t_{0c}}^{t_{fc}} \left( \iiint_V B_a \frac{\partial q}{\partial t} |\Delta H| dV \right) dt$$

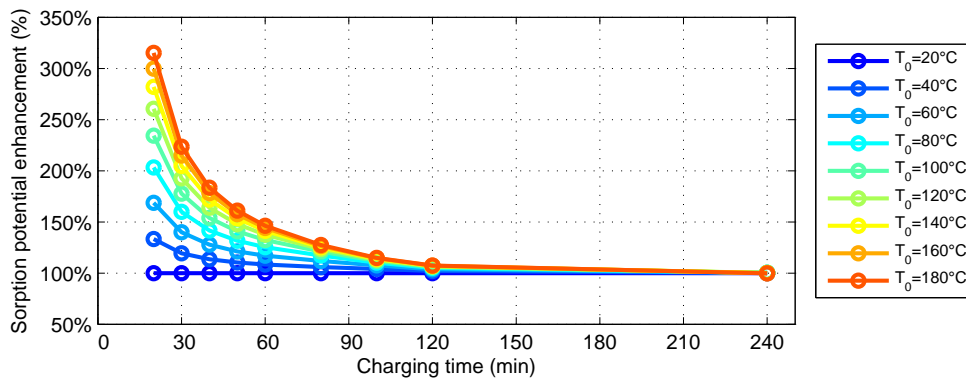
The sorption potential enhancement (%) is defined as the ratio between the sorption energy reached in given conditions and sorption energy reached with the same charging time but with default initial temperature.

Figures V.13a and V.13b display the same set of results with two different projections. In figure V.13a, the sorption potential enhancement is displayed as a function of initial temperature, for different charging times. In figure V.13b, the sorption potential enhancement is displayed as a function of charging time, for different initial temperatures.

Results from figures V.13a and V.13b show the **storage tank preheating** is definitely **interesting** for **short charging times**. The efficiency of a 20-minute charge can be reasonably enhanced by a factor as high as 2.5 with a reasonable preheating at  $110^\circ\text{C}$ . For a charging time of 1 hour, it is still improving efficiency of the partial charge by 30%. For charging times higher than 2 hours, it is not interesting anymore to preheat the storage tank for charging performances enhancement purposes. Stating that the amount of sensible energy required to warm up the tank is finite, it is logical to observe a clear decrease in the sorption potential enhancement with charging time increase. For experiments that last longer than the time required to reach a full charge state, a preheating of the storage tank has obviously no influence at all.



(a) Theoretical energy stored as sorption potential as a function of initial temperature, for several charging times



(b) Theoretical energy stored as sorption potential as a function of charging time, for several initial temperatures

Figure V.13 – Influence of initial temperature on heat storage potential for different partial charging times. Each charge starts with the same amount of water (at different initial temperatures and hence vapor pressures). Results are expressed relatively to the default initial temperature of 20°C. Both graphs display the same set of data with a different projection.

### V.3.2 Enhancement of the full system: utility of an internal heat exchanger

These results are interesting since they demonstrate the interest in storage tank preheating. But storage tank preheating requires an **internal heat exchanger**, which is a quite **expensive investment**. It also requires some adjustments in the connections between the storage tank and the other elements of the system. But besides providing heat to the storage tank for preheating purposes, the internal heat exchanger can work the other way around and **retrieve sensible heat from the storage tank** (at night for instance). The installation of an internal heat exchanger is then a good opportunity to turn the adsorption heat storage system into a **combined sensible/adsorption heat storage system**.

Besides, as shown in the Sankey diagram of page 90 (figure III.20c), a large part of inlet heat is wasted at the outlet of the storage tank during the charging process (part 2L of the diagram). It is then important to address carefully the problem of the **heat conversion chain optimization** at the global system scale, composed of the storage tank, the building and other associated systems. In this way it is important, especially in winter, to **collect** and **use** heat at the **outlet** of the storage tank (on charge) or at the outlet of the internal heat exchanger (on preheating) to **heat**

the building, when necessary.

Figure V.14 shows necessary adjustments to enable storage tank preheating, sensible storage and cascaded direct heating of the building.

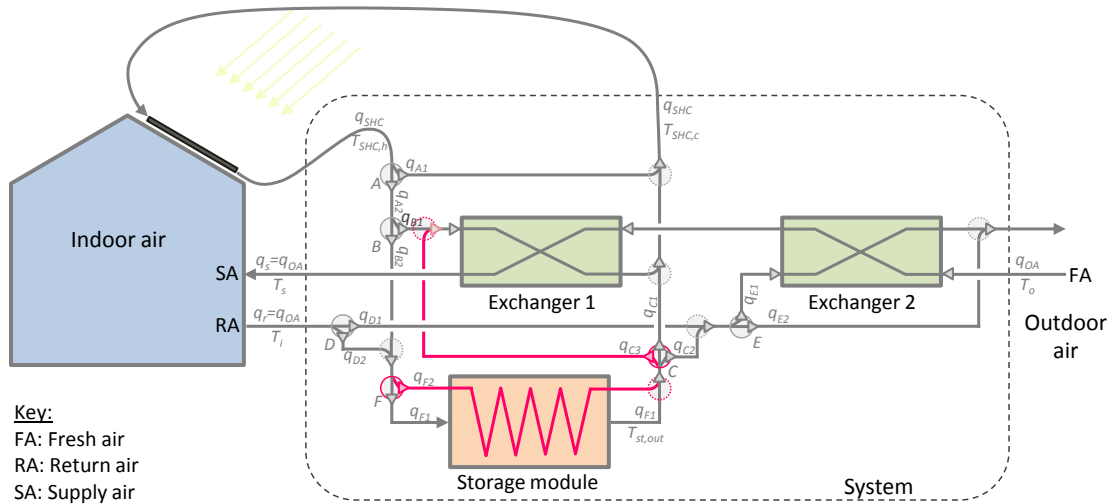


Figure V.14 – Internal heat exchanger and associated connections required to enable storage tank preheat, sensible storage and cascaded direct heating of the building

Figure 3 (appendix, page 176) displays system configuration under three additional cases enabled by the installation of an internal heat exchanger:

- storage system preheating and cascaded direct heating of the building (figure 3a),
- sensible storage discharge (figure 3b),
- heat recovery ventilation and storage system preheating (figure 3c).

### V.3.3 Cascaded use of heat for system performances increase

**Cascaded** storage tank preheating and direct building heating is interesting since it shows **wasted heat** at the outlet of one component can cleverly be used as **useful inlet heat** to another component of the system. The same approach can be thought of with the **auxiliary heater** of the building. By assuming the storage system can not fulfill all energy needs of the building, an auxiliary heater is required to take over when a discharge of the storage system is not possible or not wished.

If these auxiliary heaters are electrical, an electricity consumption will occur for heating purposes. The idea presented here is to consider replacing individual low temperature heaters by a **single high temperature heater** installed between the outlet of the solar panel and the inlet of the storage module. This heater would provide heat at high temperature to charge the system. Low temperature outlet heat would be used for instant heating purposes.

The use of an auxiliary electrical heater placed in between the solar panel and the storage tank has, at least, three advantages:

- It removes individual auxiliary heaters from the building and proposes a single heating solution (preferentially low temperature radiant floor, or forced convection). It probably tends to **lower investment costs**.
- It enables a **system charge in winter** (even at night) with full use of wasted heat, to the cost of an over-consumption. But most of this over-consumption will be recovered during the storage system discharge.
- It enables, in winter daylight, an additional power input to reach high enough temperatures to start a charging phase. It would **increase the use of the solar resource potential in winter**. The COP of this particular operation could be tremendous since most of the inlet energy would come from the sun. It would then be, from an economical point of view, a very good 'investment'.

Moreover, the auxiliary electrical heater is likely to be solicited on low-energy demand periods (in the early afternoon or at night). This hypothesis has not been tested yet and requires additional investigations to be confirmed.

### V.3.4 Charging strategy for parallel reactors

Section IV.3.4 has shown outlet power linearly depends on cross-section area. High power density systems will thus be obtained with short and wide bed storage systems. System autonomy will be achieved by designing multiple storage tanks in parallel. The question of the charging strategy is then raised.

Let's assume there are **four storage tanks** connected in **parallel** to the remainder of the system. What is the best strategy between charging one reactor at a time, or equally dividing available heat into each reactor?

Numerical investigations have been conducted to address this question. A  $240 \text{ m}^3 \text{ h}^{-1}$  flow at  $180^\circ\text{C}$  is available four times for the same duration. Between each charging cycle, the storage tank has lost all its sensible energy and is back to its initial temperature. Three charging strategies are considered:

1. Charging all reactors with 25% of the inlet flow ( $60 \text{ m}^3 \text{ h}^{-1}$ ), four times.
2. Charging two reactors at a time with 50% of the inlet flow ( $120 \text{ m}^3 \text{ h}^{-1}$ ), two times each.
3. Charging one reactor at a time with 100% of the inlet flow ( $240 \text{ m}^3 \text{ h}^{-1}$ ), on one single charge.

Results are presented on figure V.15, which displays the desorption state as a function of charging time, for these three charging strategies. The **desorption state** is defined as the amount of water removed from the reactor at the end of the charging cycle(s), compared to the initial

amount of water (identical at the beginning of all experiments). Results clearly show **higher desorption states** are reached with the **one-at-a-time strategy**, unless each charging session lasts for more than four hours. In this case, the highest desorption stage is reached for all three strategies.

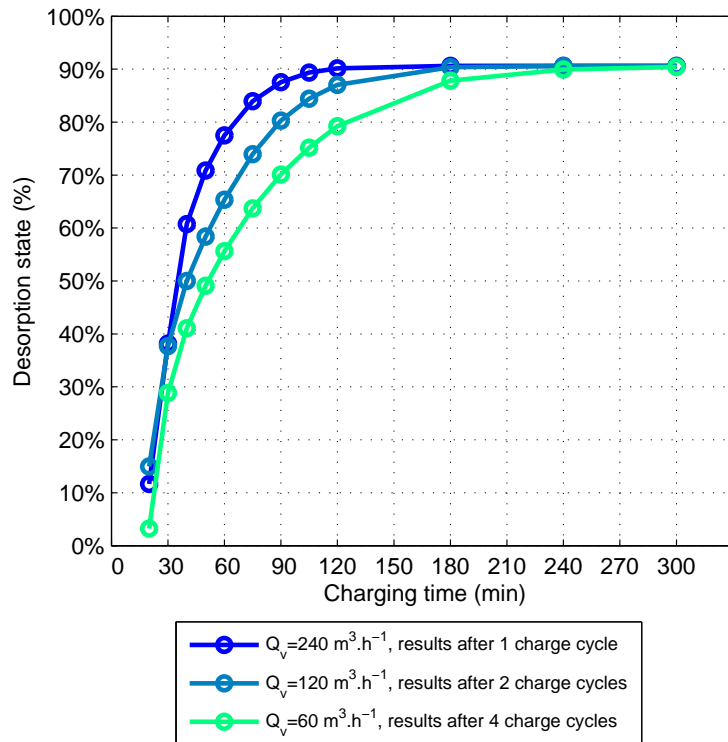


Figure V.15 – Fraction of water weight desorbed as a function of charging time, for three different charging strategies: 1 single charge at  $240 \text{ m}^3 \text{ h}^{-1}$ , 2 charge cycles at  $120 \text{ m}^3 \text{ h}^{-1}$  and 4 charge cycles at  $60 \text{ m}^3 \text{ h}^{-1}$ . The same amount of energy is provided to the tank in all three cases at the end of the charge cycle(s).

These results are clearly explainable by the same mechanisms as in the previous investigations on the influence of initial temperature. With a one at a time strategy, sensible heat is provided only one time to a smaller amount of adsorbent material. Once the material has reached high temperature, a maximum amount of energy is converted into sorption potential. On the other side, with four cycles, more heat is converted into sensible energy (and hence heat losses).

It is thus clearly demonstrated that with several storage tanks running in parallel, it is more interesting to concentrate the inlet flowrate on one reactor at a time than to charge all reactors together with a lower flowrate. Storage tanks will be discharged either one-at-a-time, or in parallel in order to meet power demand if a single reactor is not sufficient. Different levels of discharge are then expected to occur between reactors. If the **storage level** of each reactor is known, it enables the use of different levels of temperature flows. Indeed, at constant inlet humidity ratio and with one single reactor, the charging process is interesting above a given temperature that is function of the charging state. All temperatures below this threshold are not interesting. With several reactors unequally charged, the threshold temperature is different for each reactor. Lower-temperature flows can then be used for most discharged reactors while high-temperature

flows can be used to complete the charge of most charged reactors.

It is thus clearly demonstrated that the use of several storage tanks in **parallel** is **energetically more efficient** than one single reactor of equivalent volume. But multiplying small reactors necessarily tends to **increase** the **system volume** (at constant material volume) and **cost** (more complex piping network) while these are two very important issues for user acceptance.

## Conclusions

In the present chapter, a **sizing methodology** has been presented. It enables a **cross estimation** of outlet **power** and **storage capacity** as a function of climate, system autonomy, coverage fraction and discharging strategy. This is a good tool to optimize heating needs covered by the storage system with a minimum volume.

Furthermore, a reflection on the system integration to the building's HVAC system has been carried out. It came up to the following conclusions:

- Several **charging strategies** are possible depending mainly on the heat source.
- Several **discharging strategies** are worth considering depending on objectives pursued by the use of a thermal energy storage system.
- The **storage system integration** to the HVAC system requires at least **two heat exchangers**. One for heat recovery and heating on discharge. Another one for direct solar heating.
- **Initial temperature** has a strong influence on the performances of short charging phases.
- It is worth considering an **integrated heat exchanger** to:
  - enable **storage tank preheating** by mid temperature solar resource,
  - enable sensible heat storage and hence convert the adsorption storage system to a **combined sensible/adsorption storage system**. This would clearly **increase system autonomy** by the use of sensible store prior to the use of adsorption potential.
- It is worth considering the use of a **single high temperature auxiliary heater** to:
  - turn mid temperature solar resource into high temperature and hence use a **wider fraction of solar potential**,
  - avoid the use of individual auxiliary heaters and hence **lower investments costs**.

Alternative solution to the auxiliary heater is to use a dryer in order to reduce the amount of water in the inlet charging fluid, as suggested by [Mette et al. \(2013\)](#). It enables to maintain storage performances at a lower charging temperature. A comparison between the energy efficiency of both solutions must be achieved.

- The use of several storage tanks in **parallel** is energetically more efficient on both charge and discharge. In this case, **charging phases** better have to focus on **one reactor at a time**.

# Conclusions and perspectives

In this PhD thesis, all developments required to set up a numerical model describing heat and mass transfers in an adsorption heat storage tank have first been developed (chapter 2). Full coupled equations of the numerical model are presented on page 61. The consistency between numerical results and experimental data have been investigated and enhanced with the adjustment of some parameters, mostly on the adsorption model (chapter 3). Given the good accordance between experimental and numerical results, the model was considered as fully validated with a very good response to inlet humidity and temperature changes, and a few restrictions to inlet velocity changes.

Once the model was validated, numerous investigations were performed in order to enhance storage performances such as outlet power, storage density and system autonomy. An analysis of the heat conversion chain from heat source (charge) to heat released (discharge) has highlighted the need to think at two different and complementary scales: at the reactor (or material) scale to enhance heat and mass transfers within the storage tank (chapter 4) and at a system scale in order to create synergies between the HVAC system and the storage system (chapter 5).

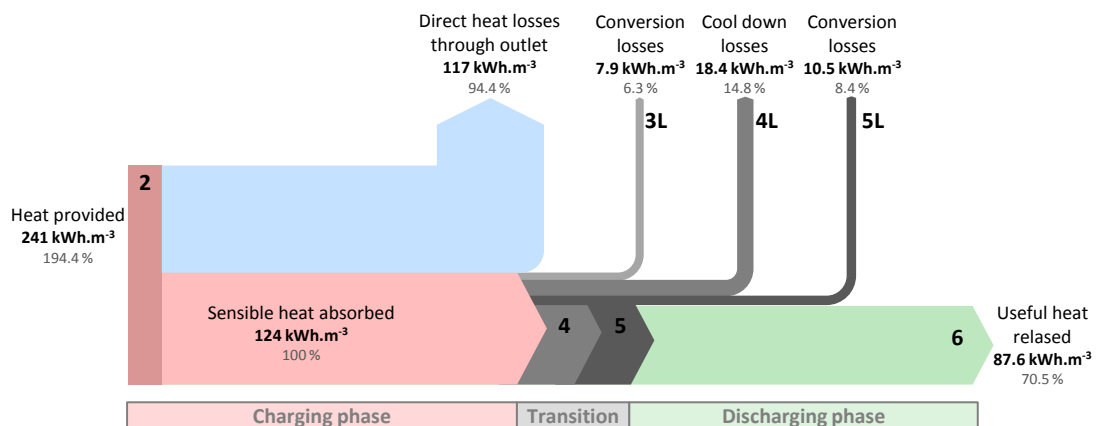


Figure V.1 – Sankey diagram representing heat conversion and losses (figure III.20c page 90)

The influence of eight physical parameters, five operating conditions and two geometrical characteristics on outlet power, energy storage density and system autonomy have been addressed. It came up to a guideline for material development, system design and control strategy optimization. Main conclusions on **material properties** are that the fluid density and adsorption capacity  $q_e$  are to be maximized while the difference between vapor heat capacity  $C_{p_v}$  and adsorbed layer heat capacity ( $c_a$ ) is to be minimized. Solid density  $\rho_s$  is also to be minimized if it



## Perspectives

Several tangible results have been consolidated in this PhD thesis. Nevertheless, some points have not been developed yet and new points have also been raised mainly in the last chapter. It naturally brings out several perspectives for future developments.

### Model developments

Care has been taken to develop an upgradeable numerical code to allow several geometries (1D, 2D axisymmetric or 3D) and systems (open or closed). This thesis focused on an open adsorption heat storage system but a closed system can easily be implemented. Closed systems introduce 3D solicitations and require at least 2D axisymmetric codes that will increase simulation time.

### Adsorption model

The adsorption model developed here is empirical and requires experimental data to be set, like most macroscopic models. It has limited our investigations to one adsorption material (13X zeolite). The development of a microscopic model that would depend only on material properties could enable the *calculation* of a macroscopic model parameters. This would open wide perspectives for material selection.

### Model reduction

Working conditions in the chosen test case were very comfortable since a 1D model was clearly sufficient to describe heat and mass transfers in the adsorbent bed. More complex geometries can lead to more complex mesh distribution and greater calculation times. In this case, the recourse to model reduction techniques could enhance simulation performances. It would also enable the implementation of a numerical model on others platforms such as Trnsys. The storage system simulation could then be dynamically coupled to the building simulation. A greater work could then be achieved on control strategies and performances assessment in realistic conditions.

### Integrated heat exchanger modeling

The modeling of the integrated heat exchanger would provide better information on the performances enhancement of a combined sensible/adsorption heat storage system, compared to a sensible storage system and to an adsorption storage system.

### Design of an experimental prototype

As this thesis was purely numerical, some guidelines are not necessarily in tune with economical and technical constraints. It would then be interesting to design a prototype based on the guidelines provided in the last chapter, in order to develop both technically and economically feasible solutions.



# Bibliography

- Ahn, H. and Lee, C.-H. (2003). Adsorption dynamics of water in layered bed for air-drying tsa process. *AIChE Journal*, 49(6):1601–1609.
- Ahn, H. and Lee, C.-H. (2004). Effects of capillary condensation on adsorption and thermal desorption dynamics of water in zeolite 13X and layered beds. *Chemical Engineering Science*, 59(13):2727–2743.
- Ampatzi, E., Knight, I., and Wiltshire, R. (2013). The potential contribution of solar thermal collection and storage systems to meeting the energy requirements of North European Housing. *Solar Energy*, 91(0):402–421.
- Archambeau, F, Méchitoua, N., and Sakiz, M. (2004). Code Saturne: A finite volume code for the computation of turbulent incompressible flows-Industrial applications. *International Journal on Finite Volumes*, 1(1):[http-www](http://www).
- Arzamendia Lopez, J. P., Kuznik, F, Baillis, D., and Virgone, J. (2013). Numerical modeling and experimental validation of a PCM to air heat exchanger. *Energy and Buildings*, 64(0):415–422.
- Azpiazu, M., Morquillas, J., and Vazquez, A. (2003). Heat recovery from a thermal energy storage based on the Ca(OH)<sub>2</sub>/CaO cycle. *Applied Thermal Engineering*, 23(6):733–741.
- Bales, C., Gantenbein, P, Hauer, A., Henning, H.-M., Jaenig, D., Kerskes, H., Núñez, T., and Visscher, K. (2005a). Thermal Properties of Materials for Thermo-chemical Storage of Solar Heat. *A Report of IEA Solar Heating and Cooling programme-Task*, 32.
- Bales, C., Gantenbein, P, Hauer, A., Jaehnig, D., Kerskes, H., Henning, H.-M., Nuñez, T., Visscher, K., Laevemann, E., and Peltzer, M. (2005b). Sorption and Thermo-Chemical Storage. In *Thermal energy storage for solar and low energy buildings : state of the art / by the IEA Solar Heating and Cooling Task 32*. Servei de Publicacions Universitat Lleida.
- Bales, C., Gantenbein, P, Jaenig, D., Kerskes, H., Summer, K., van Essen, M., and others (2008). Laboratory tests of chemical reactions and prototype sorption storage units. *A Report of IEA Solar Heating and Cooling programme-Task*, 32.
- Bauer, D., Marx, R., Nußbicker-Lux, J., Ochs, F, Heidemann, W., and Müller-Steinhagen, H. (2010). German central solar heating plants with seasonal heat storage. *International Conference CISBAT 2007*, 84(4):612–623.

- Belz, K., Kuznik, F., Werner, K., Schmidt, T., and Ruck, W. (2015). Thermal energy storage systems for heating and hot water in residential buildings. In *Advances in Thermal Energy Storage Systems*, pages 441–465. Elsevier.
- Bent, B. E. (2012). Adsorption.
- Braun, J. E. (2003). Load Control Using Building Thermal Mass. *Journal of Solar Energy Engineering*, 125(3):292.
- Brunauer, S., Deming, L. S., Deming, W. E., and Teller, E. (1940). On a theory of the van der Waals adsorption of gases. *Journal of the American Chemical Society*, 62(7):1723–1732.
- Carman, P. C. (1956). *Flow of gases through porous media*. Academic press.
- Darcy, H. (1856). *Les fontaines publiques de la ville de Dijon: exposition et application...* Victor Dalmont.
- Dubinin, M. (1960). The potential theory of adsorption of gases and vapors for adsorbents with energetically nonuniform surfaces. *Chemical Reviews*, 60(2):235–241.
- Duquesne, M. (2013). *Résolution et réduction d'un modèle non-linéaire de stockage d'énergie par adsorption sur des zéolites*. PhD thesis, Université de Bordeaux, Bordeaux, France.
- Duquesne, M., Toutain, J., Sempey, A., Ginestet, S., and Palomo del Barrio, E. (2014). Modeling of a nonlinear thermochemical energy storage by adsorption on zeolites. *Applied Thermal Engineering*, 71(1):469–480.
- Duval, X. (2012). Adsorption.
- Ergun, S. (1952). Fluid Flow through Packed Columns. *Chemical Engineering Progress*, 48:89–94.
- European commission (2009). Low energy buildings in Europe: Current state of play, definitions and best practice. [http://ec.europa.eu/energy/efficiency/doc/buildings/info\\_note.pdf](http://ec.europa.eu/energy/efficiency/doc/buildings/info_note.pdf).
- Eurostat (2010). Energy - Yearly Statistics 2008.
- Finck, C., Henquet, E., van Soest, C., Oversloot, H., de Jong, A.-J., Cuypers, R., and van 't Spijker, H. (2014). Experimental Results of a 3 kWh Thermochemical Heat Storage Module for Space Heating Application. *Energy Procedia*, 48:320–326.
- Fopah Lele, A., Kuznik, F., Rammelberg, H. U., Schmidt, T., and Ruck, W. K. (2015). Thermal decomposition kinetic of salt hydrates for heat storage systems. *Applied Energy*, 154:447–458.
- Fujimoto, S., Bilgen, E., and Ogura, H. (2002). CaO/Ca(OH)<sub>2</sub> chemical heat pump system. *Energy Conversion and Management*, 43(7):947–960.
- Fumey, B., Weber, R., Gantenbein, P., Daguene-Frick, X., Williamson, T., and Dorer, V. (2014). Development of a Closed Sorption Heat Storage Prototype. *8th International Renewable Energy Storage Conference and Exhibition (IRES 2013)*, 46(0):134–141.

- 
- Furmaniak, S., Gauden, P., Terzyk, A., and Rychlicki, G. (2008). Water adsorption on carbons - Critical review of the most popular analytical approaches. *Advances in Colloid and Interface Science*, 137(2):82–143.
- García, E. J., Pérez-Pellitero, J., Jallut, C., and Pirngruber, G. D. (2013). Modeling Adsorption Properties on the Basis of Microscopic, Molecular, and Structural Descriptors for Nonpolar Adsorbents. *Langmuir*, 29(30):9398–9409.
- Ghiaus, C. (2013). Causality issue in the heat balance method for calculating the design heating and cooling load. *Energy*, 50(0):292–301.
- Glueckauf, E. (1955). Theory of chromatography. Part 10.—Formulae for diffusion into spheres and their application to chromatography. *Transactions of the Faraday Society*, 51:1540–1551.
- Goncalves, E. (2005). Méthodes, Analyse et Calculs Numériques.
- Gondre, D., Johannes, K., and Kuznik, F. (2014). Specification requirements for inter-seasonal heat storage systems in a low energy residential house. *Energy Conversion and Management*, 77(0):628–636.
- Gray, W. G. and Miller, C. T. (2004). Examination of Darcy's Law for Flow in Porous Media with Variable Porosity. *Environmental Science & Technology*, 38(22):5895–5901.
- Guilleminot, J., Choisier, A., Chalfen, J., Nicolas, S., and Reymoney, J. (1993). Heat transfer intensification in fixed bed adsorbents. *Heat Recovery Systems and CHP*, 13(4):297–300.
- Hadorn, J.-C. (2005). The need for storage of heat and cold in a low energy buildings. In *Thermal energy storage for solar and low energy buildings : state of the art of storing heat*. Servei de Publicacions Universitat Lleida, iea task32 edition.
- Hasnain, S. (1998). Review on sustainable thermal energy storage technologies, Part I: heat storage materials and techniques. *Energy Conversion and Management*, 39(11):1127–1138.
- Hassanizadeh, S. M. and Gray, W. G. (1987). High velocity flow in porous media. *Transport in porous media*, 2(6):521–531.
- Hauer, A. (2007). ADSORPTION SYSTEMS FOR TES—DESIGN AND DEMONSTRATION PROJECTS. In Paksoy, H. Ö., editor, *Thermal Energy Storage for Sustainable Energy Consumption*, volume 234, pages 409–427. Springer Netherlands, Dordrecht.
- Hongois, S. (2011). *Stockage de chaleur inter-saisonnier par voie thermo-chimique pour le chauffage solaire de la maison individuelle*. PhD thesis, Institut National des Sciences Appliquées de Lyon, Villeurbanne.
- Hongois, S., Kuznik, F., Stevens, P., and Roux, J.-J. (2011). Development and characterisation of a new MgSO<sub>4</sub>-zeolite composite for long-term thermal energy storage. *Solar Energy Materials and Solar Cells*, 95(7):1831–1837.
-

- Hsu, C. T., Cheng, P., and Wong, K. W. (1995). A Lumped-Parameter Model for Stagnant Thermal Conductivity of Spatially Periodic Porous Media. *Journal of Heat Transfer*, 117(2):264.
- Hui, L., Edem, N. K., Nolwenn, L. P., and Lingai, L. (2011). Evaluation of a seasonal storage system of solar energy for house heating using different absorption couples. *Energy Conversion and Management*, 52(6):2427–2436.
- IEA (2009). IEA Energy Statistics - Electricity for European Union - 27.
- Jaffal, I., Inard, C., and Ghiaus, C. (2009). Fast method to predict building heating demand based on the design of experiments. *Energy and Buildings*, 41(6):669–677.
- Johannes, K., Kuznik, F., Hubert, J.-L., Durier, F., and Obrecht, C. (2015). Design and characterisation of a high powered energy dense zeolite thermal energy storage system for buildings. *Applied Energy*, 159:80–86.
- Kim, S. T., Ryu, J., and Kato, Y. (2013). Optimization of magnesium hydroxide composite material mixed with expanded graphite and calcium chloride for chemical heat pumps. *Applied Thermal Engineering*, 50(1):485–490.
- Kuwahara, F., Shirota, M., and Nakayama, A. (2001). A numerical study of interfacial convective heat transfer coefficient in two-energy equation model for convection in porous media. *International Journal of Heat and Mass Transfer*, 44(6):1153–1159.
- Kuznik, F., Arzamendia Lopez, J. P., Baillis, D., and Johannes, K. (2015a). Phase change material wall optimization for heating using metamodeling. *Energy and Buildings*, 106:216–224.
- Kuznik, F., Johannes, K., and Obrecht, C. (2015b). Chemisorption heat storage in buildings: State-of-the-art and outlook. *Energy and Buildings*, 106:183–191.
- Kuznik, F., Virgone, J., and Johannes, K. (2011). In-situ study of thermal comfort enhancement in a renovated building equipped with phase change material wallboard. *Renewable Energy*, 36(5):1458–1462.
- Labat, M., Virgone, J., David, D., and Kuznik, F. (2014). Experimental assessment of a PCM to air heat exchanger storage system for building ventilation application. *Applied Thermal Engineering*, 66(1-2):375–382.
- Lagergren, S. (1898). About the theory of so-called adsorption of soluble substances.
- Li, Z. and Yang, R. T. (1999). Concentration profile for linear driving force model for diffusion in a particle. *AIChE Journal*, 45(1):196–200.
- Liu, Y., Zheng, X., and Dai, R. (2014). Numerical study of flow maldistribution and depressurization strategies in a small-scale axial adsorber. *Adsorption*, 20(5-6):757–768.
- Makni, F. (2012). *Développement d'un outil de simulation 2D - 3D pour l'amélioration de la conception des adsorbants dédiés aux systèmes de climatisation*. PhD thesis, Conservatoire National des Arts et Métiers, Paris.

- Markus Kottek, Grieser, J., Beck, C., Rudolf, B., and Rubel, F. (2006). World Maps of Köppen-Geiger climate classification updated. *Meteorologische Zeitschrift*, page 5.
- Mastronardo, E., Bonaccorsi, L., Kato, Y., Piperopoulos, E., and Milone, C. (2016). Efficiency improvement of heat storage materials for MgO/H<sub>2</sub>O/Mg(OH)<sub>2</sub> chemical heat pumps. *Applied Energy*, 162:31–39.
- Metchueng Kamdem, S., Johannes, K., Kuznik, F., Roux, J.-J., and Hubert, J.-L. (2012). Etude des transferts de chaleur et de masse and un système de stockage thermodynamique. Nantes.
- Mette, B., Kerskes, H., and Drück, H. (2012). Concepts of long-term thermochemical energy storage for solar thermal applications – Selected examples. *Energy Procedia*, 30:321–330.
- Mette, B., Kerskes, H., and Drück, H. (2014). Experimental and Numerical Investigations of Different Reactor Concepts for Thermochemical Energy Storage. *Energy Procedia*, 57:2380–2389.
- Mette, B., Kerskes, H., Drück, H., and Müller-Steinhagen, H. (2013). New highly efficient regeneration process for thermochemical energy storage. *Applied Energy*, 109:352–359.
- Michel, B., Mazet, N., Mauran, S., Stitou, D., and Xu, J. (2012). Thermochemical process for seasonal storage of solar energy: Characterization and modeling of a high density reactive bed. *Asia-Pacific Forum on Renewable Energy 2011*, 47(1):553–563.
- Michel, B., Neveu, P., and Mazet, N. (2014). Comparison of closed and open thermochemical processes, for long-term thermal energy storage applications. *Energy*, 72:702–716.
- Ministère de l'emploi, de la cohésion sociale et du logement (2006). Réglementation thermique 2005.
- Molenda, M., Stengler, J., Linder, M., and Wörner, A. (2013). Reversible hydration behavior of CaCl<sub>2</sub> at high H<sub>2</sub>O partial pressures for thermochemical energy storage. *Thermochimica Acta*, 560:76–81.
- Neuhaus, D. (2013). Water adsorption and desorption pretreatment of surfaces increases the maximum amount of adsorbed water molecules by a multiple. *Adsorption*, 19(6):1127–1135.
- N'Tsoukpoe, K. E., Le Pierrès, N., and Luo, L. (2012). Experimentation of a LiBr-H<sub>2</sub>O absorption process for long term solar thermal storage. *Energy Procedia*, 30:331–341.
- N'Tsoukpoe, K. E., Liu, H., Le Pierrès, N., and Luo, L. (2009). A review on long-term sorption solar energy storage. *Renewable and Sustainable Energy Reviews*, 13(9):2385–2396.
- Osello, A., Acquaviva, A., Aghemo, C., Blaso, L., Dalmasso, D., Erba, D., Fracastoro, G., Gondre, D., Jahn, M., Macii, E., Patti, E., Pellegrino, A., Piumatti, P., Pramudianto, F., Savoyat, J., Spirito, M., Tomasi, R., and Virgone, J. (2013). Energy saving in existing buildings by an intelligent use of interoperable ICTs. *Energy Efficiency*, 6(4):707–723.

- Pardo, P., Deydier, A., Anxionnaz-Minvielle, Z., Rougé, S., Cabassud, M., and Cognet, P. (2014). A review on high temperature thermochemical heat energy storage. *Renewable and Sustainable Energy Reviews*, 32:591–610.
- Patankar, S. V. (1980). *Numerical heat transfer and fluid flow*. Hemisphere Pub. Corp. ; McGraw-Hill, Washington; New York.
- Pinel, P., Cruickshank, C. A., Beausoleil-Morrison, I., and Wills, A. (2011). A review of available methods for seasonal storage of solar thermal energy in residential applications. *Renewable and Sustainable Energy Reviews*, 15(7):3341–3359.
- Pons, M. and Grenier, P. (1986). SOLAR ICE MAKER WORKING WITH ACTIVATED CARBON-METHANOL ADSORBENT-ADSORBATE PAIR. In *Intersol Eighty Five*, pages 731–735. Elsevier.
- Qiu, H., Lv, L., Pan, B.-c., Zhang, Q.-j., Zhang, W.-m., and Zhang, Q.-x. (2009). Critical review in adsorption kinetic models. *Journal of Zhejiang University Science A*, 10(5):716–724.
- Ramos, C. (2013). What microscopic part of the Sun's power do we receive? (available online at [www.greensaturdays.com/en/](http://www.greensaturdays.com/en/)). <http://www.greensaturdays.com/en/>.
- Rathgeber, C., Lävemann, E., and Hauer, A. (2015). Economic top-down evaluation of the costs of energy storages—A simple economic truth in two equations. *Journal of Energy Storage*, 2:43–46.
- Rhônealénergie-Environnement (2004). La climatisation solaire.
- Ruthven, D. (1984). *Principles of Adsorption and Adsorption Processes*. A Wiley-Interscience publication. Wiley.
- Salomon, T., Marignac, Y., Jedliczka, M., and others (2012). *Manifeste Négawatt: réussir la transition énergétique*. Éditions Actes Sud.
- Schneider, B. (2013). Storing solar energy in the ground. *FIZ Karlsruhe - Leibniz Institute for Information Infrastructure*.
- Seo, Y., Jo, S.-H., Ryu, C. K., and Yi, C.-K. (2007). Effects of water vapor pretreatment time and reaction temperature on CO<sub>2</sub> capture characteristics of a sodium-based solid sorbent in a bubbling fluidized-bed reactor. *Chemosphere*, 69(5):712–718.
- Sharma, A., Tyagi, V., Chen, C., and Buddhi, D. (2009). Review on thermal energy storage with phase change materials and applications. *Renewable and Sustainable Energy Reviews*, 13(2):318–345.
- Sircar, S. and Hufton, J. (2000). Why Does the Linear Driving Force Model for Adsorption Kinetics Work? *Adsorption*, 6(2):137–147.
- Spitz, C., Mora, L., Wurtz, E., and Jay, A. (2012). Practical application of uncertainty analysis and sensitivity analysis on an experimental house. *Cool Roofs, Cool Pavements, Cool Cities, and Cool World*, 55(0):459–470.

- 
- Streicher, W., Schultz, J., Solé, C., Cabeza, Luisa F., Bony, J., and Heinz, Andreas (2007). Laboratory prototypes of PCM storage units. *Report C3 of Subtask C within the IEA solar heating and cooling programme task 32*, 32.
- Streicher, W., Schultz, Jørgen, Solé, Christian, Cabeza, Luisa F., Bony, Jacques, Citherlet, Stéphane, and Heinz, Andreas (2008). Final report of Subtask C “Phase Change Materials” The overview. *A Report of IEA Solar Heating and Cooling programme -Task 32*.
- Sun, L., Ben Amar, N., and Meunier, F. (1995). Numerical study on coupled heat and mass transfers in an absorber with external fluid heating. *Heat Recovery Systems and CHP*, 15(1):19–29.
- Sun, L.-M. and Meunier, F. (2003). Adsorption : Aspects théoriques.
- Tatsidjoudoug, P. (2014). Solar heat storage process by adsorption for building heating: modelling and numerical simulations.
- Tatsidjoudoug, P., Le Pierrès, N., Heintz, J., Lagre, D., Luo, L., and Durier, F. (2016). Experimental and numerical investigations of a zeolite 13X/water reactor for solar heat storage in buildings. *Energy Conversion and Management*, 108:488–500.
- Tatsidjoudoug, P., Le Pierrès, N., and Luo, L. (2013). A review of potential materials for thermal energy storage in building applications. *Renewable and Sustainable Energy Reviews*, 18(0):327–349.
- TESS (2008). TRNSYS - TESS : Thermal Energy System Specialists.
- The university of York (2013). Chemical reactors.
- Thullner, K. (2010). Low-energy buildings in Europe - Standards, criteria and consequences - A study of nine European countries. Technical Report TVIT-10/5019, Lunds tekniska högskola Lunds universitet, Lunds.
- Trausel, F., de Jong, A.-J., and Cuypers, R. (2014). A Review on the Properties of Salt Hydrates for Thermochemical Storage. *Energy Procedia*, 48:447–452.
- Université catholique de Louvain (2015). La machine frigorifique à ab/adsorption.
- Van Berkel, J. (2005). Storage of solar energy in chemical reactions. In *Thermal energy storage for solar and low energy buildings : state of the art of storing heat*. Iea task32 edition.
- Wakao, N. and Kagei, S. (1982). *Heat and mass transfer in packed beds*, volume 1. Taylor & Francis.
- Wang, Y. and LeVan, M. D. (2009). Adsorption Equilibrium of Carbon Dioxide and Water Vapor on Zeolites 5A and 13X and Silica Gel: Pure Components. *Journal of Chemical & Engineering Data*, 54(10):2839–2844.

- Whiting, G., Grondin, D., Bennici, S., and Auroux, A. (2013). Heats of water sorption studies on zeolite–MgSO<sub>4</sub> composites as potential thermochemical heat storage materials. *Solar Energy Materials and Solar Cells*, 112(0):112–119.
- Wongsuwan, W., Kumar, S., Neveu, P., and Meunier, F. (2001). A review of chemical heat pump technology and applications. *Applied Thermal Engineering*, 21(15):1489–1519.
- Xu, J., Wang, R., and Li, Y. (2013). A review of available technologies for seasonal thermal energy storage. *Solar Energy*.
- Yu, N., Wang, R., and Wang, L. (2013). Sorption thermal storage for solar energy. *Progress in Energy and Combustion Science*, 39(5):489–514.
- Zalba, B., Mariñ, J. M., Cabeza, L. F., and Mehling, H. (2003). Review on thermal energy storage with phase change: materials, heat transfer analysis and applications. *Applied Thermal Engineering*, 23(3):251–283.
- Zettl, B., Englmaier, G., and Steinmaurer, G. (2014). Development of a revolving drum reactor for open-sorption heat storage processes. *Applied Thermal Engineering*, 70(1):42–49.
- Zhang, X., Li, M., Shi, W., Wang, B., and Li, X. (2014). Experimental investigation on charging and discharging performance of absorption thermal energy storage system. *Energy Conversion and Management*, 85:425–434.
- Zhao, H.-x. and Magoulès, F. (2012). A review on the prediction of building energy consumption. *Renewable and Sustainable Energy Reviews*, 16(6):3586–3592.
- Zondag, H., Kikkert, B., Smeding, S., de Boer, R., and Bakker, M. (2013). Prototype thermochemical heat storage with open reactor system. *Applied Energy*, 109:360–365.
- Zou, R. and Yu, A. (1995). The packing of spheres in a cylindrical container: the thickness effect. *Chemical Engineering Science*, 50(9):1504–1507.

# Appendices



# Appendices

## A Appendix 1: Detailed coefficients of statistical models

The following section provides detailed results of statistical models for the prediction of outlet power, heat storage density and system autonomy. Each statistical model is made of different coefficients and independent variables. It is possible to select from 1 to 128 coefficient/variables pairs. The associated error values is provided in tables 2, 4 and 6. Table 1 provides information on the correspondence between coded variables used for the statistical model generation and associated physical variables.

Table 1 – Correspondence between coded variables  $x_i$  and physical variables and minimum/maximum values used for nondimensionalization

$x_i$	Physical variables	Minimum value	Maximum value
$x_1$	$L_z$	0.1 m	0.5 m
$x_2$	$S$	0.2 m <sup>2</sup>	0.8 m <sup>2</sup>
$x_3$	$\varphi_{in,charge}$	0.1 %	0.5 %
$x_4$	$\varphi_{in,discharge}$	50 %	80 %
$x_5$	$\dot{v}_{in,charge}$	60 m <sup>3</sup> h <sup>-1</sup>	250 m <sup>3</sup> h <sup>-1</sup>
$x_6$	$\dot{v}_{in,discharge}$	60 m <sup>3</sup> h <sup>-1</sup>	250 m <sup>3</sup> h <sup>-1</sup>
$x_7$	$T_{in,charge}$	110 °C	180 °C

### A.1 Statistical model of outlet power value

The following table displays sorted coefficients labels and values of a statistical model for the prediction of **outlet power density**. It also provides the mean relative error value of a statistical model with  $m$  coefficients, and the dimensionless sum of squared differences between the calculated value and the truncated statistical model value.

Table 2 – sorted coefficients labels and values and error characteristics of a statistical model for the prediction of outlet power density

A. Appendix 1: Detailed coefficients of statistical models

$m$	Coefficients labels	values	Mean error	$\epsilon_m^{2*}$	$m$	Coefficients labels	values	Mean error	$\epsilon_m^{2*}$
1	$c$	21.8	160.2%	147.5	65	$x_3^*.x_6^*$	0.41	0.94%	0.57
2	$x_6^*$	12.7	72.1%	103.8	66	$x_2^*.x_3^*.x_7^*$	0.41	0.91%	0.52
3	$x_1^*$	-12.3	-10.8%	63	67	$x_1^*.x_2^*.x_3^*.x_7^*$	-0.41	0.89%	0.48
4	$x_1^*.x_6^*$	-6.9	20.8%	50.1	68	$x_1^*.x_3^*.x_6^*.x_7^*$	0.4	0.78%	0.44
5	$x_4^*$	5.8	4%	40.9	69	$x_1^*.x_4^*.x_7^*$	0.36	0.69%	0.4
6	$x_4^*.x_6^*$	3.9	10.4%	36.7	70	$x_3^*$	-0.36	0.26%	0.36
7	$x_1^*.x_4^*$	-3.5	16.5%	33.3	71	$x_1^*.x_4^*.x_6^*.x_7^*$	0.34	0.3%	0.33
8	$x_2^*$	2.7	15.5%	31.3	72	$x_2^*.x_3^*.x_4^*.x_6^*$	0.33	0.25%	0.3
9	$x_1^*.x_2^*$	-2.7	14.6%	29.3	73	$x_1^*.x_2^*.x_3^*.x_4^*.x_6^*$	-0.33	0.2%	0.27
10	$x_2^*.x_3^*$	-2.7	13.7%	27.4	74	$x_1^*.x_2^*.x_4^*.x_6^*$	0.33	0.15%	0.24
11	$x_1^*.x_2^*.x_3^*$	2.7	12.7%	25.4	75	$x_2^*.x_4^*.x_6^*$	-0.33	0.1%	0.21
12	$x_7^*$	-2.7	8.9%	23.5	76	$x_1^*.x_3^*.x_4^*$	0.28	0.02%	0.19
13	$x_1^*.x_4^*.x_6^*$	-2.5	5.8%	21.8	77	$x_5^*.x_6^*.x_7^*$	-0.24	0.04%	0.18
14	$x_2^*.x_6^*$	2.3	5.4%	20.4	78	$x_3^*.x_5^*.x_6^*.x_7^*$	0.19	0.04%	0.17
15	$x_1^*.x_2^*.x_6^*$	-2.3	4.8%	19	79	$x_5^*.x_7^*$	-0.18	0.01%	0.16
16	$x_1^*.x_2^*.x_3^*.x_6^*$	2.3	4.4%	17.6	80	$x_4^*.x_5^*.x_6^*.x_7^*$	-0.18	0%	0.15
17	$x_2^*.x_3^*.x_6^*$	-2.3	3.9%	16.2	81	$x_3^*.x_4^*.x_5^*.x_6^*.x_7^*$	0.17	0%	0.14
18	$x_6^*.x_7^*$	-1.7	5.4%	15.3	82	$x_2^*.x_3^*.x_5^*.x_6^*.x_7^*$	-0.17	-0.01%	0.14
19	$x_1^*.x_7^*$	1.6	6.8%	14.6	83	$x_1^*.x_2^*.x_4^*.x_5^*.x_6^*.x_7^*$	-0.17	-0.01%	0.13
20	$x_5^*$	1.4	6.3%	14.1	84	$x_1^*.x_2^*.x_5^*.x_6^*.x_7^*$	-0.17	-0.01%	0.12
21	$x_3^*.x_5^*$	-1.3	6%	13.6	85	$x_2^*.x_3^*.x_4^*.x_5^*.x_6^*.x_7^*$	-0.17	-0.02%	0.11
22	$x_3^*.x_7^*$	-1.3	4.9%	13.2	86	$x_1^*.x_2^*.x_3^*.x_4^*.x_5^*.x_6^*.x_7^*$	0.17	-0.02%	0.11
23	$x_4^*.x_5^*$	1.3	4.8%	12.8	87	$x_2^*.x_4^*.x_5^*.x_6^*.x_7^*$	0.17	-0.02%	0.1
24	$x_3^*.x_4^*.x_5^*$	-1.2	4.7%	12.4	88	$x_1^*.x_2^*.x_3^*.x_5^*.x_6^*.x_7^*$	0.16	-0.03%	0.09
25	$x_5^*.x_6^*$	1.2	4.8%	12	89	$x_2^*.x_5^*.x_6^*.x_7^*$	0.16	-0.03%	0.08
26	$x_2^*.x_5^*$	-1.2	4.6%	11.6	90	$x_1^*.x_3^*.x_4^*.x_5^*.x_6^*.x_7^*$	-0.16	-0.03%	0.08
27	$x_1^*.x_2^*.x_5^*$	1.2	4.5%	11.2	91	$x_1^*.x_4^*.x_5^*.x_6^*.x_7^*$	0.15	-0.03%	0.07
28	$x_1^*.x_2^*.x_3^*.x_5^*$	-1.2	4.3%	10.8	92	$x_1^*.x_3^*.x_5^*.x_6^*.x_7^*$	-0.14	-0.04%	0.07
29	$x_2^*.x_4^*.x_5^*$	-1.2	4.2%	10.3	93	$x_3^*.x_4^*.x_7^*$	-0.14	0.01%	0.06
30	$x_1^*.x_2^*.x_4^*.x_5^*$	1.2	4%	9.9	94	$x_1^*.x_2^*.x_6^*.x_7^*$	0.12	0.01%	0.06
31	$x_2^*.x_3^*.x_4^*.x_5^*$	1.2	3.9%	9.5	95	$x_2^*.x_6^*.x_7^*$	-0.12	0.02%	0.05
32	$x_1^*.x_2^*.x_3^*.x_4^*.x_5^*$	-1.2	3.8%	9.1	96	$x_1^*.x_2^*.x_3^*.x_6^*.x_7^*$	-0.12	0.02%	0.05
33	$x_2^*.x_3^*.x_5^*$	1.2	3.6%	8.7	97	$x_2^*.x_3^*.x_6^*.x_7^*$	0.12	0.03%	0.04
34	$x_1^*.x_3^*.x_4^*.x_5^*$	1.2	3.4%	8.3	98	$x_3^*.x_5^*.x_7^*$	0.1	0.03%	0.04
35	$x_1^*.x_4^*.x_5^*$	-1.2	3.2%	7.9	99	$x_1^*.x_2^*.x_3^*.x_4^*.x_6^*.x_7^*$	0.1	0.03%	0.04
36	$x_3^*.x_5^*.x_6^*$	-1.2	3.2%	7.6	100	$x_2^*.x_3^*.x_4^*.x_6^*.x_7^*$	-0.1	0.02%	0.04
37	$x_1^*.x_3^*.x_5^*$	1.1	3.1%	7.2	101	$x_1^*.x_2^*.x_4^*.x_6^*.x_7^*$	-0.1	0.02%	0.03
38	$x_4^*.x_5^*.x_6^*$	1.1	3%	6.9	102	$x_2^*.x_4^*.x_6^*.x_7^*$	0.1	0.02%	0.03
39	$x_3^*.x_4^*.x_5^*.x_6^*$	-1.1	2.9%	6.5	103	$x_1^*.x_5^*.x_6^*.x_7^*$	0.09	0.01%	0.03
40	$x_2^*.x_5^*.x_6^*$	-1.1	2.8%	6.2	104	$x_1^*.x_3^*.x_4^*.x_7^*$	0.09	-0.01%	0.03

A. Appendix 1: Detailed coefficients of statistical models

$m$	Coefficients labels	values	Mean error	$\epsilon_m^{2*}$	$m$	Coefficients labels	values	Mean error	$\epsilon_m^{2*}$
41	$x_1^*.x_2^*.x_4^*.x_5^*.x_6^*$	1.1	2.7%	5.8	105	$x_4^*.x_5^*.x_7^*$	-0.09	0%	0.02
42	$x_1^*.x_2^*.x_3^*.x_4^*.x_5^*.x_6^*$	-1.1	2.6%	5.5	106	$x_2^*.x_4^*$	0.08	0%	0.02
43	$x_2^*.x_4^*.x_5^*.x_6^*$	-1.1	2.5%	5.1	107	$x_3^*.x_4^*.x_5^*.x_7^*$	0.07	0%	0.02
44	$x_2^*.x_3^*.x_4^*.x_5^*.x_6^*$	1.1	2.4%	4.8	108	$x_1^*.x_2^*.x_4^*$	-0.07	0%	0.02
45	$x_1^*.x_2^*.x_5^*.x_6^*$	1.1	2.3%	4.5	109	$x_2^*.x_3^*.x_4^*$	-0.07	0%	0.02
46	$x_1^*.x_2^*.x_3^*.x_5^*.x_6^*$	-1.1	2.2%	4.1	110	$x_1^*.x_2^*.x_3^*.x_4^*$	0.07	0%	0.02
47	$x_2^*.x_3^*.x_5^*.x_6^*$	1.1	2.1%	3.8	111	$x_1^*.x_3^*.x_4^*.x_6^*.x_7^*$	-0.07	-0.01%	0.01
48	$x_1^*.x_3^*.x_4^*.x_5^*.x_6^*$	1.1	2.1%	3.4	112	$x_2^*.x_3^*.x_5^*.x_7^*$	-0.07	-0.01%	0.01
49	$x_1^*.x_6^*.x_7^*$	1.1	1.4%	3.1	113	$x_1^*.x_2^*.x_5^*.x_7^*$	-0.07	0%	0.01
50	$x_1^*.x_4^*.x_5^*.x_6^*$	-1.1	1.4%	2.8	114	$x_2^*.x_3^*.x_4^*.x_5^*.x_7^*$	-0.07	0%	0.01
51	$x_1^*.x_3^*.x_5^*.x_6^*$	1.1	1.3%	2.5	115	$x_1^*.x_2^*.x_3^*.x_5^*.x_7^*$	0.07	0%	0.01
52	$x_1^*.x_3^*.x_6^*$	-1.1	1.6%	2.1	116	$x_1^*.x_2^*.x_4^*.x_5^*.x_7^*$	-0.07	0%	0.01
53	$x_1^*.x_5^*$	-1.1	1.8%	1.8	117	$x_2^*.x_4^*.x_5^*.x_7^*$	0.07	0%	0.01
54	$x_1^*.x_5^*.x_6^*$	-1	1.5%	1.6	118	$x_1^*.x_2^*.x_3^*.x_4^*.x_5^*.x_7^*$	0.07	0%	0.01
55	$x_1^*.x_3^*.x_7^*$	0.86	1.9%	1.4	119	$x_2^*.x_5^*.x_7^*$	0.07	0%	0
56	$x_1^*.x_3^*$	-0.72	1%	1.2	120	$x_1^*.x_3^*.x_4^*.x_5^*.x_7^*$	-0.06	0%	0
57	$x_3^*.x_4^*.x_6^*$	-0.65	0.72%	1.1	121	$x_1^*.x_5^*.x_7^*$	-0.05	-0.01%	0
58	$x_3^*.x_6^*.x_7^*$	-0.65	1.1%	0.99	122	$x_1^*.x_4^*.x_5^*.x_7^*$	0.05	-0.01%	0
59	$x_4^*.x_7^*$	-0.57	1.4%	0.9	123	$x_1^*.x_2^*.x_3^*.x_4^*.x_7^*$	-0.04	-0.01%	0
60	$x_1^*.x_3^*.x_4^*.x_6^*$	0.54	1.4%	0.82	124	$x_1^*.x_2^*.x_4^*.x_7^*$	0.04	-0.01%	0
61	$x_4^*.x_6^*.x_7^*$	-0.46	1.2%	0.76	125	$x_2^*.x_3^*.x_4^*.x_7^*$	0.04	-0.01%	0
62	$x_3^*.x_4^*$	-0.45	1.5%	0.7	126	$x_2^*.x_4^*.x_7^*$	-0.04	-0.01%	0
63	$x_2^*.x_7^*$	-0.41	1.4%	0.66	127	$x_3^*.x_4^*.x_6^*.x_7^*$	0.04	0%	0
64	$x_1^*.x_2^*.x_7^*$	0.41	1.4%	0.61	128	$x_1^*.x_3^*.x_5^*.x_7^*$	-0.03	0%	0

A.2 Statistical model of storage density

The following table displays sorted coefficients labels and values of a statistical model for the prediction of **storage density**. It also provides the mean relative error value of a statistical model with  $m$  coefficients, and the dimensionless sum of squared differences between the calculated value and the truncated statistical model value.

Table 4 – sorted coefficients labels and values and error characteristics of a statistical model for the prediction of storage density

$m$	Coefficients labels	values	Mean error	$\epsilon_m^{2*}$	$m$	Coefficients labels	values	Mean error	$\epsilon_m^{2*}$
1	$c$	63.2	8.9%	10.2	65	$x_1^*.x_3^*.x_5^*.x_6^*.x_7^*$	0.1	0%	0.01
2	$x_3^*$	-12.8	4.4%	4.9	66	$x_1^*.x_2^*.x_3^*.x_5^*.x_6^*.x_7^*$	-0.1	0%	0.01
3	$x_4^*$	8.9	1.8%	2.4	67	$x_1^*.x_4^*.x_5^*.x_6^*.x_7^*$	-0.1	0%	0.01

A. Appendix 1: Detailed coefficients of statistical models

$m$	Coefficients labels	values	Mean error	$\epsilon_m^{2*}$	$m$	Coefficients labels	values	Mean error	$\epsilon_m^{2*}$
4	$x_3^*.x_7^*$	-4.2	1.3%	1.9	68	$x_1^*.x_3^*.x_4^*.x_5^*.x_6^*.x_7^*$	0.1	0%	0.01
5	$x_1^*$	-3.3	1.1%	1.5	69	$x_2^*.x_3^*.x_4^*.x_5^*.x_6^*.x_7^*$	0.1	0%	0.01
6	$x_1^*.x_3^*$	2.3	0.98%	1.3	70	$x_1^*.x_2^*.x_4^*.x_5^*.x_6^*.x_7^*$	0.1	0%	0.01
7	$x_7^*$	1.9	0.97%	1.2	71	$x_1^*.x_2^*.x_3^*.x_4^*.x_5^*.x_6^*.x_7^*$	-0.1	0%	0.01
8	$x_1^*.x_2^*$	1.6	0.92%	1.1	72	$x_2^*.x_4^*.x_5^*.x_6^*.x_7^*$	-0.1	0%	0
9	$x_1^*.x_2^*.x_3^*$	-1.6	0.88%	1	73	$x_3^*.x_4^*.x_5^*.x_6^*.x_7^*$	-0.1	0%	0
10	$x_2^*.x_3^*$	1.6	0.83%	0.96	74	$x_2^*.x_3^*.x_5^*.x_6^*.x_7^*$	0.1	0%	0
11	$x_2^*$	-1.5	0.79%	0.89	75	$x_4^*.x_5^*.x_6^*.x_7^*$	0.1	0%	0
12	$x_5^*$	1.4	0.73%	0.82	76	$x_3^*.x_5^*.x_6^*.x_7^*$	-0.1	0%	0
13	$x_1^*.x_7^*$	1.4	0.68%	0.76	77	$x_2^*.x_5^*.x_6^*.x_7^*$	-0.1	0%	0
14	$x_1^*.x_5^*$	1.4	0.62%	0.71	78	$x_3^*.x_6^*$	0.1	0%	0
15	$x_3^*.x_4^*$	1.3	0.44%	0.65	79	$x_5^*.x_6^*.x_7^*$	0.1	0%	0
16	$x_1^*.x_3^*.x_4^*$	-1.3	0.4%	0.6	80	$x_3^*.x_5^*.x_7^*$	0.09	0%	0
17	$x_1^*.x_2^*.x_3^*.x_4^*$	1.3	0.37%	0.54	81	$x_3^*.x_6^*.x_7^*$	-0.08	0%	0
18	$x_2^*.x_3^*.x_4^*$	-1.3	0.34%	0.49	82	$x_3^*.x_4^*.x_6^*.x_7^*$	-0.07	0%	0
19	$x_2^*.x_4^*$	1.3	0.31%	0.43	83	$x_1^*.x_3^*.x_4^*.x_6^*.x_7^*$	0.06	0%	0
20	$x_1^*.x_2^*.x_4^*$	-1.3	0.28%	0.38	84	$x_2^*.x_3^*.x_6^*.x_7^*$	0.06	0%	0
21	$x_6^*$	1.2	0.25%	0.33	85	$x_1^*.x_2^*.x_3^*.x_4^*.x_6^*.x_7^*$	-0.06	0%	0
22	$x_4^*.x_6^*$	1.1	0.22%	0.29	86	$x_2^*.x_3^*.x_4^*.x_6^*.x_7^*$	0.06	0%	0
23	$x_4^*.x_7^*$	1.1	0.18%	0.25	87	$x_2^*.x_4^*.x_6^*.x_7^*$	-0.06	0%	0
24	$x_1^*.x_5^*.x_7^*$	-0.99	0.15%	0.22	88	$x_1^*.x_2^*.x_4^*.x_6^*.x_7^*$	0.06	0%	0
25	$x_1^*.x_3^*.x_7^*$	-0.9	0.13%	0.2	89	$x_2^*.x_6^*.x_7^*$	-0.06	0%	0
26	$x_1^*.x_4^*$	0.83	0.11%	0.17	90	$x_1^*.x_6^*.x_7^*$	0.06	0%	0
27	$x_3^*.x_5^*$	-0.77	0.1%	0.16	91	$x_1^*.x_2^*.x_3^*.x_6^*.x_7^*$	-0.06	0%	0
28	$x_1^*.x_3^*.x_5^*$	-0.72	0.09%	0.14	92	$x_1^*.x_2^*.x_6^*.x_7^*$	0.06	0%	0
29	$x_5^*.x_7^*$	-0.67	0.07%	0.12	93	$x_1^*.x_3^*.x_6^*.x_7^*$	0.06	0%	0
30	$x_1^*.x_6^*$	0.67	0.06%	0.11	94	$x_1^*.x_4^*.x_6^*.x_7^*$	0.05	0%	0
31	$x_2^*.x_7^*$	0.66	0.06%	0.1	95	$x_1^*.x_5^*.x_6^*$	0.04	0%	0
32	$x_2^*.x_3^*.x_7^*$	-0.65	0.05%	0.08	96	$x_1^*.x_3^*.x_5^*.x_6^*$	-0.03	0%	0
33	$x_1^*.x_2^*.x_3^*.x_7^*$	0.65	0.04%	0.07	97	$x_2^*.x_5^*$	-0.03	0%	0
34	$x_1^*.x_2^*.x_7^*$	-0.64	0.03%	0.06	98	$x_1^*.x_2^*.x_5^*.x_6^*$	-0.03	0%	0
35	$x_1^*.x_4^*.x_6^*$	0.62	0.02%	0.04	99	$x_1^*.x_2^*.x_3^*.x_5^*.x_6^*$	0.03	0%	0
36	$x_6^*.x_7^*$	0.47	0.02%	0.04	100	$x_1^*.x_2^*.x_3^*.x_5^*$	-0.03	0%	0
37	$x_4^*.x_6^*.x_7^*$	0.46	0.02%	0.03	101	$x_1^*.x_4^*.x_5^*.x_6^*$	0.03	0%	0
38	$x_1^*.x_3^*.x_5^*.x_7^*$	0.4	0.01%	0.02	102	$x_2^*.x_3^*.x_5^*.x_6^*$	-0.03	0%	0
39	$x_1^*.x_2^*.x_6^*$	-0.17	0.01%	0.02	103	$x_1^*.x_3^*.x_4^*.x_5^*.x_6^*$	-0.03	0%	0
40	$x_2^*.x_5^*.x_7^*$	-0.16	0.01%	0.02	104	$x_2^*.x_4^*.x_5^*.x_6^*$	0.03	0%	0
41	$x_1^*.x_2^*.x_3^*.x_5^*.x_7^*$	-0.16	0.01%	0.02	105	$x_2^*.x_3^*.x_4^*.x_5^*.x_6^*$	-0.03	0%	0
42	$x_4^*.x_5^*.x_7^*$	0.16	0.01%	0.02	106	$x_1^*.x_2^*.x_3^*.x_4^*.x_5^*.x_6^*$	0.03	0%	0
43	$x_1^*.x_3^*.x_4^*.x_5^*.x_7^*$	0.16	0.01%	0.02	107	$x_3^*.x_4^*.x_5^*.x_6^*$	0.03	0%	0

$m$	Coefficients labels	values	Mean error	$\epsilon_m^{2*}$	$m$	Coefficients labels	values	Mean error	$\epsilon_m^{2*}$
44	$x_2^*.x_3^*.x_4^*.x_5^*.x_7^*$	0.16	0.01%	0.02	108	$x_1^*.x_2^*.x_4^*.x_5^*.x_6^*$	-0.03	0%	0
45	$x_2^*.x_4^*.x_5^*.x_7^*$	-0.16	0.01%	0.02	109	$x_2^*.x_5^*.x_6^*$	0.03	0%	0
46	$x_1^*.x_2^*.x_3^*.x_4^*.x_5^*.x_7^*$	-0.16	0.01%	0.02	110	$x_4^*.x_5^*.x_6^*$	-0.03	0%	0
47	$x_3^*.x_4^*.x_5^*.x_7^*$	-0.16	0.01%	0.02	111	$x_3^*.x_5^*.x_6^*$	0.03	0%	0
48	$x_1^*.x_2^*.x_4^*.x_5^*.x_7^*$	0.16	0.01%	0.02	112	$x_1^*.x_2^*.x_5^*$	0.03	0%	0
49	$x_1^*.x_4^*.x_5^*.x_7^*$	-0.16	0.01%	0.02	113	$x_1^*.x_4^*.x_5^*$	-0.03	0%	0
50	$x_2^*.x_3^*.x_5^*.x_7^*$	0.15	0.01%	0.01	114	$x_1^*.x_3^*.x_4^*.x_5^*$	0.03	0%	0
51	$x_1^*.x_2^*.x_5^*.x_7^*$	0.15	0.01%	0.01	115	$x_1^*.x_2^*.x_4^*.x_5^*$	0.03	0%	0
52	$x_1^*.x_2^*.x_3^*.x_6^*$	0.15	0.01%	0.01	116	$x_2^*.x_3^*.x_4^*.x_5^*$	0.03	0%	0
53	$x_1^*.x_3^*.x_6^*$	-0.15	0.01%	0.01	117	$x_2^*.x_4^*.x_5^*$	-0.03	0%	0
54	$x_2^*.x_3^*.x_6^*$	-0.14	0.01%	0.01	118	$x_1^*.x_2^*.x_3^*.x_4^*.x_5^*$	-0.03	0%	0
55	$x_1^*.x_2^*.x_4^*.x_6^*$	-0.13	0.01%	0.01	119	$x_5^*.x_6^*$	-0.03	0%	0
56	$x_2^*.x_4^*.x_6^*$	0.13	0.01%	0.01	120	$x_3^*.x_4^*.x_5^*$	-0.03	0%	0
57	$x_1^*.x_4^*.x_7^*$	-0.12	0.01%	0.01	121	$x_2^*.x_3^*.x_5^*$	0.03	0%	0
58	$x_2^*.x_3^*.x_4^*.x_6^*$	-0.12	0.01%	0.01	122	$x_4^*.x_5^*$	0.03	0%	0
59	$x_1^*.x_2^*.x_3^*.x_4^*.x_6^*$	0.12	0.01%	0.01	123	$x_1^*.x_2^*.x_4^*.x_7^*$	0.01	0%	0
60	$x_1^*.x_3^*.x_4^*.x_6^*$	-0.12	0.01%	0.01	124	$x_2^*.x_4^*.x_7^*$	-0.01	0%	0
61	$x_2^*.x_6^*$	0.11	0.01%	0.01	125	$x_1^*.x_2^*.x_3^*.x_4^*.x_7^*$	-0.01	0%	0
62	$x_3^*.x_4^*.x_6^*$	0.11	0%	0.01	126	$x_2^*.x_3^*.x_4^*.x_7^*$	0.01	0%	0
63	$x_1^*.x_5^*.x_6^*.x_7^*$	-0.1	0%	0.01	127	$x_1^*.x_3^*.x_4^*.x_7^*$	0.01	0%	0
64	$x_1^*.x_2^*.x_5^*.x_6^*.x_7^*$	0.1	0%	0.01	128	$x_3^*.x_4^*.x_7^*$	0	0%	0

### A.3 Statistical model of system autonomy

The following table displays sorted coefficients labels and values of a statistical model for the prediction of **system autonomy**. It also provides the mean relative error value of a statistical model with  $m$  coefficients, and the dimensionless sum of squared differences between the calculated value and the truncated statistical model value.

Table 6 – sorted coefficients labels and values and error characteristics of a statistical model for the prediction of system autonomy

$m$	Coefficients labels	values	Mean error	$\epsilon_m^{2*}$	$m$	Coefficients labels	values	Mean error	$\epsilon_m^{2*}$
1	$c$	6.5	236.9%	127.7	65	$x_1^*.x_2^*.x_3^*.x_4^*.x_5^*.x_6^*$	0.07	0.93%	0.25
2	$x_1^*$	3.8	107.1%	85.4	66	$x_1^*.x_2^*.x_5^*.x_6^*$	-0.07	0.78%	0.23
3	$x_6^*$	-3.7	-13.5%	44.2	67	$x_2^*.x_4^*.x_5^*.x_6^*$	0.07	0.63%	0.22
4	$x_1^*.x_6^*$	-2.7	45.4%	22.6	68	$x_5^*.x_6^*.x_7^*$	0.07	0.59%	0.21
5	$x_4^*$	-1.2	30.1%	18.6	69	$x_1^*.x_2^*.x_3^*.x_5^*.x_6^*$	0.07	0.44%	0.19

A. Appendix 1: Detailed coefficients of statistical models

$m$	Coefficients labels	values	Mean error	$\epsilon_m^{2*}$	$m$	Coefficients labels	values	Mean error	$\epsilon_m^{2*}$
6	$x_3^*$	-1.1	14.1%	14.7	70	$x_2^*.x_3^*.x_6^*.x_7^*$	0.07	0.48%	0.18
7	$x_7^*$	0.95	6.9%	12	71	$x_1^*.x_2^*.x_3^*.x_6^*.x_7^*$	-0.06	0.53%	0.17
8	$x_1^*.x_7^*$	0.78	10.6%	10.2	72	$x_1^*.x_2^*.x_6^*.x_7^*$	0.06	0.59%	0.15
9	$x_1^*.x_4^*$	-0.62	16.9%	9	73	$x_2^*.x_6^*.x_7^*$	-0.06	0.65%	0.14
10	$x_6^*.x_7^*$	-0.58	19.9%	8.1	74	$x_3^*.x_4^*.x_5^*.x_6^*$	0.06	0.52%	0.13
11	$x_4^*.x_6^*$	0.57	25.2%	7.1	75	$x_3^*.x_4^*.x_6^*.x_7^*$	-0.06	0.48%	0.12
12	$x_1^*.x_4^*.x_6^*$	0.52	21.4%	6.3	76	$x_3^*.x_5^*$	0.06	0.35%	0.11
13	$x_1^*.x_6^*.x_7^*$	-0.49	19.7%	5.6	77	$x_4^*.x_5^*.x_6^*$	-0.05	0.24%	0.1
14	$x_2^*$	-0.44	16.7%	5	78	$x_2^*.x_4^*$	0.05	0.25%	0.09
15	$x_1^*.x_2^*.x_3^*$	-0.41	14.4%	4.5	79	$x_1^*.x_2^*.x_3^*.x_4^*$	0.05	0.25%	0.09
16	$x_2^*.x_3^*$	0.41	12.1%	3.9	80	$x_1^*.x_2^*.x_4^*$	-0.05	0.26%	0.08
17	$x_1^*.x_2^*$	0.4	9.4%	3.5	81	$x_2^*.x_3^*.x_4^*$	-0.05	0.26%	0.07
18	$x_1^*.x_3^*.x_6^*$	0.36	6.2%	3.1	82	$x_1^*.x_5^*.x_7^*$	-0.05	0.22%	0.06
19	$x_3^*.x_7^*$	-0.33	6.2%	2.7	83	$x_1^*.x_4^*.x_6^*.x_7^*$	0.04	0.28%	0.06
20	$x_1^*.x_3^*.x_7^*$	-0.33	6%	2.4	84	$x_3^*.x_5^*.x_6^*.x_7^*$	-0.03	0.26%	0.06
21	$x_3^*.x_6^*$	0.33	9.3%	2.1	85	$x_1^*.x_4^*.x_5^*.x_7^*$	0.03	0.28%	0.05
22	$x_1^*.x_5^*$	0.24	8.6%	1.9	86	$x_3^*.x_5^*.x_7^*$	0.03	0.29%	0.05
23	$x_1^*.x_3^*.x_6^*.x_7^*$	0.21	8.6%	1.8	87	$x_1^*.x_3^*.x_5^*.x_6^*$	-0.03	0.22%	0.05
24	$x_3^*.x_6^*.x_7^*$	0.19	8.7%	1.7	88	$x_1^*.x_4^*.x_5^*.x_6^*.x_7^*$	-0.03	0.2%	0.04
25	$x_3^*.x_4^*$	0.19	9%	1.6	89	$x_1^*.x_3^*.x_4^*.x_7^*$	0.03	0.19%	0.04
26	$x_1^*.x_3^*.x_5^*$	-0.17	8.6%	1.5	90	$x_1^*.x_3^*.x_4^*.x_5^*.x_6^*.x_7^*$	0.03	0.17%	0.04
27	$x_1^*.x_3^*.x_4^*.x_6^*$	-0.15	8.7%	1.4	91	$x_3^*.x_4^*.x_6^*$	0.03	0.19%	0.04
28	$x_5^*.x_6^*$	-0.14	8.4%	1.4	92	$x_1^*.x_2^*.x_4^*.x_5^*.x_6^*.x_7^*$	0.03	0.17%	0.04
29	$x_4^*.x_7^*$	-0.14	8.7%	1.3	93	$x_1^*.x_2^*.x_3^*.x_4^*.x_5^*.x_6^*.x_7^*$	-0.02	0.15%	0.03
30	$x_4^*.x_5^*$	-0.14	8.4%	1.3	94	$x_1^*.x_2^*.x_5^*.x_6^*.x_7^*$	0.02	0.14%	0.03
31	$x_3^*.x_4^*.x_5^*$	0.13	8.1%	1.2	95	$x_2^*.x_3^*.x_5^*.x_6^*.x_7^*$	0.02	0.12%	0.03
32	$x_1^*.x_2^*.x_6^*$	0.12	7.5%	1.2	96	$x_2^*.x_3^*.x_4^*.x_5^*.x_6^*.x_7^*$	0.02	0.1%	0.03
33	$x_1^*.x_2^*.x_5^*$	-0.12	7.3%	1.1	97	$x_1^*.x_3^*.x_4^*.x_5^*.x_7^*$	-0.02	0.11%	0.03
34	$x_1^*.x_2^*.x_3^*.x_5^*$	0.12	7%	1.1	98	$x_2^*.x_5^*.x_6^*.x_7^*$	-0.02	0.09%	0.02
35	$x_1^*.x_2^*.x_4^*.x_5^*$	-0.11	6.7%	1	99	$x_1^*.x_2^*.x_3^*.x_5^*.x_6^*.x_7^*$	-0.02	0.08%	0.02
36	$x_2^*.x_3^*.x_5^*$	-0.11	6.4%	1	100	$x_2^*.x_4^*.x_5^*.x_6^*.x_7^*$	-0.02	0.06%	0.02
37	$x_1^*.x_2^*.x_3^*.x_4^*.x_5^*$	0.11	6.2%	0.97	101	$x_3^*.x_4^*.x_5^*.x_6^*.x_7^*$	-0.02	0.04%	0.02
38	$x_2^*.x_5^*$	0.11	5.9%	0.93	102	$x_2^*.x_4^*.x_5^*.x_7^*$	0.02	0.05%	0.02
39	$x_1^*.x_2^*.x_3^*.x_6^*$	-0.11	5.4%	0.89	103	$x_2^*.x_4^*.x_6^*.x_7^*$	-0.02	0.05%	0.02
40	$x_2^*.x_3^*.x_4^*.x_5^*$	-0.11	5.1%	0.86	104	$x_2^*.x_5^*.x_7^*$	0.02	0.06%	0.02
41	$x_2^*.x_4^*.x_5^*$	0.11	4.9%	0.82	105	$x_2^*.x_3^*.x_4^*.x_5^*.x_7^*$	-0.02	0.07%	0.01
42	$x_2^*.x_3^*.x_6^*$	0.11	4.4%	0.78	106	$x_1^*.x_2^*.x_3^*.x_5^*.x_7^*$	0.02	0.08%	0.01
43	$x_2^*.x_4^*.x_6^*$	0.11	4.4%	0.74	107	$x_1^*.x_2^*.x_5^*.x_7^*$	-0.02	0.09%	0.01
44	$x_1^*.x_2^*.x_3^*.x_4^*.x_6^*$	0.11	4.3%	0.71	108	$x_1^*.x_2^*.x_3^*.x_4^*.x_5^*.x_7^*$	0.02	0.1%	0.01
45	$x_2^*.x_3^*.x_4^*.x_6^*$	-0.11	4.2%	0.67	109	$x_2^*.x_3^*.x_5^*.x_7^*$	-0.02	0.11%	0.01

A. Appendix 1: Detailed coefficients of statistical models

$m$	Coefficients labels	values	Mean error	$\epsilon_m^{2*}$	$m$	Coefficients labels	values	Mean error	$\epsilon_m^{2*}$
46	$x_1^*.x_2^*.x_4^*.x_6^*$	-0.11	4.2%	0.64	110	$x_2^*.x_3^*.x_4^*.x_6^*.x_7^*$	0.02	0.11%	0.01
47	$x_3^*.x_5^*.x_6^*$	0.1	4%	0.61	111	$x_1^*.x_2^*.x_4^*.x_5^*.x_7^*$	-0.02	0.12%	0.01
48	$x_1^*.x_3^*.x_4^*.x_5^*$	-0.1	3.7%	0.58	112	$x_1^*.x_2^*.x_4^*.x_6^*.x_7^*$	0.02	0.11%	0.01
49	$x_2^*.x_6^*$	-0.1	3.2%	0.55	113	$x_1^*.x_5^*.x_6^*.x_7^*$	0.02	0.13%	0.01
50	$x_4^*.x_6^*.x_7^*$	0.1	3%	0.52	114	$x_1^*.x_2^*.x_3^*.x_4^*.x_6^*.x_7^*$	-0.02	0.13%	0
51	$x_1^*.x_4^*.x_5^*$	0.09	2.8%	0.5	115	$x_4^*.x_5^*.x_6^*.x_7^*$	0.02	0.11%	0
52	$x_5^*.x_7^*$	-0.09	2.8%	0.47	116	$x_3^*.x_4^*.x_5^*.x_7^*$	0.01	0.12%	0
53	$x_2^*.x_3^*.x_7^*$	-0.08	2.7%	0.45	117	$x_1^*.x_3^*.x_5^*.x_6^*.x_7^*$	0.01	0.11%	0
54	$x_1^*.x_2^*.x_3^*.x_7^*$	0.08	2.5%	0.43	118	$x_1^*.x_3^*.x_4^*$	0.01	0.09%	0
55	$x_1^*.x_4^*.x_5^*.x_6^*$	0.08	2.4%	0.41	119	$x_1^*.x_2^*.x_4^*.x_7^*$	-0.01	0.09%	0
56	$x_1^*.x_2^*.x_7^*$	-0.08	2.2%	0.39	120	$x_2^*.x_3^*.x_4^*.x_7^*$	-0.01	0.09%	0
57	$x_2^*.x_7^*$	0.08	2%	0.37	121	$x_1^*.x_3^*$	0.01	-0.04%	0
58	$x_3^*.x_4^*.x_7^*$	0.08	2%	0.35	122	$x_1^*.x_2^*.x_3^*.x_4^*.x_7^*$	0.01	-0.04%	0
59	$x_1^*.x_4^*.x_7^*$	-0.08	1.9%	0.34	123	$x_5^*$	0.01	-0.03%	0
60	$x_1^*.x_3^*.x_4^*.x_5^*.x_6^*$	-0.08	1.7%	0.32	124	$x_1^*.x_5^*.x_6^*$	-0.01	-0.01%	0
61	$x_2^*.x_3^*.x_5^*.x_6^*$	-0.07	1.5%	0.3	125	$x_2^*.x_4^*.x_7^*$	0.01	-0.01%	0
62	$x_2^*.x_3^*.x_4^*.x_5^*.x_6^*$	-0.07	1.4%	0.29	126	$x_1^*.x_3^*.x_5^*.x_7^*$	-0.01	0%	0
63	$x_2^*.x_5^*.x_6^*$	0.07	1.2%	0.28	127	$x_4^*.x_5^*.x_7^*$	-0.01	0%	0
64	$x_1^*.x_2^*.x_4^*.x_5^*.x_6^*$	-0.07	1.1%	0.26	128	$x_1^*.x_3^*.x_4^*.x_6^*.x_7^*$	0	0%	0

## B Appendix 2: Detailed results from energy analysis

Numbers in header lines are provided to disambiguate refer to the same numbers than in table III.9 and figure III.20c. Differential values are given in intensive units and relative units.

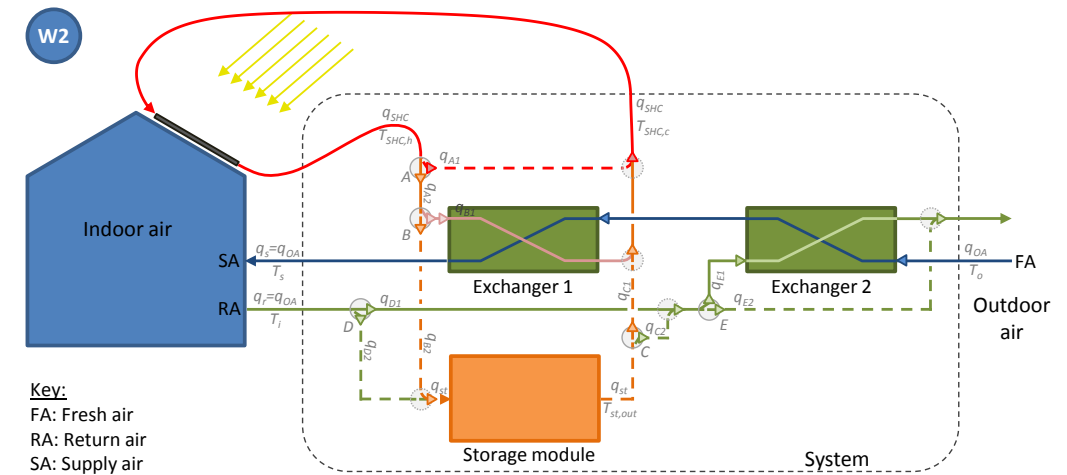
Table 8 – Influence of thermophysical properties on heat conversion and heat losses. Heat variations are expressed in  $kWh.m^{-3}$ .

Factors	Heat densities		Conversion efficiency 6/3	Heat losses variations		
	Absorbed 3	Released 6		Direct 2L	Cooldown 3L+4L	Discharge 5L
$\gamma_{\Delta H}$	+66.4	+46.7	+22.4 <i>pt</i>	+29.2	-0.1	+19.8
	+53.6%	+53.3%	+31.7%	+16.3%	-0.4%	+197.3%
$M_v$	-57.6	-33.3	-9.9 <i>pt</i>	-196.4	+0.5	-24.8
	-46.5%	-38.0%	-14.0%	-109.6%	+1.9%	-247.6%
$\gamma_{q_e}$	+50.8	+31.9	+10.9 <i>pt</i>	+18.3	-0.3	+19.2
	+41.0%	+36.4%	+15.4%	+10.2%	-1.0%	+191.5%
$c_a$	-13.1	-11.8	-8.3 <i>pt</i>	-24.3	+0.1	-1.5
	-10.6%	-13.4%	-11.7%	-13.5%	+0.5%	-14.8%
$C_{p_v}$	+0.9	-1.8	-1.6 <i>pt</i>	+24.8	+0.0	+2.7
	+0.8%	-2.0%	-2.3%	+13.8%	0.0%	+27.1%
$\lambda_f$	+25.4	+0.3	-8.9 <i>pt</i>	+8.7	+29.2	-4.1
	+20.5%	+0.3%	-12.6%	+4.9%	+111.2%	-40.6%
$\rho_s$	+13.9	-9.5	-12.9 <i>pt</i>	-12.4	-2.8	+26.2
	+11.2%	-10.9%	-18.2%	-6.9%	-10.7%	+261.5%
$\epsilon_b$	-11.4	-4.3	0.0 <i>pt</i>	-3.7	-4.2	-2.9
	-9.2%	-5.0%	0.0%	-2.1%	-15.8%	-28.5%

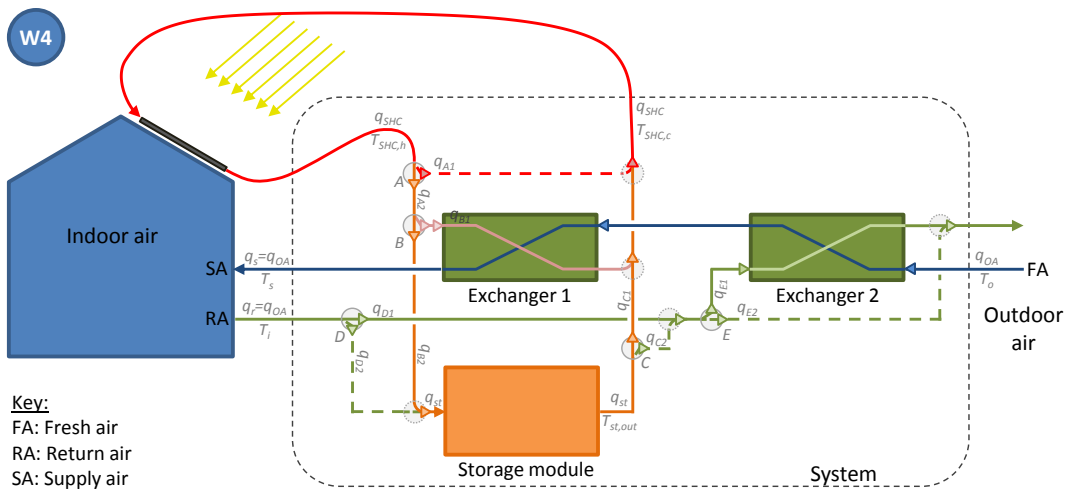
Table 9 – Influence of operating conditions and reactor shape on heat conversion and heat losses. Heat variations are expressed in  $kWh.m^{-3}$ .

Factors	Heat densities		Conversion efficiency	Heat losses variations		
	Absorbed 3	Released 6		Direct 2L	Cooldown 3L+4L	Discharge 5L
$\varphi_{in,charge}$	-23.9	-25.5	-10.0 <i>pt</i>	-15.9	-1.0	+2.7
	-19.3%	-29.1%	-14.2%	-8.9%	-4.0%	+26.7%
$\varphi_{in,discharge}$	-0.7	+17.8	+19.9 <i>pt</i>	+1.8	-0.2	-18.3
	-0.5%	+20.3%	+28.1%	+1.0%	-0.7%	-182.5%
$L_z$	-5.5	-6.7	-2.8 <i>pt</i>	+3.2	-1.7	+2.9
	-4.5%	-7.6%	-3.9%	+1.8%	-6.5%	+28.6%
$\dot{V}_{in,discharge}$	-0.5	+2.5	+3.0 <i>pt</i>	-0.3	-0.2	-2.8
	-0.4%	+2.8%	+4.2%	-0.1%	-0.7%	-28.0%
$T_{in,charge}$	+17.3	+3.9	-8.6 <i>pt</i>	+48.4	+10.4	+3.0
	+13.9%	+4.4%	-12.2%	+27.0%	+39.7%	+29.6%
$\dot{V}_{in,charge}$	+2.3	+2.9	+1.3 <i>pt</i>	+31.6	+0.3	-0.9
	+1.8%	+3.3%	+1.9%	+17.6%	+1.2%	-8.8%
$S$	-4.2	-3.0	+0.0 <i>pt</i>	+5.2	-1.2	+0.1
	-3.4%	-3.4%	+0.1%	+2.9%	-4.7%	+0.8%

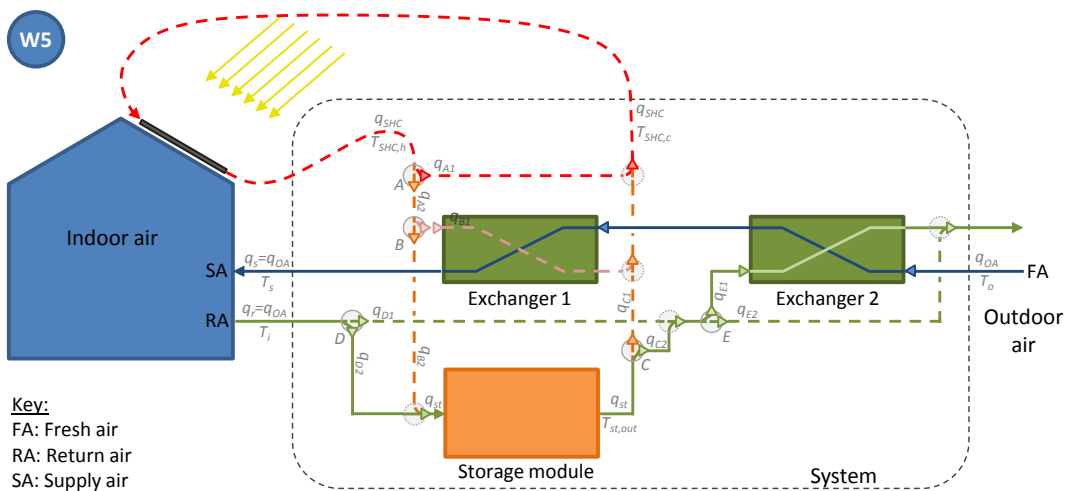
## C Appendix 3: Possible system configurations



(a) Heat recovery and solar heating configuration (W2)

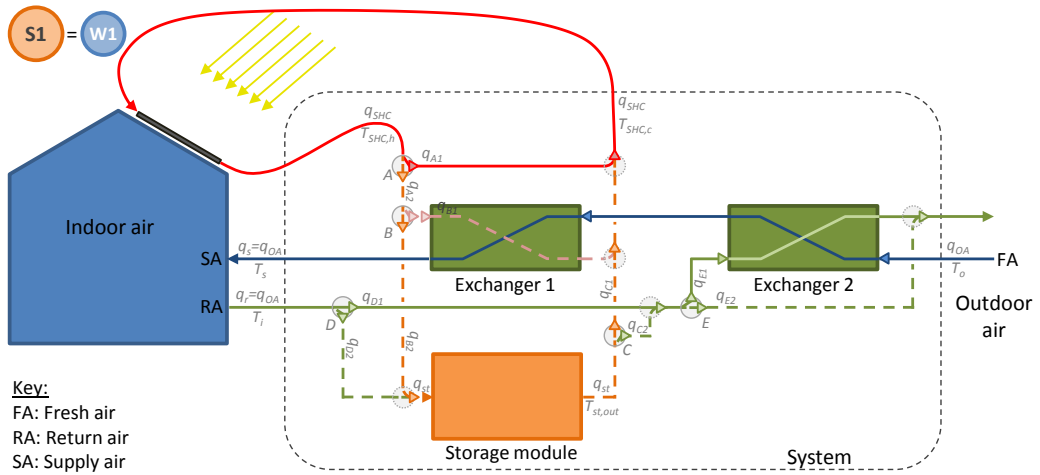


(b) Solar heating and heat storage configuration (W4)

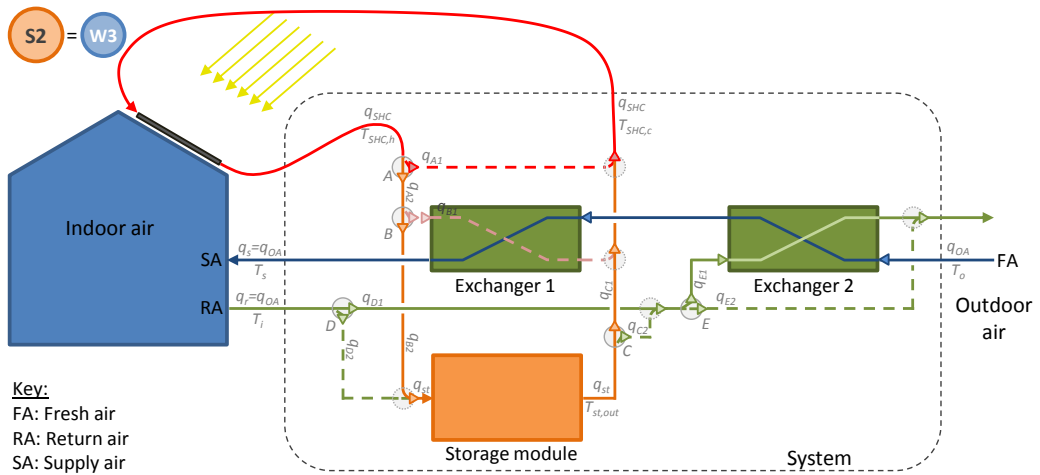


(c) Storage discharge configuration (W5)

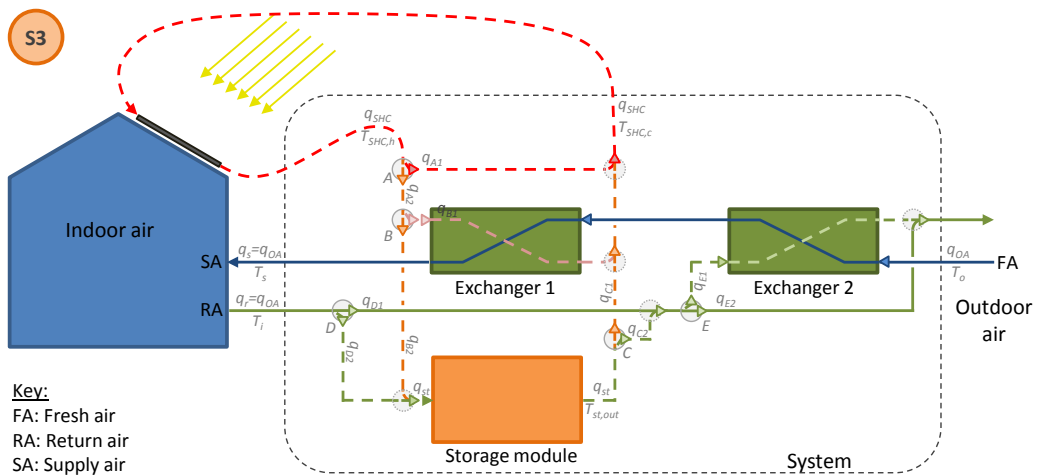
Figure 1 – System variants



(a) Heat recovery configuration (W1 and S1)



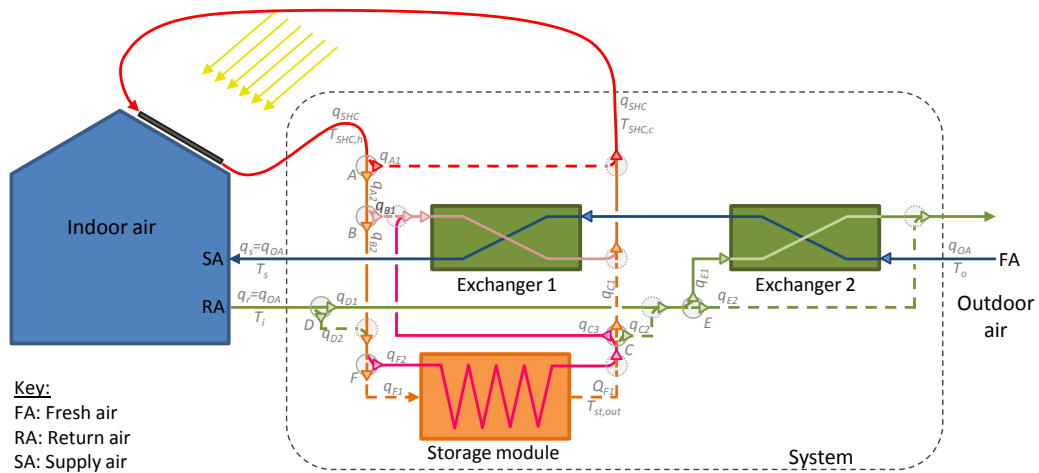
(b) Heat recovery and heat storage configuration (W3 and S2)



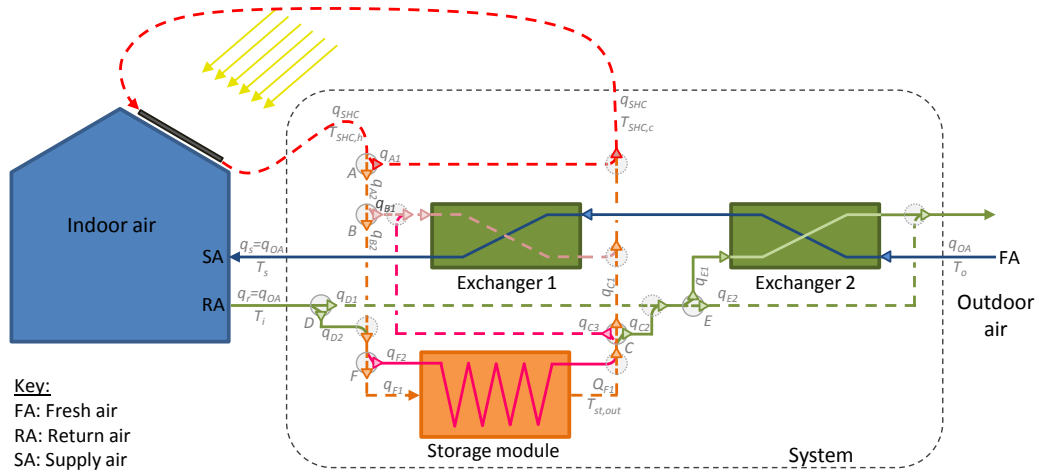
(c) Free-cooling (night ventilation - S3)

Figure 2 – System variants

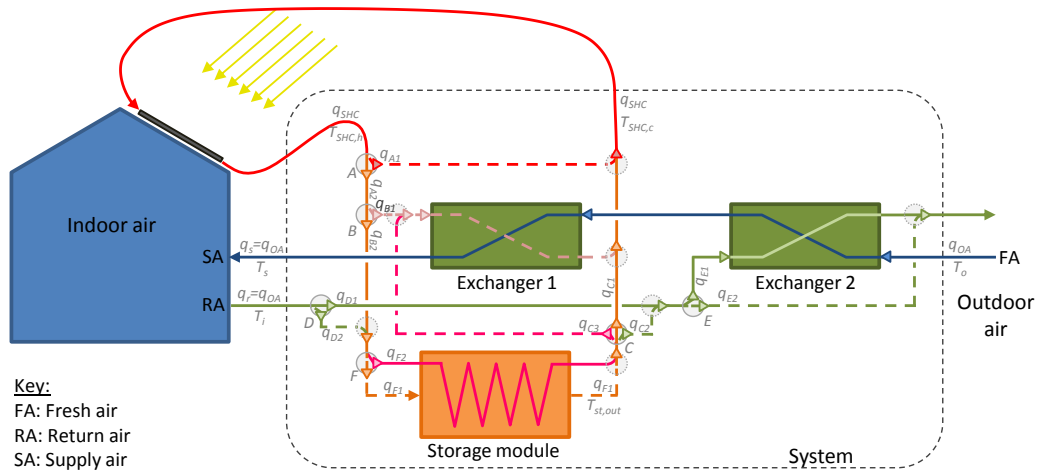
C. Appendix 3: Possible system configurations



(a) Storage system preheating and cascaded direct heating of the building (W6 - Enhanced system)



(b) Sensible storage disch (W7 - Enhanced system)



(c) heat recovery ventilation and storage system preheating (S4 - Enhanced system)

Figure 3 – Enhanced system variants



# Specification Requirements for Inter-Seasonal Heat Storage Systems in a Low Energy Residential House

Damien GONDRE<sup>a,b,\*</sup>, Kévyen JOHANNES<sup>a,c</sup>, Frédéric KUZNIK<sup>a,b</sup>

<sup>a</sup> Université de Lyon, CNRS

<sup>b</sup> INSA-Lyon, CETHIL, UMR5008, F-69621, Villeurbanne, France

<sup>c</sup> Université Lyon 1, F-69622, France

---

## Abstract

This paper aims at providing sizing information concerning a thermal storage system in the case of a low energy consumption building ( $< 50 \text{ kWh/m}^2.y$ ). Numerical simulations for a reference individual building were run for twenty-three different cities in Europe. Results show a clear correlation between annual heat demand  $Q_y$  and annual heating degree-day (HDD):  $Q_y = f_1(HDD)$ . There is also a good correlation between power demand and  $HDD$ . But as heat coverage of the entire heating period may be too ambitious, the analysis goes further. It presents a correlation between heating demand  $Q$  and  $HDD$  as a function of the storage system autonomy  $t$  of the form  $Q = (1 - \exp(-\frac{t}{\tau})) \times Q_y$  with  $\tau = f_2(HDD)$ . It also gives the absolute distribution of sorted power demand values as a function of  $HDD$  in the form of a power sizing chart. The purpose of this chart is to provide specifications for the sizing of a thermal storage system intended to partially cover energy needs and power demand of a low energy residential house.

### Keywords:

Low energy residential house, heat energy demand estimation, heat power demand estimation, heating degree days, thermal storage system sizing

---

## Nomenclature

Symbols					
		$Q_y$	annual thermal energy needs,		$\text{kWh.m}^{-2}.y^{-1}$
$HDD$	heating degree-day	$R_{max}^{[t]}$	maximum fraction of annual energy needs to be provided in order to cover any period of $t$ consecutive days		
$HDH$	heating degree-hour				
$P_d$	design power,	$W.m^{-2}$		$t$	system autonomy, <i>days</i>
$P_{max}$	maximum power,	$W.m^{-2}$		$T$	temperature, °C
$Q$	thermal energy needs,	$\text{kWh.m}^{-2}$		$T_b$	base temperature for HDD calculation, °C
$Q_{st}$	thermal energy to be stored,	$\text{kWh.m}^{-2}.y^{-1}$		$T_{max}$	daily maximum temperature, °C
				$T_{mean}$	daily average temperature, °C
				$T_{sp}$	setpoint temperature, °C

---

\* Phone: +33 472 438 468, Fax: +33 472 438 522

Email address: damien.gondre@insa-lyon.fr

(Damien GONDRE)

Preprint submitted to Energy Conversion and Management

03/01/2016

Heating Degree Days (*HDD*) is one of those methods and it depends only on weather conditions. A clear correlation between building energy needs and *HDD* can then be found only if building energy performance and internal gains remain constant. As stated in the introduction part, storage volume is an important issue for user acceptance. It is shown in [8] that reasonable storage volume can be achieved only with chemical heat storage which also has the advantage to be low time dependent. Energy densities of  $250 \text{ kWh.m}^{-3}$  are mentioned in [17] for adsorption processes and up to  $780 \text{ kWh.m}^{-3}$  for chemisorption. Potential materials suitable for chemical heat storage in residential applications are listed in [18] but research in this field is still at an early stage and there are large differences between theoretical energy densities and experimental results ([9]). In this paper, the building energy performance is designed to meet low-energy buildings requirements. Reasonable seasonal heat storage is indeed possible only if building energy needs are low. Figure 1 displays storage volume of a TES system covering full annual thermal energy needs of a  $100 \text{ m}^2$  low energy residential house. It shows storage volume may already be higher than an acceptable value considering the climate harshness and the thermal energy storage density of the system. For that reason, this paper only focuses on low energy residential buildings. Figure 1 also illustrates why it is important to be able to design a TES system that is aimed at providing only a partial coverage of annual thermal energy needs.

Figure 1 shows the system volume is already an issue if the volume calculation is based on energy storage capacity. But as kinetics considerations appears to be even more limiting than energy storage density [12], volume issues will be higher when using heating power demand as a sizing factor unless the system is not designed on maximum power demand.

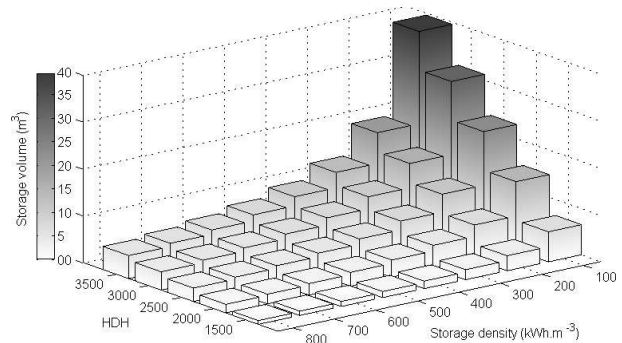


Figure 1: Storage volume of a TES system covering full annual thermal energy needs of a  $100 \text{ m}^2$  low energy residential house as a function of energy storage density of TES system and as a function of climate (given by HDH value - see equation 2 below for more details)

## 2.1. Methodology

### 2.1.1. Building thermal energy needs estimation

Trnsys 17 software is used for all the simulations [19]. Simulation time step and time base (used for wall transfer function calculation in the multizone building component (type 56)) are both set to 15 minutes in order to accurately estimate heat power demand. The test case of this study is a two-story residential house of  $100 \text{ m}^2$  [20]. Wall layout and material properties used in the simulation are described in table 1.

Each floor is described by a rectangular cuboid of  $6.5 \text{ m}$  by  $7.5 \text{ m}$  by  $2.7 \text{ m}$ . Windows have a U-value of  $1.29 \text{ W.m}^{-2}.K^{-1}$  and a frame fraction of 15 %. Wall surfaces and glazing ratios are described in table 2. The south oriented facade is over-hanged by a balcony on the ground floor and by the roof on the first floor.

The construction is designed for a four-member family with three bedrooms, a bathroom upstairs and a living room downstairs including a kitchen. Occupancy profiles and internal gains are arbitrarily defined to represent the thermal load generated by this family. A sensible heat load of  $80 \text{ W}$  per

Table 2: Wall surfaces and glazing ratios

Floor	Side	Area ( $m^2$ )	Glazing ratio
First	South	20.25	30 %
	North	20.25	4.3 %
Floor	East	17.55	7.5 %
	West	17.55	13 %
Ground	South	20.25	51 %
	North	20.25	4.3 %
floor	East	17.55	5.7 %
	West	17.55	20 %

person is taken into account. Appliances run mainly in the early morning and in the evening and account for all electronic devices used in the house. The same appliances profile is repeated every day while two different occupancy profiles are used for weekdays and weekends as shown in figure 2. A value of  $10 W.m^{-2}$  is considered for lighting loads when occupancy is planned and total solar radiation ( $IT$ ) is too low. Lights are turned on when  $IT$  is lower than  $120 W.m^{-2}$  and turned off when  $IT$  is higher than  $200 W.m^{-2}$  defining a hysteresis effect which describes user behavior. An ideal heating system calculates at each timestep the exact amount of heat to be supplied to the house in order to reach a given setpoint temperature. Setpoint temperature is changed on schedule :  $19^\circ C$  when occupants are home without sleeping and  $16^\circ C$  when occupants are not home or are supposed to sleep.

Simulations have been carried out for the twenty-four European cities listed in table 3 and representing most European climates according to the Köppen-Geiger classification [21]. For each simulation, energy needs and heat power requirements have been monitored and linked to the  $HDD$ .

### 2.1.2. Calculation of heating degree-day ( $HDD$ )

Annual Heating Degree-Day ( $HDD$ ) is a measurement designed to reflect the energy

Table 1: Wall layout and material properties

Wall Type	Material	Thickness	Thermal cond.	Density	Heat capacity	U-value
		$mm$	$W.m^{-1}.K^{-1}$	$kg.m^{-3}$	$J.kg^{-1}.K^{-1}$	$W.m^{-2}.K^{-1}$
External wall	Concrete	150	0.740	800	648	0.163
	Insulation	200	0.035	12	840	
	Concrete	150	0.740	800	648	
Ground floor	Insulation	250	0.029	15	880	0.114
	Hollow-core slab	160	1.23	1 300	648	
	Concrete	40	1.75	2 400	880	
	Insulation	400	0.035	12	840	
Attic	Plasterboard	13	0.320	850	799	0.087
	Concrete	220	1.75	2 400	880	
Intern. floor	Concrete	220	1.75	2 400	880	7.95

Table 3: List of cities included in the study

Agen (FRA)	London (GB)
Amsterdam (NLD)	Macon (FRA)
Berlin (DEU)	Moscow (RUS)
Bern (DEU)	Nancy (FRA)
Brussels (BEL)	Nice (FRA)
Bucharest (ROU)	Prague (CZE)
Budapest (HUN)	Rennes (FRA)
Carpentras (FRA)	Riga (LVA)
Copenhagen (DNK)	Stockholm (SWE)
Dublin (IRL)	Trappes (FRA)
Helsinki (FIN)	Vienna (AUT)
La Rochelle (FRA)	Warsaw (POL)

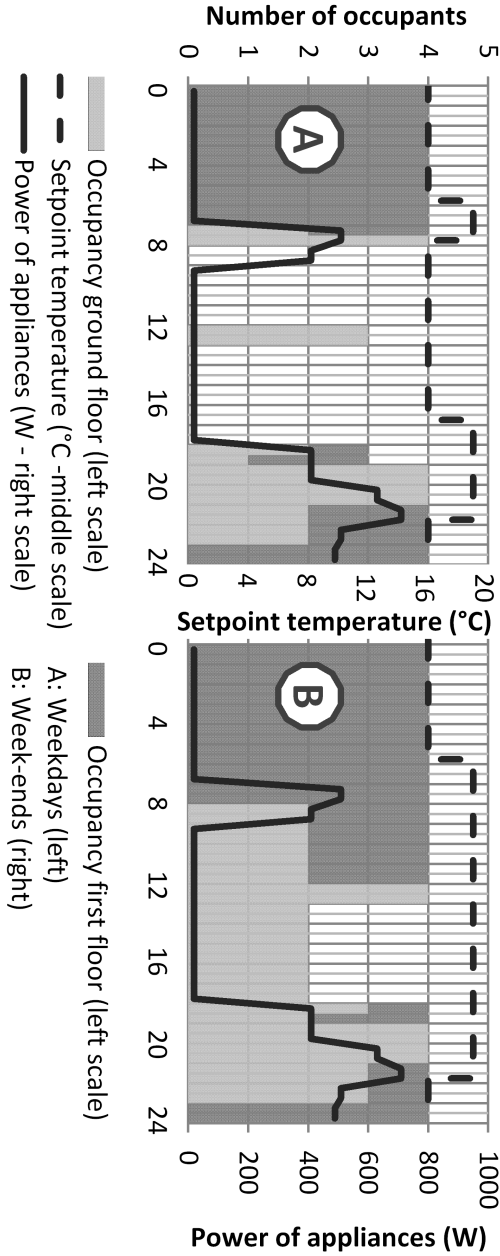


Figure 2: Occupancy schedules, internal gains and set-point temperatures for weekdays and weekends as a function of time

needs of a building. *HDD* are usually defined as:

$$HDD = \sum_{k=1}^{365} \max \left[ \left( T_b - \frac{T_{k,max} - T_{k,min}}{2} \right) \times 24; 0 \right] \times \delta_k \quad (1)$$

$$\begin{cases} \text{with} \\ T_b : \text{base temperature} \\ T_{k,max} : \text{max temperature of the } k^{\text{th}} \text{ day} \\ T_{k,min} : \text{min temperature of the } k^{\text{th}} \text{ day} \\ \delta_k = \begin{cases} 1, & \text{during heating season} \\ 0, & \text{else} \end{cases} \end{cases}$$

Definition of  $\delta_k$  may vary from a reference to another. The base temperature  $T_b$  is set as a constant for the whole calculation. It is linked to the setpoint temperature reduced by the average contribution of solar gain (generally  $3^\circ\text{C}$ ). For a setpoint temperature of  $21^\circ\text{C}$ , the corresponding base temperature is  $18^\circ\text{C}$ . The principle of the *HDD* method lies in the fact that daily heating needs are proportional to the temperature difference between  $T_b$  and  $T_{mean}$  (daily average temperature). But as the setpoint temperature used in the simulation is not constant, it is not relevant to use a constant base temperature. A better correlation is found between energy needs (or power) and *HDD* with a variable base temperature. The calculation is not based on a one-day scale anymore but on an hourly scale. The index thus defined can be

named Heating Degree-Hour (*HDH*).

$$HDH = \sum_{k=1}^{8760} \max[(T_{sp,k} - 3) - T_k; 0] \times \delta_k \quad (2)$$

$$\left\{ \begin{array}{l} \text{with} \\ T_{sp,k} : \text{setpoint temperature of the } k^{th} \text{ hour} \\ T_k : \text{temperature of the } k^{th} \text{ hour} \\ \delta_k = \begin{cases} 1, & \text{during heating season} \\ 0, & \text{else} \end{cases} \end{array} \right.$$

As Europe is in northern hemisphere,  $\delta_k$  will be set to 1 at the calculation beginning (January). It will change to 0 at the end of the heating season and finally change back to 1 at next heating season beginning. Since different climates are tested, heating season must be mathematically defined. Four days are chosen as constants:  $D_{\downarrow w,b}$  (March 15<sup>th</sup>),  $D_{\downarrow w,e}$  (June 15<sup>th</sup>),  $D_{\uparrow w,b}$  (August 15<sup>th</sup>),  $D_{\uparrow w,e}$  (November 15<sup>th</sup>).

- In the range  $[D_{\uparrow w,e}; D_{\downarrow w,b}]$ ,  $\delta_k = 1$  (heating season for all climates).
- In the range  $[D_{\downarrow w,e}; D_{\uparrow w,b}]$ ,  $\delta_k = 0$ .
- In the range  $[D_{\downarrow w,b}; D_{\downarrow w,e}]$ ,  $\delta_k$  may change from 1 to 0 if  $T_{max,k} > 18$  and  $T_{sp,mean} - 3 - T_{mean} \leq 2$ .
- Conversely,  $\delta_k$  may change from 0 to 1 in the range  $[D_{\uparrow w,b}; D_{\uparrow w,e}]$ , if  $T_{max,k} < 18$  and  $T_{sp,mean} - 3 - T_{mean} \geq 2$ .

## 2.2. Results

Results show a clear correlation between annual thermal energy needs  $Q_y$  and *HDH* but also between maximal power consumption  $P_{max}$  and *HDH* (figure 3) for climates with *HDH* above 1000. *HDH* under 1000 have been excluded from the correlation since they correspond to very mild climates where the installation of a TES system is not profitable.

These results can be used for a rough estimation of thermal energy needs and maximum

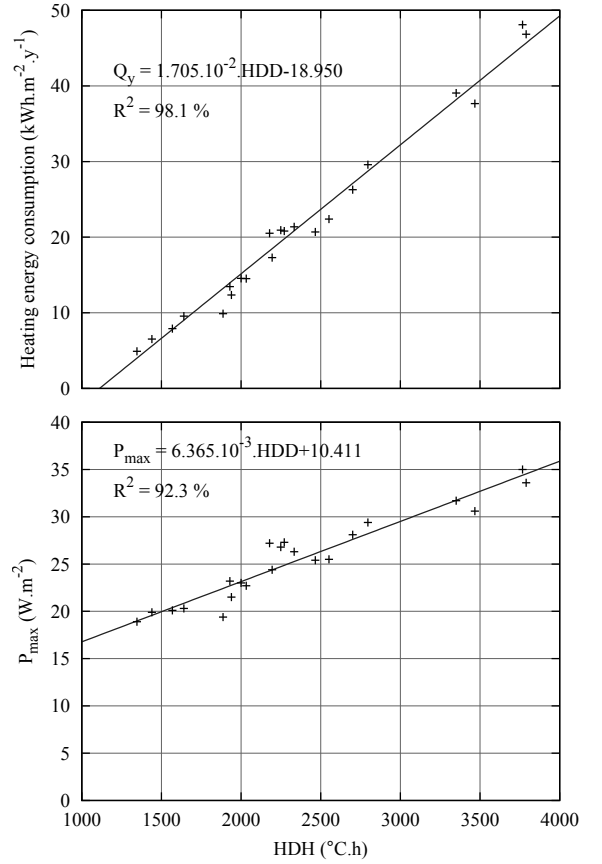


Figure 3: Annual energy needs and maximal power as a function of HDH

power consumption of low energy residential houses similar to the present case-study and for all kind of climates (at least in Europe) with a *HDH* above 1000. A linear correlation between  $P_{max}$  and *HDH* (equation 3) is found with a correlation factor of 89.8 %.

$$Q_y = 1.705 \cdot 10^{-2} \times HDH - 18.95 \quad (3)$$

and

$$P_{max} = 6.365 \cdot 10^{-3} \times HDH + 10.41 \quad (4)$$

As explained in the current section introduction, these two variables depend on climate but also on building performance and internal gains. These results may then not be extended to residential houses with different energy performances or too different internal gains. But the method may be reproduced easily in particular in buildings with lower energy standards ( $> 50 \text{ kWh} \cdot \text{m}^{-2} \cdot \text{y}^{-1}$ ). Indeed, the *HDH* method is a good estimation of heat losses while internal gains and solar gains tend to modify the results. A building with a lower energy performance will have a higher share of heat losses and then the correlation between *HDH* and heating demand will be better.

The same kind of correlation can also be found for a partial coverage of the energy needs. Results can be exploited only for the twenty or forty coldest days for instance. It may also be focused on a specific part of the day when the overall domestic energy demand is the highest. These detailed results may be interesting for the design of a thermal inter-seasonal storage system that is not bound to provide building overall heating needs but only aims at reducing power peak demand.

### 3. Detailed design information for a long-term energy storage system

#### 3.1. Design based on heating energy needs

A long-term energy storage system is not necessarily designed to fulfill annual thermal

energy needs of a building. It may be designed to work only under certain conditions as mentioned previously. The system might work only during the coldest days or only during a specific part of the day. It may also – in addition – use part load and store energy in mid-season or even in winter. In order to design the system for a shorter period of time than the entire heating season, it is interesting to calculate the maximum possible energy needs to be provided over a given period of time. In other words, the goal is to find - for a given autonomy (in the range of 1 to 150 days) - the worst series of days as regards to energy consumption and express this amount of energy to be provided as a percent value of the overall annual energy needs. One example is given in figure 4 for the city of London (UK).

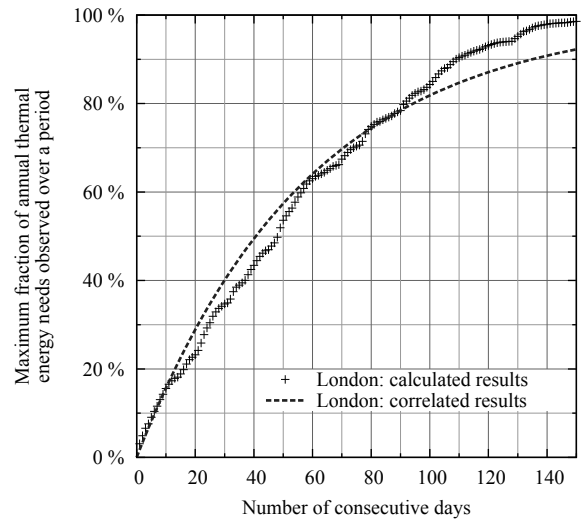


Figure 4: Maximum fraction of annual thermal energy needs observed over a period of consecutive days for the city of London

Figure 4 displays the maximum fraction  $R_{max}^{[t]}$  of annual thermal energy needs over a given period of time  $t$  (expressed in consecutive days). This evolution follows an exponential law:

$$R_{max}^{[t]} = 1 - \exp\left(\frac{-t}{\tau}\right) \quad (5)$$

where  $\tau$  is the time constant of evolution (expressed in  $day^{-1}$ ). It characterizes the distribution of heating needs during increasingly longer periods of consecutive coldest days. The time constant value is equal to the duration of the shortest (and coldest) period of consecutive days when 63 % of the annual needs are required to meet comfort requirements.  $\tau$  is the only correlation parameter and is set in order to minimize the root mean square (rms) difference between calculated and correlated values. The method is repeated for each of the twenty-four cities studied. The overall shape of the calculation curve is always the same. The time constant  $\tau$  can then be calculated for each city. The  $\tau$  values are correlated to the  $HDH$  values as shown in figure 5.

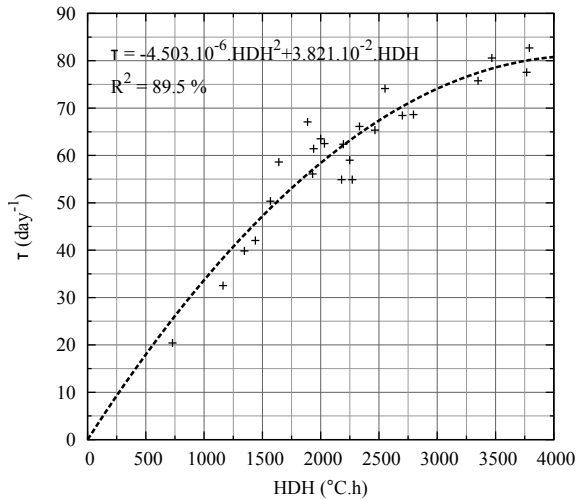


Figure 5: Evolution of time constant of maximum energy needs over a period of consecutive days as a function of  $HDH$

Correlated values of  $\tau$  are calculated using equation 6 which is a result from figure 5.

$$\tau = -4.50 \cdot 10^{-6} \times HDH^2 + 3.82 \cdot 10^{-2} \times HDH \quad (6)$$

The use of correlated values of  $\tau$  instead of calculated values increases the rms difference between correlated and calculated values of  $R_{max}^{[t]}$  from 0.270 to 0.371 (for 150 values) but

does not change the standard deviation (4.26 % vs. 4.24 %). Then, it is satisfying to use correlated values of  $\tau$  in order to estimate  $R_{max}^{[t]}$  values (even if the coefficient of determination  $R^2$  is only 89.5 %). It means that  $R_{max}^{[t]}$  values depend only on  $HDH$  as expressed in equation 5 and equation 6.

Since it is possible to assess the annual thermal energy needs of a low energy residential house only by knowing the  $HDH$  of its climate (see equation 2), it is then also possible to estimate the energy  $Q_{st}^{[t]}$  to be stored by a thermal storage system by setting its autonomy and by knowing the  $HDH$  of the place where it will be used (equation 7).

$$Q_{st}^{[t]} = \left( 1 - \exp\left(\frac{-t}{\tau}\right) \right) \times (1.705 \cdot 10^{-2} \times HDH - 18.95) \quad (7)$$

with  $\tau = -4.50 \cdot 10^{-6} \times HDH^2 + 3.82 \cdot 10^{-2} \times HDH$

Equation 7 enables to draw the sizing chart of figure 6. The sizing chart is a very fast way to get a rough idea of the size of a storage system used in a low energy residential house.

### 3.2. Design based on maximum power

The same kind of considerations can be carried out on maximal power. In order to size a storage system, the energy to be stored will not necessarily be the limiting factor. Even in low energy buildings, thermal power involved to heat the building can be large. As thermal power developed by a thermal storage system is often an issue [12], such systems are not always designed to meet maximum power demand. This section presents a study on power demand distribution and establishes a correlation between  $HDH$  and power demand distribution.

Maximum power values obtained from Trnsys simulations are high compared to literature

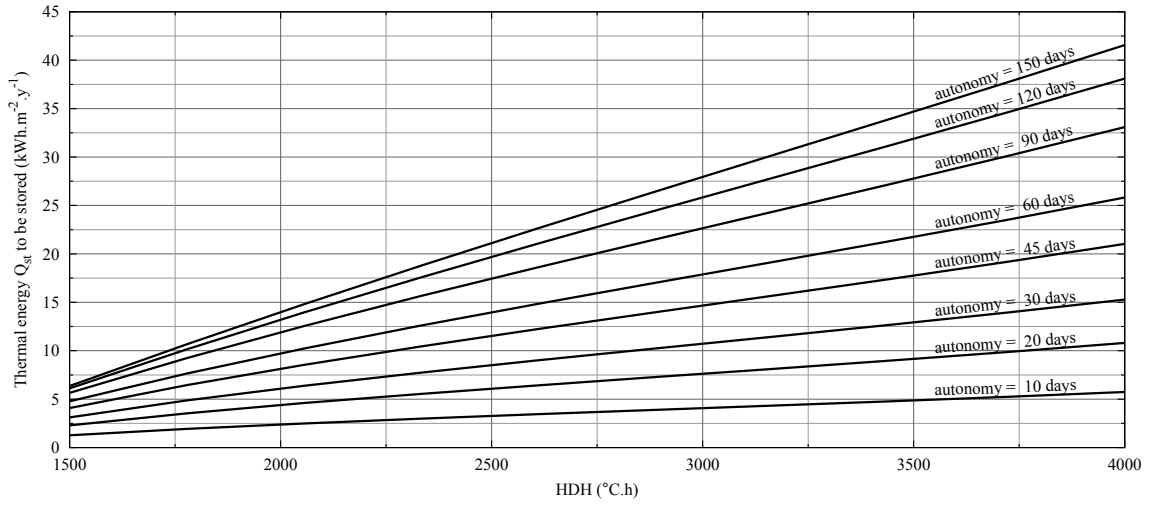


Figure 6: Energy to be stored as a function of HDH and system autonomy

[22]. But a detailed analysis shows that less than 5 % of the values are higher than expected. Three combined factors can explain these differences. First, the setpoint temperature is not constant along the day, second the maximal power is set to an unlimited value in Trnsys and third the time step is 15 minutes. A sudden change in setpoint temperature from 16°C to 19°C leads to a peak demand. As the power is unlimited, it is calculated so that the setpoint temperature is reached within one time step. It leads to significant differences between a one-hour time step calculation and a 15-minute time step calculation. Power values obtained in first instance are then over-estimated [23]. Average power demand  $\bar{P}_k$  and standard deviation  $\sigma_{P,k}$  are calculated for each city. Only values lower than  $\bar{P}_k + 2 \times \sigma_{P,k}$  are considered in the remainder of the study which is, on average, 95 % of the non-zero initial values.

Filtered power demand results are then sorted in decreasing order. Sorted power values follow an exponential decay with a variable decay coefficient (see figure 7). The decay coefficient is calculated on different points in order to get a correlated curve that fit the exponential decay curve. Figure 7 shows for instance

that power demand is below  $15 \text{ W.m}^{-2}$  about 80 % of the time for the city of Berlin. At each point, the decay variable value  $\tau_k(x)$  is given by equation 8.

$$P_k(x) = P_{max,k} \times \exp\left(\frac{-x}{\tau_k(x)}\right)$$

$$\implies \tau_k(x) = \frac{-x}{\ln\left(\frac{P_k(x)}{P_{max,k}}\right)} \quad (8)$$

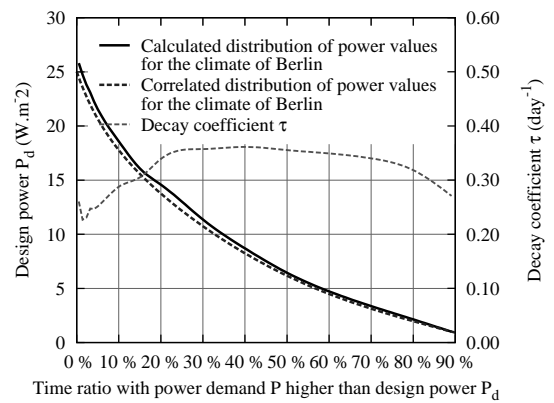


Figure 7: Calculated and correlated distributions of power values sorted in descending order

For Berlin climate, figure 7 gives

$P_{max} = 25.8 \text{ W.m}^{-2}$  and  $P_d = 14.6 \text{ W.m}^{-2}$  at  $x = 20 \%$  which leads to  $\tau_k(20 \%) = 0.34 \text{ day}^{-1}$ .

The decay coefficient variation can be interpolated by a polynomial of degree 5 for each of the twenty-four cities studied (equation 9). The shape of the curve is the same except for the cities of Nice ( $HDH < 1000$ , excluded from the calculations) and La Rochelle (oceanic climate).

$$\tau_k = \sum_{i=0}^5 c_{i,k} \cdot x^i \text{ for } k = \{1, 2, \dots, 24\} \quad (9)$$

The series  $\{c_{5,1}, c_{5,2}, \dots, c_{5,23}\}$ ,  $\{c_{4,1}, c_{4,2}, \dots, c_{4,23}\}$ , ...,  $\{c_{0,1}, c_{0,2}, \dots, c_{0,23}\}$  depend on  $HDH$  value. For each of the six coefficients of equation 9, a linear interpolation is done based on the results of the twenty-three cities considered. An average expression  $\bar{c}_i$  of each of the six coefficients is then proposed (equation 10).

$$\bar{c}_i(HDH) = a_i \times HDH + b_i \text{ for } i = \{0, 1, \dots, 5\} \quad (10)$$

It enables to get a mean expression of  $\tau$  as a function of  $x$  and  $HDH$  (equation 11).

$$\bar{\tau}(x, HDH) = \sum_{i=0}^5 (a_i \times HDH + b_i) \times x^i \quad (11)$$

If the city of Nice ( $HDH < 1000$ ) is excluded, the use of a mean distribution leads to a relative error of 6.4 % in average (and 13.5 % maximum for the Dublin climate) which seems acceptable. The standard deviation of the relative errors distribution is 3.2 %.

Equation 11 is used in order to calculate a correlated distribution of power values. The maximum power value is estimated according to the  $HDH$  value (see equation 4). It is then possible to estimate a design power  $P_d$  according to  $HDH$  value and to the ratio of time  $x$

when the power value will be higher than  $P_d$  (over a year).

$$P_d(x, HDH) = \exp\left(\frac{-x}{\bar{\tau}(x, HDH)}\right) \times (6.365 \cdot 10^{-3} \times HDH + 10.41) \quad (12)$$

Equation 12 is used in order to draw a power sizing chart (figure 8). This chart is a good engineering tool to estimate the maximum power to be delivered by a thermal storage system installed in a low energy residential house.

### 3.3. Design based on both energy needs and power

Sections 3.1 and 3.2 provide information for system sizing based on the energy storage capacity or on the maximum delivering power. But it is not possible to link those two results. That is the purpose of the following section.

The design can be done at first either on energy storage capacity or on deliverable power. Once one of these two parameters is fixed using figure 9 (if energy storage capacity is the designing factor) or figure 10 (if deliverable power is the designing factor), the second one can be optimized using figure 13.

Figure 9 presents a relationship between normalized storage capacity ( $\frac{Q_{st}}{Q_y}$ ), system autonomy (expressed in consecutive days, see section 3.1 for more details) and heating degree-hour ( $HDH$ ). For instance, the city of Lyon has a calculated  $HDH$  of 1741 (as regards with equation 2 and with setpoint temperature profile defined in figure 2). Figure 9 then shows that heating demand for the 60 coldest consecutive days will represent 68 % of the annual heating needs  $Q_y$ .

If the design is primarily done on deliverable power then figure 10 is used instead of figure 9. Figure 10 shows the normalized design power ( $\frac{P_d}{P_{max}}$ ) as a function of time percentage when power will be sufficient for different values of  $HDH$ . In Lyon ( $HDH = 1741$ ), a design power  $P_d$  of only 50 % of the maximum power

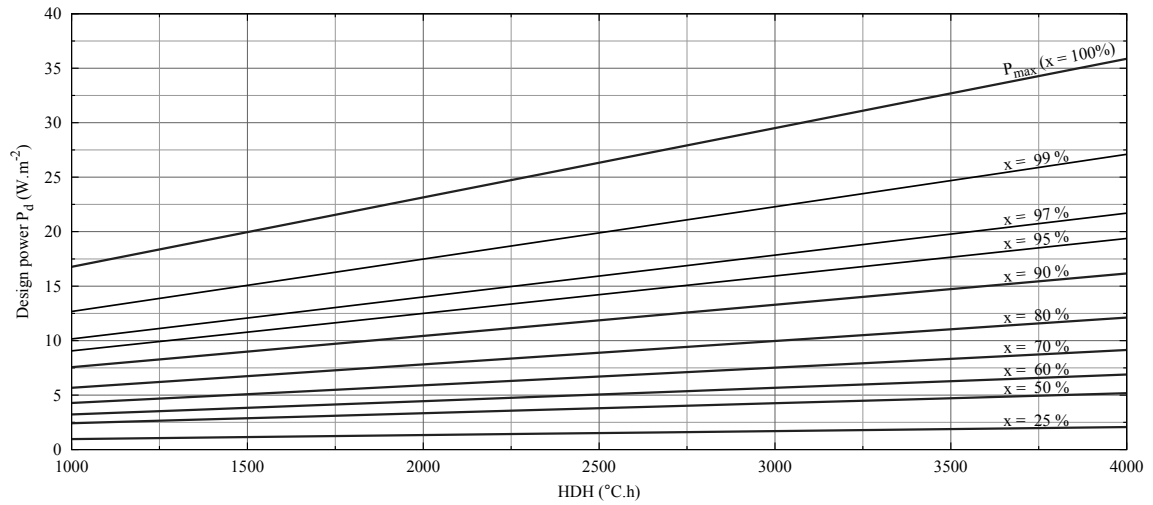


Figure 8: Power sizing chart - Design power value to choose in order to meet power demand in  $x$  percent of the heating time with respect to  $HDH$  value

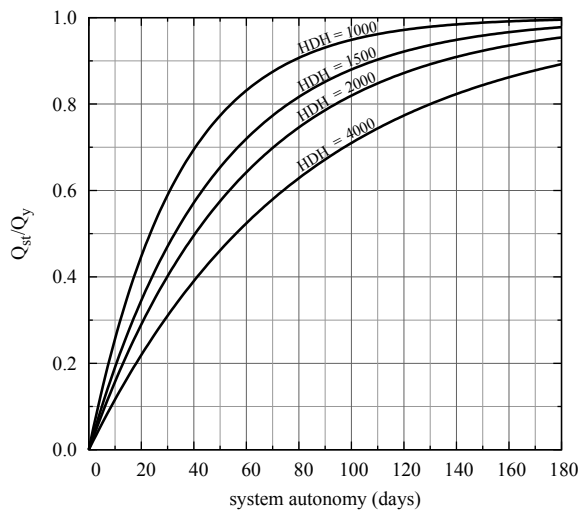


Figure 9: Fraction of annual thermal energy to be stored as a function of designed system autonomy

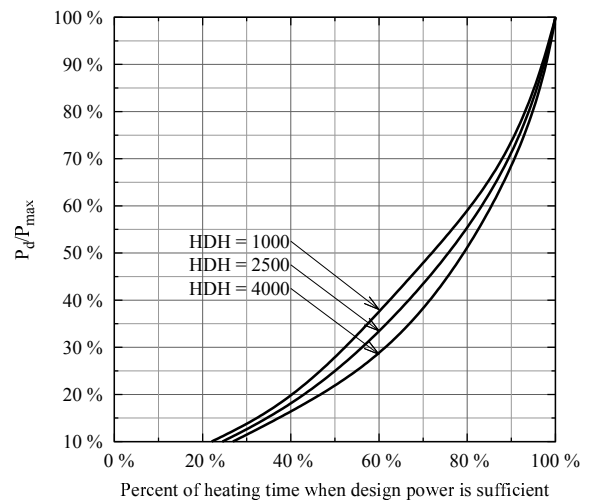


Figure 10: Design power as a function of designed TES system time coverage

$P_{max}$  is sufficient for about 78 % of the time when heat is required.

Once one ratio is defined (either  $\frac{Q_{st}}{Q_y}$  or  $\frac{P_d}{P_{max}}$  depending on which one is supposed to be the limiting factor), the second ratio can be optimized so that both ratios are sized to be system limiting factors. There are three ways to consider the link between heating needs and

deliverable power. This is linked to the control strategy of the system. A TES system can indeed be used either on base-mode (the TES system is used as soon as heat is required - see figure 11.1) or on shaving-mode (the TES system is used only above a given threshold i.e. for peak demand). In this case, it can either be used in order to smooth heating demand (a base production is always provided by an aux-

iliary heater - see figure 11.2) or to reduce peak energy cost (the TES system is used in order to provide most of the heat share during peak demand, when energy is the most expensive - see figure 11.3). The choice between these three strategies will be done according to the TES system strengths and weaknesses. If deliverable power is the limiting factor, the first strategy will be better. If heat storage capacity is the limiting factor, the second strategy will be more appropriate. If deliverable power and energy needs are well balanced, the third strategy could be the most relevant for economic profitability of the system. But in 2013, most of seasonal heat storage systems are more limited by their deliverable power than by their heat storage density. That is the reason why the following results are presented in base-mode (1). It is easy to deduce results for the second strategy from the first one. Results for the third strategy are not presented here.

In the case where none of the three different control strategies presented is excluded because of system constraints, the choice would probably depend on two main factors: the system owner and the electricity pricing policy. If the TES system is purchased by an individual, he will expect an economic profitability. If electricity pricing is constant, the best economic profitability will be reached with the first control strategy (which maximizes use of building integrated renewable intermittent energy source). If electricity pricing depends on demand, the third control strategy will be more profitable for the individual since he will avoid using electricity from the network when it is the most expensive. Now if the TES system is installed or subsidized by the network manager or by the government, it will aim at smoothing peak demand. The second control strategy will better fit if the system is widely diffused but the third one will be more relevant if it remains more confidential (so that one TES system installed in one individual house can offset several non-equipped houses during peak demand).

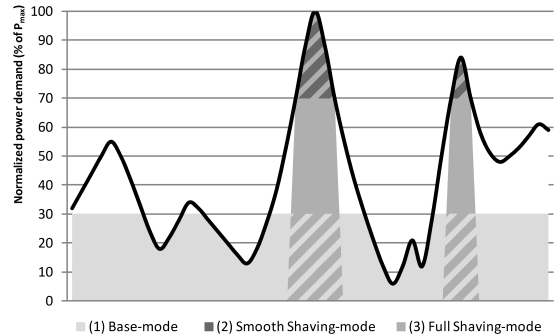


Figure 11: Schematic chart of the three different control strategies discussed. Base-mode (1), Smooth-shaving-mode (2) and Full-shaving-mode (3)

The relationship between the normalized storage capacity and the normalized design power depends on the system autonomy. If the autonomy is set for instance to 30 days, the energy to be stored  $Q_{st}$  will be lower than if the autonomy is set to 90 days whereas annual heating needs  $Q_y$  remains constant.

Figure 12 gives results for a complete seasonal storage (i.e. the autonomy is sufficient to provide heat for the entire heating season). For each of the twenty-four cities of the study, the normalized storage capacity  $Q_{st}$  is calculated for different values of the normalized design power as expressed in equation 13 below.

$$Q_{st,m} = \sum_{i=1}^{8760 \times 4} \min\left(P_i, P_{max} \times \frac{m}{10}\right) \quad (13)$$

with  $m = \{1, 2, \dots, 10\}$

Figure 12 displays one curve for each of the twenty-four cities studied and one mean curve (dashed line). If the cities of Nice and La Rochelle are excluded from the mean curve calculation, the average standard deviation between the mean curve and the calculated curves is no more than 0.5 %.

The same graph can be drawn for different autonomies. The set of curves is then more dispersed than for figure 12 but the average standard deviation between the mean curve and the

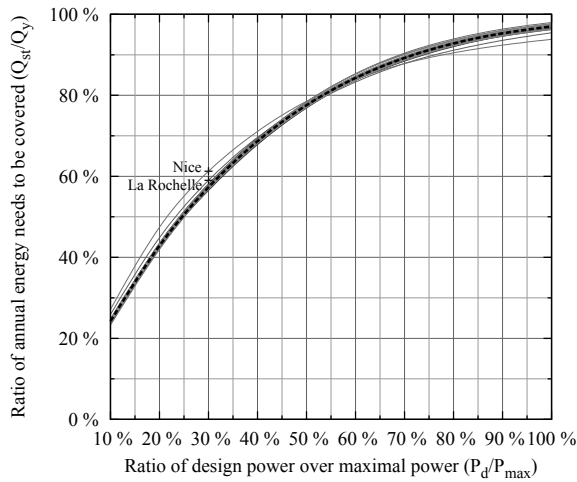


Figure 12: Relationship between normalized storage capacity and normalized design power for the twenty-four cities studied and mean curve (dashed line) for a complete seasonal storage

calculated curves is 3.8 % (maximum 6.0 % for an autonomy if 90 days). Figure 13 displays the mean curves for different autonomies.

*Example of application.* A thermal storage system has to be installed near Lyon, in France, in a 100 m<sup>2</sup> residential house. The system is designed for an autonomy of 90 days and the deliverable power has to be sufficient for at least 80 % of the time. Heating needs capacity will be optimized so that it is neither over-sized nor limiting.

Lyon has an *HDH* of 1741. Equations 3 and 4 give annual energy needs of 10.7 kWh.m<sup>-2</sup>.y<sup>-1</sup> and maximum power of 21.5 W.m<sup>-2</sup> which lead to 1070 kWh.y<sup>-1</sup> and 2.15 kW. Design power is chosen according to figure 10 to 53 % of the  $P_{max}$  :  $P_d = 1.15$  kW. Figure 13 is then used in order to find the best normalized heating capacity. A normalized design power of 53 % and an autonomy of 90 days give a  $\frac{Q_{st}}{Q_y}$  ratio of 60 %. The TES system will then need to store 644 kWh.

These considerations does not take into account a possible attenuation of the power delivered by the TES system along its discharge.

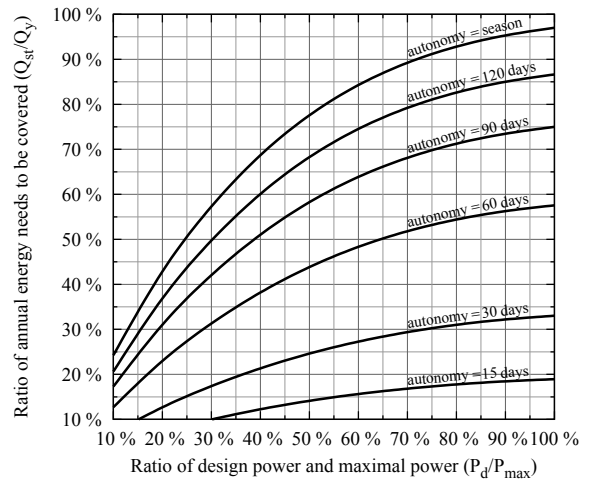


Figure 13: Average relationship between normalized storage capacity and normalized design power for different system autonomies (15, 30, 60, 90, 120 days and the whole heating season)

#### 4. Discussion and conclusion

This paper presents a methodology that enables an estimation of annual thermal energy needs and maximum power consumption for most European climates characterized by their heating degree hour (*HDH*). It also gives detailed information for the design of a thermal storage system that does not aim at providing 100 % of heating needs. It is then possible to assess the energy to be stored by a thermal storage system as a function of the required autonomy. It is also possible to determine the design power based on the percentage of running time when design power is sufficient. This methodology is developed for low energy residential buildings. Results are then only applicable to this kind of buildings which is the best application for thermal storage systems. However the same methodology can be easily applied for other building types.

#### Acknowledgments

This project is funded by the STAID 2010 project of the ANR-Stock E program of the

French National Research Agency and supported by the French competitive clusters AXELERA and TENERDIS.

## References

- [1] IEA, IEA energy statistics - electricity for european union - 27, 2009.
- [2] Eurostat, Energy - yearly statistics 2008, Publications Office of the European Union (2010).
- [3] IEA, OECD, Hydropower essentials, 2010.
- [4] G. W. Hutterer, Geothermal heat pumps: An increasingly successful technology, *World Renewable Energy Congress IV Renewable Energy, Energy Efficiency and the Environment* 10 (1997) 481-488.
- [5] B. Schneider, Storing solar energy in the ground, *FIZ Karlsruhe - Leibniz Institute for Information Infrastructure* (2013).
- [6] E. Ampatzi, I. Knight, R. Wiltshire, The potential contribution of solar thermal collection and storage systems to meeting the energy requirements of north european housing, *Solar Energy* 91 (2013) 402-421.
- [7] J.-C. Hadorn, The need for storage of heat and cold in a low energy buildings, in: *Thermal energy storage for solar and low energy buildings : state of the art / by the IEA Solar Heating and Cooling Task 32, Servei de Publicacions Universidad Lleida*, 2005.
- [8] P. Pinel, C. A. Cruickshank, I. Beausoleil-Morrison, A. Wills, A review of available methods for seasonal storage of solar thermal energy in residential applications, *Renewable and Sustainable Energy Reviews* 15 (2011) 3341-3359.
- [9] S. Hongois, F. Kuznik, P. Stevens, J.-J. Roux, Development and characterisation of a new mgso<sub>4</sub>-zeolite composite for long-term thermal energy storage, *Solar Energy Materials and Solar Cells* 95 (2011) 1831-1837.
- [10] D. Bauer, R. Marx, J. Nußbicker-Lux, F. Ochs, W. Heidemann, H. Müller-Steinhagen, German central solar heating plants with seasonal heat storage, *International Conference CISBAT 2007* 84 (2010) 612-623.
- [11] B. Michel, N. Mazet, S. Mauran, D. Stitou, J. Xu, Thermochemical process for seasonal storage of solar energy: Characterization and modeling of a high density reactive bed, *Asia-Pacific Forum on Renewable Energy* 2011 47 (2012) 553-563.
- [12] S. Hongois, Stockage de chaleur inter-saisonnier par voie thermochimique pour le chauffage solaire de la maison individuelle, Ph.D. thesis, Institut National des Sciences Appliquées de Lyon, Villeurbanne, 2011.
- [13] M. de l'emploi de la cohésion sociale et du logement, Arrêté du 24 mai 2006 relatif aux caractéristiques thermiques des bâtiments nouveaux et des parties nouvelles de bâtiments, 2006.
- [14] E. commission, Low energy buildings in europe: Current state of play, definitions and best practice, 2009.
- [15] I. Jaffal, C. Inard, C. Ghiaus, Fast method to predict building heating demand based on the design of experiments, *Energy and Buildings* 41 (2009) 669-677.
- [16] H.-x. Zhao, F. Magoulès, A review on the prediction of building energy consumption, *Renewable and Sustainable Energy Reviews* 16 (2012) 3586-3592.
- [17] K. E. N'Tsoukpoe, H. Liu, N. Le Pierrès, L. Luo, A review on long-term sorption solar energy storage, *Renewable and Sustainable Energy Reviews* 13 (2009) 2385-2396.
- [18] P. Tatsidjodoung, N. Le Pierrès, L. Luo, A review of potential materials for thermal energy storage in building applications, *Renewable and Sustainable Energy Reviews* 18 (2013) 327-349.
- [19] TESS, TRNSYS - TESS : Thermal energy system specialists, 2008.
- [20] C. Spitz, L. Mora, E. Wurtz, A. Jay, Practical application of uncertainty analysis and sensitivity analysis on an experimental house, *Cool Roofs, Cool Pavements, Cool Cities, and Cool World* 55 (2012) 459-470.
- [21] Markus Kotteck, J. Grieser, C. Beck, B. Rudolf, F. Rubel, World maps of köppen-geiger climate classification updated, *Meteorologische Zeitschrift* (2006) 5.
- [22] K. Thullner, Low-energy buildings in Europe - Standards, criteria and consequences - A study of nine European countries, Technical Report TVIT-10/5019, Lunds tekniska högskola Lunds universitet, Lunds, 2010.
- [23] C. Ghiaus, Causality issue in the heat balance method for calculating the design heating and cooling load, *Energy* 50 (2013) 292-301.



## FOLIO ADMINISTRATIF

### THESE DE L'UNIVERSITE DE LYON OPEREE AU SEIN DE L'INSA LYON

**NOM :** GONDRE

**DATE de SOUTENANCE :** 21/03/2016

**Prénoms :** Damien, Laury

**TITRE :** Numerical modeling and analysis of heat and mass transfers in an adsorption heat storage tank: influences of material properties operating conditions and system design on storage performances

**NATURE :** Doctorat

**Numéro d'ordre :** 2016LYSEI022

**Ecole doctorale :** MEGA

**Spécialité :** Énergétique

**RÉSUMÉ :** Le développement de solutions de stockage de l'énergie est un défi majeur pour permettre la transition énergétique d'un mix énergétique fortement carboné vers une part plus importante des énergies renouvelables. La nécessité de stocker de l'énergie vient de la dissociation, spatiale et temporelle, entre la source et la demande d'énergie. Stocker de l'énergie répond à deux besoins principaux : disposer d'énergie à l'endroit et au moment où on en a besoin. La consommation de chaleur à basse température (pour le chauffage des logements et des bureaux) représente une part importante de la consommation totale d'énergie (environ 35 % en France en 2010). Le développement de solutions de stockage de chaleur est donc d'une grande importance, d'autant plus avec la montée en puissance des énergies renouvelables.

La volume d'un système est un critère important pour la viabilité d'une technologie de stockage et pour son acceptation par ses utilisateurs. Plusieurs technologies de stockage sont envisageables, parmi lesquelles le stockage par adsorption est le plus prometteur en termes de densité de stockage et de maintien des performances sur plusieurs cycles de charge-décharge. Cette thèse se focalise donc sur le stockage de chaleur par adsorption, et traite de l'amélioration des performances du stockage ainsi que de l'amélioration de l'intégration du système au bâtiment. L'approche développée pour répondre à ces questions est purement numérique. Un modèle numérique de réacteur de stockage de chaleur par adsorption est donc développé et validé par des données expérimentales.

A l'heure actuelle, la puissance récupérable en sortie de réacteur est le facteur limitant le développement de solutions viables technologiquement et économiquement. L'influence des propriétés thermophysiques de l'adsorbant et du fluide sur la densité de puissance d'une part, mais aussi sur la densité de stockage et l'autonomie du système, est étudiée. L'analyse des résultats permet de sélectionner les propriétés des matériaux les plus influentes et de mieux comprendre les transferts de chaleur et de masse au sein du réacteur. L'influence des conditions opératoires est aussi mise en avant. Cela montre l'influence de l'humidité relative à la fois sur la capacité de stockage et sur la puissance récupérable et l'influence du débit de décharge sur la puissance. Enfin, il est montré que la capacité de stockage est linéairement dépendante du volume de matériau, tandis que la puissance dépend de la section de passage et que l'autonomie dépend de la longueur du lit d'adsorbant.

Par ailleurs, une analyse de la chaîne énergétique montre que le rapport entre l'énergie absorbée (charge) et relâchée (décharge) est d'environ 70 %. Mais pendant la phase de charge, environ 60% de la chaleur entrant dans le réacteur n'est pas absorbée et est directement relâchée à la sortie. La conversion globale entre l'énergie récupérable et l'énergie fournie n'est donc que de 25 %. Cela montre qu'un système de stockage de chaleur par adsorption ne peut pas être pensé comme un système autonome mais doit être intégré aux autres systèmes de chauffage du bâtiment et aux lois de commande qui les régissent. Une réutilisation intelligente des pertes de chaleur pour le chauffage direct du bâtiment (en hiver) ou pour le préchauffage du fluide chaud (en été) améliore les performances énergétiques globales du bâtiment.

La couverture des besoins par le système de stockage peut être améliorée par une optimisation de l'utilisation de la ressource solaire disponible, particulièrement en hiver. Contrairement aux idées reçues, l'utilisation de la ressource solaire pour chauffer directement le bâtiment n'est pas forcément la meilleure façon d'optimiser la part solaire dans le mix énergétique. Quand l'énergie solaire n'est pas suffisante pour atteindre des températures raisonnablement hautes pour envisager une phase de stockage, le flux à basse température peut être utilisé pour préchauffer le réacteur. En effet, si le matériau de stockage est déjà chaud, le flux à haute température sera plus rapidement utilisé pour désorber de l'eau puisque moins d'énergie sera utilisée pour chauffer le matériau. La ressource solaire utilisée pour le préchauffage n'est pour autant pas perdue. La part récupérée en sortie peut être réutilisée pour le chauffage direct du bâtiment. La part stockée sous forme sensible peut être récupérée plusieurs heures plus tard. Cela confère, a minima, l'avantage de transformer le système de stockage de chaleur par adsorption en un système de stockage combiné sensible/adsorption, avec une solution pour du stockage à long terme et pour du stockage à court terme. L'utilisation du stockage sensible permet en outre d'éviter des décharges sur le potentiel d'adsorption et ainsi d'augmenter l'autonomie globale du système de stockage, tout en optimisant les chances de recharges partielles en hiver.

**MOTS-CLÉS :** Stockage de chaleur hybride sensible/adsorption, isothermes d'adsorption, modèle LDF, transferts couplés de chaleur et de masse, méthodes numériques, optimisation, chaîne de conversion d'énergie, stockage de chaleur.

**Laboratoire de recherche :** Centre d'Énergétique et de Thermique de Lyon (CETHIL – UMR5008)

**Directeur de thèse :** Frédéric KUZNIK

**Président de jury :**

**Composition du jury :** Loïc FAVERGEON, Kévyng JOHANNES, Henner KERSKES, Frédéric KUZNIK, Lingai LUO, Michel PONS, Jean-Jacques ROUX, Jean TOUTAIN